Novel remote sensing of electromagnetic properties

Georgiana Dima

Supervised by

Prof. Ekaterina Shamonina,

Prof. Christopher J. Stevens,

Dr. Anna Radkovskaya

August 15, 2025

Novel remote sensing of electromagnetic properties

Georgiana Dima

Acknowledgements

I would like to express my deepest gratitude to my supervisors, Professor Ekaterina Shamonina, Professor Chris Stevens, and Dr. Anna Radkovskaya, for their guidance and support throughout this journey. Your insight, encouragement, and patience helped shape this work and pushed it in directions I never would have considered on my own.

I also want to thank my colleagues and fellow researchers who have contributed to both the academic and personal experience of this DPhil. I am especially grateful to Grahame Faulkner for his insight, patience, and kindness. Thank you also to Joshua Feis, Ioannis Spanos, Kailun Xu, Jiaruo Yan, Shan Chu, James Farmer, Daffodil Dhaya, Callum Long, Huirui Dai, and Xinyang Li for their contributions, support, and camaraderie.

To my mother – there are no words that do justice to the gratitude I feel. Your strength, love, and unwavering belief in me carried me through even the hardest days. Thank you for everything. I also want to thank my wider family for their continued encouragement, love and kindness throughout the years.

To my wonderful friends (Irina, Diana, Ben, Andreea, Cornelia, Sihana, Fernando, Lucian, Noemi, Paul, Ruxi, Namrah, Cristi, and Saarah) – thank you for being part of my life and bringing so much joy and laughter into it.

To Billy – thank you for your love, patience, and kindness. You've been there through every high and low, and I feel incredibly lucky to share life with you.

Finally, to my therapist – no version of this thesis would exist without you. Your wisdom, compassion, and consistency gave me the tools to carry on when things felt impossible. Thank you for helping me believe in myself again.

Thank you all – this thesis has my name on it, but it was built on your support, love, and belief in me every step of the way.

Novel remote sensing of electromagnetic properties

Georgiana Dima

Abstract

Electromagnetic sensing plays a crucial role in modern technology, enabling contactless detection and monitoring across fields as diverse as medical diagnostics, industrial inspection, security systems, and materials testing. Among the various approaches, inductive sensing stands out for its simplicity, passive nature, and sensitivity to material properties such as conductivity and permeability. While widely used in applications like metal detection or imaging through eddy currents, the fundamental mechanisms that govern these interactions are still not fully understood – particularly when it comes to mapping electromagnetic property variations or localising objects with high spatial accuracy.

This thesis explores how changes in the self-inductance of a resonant element can be exploited to characterise unknown materials and localise conductive objects. It begins with introducing a detailed analytical model describing the behaviour of a single split-ring resonator (SRR) placed near a sample. An analytical method is developed that allows the extraction of electromagnetic properties of materials – specifically, conductivity and permeability – from the shifts in resonant frequency and quality factor caused by the presence of the sample. The model accounts for skin depth effects and probe geometry and is validated both by numerical simulations and experimental results. The method was used to detect low-conductivity saline solutions with a tolerance of 5.5%, and was further tested in a biomedical setting using a 3D simulation of a human torso. Here, changes in lung conductivity caused by fluid accumulation (as might occur in pneumonia or COVID-19) produced measurable shifts in the resonator's response, supporting the potential for low-cost, non-invasive lung monitoring systems based on a single coil.

The second half of the thesis focuses on localisation using magneto-inductive arrays – structured surfaces made of resonant cells coupled to one another. The presence of a conductive object alters the array's local properties, disrupting wave propagation and producing reflections that can be traced back to the object's location. In a one-dimensional

waveguide, both time-domain and frequency-domain reflectometry were used to localise a metallic object. Both methods were aided by the use of a machine learning algorithm, which mapped the changes in the time and frequency domain to object locations with an accuracy exceeding 90%, when objects were placed up to 15 mm above the array. Most notably, the time-domain reflectometry approach achieved error-free localisation up to 12 mm above the array and proved to be a more successful approach when localising objects on one-dimensional arrays. On the other hand, frequency-domain reflectometry proved to be a versatile method which was easily extended to two-dimensional arrays. A neural network was used to localise multiple objects with over 98% accuracy and distinguish between them with 97% confidence. A finger phantom was also successfully tracked, highlighting the potential for smart touch interfaces and human–machine interaction.

Together, these studies demonstrate the versatility of magneto-inductive sensing – from characterising subtle changes in material properties to enabling precise object tracking on structured surfaces. The goal of this thesis is to advance our understanding of how resonant elements and their mutual interactions can be harnessed to develop sensitive, low-cost, and scalable sensing systems for real-world applications.

Contents

CHAPTER 1

Fundamentals

1.1 Introduction

Sensing technologies are the foundation of automated systems. Amongst many, sensors generate inputs for feedback control loops, monitor environmental factors such as humidity and temperature, enable interfaces between humans and computers, and image inside the human body. With technology developing rapidly, research into high-performance sensors is gaining popularity. Electromagnetic sensors are non-invasive, compact, and versatile devices that leverage the different electromagnetic properties of materials. Electromagnetic sensors function on various principles and have a wide range of applications. Inductive proximity sensors, such as metal detectors [1–3], identify the location of metallic or magnetic objects. Hall effect sensors [4–6] measure the magnitude of magnetic fields and are employed in the automotive industry to monitor wheel speed for anti-lock braking systems (ABS). Radar sensors [7–9] emit electromagnetic waves and monitor the reflections to infer properties of objects such as material, shape, and speed. Because of their non-invasive nature, electromagnetic sensors are widely popular in medicine,

with techniques including magnetocardiography (MCG) [10, 11], magnetoencephalography (MEG) [12], magnetic resonance imaging (MRI) [13], and electric impedance tomography (EIT) [14].

This thesis explores the use of inductive sensors for electromagnetic property detection, focusing on split-ring resonators (SRRs) and their interactions with nearby materials. A range of sensing applications are developed by leveraging the changes in self-inductance when a resonator is placed near a medium with properties different from air.

Chapter 1 introduces the fundamentals of metamaterials, which will be relevant for the remainder of the thesis. **Chapter 2** develops an analytical framework for electromagnetic property detection using a single SRR, adapting the well-established model of Dodd and Deeds [15, 16] to resonant elements. Conductivity and permittivity extraction methods are formulated, and design principles for optimising sensor performance are provided. **Chapter 3** extends this work to detecting low-conductivity materials, achieving experimental measurement of conductivities in the range of $(0.04 - 20)\,\mathrm{S/m}$ with an accuracy of 94.5%. CST Studio Suite [17] is used to numerically simulate water accumulation in the lungs and explore the feasibility of using a single SRR sensor to detect it.

Chapters 4 and 5 shift focus to object localisation using magnetoinductive (MI) waveguides – arrays of SRRs with strong inter-element coupling, enabling propagation of slow magnetoinductive waves. **Chapter 4** extends the frequency-domain localisation work of Yan et al. [18] by using a neural network algorithm to localise objects of different shapes and conductivity on 1D and 2D metamaterial arrays. This method relies on the changes in the standing wave pattern of an array caused by the presence of foreign objects. Characterisation of different high-conductivity objects is performed, further enhancing the practical viability of the method. **Chapter 5** further extends the localisation work by developing an alternative method which uses time-domain reflectometry of MI waves and analysing the time-domain localisation abilities of 1D arrays. Trivedi et al. [19] had previously proven that ideal defects can be located on a 1D MI array by monitoring the time of flight of the reflection pulse. In this work, the method is significantly expanded

by incorporating partial disruptions of the array caused by an object placed at different distances above the array. The strength of the reflection is used to gain insight into the object's vertical position above the array. Two different types of excitation pulses (i.e. a square pulse and a modulated Gaussian pulse) are analysed and compared. Localisation and characterisation are performed using two distinct methods. The first method is an analytical one, based on the time-of-flight and strength of the reflection pulse, whilst the second one is a neural network-based approach.

This thesis studies the sensing capabilities of metamaterial atoms and arrays through analytical modelling, experimental validation, and numerical simulations. Novel sensing of electromagnetic properties is achieved using a simple split-ring resonator, and MI arrays are used to successfully localise real objects. The findings of this thesis deepen the understanding of non-invasive magnetic sensors and bring them closer to real-world applications such as biomedical diagnosis, industrial sensing, and object tracking.

The work in this thesis resulted in the following publications:

- G. Dima, A. Radkovskaya, L. Solymar, *et al.*, "Inductive sensing of lung conductivity for fluid accumulation detection," in *Proc. 19th Int. Congr. Artif. Mater. Novel Wave Phenom. (Metamaterials 2025)*, 2025. under review
- G. Dima, C. Stevens, H. Dai, "Neural network based remote localiser for two objects," in *Proc. 19th Int. Congr. Artif. Mater. Novel Wave Phenom. (Metamaterials 2025)*, 2025. under review
- G. Dima, C. J. Stevens, "Spatial localisation and sensing in two dimensions via metasurfaces," *Sci. Rep.*, vol. 14, 24156, 2024
- G. Dima, I. Spanos, C. J. Stevens, "2D localisation using magneto-inductive waveguides," in *Proc. 18th Int. Congr. Artif. Mater. Novel Wave Phenom. (Metamaterials 2024)*, 2024
- G. Dima, C. McMahon, A. Radkovskaya, *et al.*, "Time-domain reflectometry for imaging conductive environment," in *Proc. 18th Int. Congr. Artif. Mater. Novel Wave Phenom. (Metamaterials 2024)*, 2024

- G. Dima, A. Radkovskaya, C. J. Stevens, *et al.*, "Design of a remote, multi-range conductivity sensor," *Sensors*, vol. 23, 9711, 2023
- G. Dima, A. Radkovskaya, C. Stevens, *et al.*, "Full-range contactless conductivity detection," in *Proc. 16th Int. Congr. Artif. Mater. Novel Wave Phenom. (Metamaterials 2022)*, 128, 2022
- X. Li, G. Dima, A. Radkovskaya, *et al.*, "Neural network-based conductivity imaging using time-domain reflectometry," in *Proc. 19th Int. Congr. Artif. Mater. Novel Wave Phenom. (Metamaterials 2025)*, 2025. under review
- D. Dhayaa, C. Long, A. Radkovskaya, *et al.*, "Sensing using magnetoinductive waves," in *Coupled Structures for Microwave Sensing*, 427, Springer, Cham, 2024
- C. Long, A. Radkovskaya, G. Dima, *et al.*, "Metamaterials for characterisation of conductive objects using time-domain reflectometry of magnetoinductive waves," in *Proc. 17th Int. Congr. Artif. Mater. Novel Wave Phenom. (Metamaterials 2023)*, 205, 2023
- D. Dhayaa, A. Radkovskaya, J. Yan, *et al.*, "Metamaterials for sensing conductive objects using time-domain reflectometry of magnetoinductive waves," in *Proc. 16th Int. Congr. Artif. Mater. Novel Wave Phenom. (Metamaterials 2022)*, 125, 2022

The experimental data and relevant codes are available in a public GitHub repository.

1.2 Metamaterials

Metamaterials are artificial structures with properties not exhibited by naturally occurring materials. Even if their practical implementation was only achieved in 2000 by Smith et al. [31], their history dates back to 1904 when Schuster [32] discussed the possibility of a negative phase velocity. In 1967, Veselago [33] analysed the theoretical behaviour of a material with simultaneous negative permittivity and permeability. He concluded that such a material would have a negative refractive index and could serve as a novel lens. More than 30 years later, Smith et al. [31] combined rods, found to exhibit negative permittivity by Rotman [34] and Pendry et al. [35], with split-ring resonators, found to

exhibit negative permeability by Thompson [36] and Pendry et al. [37]. The result was the first practical implementation of what Schuster and Veselago had theorised decades before: a material with a negative refractive index capable of supporting backwards-propagating waves. In the past 25 years, the field of metamaterials has grown rapidly, leading to a wide range of applications including wireless power transfer [38], invisibility cloaks [39], subwavelength imaging [40], and highly directive antennas [41]. The field is growing further, and the applications are becoming more advanced and directed towards public needs. Metamaterials enable accurate control over electromagnetic responses, making them suitable for sensing applications, which were studied extensively in the recent years [42–45]. For instance, terahertz metamaterial absorbers demonstrated enhanced resonance shifts and amplitude modulation in response to analyte refractive index variations, with figures-of-merit significantly higher than conventional designs [43, 46]. In the microwave regime, triple-circle SRR sensors operating around 9–10 GHz show frequency shifts up to 100 MHz and amplitude changes of several dB when exposed to different oils or chemical liquids [47, 48]. Such platforms have been applied in practical sensing—including food quality testing, chemical contamination detection, biomedical diagnostics, and environmental monitoring—by leveraging compact, low-cost, and integrable metamaterial sensor designs [43–45]. In biomedical sensing, metamaterials are increasingly applied to detect biomolecules, monitor physiological parameters, and enable non-invasive diagnostics [46, 49, 50]. Split-ring resonator–based biosensors have been used for label-free glucose detection in aqueous solutions, achieving sensitivities of several MHz per mg/dL glucose concentration [49]. Terahertz metasurfaces allow identification of proteins, DNA, and even individual viruses by detecting sub-femtomolar changes in dielectric properties [46]. Metamaterial-based wearable sensors have also been demonstrated for real-time monitoring of hydration levels, sweat composition, and blood glucose in non-invasive configurations, offering compactness and compatibility with flexible substrates [50].

This thesis focuses on tailoring the properties of meta-atoms, the unit constituents of metamaterials, and on their interactions to facilitate the remote sensing of electromagnetic properties.

1.2.1 Split-ring resonators (SRRs)

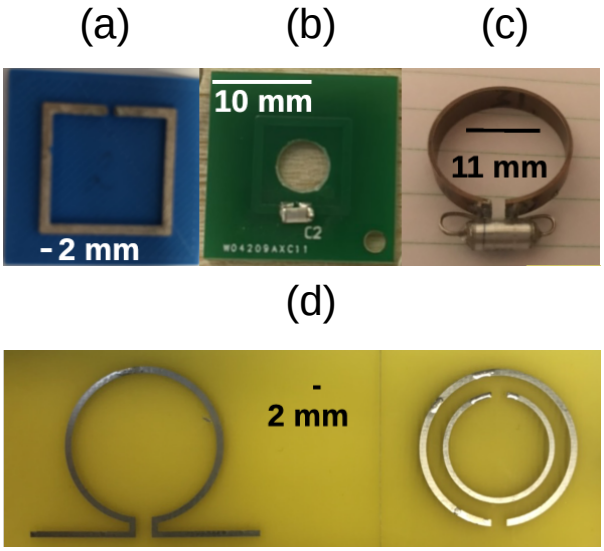

Figure 1.1: Examples of split-ring resonators: (a) 3D printed, single-gap resonator created with silver conductive paint, (b) printed circuit board (PCB), single gap resonator tuned using an off-the-shelf surface mount capacitor, (c) split pipe tuned using an off-the-shelf axial capacitor, (d) Ω-shaped (left) and double-split (right) PCB resonators.

Split-ring resonators (SRRs) are a class of meta-atoms which exhibit electrical resonances. They are usually simple metallic loops tuned to a specific frequency (known as the resonant frequency, f_{res}) through an attached capacitor or a carefully tailored physical gap. Fig. 1.1 shows examples of split-ring resonators fabricated using 3D printing (a), printed circuit board technology (b, d), and as free-standing structures (c). The designs include both square-shaped resonators (a, b) and circular-shaped ones (c, d).

From a circuit-theory standpoint, the element can be modelled as an RLC circuit – a series network containing a resistor (R), a capacitor (C) and an inductor (L), shown in Fig. 1.2. The equivalent impedance (Z) of an element can be written as follows:

$$Z = R + j\omega L + \frac{1}{j\omega C}. \tag{1.1}$$

When the element is excited with a voltage, V, the current, I, in the element is given by:

$$I = \frac{V}{Z} = \frac{V}{R + j\omega L + \dfrac{1}{j\omega C}} \tag{1.2}$$

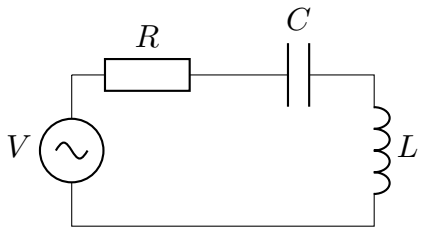

Figure 1.2: RLC circuit model for a split ring resonator.

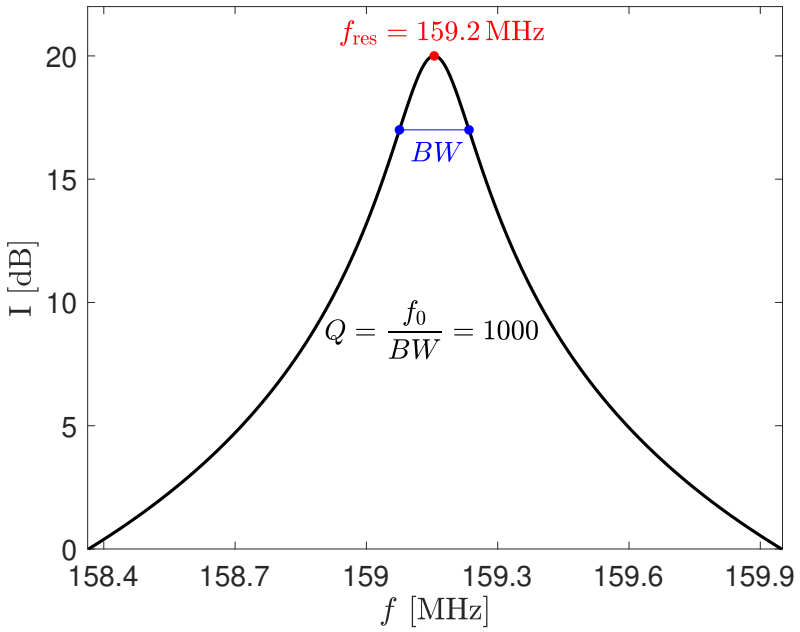

Figure 1.3: Current in split-ring resonator with $R = 0.1\,\Omega$, $C = 10\,\text{pF}$ and $L = 100\,\text{nH}$.

The absolute value of the current, I, is plotted in Fig. 1.3 for a fictitious element of resistance $R = 0.1\,\Omega$, inductance $L = 100\,\text{nH}$ and capacitance $C = 10\,\text{pF}$.

The SRR's response under excitation is a resonant peak characterised by two properties: the resonant frequency, f_{res}, and the quality factor, Q. The resonant frequency, f_{res}, is the frequency location where the current peaks whilst the quality factor, Q, quantifies the sharpness of the peak. From a circuit analysis perspective, the definitions of these parameters are derived by rearranging Eq. (1.2) into a damped second-order harmonic oscillator form. The two parameters are described as follows:

$$f_{\text{res}} = \frac{\omega_{\text{res}}}{2\pi} = \frac{1}{2\pi\sqrt{LC}}, \tag{1.3}$$

$$Q = \frac{\omega_{\text{res}} L}{R}, \tag{1.4}$$

where ω_{res} is the angular resonant frequency.

Notably, other types of electrically resonating meta-atoms, such as helical resonators with multiple turns, exhibit the same resonant behaviour.

1.2.2 Characterising SRRs

As previously mentioned, the behaviour of split-ring resonators is characterised by the quality factor, Q, and resonant frequency, f_{res}. Therefore, the accurate extraction of these parameters is essential for the experimental descriptions of the upcoming chapters. Practically, this is done using a vector network analyser (VNA), which can measure the scattering parameters of a 2-port network. This thesis will use two feeding techniques to extract the quality factor: a direct-feed and an inductive-feed approach. In the direct-feed approach, an SMA connector is attached to the terminals of the split-ring resonator, the S_{11} parameter is measured and then converted to the load impedance spectrum, Z_{11}, using the following equation [51]:

$$Z_{11} = Z_L \frac{S_{11} + 1}{S_{11} - 1}, \tag{1.5}$$

where $Z_L = 50\,\Omega$ is the known VNA load. The Z_{11} parameter exhibits the resonance as a minimum point. The characteristic peak of the system can then be obtained by computing the admittance of the load, $Y_{11} = 1/Z_{11}$. This excitation scheme yields a strong response that is more robust in the presence of noise but changes some of the characteristics of the resonator by adding additional resistance and capacitance associated with the SMA connector. In the inductive-feed approach, two non-resonant loops, an exciting one and a receiving one, are placed near the split-ring resonator. This allows for the measurement of the S_{21} parameter, which exhibits a peak at the resonant frequency. This scheme is more sensitive to noise due to the weaker signal generated, but it is more appropriate when arrays of identical resonators are used. Regardless of the excitation scheme chosen, post-processing is necessary to extract Q and f_{res}. The three methods explored are outlined below, alongside their advantages and disadvantages. Comprehensive explanations of these methods and other alternatives are presented in [52, 53].

The 3 dB method

The first method of extraction for f_{res} and Q is the 3 dB method. Here, f_{res} is the frequency where S_{21} reaches its peak value. The quality factor is calculated as:

$$Q = \frac{f_{\text{res}}}{BW}, \tag{1.6}$$

where BW is the bandwidth, the distance between the two half-power points where the magnitude of the S_{21} parameter drops by a factor of $\sqrt{2}$ (i.e. by 3 dB).

This method is susceptible to a series of problems. The first issue is the noise in the data, which can result in erroneous identification of the resonant peak (or 3 dB points). To mitigate this issue, this thesis uses a Savitzky-Golay filter [54–56] to smooth the data and reduce the impact of noise. A Savitzky–Golay filter is a digital smoothing filter that fits successive subsets of adjacent data points with a low-degree polynomial via least squares. This filter was chosen because it attenuates noise, whilst preserving the important features (peak height, location and width). A second problem is the limited number of points a VNA can collect. The largest number of frequency points in a single VNA measurement is fixed at 1601. If the frequency step is too large, this results in intrinsic errors in the bandwidth, which, for a large quality factor resonator, translate into large errors in determining the quality factor. Usually, this issue can be avoided through a narrow frequency span. However, this is not a possible strategy in this thesis since the purpose is to monitor changes in the resonant frequency and quality factor as different materials are placed near the resonators. Instead, once the signal is filtered, one can linearly interpolate a large number of points in the data to account for these errors, assuming that the Q factor is not so high as to make the linear assumption between two adjacent points unreliable. An example of the postprocessing performed for 3 dB extraction is shown in Figure 1.4.

Lorentzian fit

The next method used for extracting f_{res} and Q is a Lorentzian fit, described in detail

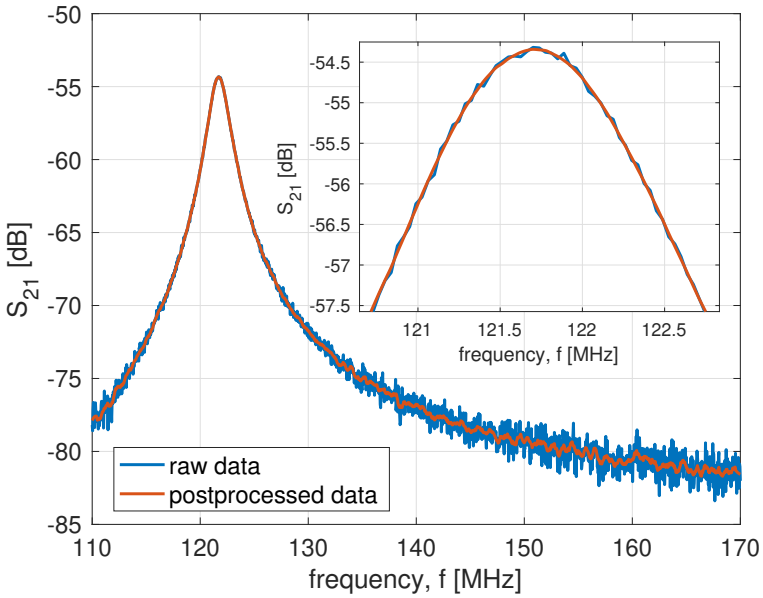

Figure 1.4: Example for magnitude of S_{21} parameter: raw data (blue) and post-processed using 3 dB method (red).

in [53]. In this method, the dataset is fitted by the following curve:

$$|S(f)| = A_1 + A_2 f + \frac{|S_{\max}| + A_3 f}{\sqrt{1 + 4\left(\dfrac{f - f_{\text{res}}}{\Delta f_{\text{Lorentz}}}\right)^2}}, \tag{1.7}$$

where $S(f)$ is the scattering parameter used for extraction at frequency f, $|S_{\max}|$ is the maximum value of $|S(f)|$ and the fitting parameters are A_1 (the constant bandwidth), A_2 (the slope of the background), A_3 (the skew of the data), and $\Delta f_{\text{Lorentz}}$ (the bandwidth). For a good fit, one must select the relevant part of the spectra and provide initial estimates for the fitting parameters. A good approach for using this fitting-based technique is to use the 3 dB method results, if available, as initial guesses for $\Delta f_{\text{Lorentz}}$ and f_{res}. It is important to note that the Lorentzian fit method still works when the signal amplitude is lower than 3 dB, but initial parameter estimations become more challenging. This technique is more resilient to the impact of noise and the limited number of spectral points. A sample Lorentzian fit is shown in Figure 1.5.

Both techniques presented are usually robust enough for most desired applications. However, the 3 dB method requires a large enough signal to estimate the 3 dB points, whilst the Lorentzian fit requires initial estimations for accurate predictions. When Q drops

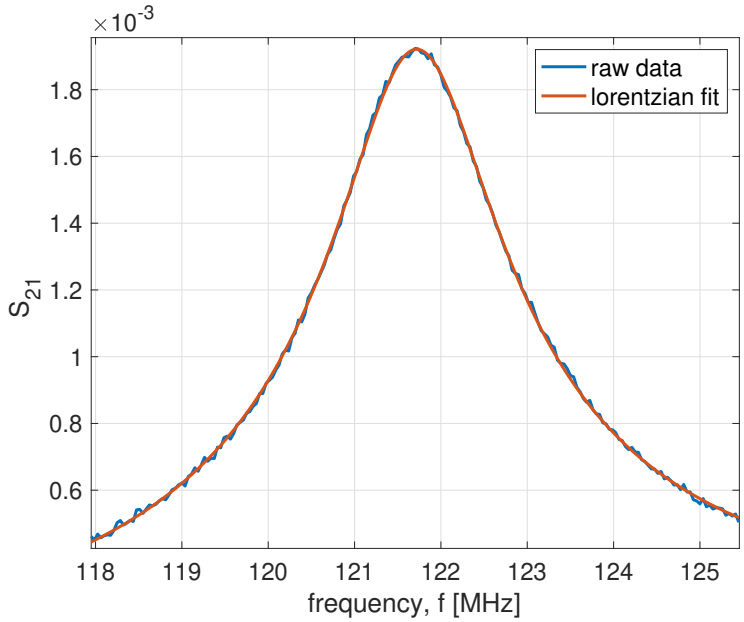

Figure 1.5: Magnitude of S_{21} parameter: raw data (blue) and Lorentzian fit (red).

significantly, the 3 dB method fails. Since the 3 dB method results were the first approximations for the Lorentzian fit, this also results in a more unstable Lorentzian method. In these circumstances, using a different method might be beneficial.

Phase method

The phase method is an alternative technique that uses both the real and imaginary parts of the signal to determine the characteristics of an electrical resonator. Usually, the phase method is used when an inductive feed approach is involved due to the smaller amplitudes of the signal in these circumstances. The S_{21} parameter is, therefore, the one generally involved in these calculations. The first step in using this method is fitting the complex S_{21} data to a circle using a least-squares method. The weight of each point, with real part x_i and imaginary part y_i, is set in such a way that points close to the resonant frequency are more relevant in determining the characteristics of the circle:

$$W_i = \left[(x_{\text{ref}} - x_i)^2 + (y_{\text{ref}} - y_i)^2\right]^2, \tag{1.8}$$

where (x_{ref},y_{ref}) is the point midway between the last and the first data point. The resulting circle is rotated in such a way that its origin corresponds to the origin of the

S_{21} plane as described in [53]. The data is then fit to:

$$\theta(f) = \theta_0 + 2\tan^{-1}\left[2Q\left(1 - \frac{f}{f_{\text{res}}}\right)\right], \tag{1.9}$$

where $\theta(f)$ is the angle formed by the point at frequency f of the circle with the positive real axis and θ_0 is the angle at which the resonant frequency, f_{res}, occurs.

The phase method was used in Section 4.5, where Q was too low for accurate f_{res} and Q extraction with the other two techniques.

1.2.3 Interaction between SRRs

The interaction between meta-atoms is at the core of metamaterial research, as it allows for the propagation of magnetoinductive (MI) waves [57–59]. When a transmitting split-ring resonator is excited by a time-varying signal, it generates a magnetic field, **B**. If a different split-ring resonator (a receiver) is close in proximity to the transmitting SRR, some of the magnetic field lines generated will pass through it, creating a time-varying magnetic flux, ϕ_{21}. This induces an electromotive force (emf, $\mathcal{E}$) in the receiver according to Lenz's law:

$$\mathcal{E} = -\frac{\partial \phi_{21}}{\partial t}, \tag{1.10}$$

which under the plane wave assumption of $\phi_{21} = \phi_{21,0}\mathrm{e}^{j\omega t}$ becomes Eq. (1.11):

$$\mathcal{E} = -j\omega\phi_{21,0}\mathrm{e}^{j\omega t} = -j\omega\phi_{21}. \tag{1.11}$$

The electromotive force, $\mathcal{E}$, is proportional to the current in the transmitting element, I_1. The constant of proportionality is the mutual impedance between the two split-ring resonators, given by:

$$Z_M = -\frac{\mathcal{E}}{I_1} = j\omega\frac{\phi_{21}}{I_1} = j\omega M, \tag{1.12}$$

where M is the mutual inductance between elements, which depends on the geometrical characteristics of the system. An additional minus sign was added to account for the fact that the induced electromotive force ($\mathcal{E}$) inherently opposes the magnetic field generated by the transmitter, as dictated by Lenz's law.

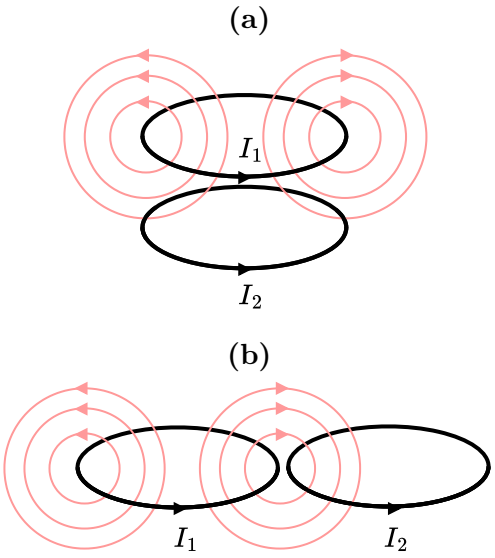

Figure 1.6: Different arrangements of coupled SRRs: (a) axial and (b) planar.

Due to reciprocity, changing the roles of the two resonators results in the same mutual inductance, implying that:

$$M = \frac{\phi_{21}}{I_1} = \frac{\phi_{12}}{I_2}, \tag{1.13}$$

where ϕ_{21} is the magnetic flux in the second SRR when the first SRR is excited by a current I_1 and ϕ_{12} is the magnetic flux in the first SRR when the second SRR is excited by a current I_2. The mutual inductance can be positive if the current in the receiving element travels in phase with the current in the excitation one, or negative if it travels in anti-phase. The positioning of elements with respect to one another determines the sign of the mutual inductance. When split-ring resonators are arranged axially, the resulting mutual inductance is positive, whilst, in a planar arrangement, it is negative. Fig. 1.6 shows an example of these two arrangements.

Maxwell [60] proposed using elliptical integrals to calculate the mutual inductance between two filament coaxial resonators. This was soon adopted as the standard approach in literature alongside numerous approximations and generalisations [61–63]. The mutual inductance between two SRRs of radii r_1 and r_2 placed a distance h apart in the vertical (i.e. axial) direction and d apart in the horizontal (i.e. lateral) direction, as

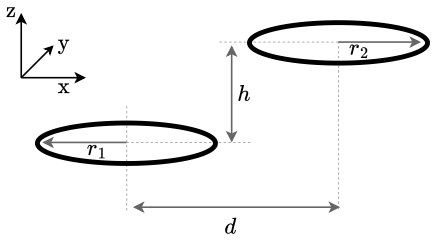

Figure 1.7: General arrangement of two circular SRRs with normal along the z axis, with axial (h) and lateral (d) shifts between them.

shown schematically in Fig. 1.7, is given by:

$$M = \frac{\mu_0}{\pi}\sqrt{r_1 r_2}\int_0^{\pi} \frac{\left(1 - \dfrac{d}{r_1}\cos\psi\right)\,\phi(\xi)}{A^{3/2}}\,d\psi. \tag{1.14}$$

Here, μ_0 is the permeability of free-space, ψ is the azimuthal angle between the two split-ring resonators, measured around the axis of the first resonator, and

$$\begin{aligned} A &= \sqrt{1 + \left(\frac{d}{r_1}\right)^2 - 2\frac{d}{r_1}\cos\psi}, \\ \rho &= \frac{r_1}{r_2}, \quad \tau = \frac{h}{r_1}, \\ \xi^2 &= \frac{4\rho A}{(1+\rho A)^2 + \tau^2}, \\ \phi(\xi) &= \left(\frac{2}{\xi} - \xi\right)K(\xi) - \frac{2}{\xi}E(\xi). \end{aligned}$$

The functions $K(\xi)$ and $E(\xi)$ are the complete elliptic integrals of the first and second kind, respectively, defined as:

$$K(\xi) = \int_0^{\frac{\pi}{2}} \frac{d\gamma}{\sqrt{1 - \xi^2\sin^2\gamma}}, \tag{1.15}$$

$$E(\xi) = \int_0^{\frac{\pi}{2}} \sqrt{1 - \xi^2\sin^2\gamma}\,d\gamma. \tag{1.16}$$

Figure 1.8 shows the mutual inductance between two identical split-ring resonators of radius $r_0 = 10\,\text{mm}$ with axial and lateral displacement variations. In the case of coaxial resonators, the mutual inductance is always positive and strictly decreases with the

distance between them. If the resonators, originally arranged axially, are displaced laterally, the mutual inductance starts as positive but then drops towards negative values. The red line indicates the configurations where the mutual inductance vanishes and no interaction exists between the resonators.

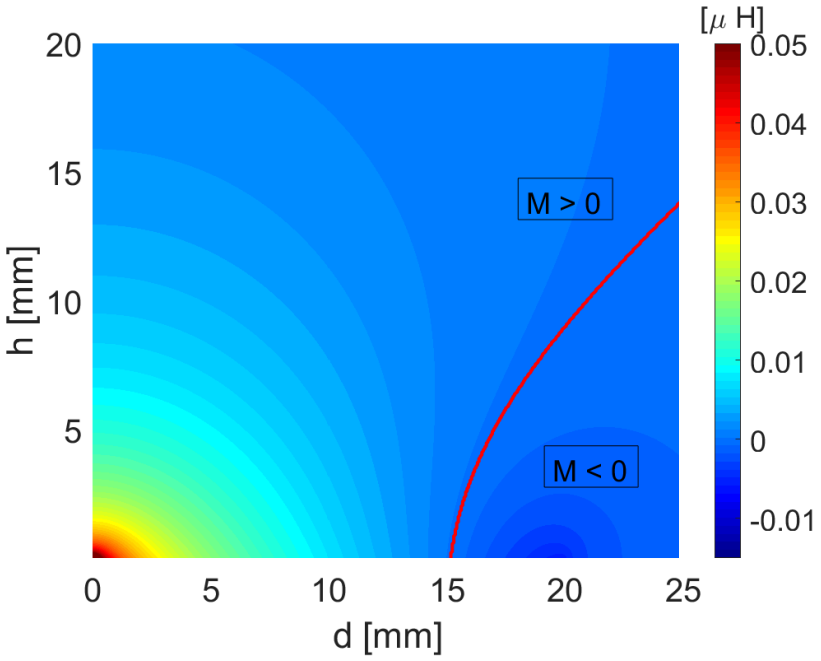

Figure 1.8: Mutual inductance between two identical SRRs of $r_0 = 10\,\text{mm}$ as the axial (h) and lateral (d) distances between them are varied.

The coupling coefficient represents a way to describe the interaction between two meta-atoms and is defined as:

$$\kappa = \frac{2M}{\sqrt{L_1 L_2}}. \tag{1.17}$$

The equivalent circuit of two coupled resonators is shown in Fig. 1.9, and is described analytically as follows:

$$\begin{bmatrix} V \\ 0 \end{bmatrix} = \begin{bmatrix} R_1 + j\omega L_1 + \dfrac{1}{j\omega C_1} & j\omega M \\ j\omega M & R_2 + j\omega L_2 + \dfrac{1}{j\omega C_2} \end{bmatrix} \begin{bmatrix} I_1 \\ I_2 \end{bmatrix}. \tag{1.18}$$

Equation (1.18) can be used to determine the current in both resonators. The current spectra for two identical resonators with $L_1 = L_2 = 100\,\text{nH}$, $C_1 = C_2 = 10\,\text{pF}$ and $R_1 = R_2 = 0.1\,\Omega$ coupled through $M = 10\,\text{nH}$ are shown in Fig. 1.10. The fictitious elements used have $Q = 1000$, which is quite unrealistic for practical applications because of the

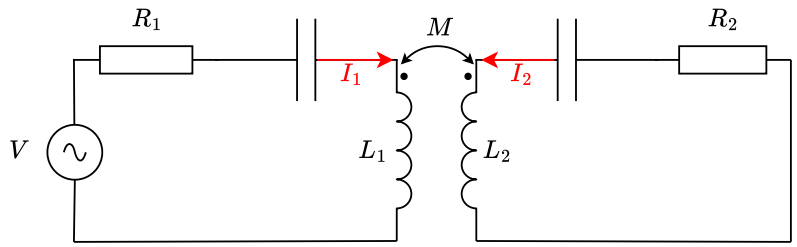

Figure 1.9: Equivalent circuit for two coupled resonant elements.

additional capacitor resistance (called ESR) and resistances associated with soldering. However, a high-Q element is suitable for illustrating the physical behaviour of coupled resonators. Instead of a single resonant peak, as in the case of a single SRR, coupling between two elements causes peak splitting, resulting in two distinct resonances. The splitting is more pronounced when the coupling is larger. For positive coupling, the lower resonance is symmetric (which means that I_1 and I_2 are in phase), while the upper resonance is anti-symmetric (I_1 and I_2 are in antiphase). The opposite is true for negative coupling (i.e. the lower resonance is anti-symmetric and the upper resonance is symmetric). If the quality factor is large enough such that the resonators can be assumed lossless, the position of the two peaks can be used to determine the coupling coefficient:

$$\kappa = \sqrt{1 - \frac{f_{\text{res},1}^2 + f_{\text{res},2}^2}{2(f_+^2 + f_-^2)}}, \tag{1.19}$$

where $f_{\text{res},1}$ and $f_{\text{res},2}$ are the resonant frequencies of the two split-ring resonators, whilst f_- and f_+ are the positions of the lower and upper peaks in the current spectra. For lossy resonators, different techniques can be employed for estimating the coupling coefficient [59, 64, 65].

1.2.4 Magnetoinductive waves in 1D

When multiple split-ring resonators are arranged in a regular array, electromagnetic coupling occurs between neighbouring elements. This interaction gives rise to magnetoinductive (MI) waves — collective modes that propagate through the array. The wavelength of these MI waves is typically much larger than the spacing between adjacent resonators. This new class of waves was first proposed and analysed by [57]. A

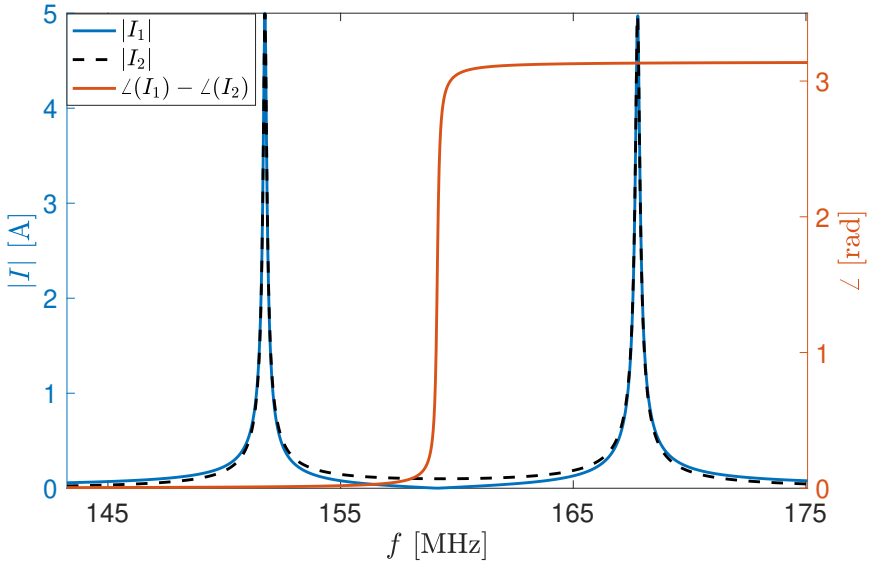

Figure 1.10: Currents in two identical coaxial SRRs with $L_1 = L_2 = 100\,\text{nH}$, $C_1 = C_2 = 10\,\text{pF}$ and $R_1 = R2 = 0.1\,\Omega$ coupled through $M = 10\,\text{nH}$.

comprehensive description of magnetoinductive waves is provided in [58].

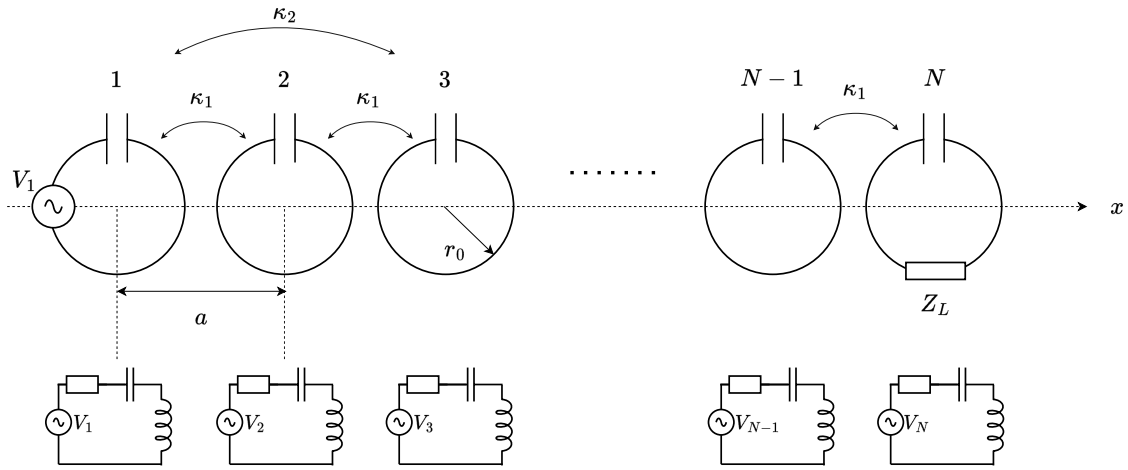

Figure 1.11: 1D magnetoinductive array and its equivalent circuit.

A 1D MI array of resonators is shown in Fig. 1.11 alongside a schematic representation of its equivalent circuit. Assuming an infinitely large array ($N \to \infty$) with no excitation voltage present for the n^{th} split-ring resonator, Kirchhoff's law can be written as:

$$0 = I_n Z_0 + j\omega M_1 \left(I_{n-1} + I_{n+1}\right) + j\omega M_2 \left(I_{n-2} + I_{n+2}\right) + \cdots, \tag{1.20}$$

where $Z_0 = R + j\omega L + \dfrac{1}{j\omega C} = j\omega L \left[1 + \dfrac{\omega_{\text{res}}}{j\omega Q} - \left(\dfrac{\omega_{\text{res}}}{\omega}\right)^2\right]$ is the self-impedance of the split-ring resonator, I_n is the current in element n, and M_n is the n^{th} order mutual inductance. For the planar arrangements considered in this thesis, the nearest neighbour

coupling is much larger than the higher order ones, which can, therefore, be ignored:

$$I_n Z_0 + j\omega M_1 \left(I_{n-1} + I_{n+1}\right) = 0. \tag{1.21}$$

Under a wave assumption, the current I_n can be written as [58]:

$$I_n = I_0 \exp[(-jkna)], \tag{1.22}$$

where $k = \beta - j\alpha$ is the wave number, β is the propagation coefficient and α is the attenuation coefficient. Substituting the wave relation in Eq. waverelation into Kirchhoff's Eq. (1.21) leads to the dispersion equation for MI waves:

$$1 - \left(\frac{\omega_{\text{res}}}{\omega}\right)^2 + \kappa \cos \beta a \cosh \alpha a = 0, \tag{1.23}$$

$$\frac{\omega_{\text{res}}}{\omega Q} - \kappa \sin \beta a \sinh \alpha a = 0. \tag{1.24}$$

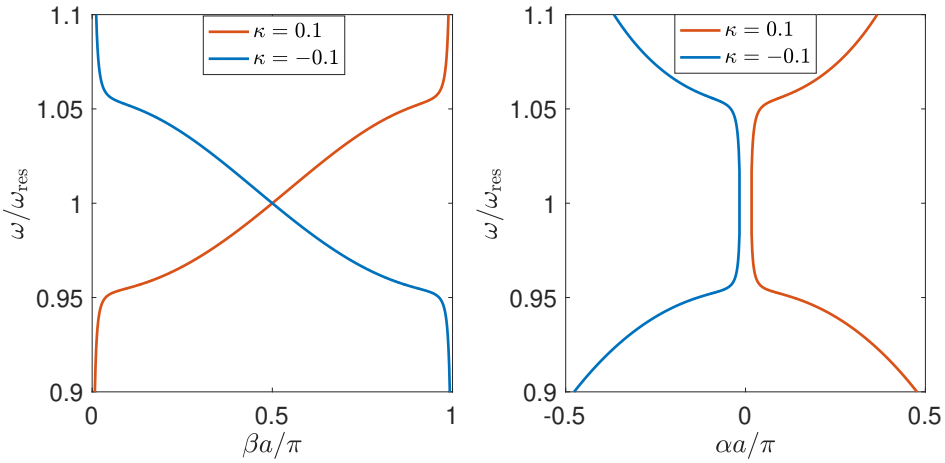

Figure 1.12: MI wave dispersion of an array of resonators with $Q = 200$ and nearest neighbour coupling $\kappa = 0.1$ (red) and $\kappa = -0.1$ (blue).

Figure 1.12 shows how propagation and attenuation vary with frequency for an array of resonators with quality factor $Q = 200$, and nearest neighbour coupling $\kappa = 0.1$ (red) and $\kappa = -0.1$ (blue). The dispersion plots highlight the existence of a passband where MI waves can propagate freely with low attenuation. In the presented case, the passband is roughly between $0.95\,\omega_{\text{res}}$ and $1.05\,\omega_{\text{res}}$. Outside the passband, MI waves are highly attenuated. A salient feature of the dispersion plots is the change in the slope of the propagation, βa, between positive and negative κ. The importance of this feature is

linked to the group velocity and phase velocity. The group velocity is the velocity of a wave packet or the velocity with which the energy of the wave travels inside the array:

$$v_{\mathrm{g}} = \frac{d\omega}{d\beta}. \tag{1.25}$$

In contrast, the phase velocity describes the individual velocity of a wave phase:

$$v_{\mathrm{p}} = \frac{\omega}{\beta}. \tag{1.26}$$

When the coupling is positive, both the phase and group velocities are positive. The resulting waves are known as forward waves. When the coupling is negative, the group velocity is negative, meaning that the phase travelling direction and the energy flow are opposite. These kinds of waves are known as backwards waves, and they are a key feature of left-handed materials or negative-index metamaterials [58, 66].

The above derivation considers an infinitely large array with no excitations. For a finite array of N elements, the currents, I_n, and excitations, V_n, are linked by the generalised Kirchhoff's law:

$$\begin{bmatrix} V_1 \\ V_2 \\ \dots \\ V_N \end{bmatrix} = \begin{bmatrix} Z_0 & j\omega M & 0 & 0 & \dots & 0 & 0 \\ j\omega M & Z_0 & j\omega M & 0 & \dots & 0 & 0 \\ \vdots & \vdots & \vdots & \vdots & \ddots & \vdots & \vdots \\ 0 & 0 & 0 & 0 & \dots & Z_0 & j\omega M \\ 0 & 0 & 0 & 0 & \dots & j\omega M & Z_0 \end{bmatrix} \begin{bmatrix} I_1 \\ I_2 \\ \dots \\ I_N \end{bmatrix}, \tag{1.27}$$

, where the column current vector, $\begin{bmatrix} I_1 & I_2 & \dots & I_N \end{bmatrix}^T$, can be replaced by $\mathbf{I}$, the column voltage vector, $\begin{bmatrix} V_1 & V_2 & \dots & V_N \end{bmatrix}^T$, by $\mathbf{V}$, and the impedance matrix by Z:

$$\mathbf{V} = Z\mathbf{I}. \tag{1.28}$$

The currents in all elements can be computed by inverting the impedance matrix, Z:

$$\mathbf{I} = Z^{-1}\mathbf{V}. \tag{1.29}$$

The resonances of a finite 1D MI waveguide are closely linked to the dispersion equation. The wave numbers for the resonances of the system are derived in [57, 58] as:

$$k_l a = \frac{l\pi}{N+1}, \tag{1.30}$$

where $l = 1,\ 2, \cdots\ N$ is the index of the resonance. As a result, the current in each element, for each resonance, can be written as:

$$I_{l,n} = \frac{2}{N+1}\sin\left(nk_l a\right). \tag{1.31}$$

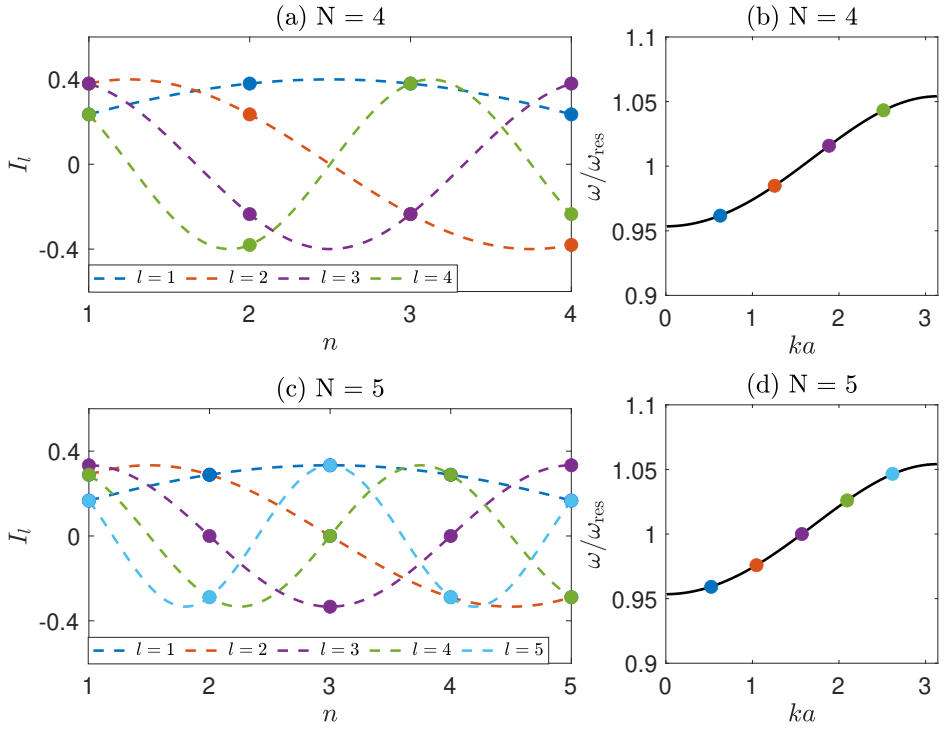

Figure 1.13: Currents under resonant conditions in an array of (a) four elements, and (c) five elements, and normalised frequency against wave numbers with dots indicating each resonance for a (b) four-element array, and (d) five-element array.

The currents under resonant conditions for an array of four and five elements are shown in Fig. 1.13(a, c) alongside the wave numbers corresponding to each resonance [Fig. 1.13(b, d)]. These current curves represent the modes supported by the system, and they can

be excited at the frequencies corresponding to each resonant wave number. Therefore, the analysis of the current spectra is a powerful tool when describing the standing wave patterns that can propagate inside the structure. The nodes of the standing wave pattern (i.e. the locations where the current is always forced to be 0) are located immediately outside the array, at the virtual locations 0 and $N+1$. It is important to note that the excitation location determines the number of modes that can be practically excited in a structure. In a symmetric excitation pattern, only the symmetric modes will be present [for $N = 4$, this corresponds to $l = 1, 3$ in Fig. 1.13(a), and for $N = 5$, to $l = 1, 3, 5$ in Fig. 1.13(c)], whilst in an anti-symmetric excitation pattern, only the anti-symmetric modes will be present ($l = 2, 4$ for both $N = 4$ and $N = 5$). The

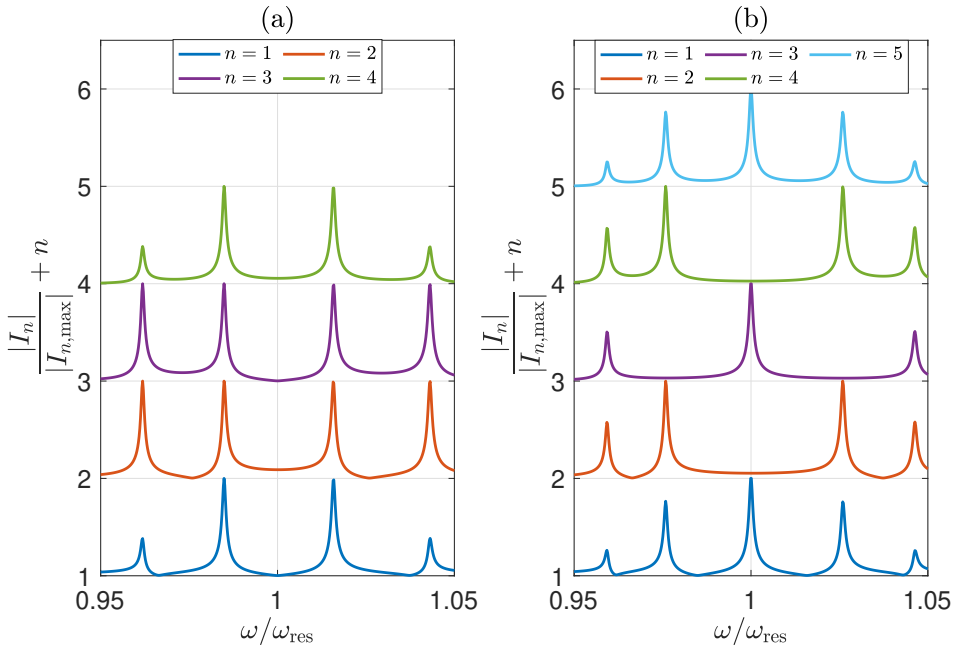

Figure 1.14: Normalised current spectra in all elements of an array with (a) four resonators, and (b) five resonators. Each graph is translated by the index of the resonator for ease of visualisation.

normalised current magnitude spectra for all the elements in two different arrays of four (a) and five (b) resonators are shown in Fig. 1.14 for the low-loss case ($Q = 10000$). The current in each element was displaced by the element index for ease of visualisation. In each case, the first element of the array is excited. This is equivalent to superimposing a symmetric excitation ($V_1 = 0.5$, $V_N = 0.5$) and an anti-symmetric excitation ($V_1 = 0.5$, $V_N = -0.5$). This combination ensures that all the possible modes of the structure are excited. For both arrays, it can be seen that the peak positions perfectly overlap,

indicating the resonances present, and the magnitude of the peaks is correlated with the amplitude of the currents shown in Fig. 1.13(a, c).

When the array has an even number of resonators, as in Fig. 1.13(a, b) and Fig. 1.14(a), all modes can be excited as the magnitude of each current mode in Fig. 1.13(a) is non-zero for all elements. However, when the array has an odd number of resonators, some modes exhibit nulls for certain elements [e.g. in Fig. 1.13(c) for $l = 3$ and $n = 2$, 4 or $l = 4$ and $n = 3$]. The current spectra in these elements have missing modes in Fig. 1.14.

1.2.5 Magnetoinductive waves in 2D

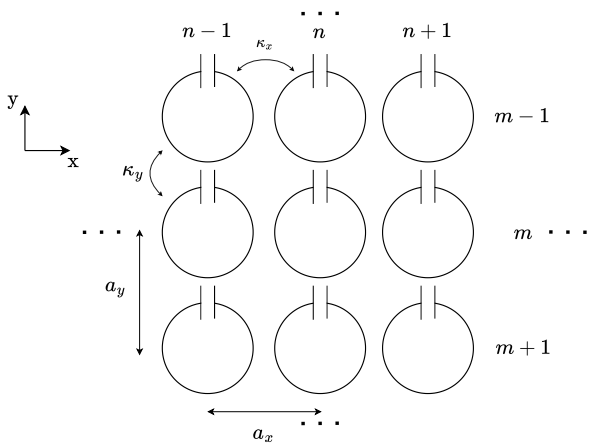

Figure 1.15: Two-dimensional array of coupled resonators.

A two-dimensional array of resonators, shown schematically in Fig. 1.15, can be treated similarly. If no voltage is present and only the nearest neighbour coupling is considered, Kirchhoff's law for element (n, m) is:

$$I_{n,m}Z_0 + j\omega M_x(I_{n-1,m} + I_{n+1,m}) + j\omega M_y(I_{n,m-1} + I_{n,m+1}) = 0, \tag{1.32}$$

where M_x and M_y are the first neighbour coupling in the x and y directions. The current in element (n, m) can be written as:

$$I_{n,m} = I_0 \exp\left[-j(nk_x a_x + mk_y a_y)\right], \tag{1.33}$$

where k_x and k_y are the x and y components of the wave vector $\mathbf{k}$, whilst a_x and a_y are

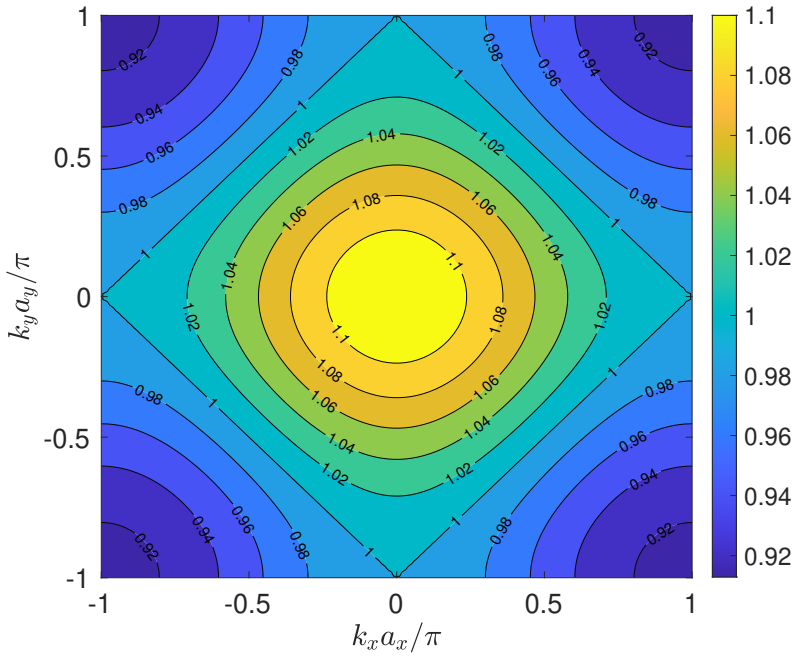

Figure 1.16: Dispersion contours for a 2D array with $\kappa_x = \kappa_y = -0.1$.

the sizes of the periods in x and y directions, respectively.

Substituting the wave Eq. (1.33) into Kirchhoff's Eq. (1.32) results in the following dispersion equation:

$$1 - \frac{\omega_{\text{res}}^2}{\omega^2} - j\frac{\omega_{\text{res}}}{\omega Q} + \kappa_x \cos k_x a_x + \kappa_y \cos k_y a_y = 0, \tag{1.34}$$

where κ_x and κ_y are the first neighbour coupling in the x and y directions. The contour plot of constant normalised frequency for a lossless symmetric array where $\kappa_x = \kappa_y$ and $a_x = a_y$ is shown in Fig. 1.16 for $\kappa_x = \kappa_y = -0.1$. Since $\omega/\omega_{\text{res}}$ decreases as $k_y a_y$ and $k_x a_x$ increase, this is another representation of backwards waves.

For an array of $N = N_x \times N_y$ resonators, where N_x is the number of columns and N_y, the number of rows, the current in each element, (n, m), can be found through the $\mathbf{V} = Z\mathbf{I}$ approach used in the 1D case [Eq. (1.27) and (1.28)] with the impedance matrix adapted for a two-dimensional array $Z \in \mathbb{C}^{N \times N}$:

$$Z = \begin{bmatrix} Z_0 & j\omega M_{1,2} & ... & j\omega M_{1,N-1} & j\omega M_{1,N} \\ j\omega M_{2,1} & Z_0 & ... & j\omega M_{2,N-1} & j\omega M_{2,N} \\ \vdots & \vdots & ... & \vdots & \vdots \\ j\omega M_{N-1,1} & j\omega M_{N-1,2} & ... & Z_0 & j\omega M_{N-1,N} \\ j\omega M_{N,1} & j\omega M_{N,2} & ... & j\omega M_{N,N-1} & Z_0 \end{bmatrix}. \tag{1.35}$$

The currents and voltages of each element are represented as $1 \times N$ column vectors. The computed current spectra will exhibit a series of resonances that can be linked to the dispersion plot similarly to the 1D array case [57].

1.2.6 Interaction between SRRs and nearby objects

This thesis studies the impact of nearby materials on SRR behaviour. Three fundamental electromagnetic properties of materials are of interest: conductivity, σ, permeability, μ, and permittivity, ε.

Conductivity, σ, characterises a material's ability to conduct electric current and is defined through Ohm's law as:

$$\mathbf{J} = \sigma \mathbf{E}, \tag{1.36}$$

where $\mathbf{J}$ is the current density and $\mathbf{E}$ is the electric field.

Permittivity, ε, quantifies how a material responds to an electric field by polarising and storing electric energy; it relates the electric displacement field, $\mathbf{D}$, to the electric field, $\mathbf{E}$, through:

$$\mathbf{D} = \varepsilon \mathbf{E}. \tag{1.37}$$

Permeability, μ, describes the material's response to magnetic fields and its ability to support magnetic flux, with the relation:

$$\mathbf{B} = \mu \mathbf{H}, \tag{1.38}$$

where $\mathbf{B}$ is the magnetic flux density and $\mathbf{H}$ is the magnetic field strength.

When an SRR is brought into the vicinity of a material with different electromagnetic properties than air, the magnetic field generated by the resonator interacts with the material. It induces eddy and displacement currents, which in turn modify the magnitude, phase, and direction of the magnetic field. This causes both the self-inductance of an SRR and the mutual inductance between two SRRs to become complex quantities and change their magnitude and phase. In this thesis, we develop a model capable of describing and utilising these changes to determine material properties. The primary model used for describing these changes was proposed by Dodd and Deeds [16] in 1967 and has been a work of reference for more than 1300 peer-reviewed publications. Dodd and Deeds [16] start from a partial differential equation for the vector potential, $\mathbf{A}$, in a specific location which is excited by a current density $\mathbf{i}$.

$$\nabla^2\mathbf{A} = -\mu\mathbf{i} + \mu\sigma\frac{\partial\mathbf{A}}{\partial t} + \mu\varepsilon\frac{\partial^2\mathbf{A}}{\partial t^2} + \mu\nabla\left(\frac{1}{\mu}\right) \times (\nabla \times \mathbf{A}), \tag{1.39}$$

where μ is the permeability, σ, the conductivity and ε, the permittivity of the medium.

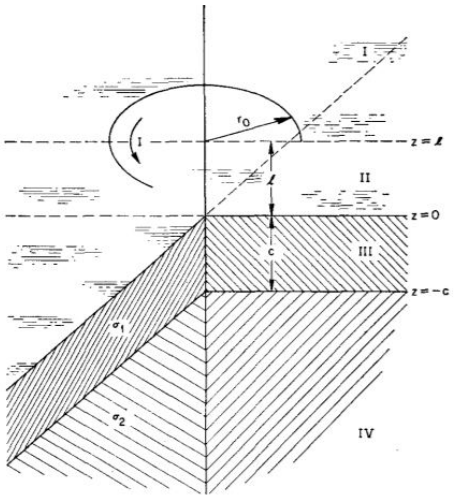

Figure 1.17: Geometry used in [16]: resonator above two conductive layers. Reprinted from [16], with the permission of ©AIP Publishing 1968 by C.V. Dodd and W.E. Deeds.

The equation is derived from Maxwell's equations [15], ensuring the generality of the method. A series of assumptions described in detail in [16] simplify the equation and make it solvable for two geometries. The setup used in [16] is shown in Fig. 1.17, and it is represented by a resonator placed above two conductive slabs, which are infinitely wide, one with thickness c and the other one of infinite thickness.

To solve these geometries, the vector potential is calculated in each region (I, II, III, IV), and the integration constants are found by imposing boundary conditions at the interface between each of the two layers. Similar approaches can be used for other geometries, such as a split-ring resonator above a single material [67, 68] or above a different number of conductive layers, and a split-ring resonator immersed in a conductive medium [69]. The derivation for the geometry of interest will be discussed in Chapter 2.

The method proposed by Dodd and Deeds [15, 16] gained popularity within the non-destructive testing field (NDT), which resulted in multiple publications on the measurement of coatings' thicknesses [70–79], conductivity detection [72–76, 80–83], permeability detection [84–86], quality control through cracks and defects detection [87–95] and foreign object detection [96, 97]. Besides NDT, this method has started to gather momentum in other areas, such as eddy current tomography [98, 99] and breathing monitoring [100, 101]. Although many studies demonstrate the feasibility of conductivity detection, the field still offers room for improvement. One major drawback of currently available devices is their range of functionality: most papers focus on extremely large conductivities (e.g. [72, 74, 75]) with few addressing low-σ regimes (e.g. [82]). A device capable of operating in a wide range would represent a benefit. In addition, many methods rely on numerical models or use complicated calibrations [79, 83]. Most commercially available products require the use of a calibration solution to operate the device. This is expensive and inconvenient, and may result in inaccurate readings if users do not follow instructions properly. This thesis aims to minimise the calibration steps required.

The field of magnetoinductive tomography is also an application with significant potential, which this thesis will discuss in Chapter 3.

CHAPTER 2

Analytical model for detecting material parameters

2.1 Introduction

Sensing technologies play an important role in our society by enabling real-time monitoring and the implementation of feedback control loops. Sensors are widely popular, with applications spanning areas from environmental monitoring to biomedical diagnostics. Amongst sensors, electromagnetic ones stand out as one way to noninvasively characterise materials. The key parameters that determine a material's electromagnetic response are conductivity, permittivity, and permeability.

Sensing electromagnetic properties has applications in various fields, such as biomedical engineering, 3D printing and designing high-performance electrical components. In biomedical engineering, the different properties of tissues can be used for imaging purposes. Induction and impedance tomography are just two emerging methods that can assess a body's functioning based on the response of a resonant system [98, 102–107]. Similarly, industrial materials such as composites or semiconductors rely on accurate electromagnetic characterisation for consistent performance [108–110]. Developing novel

materials in these areas also relies on the ability to characterise their behaviour.

This chapter develops an analytical model, which enables tracking the changes in the response of a resonant loop placed above a testing material and mapping these changes to electromagnetic properties. The shifts in the resonant frequency and quality factor of the elements are of particular interest for detecting a material's conductivity and relative permeability.

The first part of this chapter presents the analytical model developed to determine the changes in the self-inductance of an element placed above a sample. The model improves upon the approach used by Dodd and Deeds in [16] by accounting for the small variations caused by the relative permittivity of materials. In this thesis, the self-inductance of the probe is approximated as the mutual inductance between two filament coils placed a geometric mean distance (GMD) apart [60, 61]. The GMD calculation incorporates the frequency dependence of the system, significantly increasing the computation speed without affecting the accuracy. An additional element of novelty introduced in this thesis is the focus on the resonant frequency, f_{res}, and quality factor, Q, of the probe. These parameters more comprehensively capture the probe's electromagnetic response and can be measured with greater accuracy and robustness than the subtle changes in self-inductance alone.

Using the developed model, different system parameters, such as the probe radius and its resonant frequency, are then varied to optimise the detection of conductivity and permeability. Design guidance is offered for various ranges of these parameters. The final section of this chapter addresses permittivity. Although the model does vary with permittivity, the changes are comparable to the expected experimental uncertainty. This is because permittivity characterises a material's response to electric fields, whereas the measurements in this thesis rely on magnetic field interactions.

This chapter provides a crucial tool for designing and analysing the sensing and imaging sensors developed in Chapters 3, 4, and 5.

The contents of this chapter integrate results and figures from the following two pa-

pers [25, 26]:

- G. Dima, A. Radkovskaya, C. J. Stevens, *et al.*, "Design of a remote, multi-range conductivity sensor," *Sensors*, vol. 23, 9711, 2023
- G. Dima, A. Radkovskaya, C. Stevens, *et al.*, "Full-range contactless conductivity detection," in *Proc. 16th Int. Congr. Artif. Mater. Novel Wave Phenom. (Metamaterials 2022)*, 128, 2022

2.2 Analytical model

Figure 2.1(a) shows a schematic representation of the detection probe and the specimen under test. The circular probe of radius r_0 is made from a circular wire of thickness w, and it is tuned using a lumped capacitor to a free space resonant frequency of f_0. The distance between the centre of the coil and the specimen under test is h. The specimen is a slab of infinite width and thickness t, with conductivity σ, relative permeability μ_r and relative permittivity ε_r.

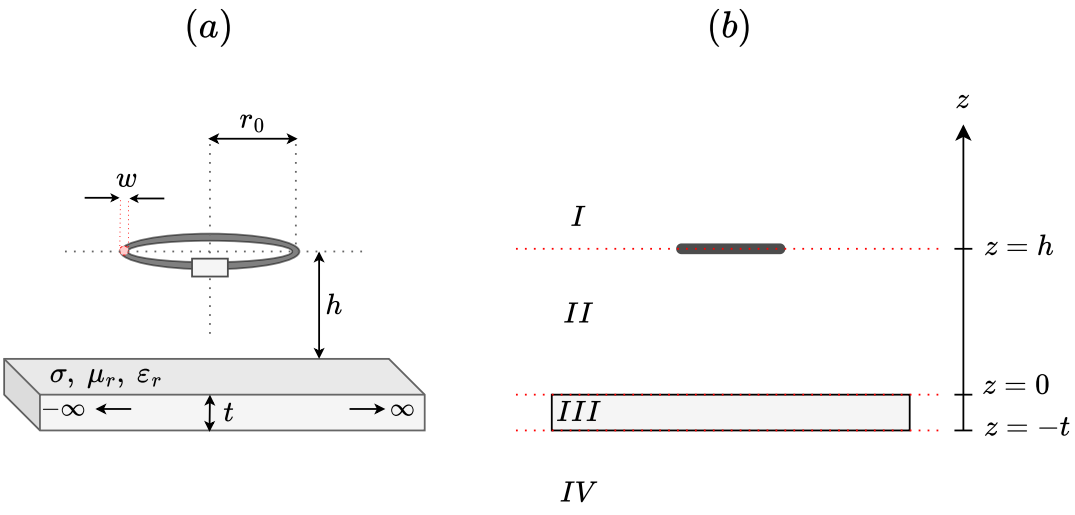

Figure 2.1: Schematic diagram of the system showing (a) the relevant geometrical parameters, and (b) the regions $(I - IV)$ where the material properties change and boundary conditions are imposed, alongside the z-coordinates corresponding to each layer.

Exciting the resonator with a time-varying current I leads to a proportional magnetic flux, Φ, given by:

$$\Phi = LI, \tag{2.1}$$

where L is the self-inductance of the element.

When the testing sample is near the coil, the time-varying magnetic flux generated by the coil induces eddy and displacement currents inside the sample. The currents generated alter the magnitude of the magnetic flux, resulting in a different self-inductance. The presence of the slab also results in a deflection of the magnetic field. The newly induced currents generate their own magnetic fields, which interact with the coil's magnetic field, resulting in its partial cancellation. As a result, the overall magnetic field has a different orientation. This translates into a complex self-inductance.

The self-inductance changes are used in this thesis to determine the slab's electromagnetic properties and are found using a method similar to that presented by Dodd and Deeds [15, 16]. The following partial differential equation is used to calculate the vector potential, $\mathbf{A}$, due to an applied current density $\mathbf{i}$, given by Eq. (1.39) and reproduced here again for convenience:

$$\nabla^2\mathbf{A} = -\mu\mathbf{i} + \mu\sigma\frac{\partial\mathbf{A}}{\partial t} + \mu\varepsilon\frac{\partial^2\mathbf{A}}{\partial t^2} + \varepsilon\nabla(\frac{1}{\mu}) \times (\nabla \times \mathbf{A}). \tag{2.2}$$

Equation (2.2) stems from Maxwell's equations [60, 71], making it widely applicable. The geometry analysed is divided into layers where the electromagnetic properties are constant. In our case, four isotropic, linear and homogeneous layers, denoted I, II, III, and IV in Fig. 2.1(b), are present. The homogeneity ensures that μ and ε are independent on r and z. A filament excitation current, $\mathbf{i}$ is assumed to be placed at the boundary between the first two layers. Because of the axial symmetry of the system, only the azimuthal component, θ, is present: $\mathbf{A} = A\mathbf{i}_\theta$ and $\mathbf{i} = i\mathbf{i}_\theta$. The scalars A and i are the amplitudes of the vector potential and excitation current, respectively, whilst $\mathbf{i}$ is the azimuthal unit vector of the cylindrical coordinate system. The axial symmetry and homogeneity of the layers simplify Eq. (2.2) to:

$$\frac{\partial^2 A}{\partial r^2} + \frac{1}{r}\frac{\partial A}{\partial r} + \frac{\partial^2 A}{\partial z^2} - \frac{A}{r^2} = -\mu i + \mu\sigma\frac{\partial A}{\partial t} + \mu\varepsilon\frac{\partial^2 A}{\partial t^2}. \tag{2.3}$$

Assuming A and i are harmonic functions of time ($A = A_0 e^{j\omega t}$ and $i = i_0 e^{j\omega t}$), Eq. (2.3)

simplifies further to:

$$\frac{\partial^2 A_0}{\partial r^2} + \frac{1}{r}\frac{\partial A_0}{\partial r} + \frac{\partial^2 A_0}{\partial z^2} - \frac{A_0}{r^2} = -\mu i_0 + j\omega\mu\sigma A_0 - \omega^2\mu\varepsilon A_0. \tag{2.4}$$

If the coil is much thinner than its radius, the following filament-coil assumption can be used:

$$I = \frac{i_0}{\delta(r - r_0)\delta(z - z_0)}, \tag{2.5}$$

where z_0 is the axial (i.e. vertical) position of the centre of the coil. Assigning $z = 0$ for the surface of the slab closest to the coil implies that $z_0 = h$ as in Fig. 2.1. Equation (2.4), therefore, takes the form:

$$\frac{\partial^2 A_0}{\partial r^2} + \frac{1}{r}\frac{\partial A_0}{\partial r} + \frac{\partial^2 A_0}{\partial z^2} - \frac{A_0}{r^2} = -\mu I\delta(r - r_0)\delta(z - z_0) + j\omega\mu\sigma A_0 - \omega^2\mu\varepsilon A_0. \tag{2.6}$$

Since no excitation is present inside the layers, the current only becomes relevant when applying the boundary conditions and the partial differential equation inside the layers is simplified as follows:

$$\frac{\partial^2 A_{0,n}}{\partial r^2} + \frac{1}{r}\frac{\partial A_{0,n}}{\partial r} + \frac{\partial^2 A_{0,n}}{\partial z^2} - \frac{A_{0,n}}{r^2} - j\omega\mu_n\sigma_n A_{0,n} + \omega^2\mu_n\varepsilon_n A_{0,n} = 0, \tag{2.7}$$

where the index n is used to indicate the specific properties of the layer under analysis.

This equation is solved using the method of separation of variables, assuming $A_{0,n}(r, z) = R_n(r)Z_n(z)$, which results in:

$$\frac{1}{R_n(r)}\frac{d^2 R_n(r)}{dr^2} + \frac{1}{rR_n(r)}\frac{dR_n(r)}{dr} + \frac{1}{Z_n(z)}\frac{d^2 Z_n(z)}{dz^2} - \frac{1}{r^2} - j\omega\mu_n\sigma_n + \omega^2\varepsilon_n\mu_n = 0. \tag{2.8}$$

Two new differential equations are obtained, where α^2 is the term independent of r and z which connects the two partial differential equations and can take any real value:

$$\frac{1}{R_n(r)}\frac{d^2 R_n(r)}{dr^2} + \frac{1}{rR_n(r)}\frac{dR_n(r)}{dr} - \frac{1}{r^2} + \alpha^2 = 0, \tag{2.9}$$

$$\frac{1}{Z_n(z)}\frac{d^2 Z_n(z)}{dz^2} = \alpha^2 + j\omega\mu_n\sigma_n - \omega^2\varepsilon_n\mu_n = \alpha_n^2, \tag{2.10}$$

where $\alpha_n = \sqrt{\alpha^2 + j\omega\mu_n\sigma_n - \omega^2\varepsilon_n\mu_n}$. The solution of Eq. (2.10) is given by:

$$Z_n(z) = B_n(\alpha)e^{z\alpha_n} + C_n(\alpha)e^{-z\alpha_n}, \tag{2.11}$$

where B_n and C_n are coefficients corresponding to region n.

Equation (2.9) is a first-order Bessel equation; hence, the non-diverging solution in the n^{th} layer can be written in the form:

$$R_n(r) = D_n(\alpha)J_1(\alpha r), \tag{2.12}$$

where J_1 is the Bessel function of the first order and first kind.

Therefore, the vector potential in each region can finally be written as:

$$\begin{aligned} A_n(r,z) &= \int_0^\infty \left[B_n(\alpha)e^{z\alpha_n} + C_n(\alpha)e^{-z\alpha_n}\right] D_n(\alpha)J_1(\alpha r)d\alpha \\ &\equiv \int_0^\infty \left[X_n(\alpha)e^{z\alpha_n} + W_n(\alpha)e^{-z\alpha_n}\right] J_1(\alpha r)d\alpha. \end{aligned} \tag{2.13}$$

Setting $X_I(\alpha) = 0$ prevents divergence in region I, where $z \to \infty$. Similarly, in region IV, where $z \to -\infty$, we set $W_{IV}(\alpha) = 0$. Boundary conditions are used to determine the remaining coefficients. The general boundary conditions between regions n and $n+1$ are that the normal component of the magnetic flux, $B_{\perp n}$, and the tangential component of the magnetic field, $H_{\parallel n}$, are continuous:

$$B_{\perp n} = B_{\perp n+1}, \tag{2.14}$$

$$H_{\parallel n} = H_{\parallel n+1}, \tag{2.15}$$

where the magnetic flux can be calculated as $\mathbf{B_n} = \nabla \times \mathbf{A}_n = -\dfrac{\partial A_n}{\partial z}\mathbf{i}_r + \dfrac{1}{r}\dfrac{\partial (rA_n)}{\partial r}\mathbf{i}_z$ and the magnetic field as $\mathbf{B}_n = \mu_n\mathbf{H}_n$. Here, z is the direction of the normal component, with $\mathbf{i}_r$ as its unit vector, and r is the direction of the tangential one, with $\mathbf{i}_z$ as its corresponding unit vector.

The boundary conditions for the vector potential are therefore:

$$\left(\frac{1}{r}A_n + r\frac{\partial A_n}{\partial r}\right)\Big|_{z=z_n} = \left(\frac{1}{r}A_{n+1} + r\frac{\partial A_{n+1}}{\partial r}\right)\Big|_{z=z_n} \implies A_n\Big|_{z=z_n} = A_{n+1}\Big|_{z=z_n}, \quad (2.16)$$

$$\left(\frac{1}{\mu_n}\frac{\partial A_n}{\partial z}\right)\Big|_{z=z_n} = \left(\frac{1}{\mu_{n+1}}\frac{\partial A_{n+1}}{\partial z}\right)\Big|_{z=z_n}. \quad (2.17)$$

where z_n is the boundary between layers n and $n+1$.

Substituting the boundary conditions from Eqs. (2.16) and (2.17) into Eq. 2.13, we arrive at the following system of equations for the coefficients describing the vector potential in each region:

$$W_I e^{-h\alpha_I} = X_{II}e^{h\alpha_{II}} + W_{II}e^{-h\alpha_{II}}, \quad (2.18)$$

$$-\alpha_I W_I e^{-h\alpha_I} = \alpha_{II}X_{II}e^{h\alpha_{II}} - \alpha_{II}W_{II}e^{-h\alpha_{II}} - \gamma, \quad (2.19)$$

$$X_{II} + W_{II} = X_{III} + W_{III}, \quad (2.20)$$

$$\alpha_{II}X_{II} - \alpha_{II}W_{II} = \alpha_{III}X_{III} - \alpha_{III}W_{III}, \quad (2.21)$$

$$X_{III}e^{-t\alpha_{III}} + W_{III}e^{t\alpha_{III}} = X_{IV}e^{-t\alpha_{IV}}, \quad (2.22)$$

$$\alpha_{III}X_{III}e^{-t\alpha_{III}} - \alpha_{III}W_{III}e^{t\alpha_{III}} = \alpha_{IV}X_{IV}e^{-t\alpha_{IV}}, \quad (2.23)$$

where $\gamma = \mu_0 I r_0 J_1(\alpha r_0)$ and $\alpha_I = \alpha_{II} = \alpha_{IV} = \alpha_0$ since layers II, III and IV are air. For simplicity, we will from now on refer to α_{III} as α_1. Solving the system (2.18) – (2.24) we find:

$$X_{II} = \frac{1}{2}\mu_0 I J_1(\alpha r_0) r_0 e^{-\alpha_0 h}, \quad (2.24)$$

$$X_{III} = \mu_0 I J_1(\alpha r_0) r_0 \frac{\alpha_0(\alpha_0+\alpha_1)e^{-\alpha_0 h}e^{2\alpha_1 t}}{(\alpha_1+\alpha_0)^2 e^{2\alpha_1 t} - (\alpha_0-\alpha_1)^2}, \quad (2.25)$$

$$X_{IV} = \mu_0 I J_1(\alpha r_0) r_0 \frac{2\alpha_1\alpha_0 e^{-\alpha_0 h}e^{t(\alpha_1+\alpha_0)}}{(\alpha_1+\alpha_0)^2 e^{2\alpha_1 t} - (\alpha_0-\alpha_1)^2}, \quad (2.26)$$

$$W_I = \frac{1}{2}\mu_0 I J_1(\alpha r_0) r_0 \left[e^{\alpha_0 h} + \frac{1}{2}e^{-\alpha_0 h}\frac{(\alpha_0^2-\alpha_1^2) - (\alpha_1^2-\alpha_0^2)e^{2\alpha_1 t}}{(\alpha_1+\alpha_0)^2 e^{2\alpha_1 t} - (\alpha_0-\alpha_1)^2}\right] \quad (2.27)$$

$$W_{II} = \frac{1}{2}\mu_0 I J_1(\alpha r_0) r_0 \frac{(\alpha_0^2-\alpha_1^2)e^{-\alpha_0 h}(e^{2\alpha_1 t}-1)}{(\alpha_1+\alpha_0)^2 e^{2\alpha_1 t} - (\alpha_0-\alpha_1)^2}, \quad (2.28)$$

$$W_{III} = \mu_0 I J_1(\alpha r_0) r_0 \frac{\alpha_0(\alpha_0-\alpha_1)e^{-\alpha_0 h}}{(\alpha_1+\alpha_0)^2 e^{2\alpha_1 t} - (\alpha_0-\alpha_1)^2}. \quad (2.29)$$

These coefficients allow for the calculation of the vector potential in each region using Eq. (2.13). It is now possible to calculate the mutual inductance between the excited coil placed between layers I and II and another filament coil placed in region n:

$$M = \frac{1}{I} \oint_L \mathbf{A} \cdot d\mathbf{l} = \frac{1}{I} \int_0^{2\pi} A_n(\phi)\rho(\phi)d\phi, \tag{2.30}$$

where ρ is the distance between the centre of the excited coil and the receiver's track.

The self-inductance can be computed using the geometric mean distance (GMD) method similar to [60, 61, 111, 112]. In this method, the self-inductance of a coil is approximated as the mutual inductance between the transmitter coil and a pseudo-receiver coil placed at a distance R_{GMD} below it. This distance is given in [61, 111, 112] as:

$$\log R_{\mathrm{GMD}} = \log \frac{w}{2} - \frac{w_{\mathrm{i}}^4}{(w^2 - w_{\mathrm{i}}^2)^2} \log \frac{w}{w_{\mathrm{i}}} + \frac{3w_{\mathrm{i}}^2 - w^2}{4(w^2 - w_{\mathrm{i}}^2)}, \tag{2.31}$$

where w and w_i are effective distances which approximate the current flow inside the coil: since the fields can penetrate only down to the skin depth, the current flows in an annular area of outer radius $w/2$ and inner radius $w_i/2 = w/2 - \delta$, where $\delta = \sqrt{\dfrac{2}{\sigma\mu\omega}}$ is the skin depth.

The two coils are assumed to be positioned at $+R_{\mathrm{GMD}}/2$ and $-R_{\mathrm{GMD}}/2$ with respect to the centre of the coil, i.e. at the axial coordinate $z = h$. With these assumptions, the self-inductance can be written in the form:

$$L = \pi r_0^2 \mu_0 \int_0^{\infty} \alpha_0 J_1^2(\alpha r_0) \left[e^{\alpha_0 R_{\mathrm{GMD}}} + \frac{(\alpha_0^2 - \alpha_1^2) e^{-\alpha_0 2h} (e^{2\alpha_1 t} - 1)}{(\alpha_1 + \alpha_0)^2 e^{2\alpha_1 t} - (\alpha_0 - \alpha_1)^2} \right] d\alpha. \tag{2.32}$$

It is also possible to calculate the self-inductance by integrating the vector potential over the entire area of the coil. However, the GMD approach is computationally less expensive, which means that a sensor based on this method could operate in real time.

Regarding this derivation, it is important to note that the term $\mu\varepsilon \dfrac{\partial^2 A}{\partial t^2}$ is included,

similar to [67–69]. This term is often ignored in the literature, including the original work of Dodd and Deeds [15]. However, when operating at high frequencies and low conductivities, this term becomes comparable with the term $\mu\sigma\frac{\partial A}{\partial t}$, and including it leads to more accurate results.

Once the self-inductance of the element is computed, the change in resonant frequency and quality factor of the element can be assessed. The changes in these two parameters will be mapped onto the sample properties, allowing for their extraction. In free space, these parameters will be referred to as f_0 for the resonant frequency and Q_0 for the quality factor:

$$f_0 = \frac{1}{2\pi\sqrt{LC}}, \tag{2.33}$$

$$Q_0 = \frac{2\pi f_0 L}{R}. \tag{2.34}$$

When a material is present, the two parameters will be referred to as f_{res} and Q. When the self-inductance is equal to $L = L_{\text{r}} + jL_{\text{i}}$, f_{res} and Q are:

$$f_{\text{res}} = \frac{1}{2\pi\sqrt{L_{\text{r}}C}}, \tag{2.35}$$

$$Q = \frac{2\pi f_{\text{res}} L_{\text{r}}}{R - 2\pi f_{\text{res}} L_{\text{i}}}. \tag{2.36}$$

The change in the real part of the self-inductance drives the change in the resonant frequency, f_{res}, whilst the imaginary part of the self-inductance mimics an additional resistance.

The spatial variation of the magnetic field can also be reconstructed from the vector potential A by using the standard electromagnetic relations:

$$B_{\perp} = -\frac{\partial A}{\partial z}, \tag{2.37}$$

$$B_{\parallel} = \frac{A}{r} + \frac{\partial A}{\partial r}. \tag{2.38}$$

The magnetic field components, $H_{\perp}$ and $H_{\parallel}$, are then obtained by dividing the corre-

sponding B-fields by the local permeability, μ, depending on the medium.

The magnitude of the magnetic field was calculated as the Euclidean norm:

$$|H| = \sqrt{|H_{\perp}|^2 + |H_{\parallel}|^2}. \tag{2.39}$$

The polarisation state was extracted following a Jones-based polarisation analysis [113]. The complex ratio

$$W = \frac{H_{\perp}}{H_{\parallel}} \tag{2.40}$$

was evaluated at each spatial point to capture the local polarisation characteristics. From W, polarisation ellipses were generated, allowing the extraction of two key parameters: the ellipticity (describing the eccentricity of the magnetic field vector's tip motion) and the inclination (describing the orientation of the major axis with respect to the horizontal). This method enables the distinction between linear, left-handed elliptical, and right-handed elliptical polarisations depending on the value of W.

The developed analytical framework enables the visualisation of the magnitude and polarisation of the magnetic field in a plane perpendicular to the slab, which intersects with the centre of the coil. This is shown in Figure 2.2 for three different conductivities: (a) 0.1 S/m, (b) 10 S/m, and (c) 1000 S/m. The coil in the system has radius $r_0 = 25\,\text{mm}$, width $w = 1\,\text{mm}$, resonant frequency $f_0 = 50\,\text{MHz}$, and free-space quality factor $Q_0 = 250$. The distance between the coil and the slab of thickness $t = 10\,\text{mm}$ is $h = 5\,\text{mm}$. The relative permittivity and permeability of the slab are maintained constant, $\mu_r = \varepsilon_r = 1$. The slab's surface closest to the coil is assigned a $z = 0\,\text{mm}$ coordinate. At the centre of the slab ($z = 0\,\text{mm}$), the magnitude of the field strength decreases with increasing conductivity from 1.33 A/m for $\sigma = 0.1\,\text{S/m}$ to 0.5 A/m for $\sigma = 10\,\text{S/m}$, and further to 8.9×10^{-10} for $\sigma = 1000\,\text{S/m}$. This drop appears because as conductivity increases, the skin depth of the slab, given by $\delta = \sqrt{\frac{1}{\pi f \mu \sigma}}$, reduces with increasing conductivity. Figure 2.2 validates the strong interaction between the resonator and a conductive material.

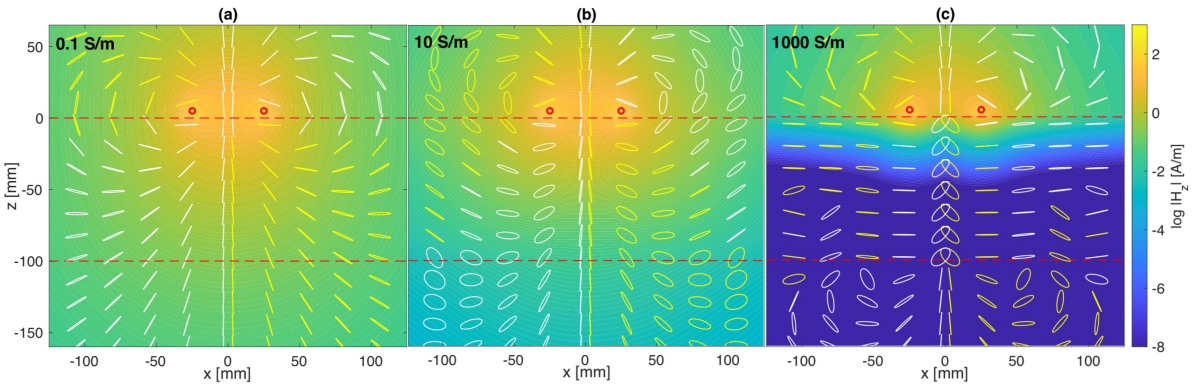

Figure 2.2: Logarithmic plot of the magnitude and polarisation of the magnetic field, H, when a coil of radius, $r_0 = 25\,\text{mm}$, width, $w = 1\,\text{mm}$, resonant frequency, $f_0 = 50\,\text{MHz}$ and free-space quality factor, $Q_0 = 250$ is placed a distance $h = 5\,\text{mm}$ above a sample of thickness, $t = 10\,\text{cm}$, whose relative permittivity and permeability are unity, $\mu_r = \varepsilon_r = 1$. The conductivity of the sample is: (a) $0.1\,\text{S/m}$; (b) $10\,\text{S/m}$; (c) $1000\,\text{S/m}$. Reproduced from [26]. Ref. [26] is licensed under a Creative Commons Attribution 4.0 License. ©2023 MDPI by G. Dima, A. Radkovskaya, C. J. Stevens, L. Solymar and E. Shamonina.

This section has equipped us with the analytical model for a split-ring resonator's resonant frequency and quality factor when an infinitely wide material is placed underneath it. The derivation was mainly based on the Dodd and Deeds approach, with the following differences:

- the permittivity term, $\mu\varepsilon\dfrac{\partial^2 A}{\partial t^2}$ was included, similar to [67–69] to improve accuracy when operating at low frequency and testing low conductivity samples.
- the geometric mean distance, GMD, previously used for calculating self-inductances [60, 61, 111, 112], was integrated with the results obtained from the Dodd and Deeds derivation to improve the computation speed of the self-inductance of a resonator.
- formulas for the resonant frequency (f_{res}) and quality factor (Q) of a resonator placed above a conductive material were presented. These two parameters will be monitored in the following section to gain more insight into the system behaviour.

The following sections will focus on the feasibility of extracting the three electromagnetic properties of materials: conductivity, permeability, and permittivity. The impact of various system parameters will be studied to offer guidance on optimising detection in different scenarios. The model developed in this section and the conclusions drawn in

the rest of the chapter provide the theoretical foundation for this thesis. In Chapter 3, these foundations are used to design a probe for low-conductivity measurements. The approach involves comparing changes in the experimentally extracted f_{res} and Q with values predicted by the analytical model, allowing for an estimate of the conductivity that would best explain the observed behaviour.

2.3 Conductivity detection

The conductivity of a material quantifies its ability to conduct electrical currents. In the real world, material conductivities vary from nearly $0\,\text{S/m}$ for ideal insulators to approximately $6.3 \times 10^7\,\text{S/m}$ for silver, the most conductive naturally occurring metal. Most studies focused on conductivity detection focused on the higher end of this spectrum. Non-invasive techniques such as eddy current analysis have been used to measure large conductivities [72–76, 80, 81, 83], estimate plate thicknesses [70–79, 114] or identify cracks and other defects in metals [87–97]. Moulder et al. [72] used the changes in the electrical impedance of air-core and ferrite-core coils to measure the conductivity and thickness of different aluminium and copper samples for different frequencies with accuracy above 90%. However, simultaneous extraction was only possible for samples for which the ratio between the thickness of the sample and the radius of the coil was $0.2 - 0.5$. Tai et al. [74] used pulsed eddy-current detection and monitored the transient current response after injecting a step-function as a voltage to extract the conductivity and thickness of aluminium samples ranging in thickness from 0.04 mm to 1.00 mm. The error in determining thickness was 13%, and that in measuring conductivity ranged between 20-30%. In recent years, Burkhardt [76] used a similar eddy current method and created a calibration volume which allowed conductivity extraction with 4% error and thickness calculation with 20% error. Whilst creating a strong foundation for electromagnetic-based sensing techniques, this narrow focus on very high conductivity samples excludes potential applications involving materials with low $(\approx 0 - 10)\,\text{S/m}$ and mid-range $(\approx 10 - 10^6)\,\text{S/m}$ conductivities. Some applications where remote conductivity detection in these ranges would be beneficial are 3D-printed conductive materials and human-body imaging.

2.3.1 3D printed conductive materials

In recent years, 3D printing has gained immense popularity, becoming a standard approach for creating objects with various shapes and sizes. Its main advantages over the previous approaches are the versatility of creating almost any desired shape without the need for mass production, its cheaper cost compared with other techniques such as moulding and the convenience of using it inside one's home. Advances in additive manufacturing have pushed the limits of resolution, enabling the fabrication of features down to the nanometre scale [115]. The next big challenge for additive manufacturing is being able to print objects for electrical and electronic applications. This would enable faster and more cost-effective fabrication of circuits. It would also make it feasible to test multiple prototypes — a process that is currently impractical due to the high cost of PCB manufacturing and the importance of maintaining a high yield for profitability. Additive manufacturing could greatly benefit metamaterials, enabling isotropic structures or controlled anisotropy through 3D geometries. However, most metals melt at temperatures significantly higher than plastics. For comparison, copper melts at 1085°C and aluminium at 660°C, whilst most plastics used in 3D printing melt at temperatures lower than 250°C; this makes it challenging to fabricate objects that have very large conductivities. Currently, there are three categories of 3D-printed conductive materials, described in [116]:

- surface direct writing techniques based on conductive inks deposited on a 2D surface through various methods such as aerosol, piezoelectric or electrohydrodynamic (EHD) printing [117–119]. The disadvantage of this method is that it does not allow for 3D printing fabrication.
- post-processing by injection or electroplating techniques [120, 121]. This method can be potentially dangerous as the fumes generated by the electroplating can be toxic.
- free-form 3D printing (also known as fused-filament deposition, fused deposition modelling or robo-casting). This is the most versatile alternative, which melts a material on a print bed in layers until the desired shape is created. The filaments are usually not conductive. However, one can include particles of conductive sub-

stances to make the filament conductive [116, 122–125]. Table 2.1 [121] lists the values of conductivities of some of the more popular filaments.

Table 2.1: Conductivities of typical 3D printing conductive samples [121].

Material	Conductivity [S/m]
Graphite particles (Proto Pasta)	8.3 - 9.5
Graphene particles (Black Magic)	83-125
Multi-walled carbon nanotubes	100
Electrifi	1.67×10^4
Silver coated copper nanowire	5×10^4

One of the main challenges of 3D printing conductive materials is confirming that the printed sample has the desired properties and that the conductivity is homogeneous. Conductive particles are often unevenly distributed, resulting in localised high- and low-conductivity regions that can disrupt circuit performance. The remote sensor proposed in this thesis is capable of estimating mid-range conductivities. This work can be further developed by incorporating scanning probes into the 3D printers, which can assess print quality during fabrication.

2.3.2 Human Tissue imaging

In the lower conductivity range, the difference between human tissue conductivities can represent a method of remotely imaging inside the human body. Conductivity variations cause resonators to interact differently with different types of tissue. Magnetic induction tomography [102, 103] is a new method which explores this avenue by mapping different body conductivities and identifying abnormalities inside the human body through a transmitting and a receiving coil. Despite some publications proving the working principle of magnetic induction tomography, there is still a significant gap between the concept and the final design. This is caused by the complexity of the human body, which is very hard to capture analytically, by the difference in body composition of different individuals, and by the very low conductivities involved in measurements.

The first step in using conductivity differences for human body applications is estimating the electromagnetic properties of body tissues. Cole and Cole [129] proposed a relaxation model that can be used to describe the complex dielectric constant of a polymer as a

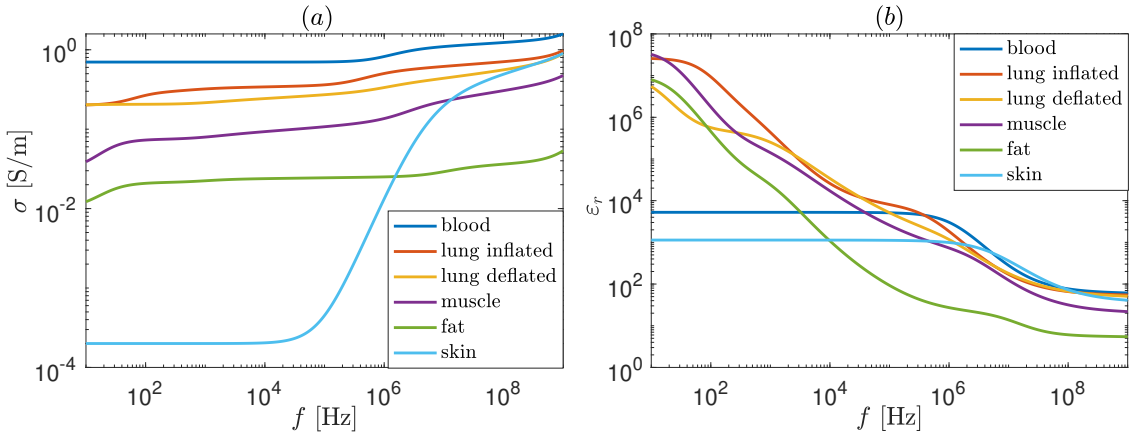

Figure 2.3: Conductivity, σ (a) and relative permittivity, ε_r (b) for various biological tissues using the model described in [126–128].

function of frequency:

$$\varepsilon^* = \varepsilon_\infty + \sum_n \frac{\varepsilon_{s,n} - \varepsilon_\infty}{1 + (j\omega\tau_n)^{(1-\alpha_n)}} + \frac{\sigma_\mathrm{i}}{j\omega\varepsilon_0}, \tag{2.41}$$

where ω is the angular frequency and ε_∞ is the permittivity at high frequencies, where no further dielectric relaxation occurs. The summation accounts for n distinct relaxation processes, each characterised by a permittivity change $\Delta\varepsilon_n = \varepsilon_{s,n} - \varepsilon_\infty$, a relaxation time τ_n, and a broadening parameter α_n. The parameter α_n (with $0 \leq \alpha_n < 1$) describes the spread in relaxation times; when $\alpha_k = 0$, the model reduces to a Debye relaxation. The final term includes the static conductivity, σ_i, and the permittivity of free space, ε_0.

Gabriel et al. [126–128] measured the complex dielectric permittivity for multiple biological tissues and parameterised Cole-Cole's equation. Gabriel et al. [128] offer the parameters needed to simulate a large number of tissue types. These results were implemented in Matlab, and Fig. 2.3 shows a selection of the materials described in [128], considered most relevant for simulations in this thesis.

An application of interest in this thesis is the detection of water accumulation in the lungs. The conductivity of healthy lung tissue is approximately 0.28 S/m when inflated and 0.52 S/m when deflated [126–128]. In the presence of excess fluid—such as in cases of pneumonia or COVID-19—these values increase significantly, with inflated lungs exhibiting conductivities in the range of approximately 0.5–0.7 S/m, and deflated lungs reaching around 0.7–0.9 S/m. Detecting these differences in conductivity during the

breathing cycle can be the first indicator of lung abnormalities. It is important to note that the conductivities of infiltrated lungs are estimated based on the available literature [130–139]. While several studies have investigated the impact of water accumulation on lung conductivity in both animal models [130, 137–139] and humans [131, 133, 134] and strongly support the increase in conductivity, a comprehensive model describing how lung conductivity varies with both frequency and water content does not exist. Moreover, even if such a model were available, the conductivity values would likely vary significantly between individuals due to physiological differences.

Other areas where remote monitoring of the electromagnetic properties of different types of tissue could be beneficial are breathing cycle and low oxygen level monitoring [100, 101].

This thesis proposes a method capable of identifying low conductivities and suggests further improvements that can be applied in magnetic induction tomography. Yin et al. [82] performed a similar study by investigating the conductivity and the thickness of a salty water solution. The error in conductivity detection was 3%. However, the range of conductivities studied was relatively narrow, with only four values considered (3.7, 6.4, 8.3, and 10.2 S/m).

2.3.3 Conductivity impact on f_{res} and Q

The variation in resonant frequency, f_{res} and quality factor, Q, as conductivity changes in the range $(10^{-2} - 10^{8})$ S/m, is shown in Fig. 2.4. These analytical simulations were performed using Eqs. (2.32), (2.35), and (2.36) for a coil of $r_0 = 25$ mm, $w = 1$ mm, $f_0 = 50$ MHz and $Q_0 = 250$, placed a distance $h = 5$ mm apart from a testing sample of thickness $t = 10$ cm, and unity permittivity, ε_r, and permeability, μ_r.

Figure 2.4(a) shows that f_{res} changes only slightly with σ up to $\sigma = 10$ S/m and then grows abruptly with σ in the mid-conductivity range [here, $\sigma \in (10, 10^4)$ S/m]. After this growth, the resonant frequency settles towards a constant value corresponding to the ideal conductor case. In this high-σ case, the sample carries a large mirror current, which appears due to the very narrow penetration depth (or skin depth). The field generated

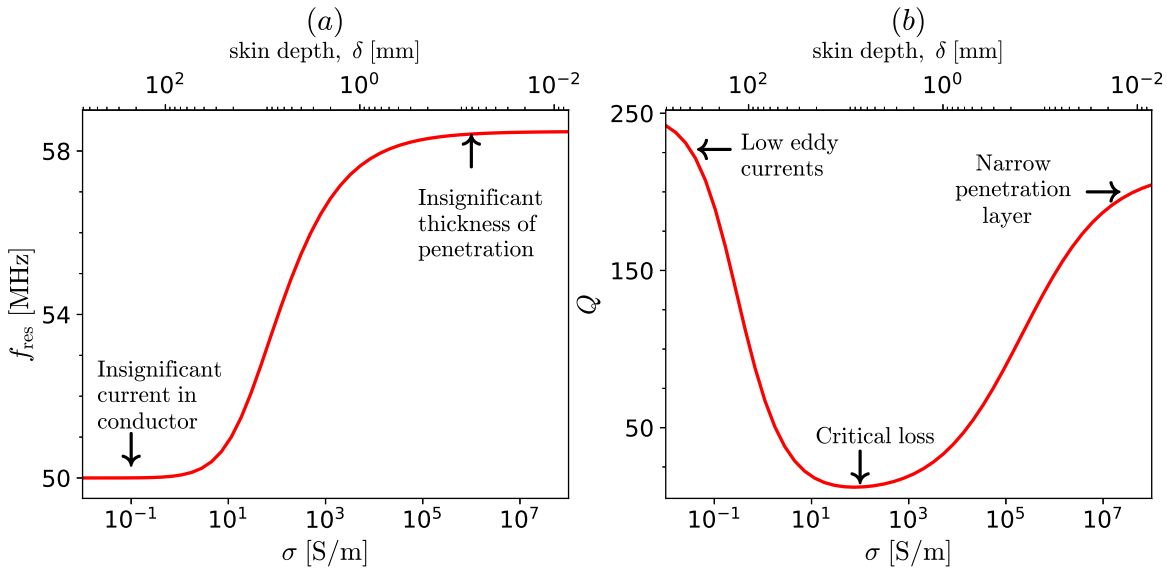

Figure 2.4: Variation of (a) f_{res} and (b) Q with conductivity, σ. The system parameters are $r_0 = 25\,\text{mm}$, $w = 1\,\text{mm}$, $f_0 = 50\,\text{MHz}$, $h = 5\,\text{mm}$, $Q_0 = 250$, $t = 10\,\text{cm}$, and $\mu_r = \varepsilon_r = 1$. Reproduced from [26]. Ref. [26] is licensed under a Creative Commons Attribution 4.0 License. ©2023 MDPI by G. Dima, A. Radkovskaya, C. J. Stevens, L. Solymar and E. Shamonina.

by the slab mimics the presence of a secondary coil placed $2h$ away from the primary coil, where h is the distance between the primary coil and the slab. Only the asymmetric mode is supported because the system acts similarly to a mirror. This is consistent with the boundary conditions for a perfect electric conductor, where the tangential electric field must vanish at the surface. In a system with two resonators arranged axially, the asymmetric mode corresponds to the system's upper resonance as discussed in Section 1.2.3. As σ increases, f_{res} of a single resonator placed above a conductive slab converges to the position of the upper resonant peak of a system with two resonators. The overlap between these two cases is shown in Fig. 2.5 where the normalised current as a function of frequency is shown for a system containing a single coil a distance h above a conductor with $\sigma = 10^8\,\text{S/m}$ (red) and for a system with two identical coils placed $2h$ apart axially (black). The secondary peak in the two-coils system coincides with the resonant peak of a single coil above an ideal conductor. When the conductivity of the slab decreases, the magnetic field is able to penetrate deeper, resulting in intermediary values of f_{res}.

Figure 2.4(b) shows the variation of Q with σ. Q varies significantly with σ for low and high σ ($\sigma < 10\,\text{S/m}$ and $\sigma > 10^4\,\text{S/m}$, respectively) but remains relatively steady in the

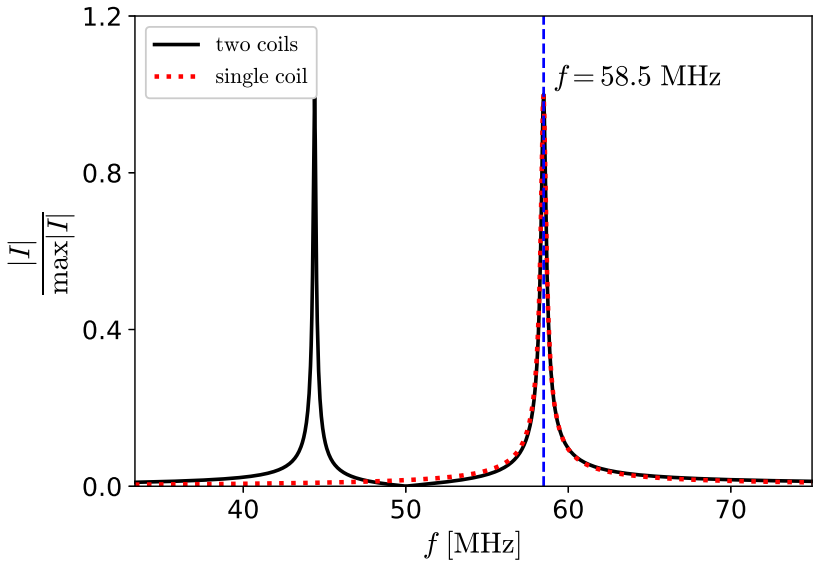

Figure 2.5: Absolute normalised current for a coil placed $h = 5\,\text{mm}$ above a $10\,\text{cm}$ thick conductor of $\sigma = 10^8\,\text{S/m}$ (red dotted line) and for a system of two axially coupled coils placed $2h = 10\,\text{mm}$ apart (black line). The coils have $r_0 = 25\,\text{mm}$, $w = 1\,\text{mm}$, $f_0 = 50$ MHz and $Q_0 = 250$. Reproduced from [26]. Ref. [26] is licensed under a Creative Commons Attribution 4.0 License. ©2023 MDPI by G. Dima, A. Radkovskaya, C. J. Stevens, L. Solymar and E. Shamonina.

mid-conductivity range. This U-shaped relationship is a consequence of two competing phenomena. Initially, as σ increases, the magnitude of the eddy and displacement currents increases, causing greater energy dissipation in the sample. As σ grows further, the decrease in the skin depth, δ, narrows the region where energy dissipates and counterbalances the increase in current magnitude. This phenomenon becomes dominant for high σ, allowing Q to grow close to its original value. The transition between these phenomena depends on the operating frequency and the geometrical parameters of the system.

Full-range conductivity detection can be achieved by detecting variations of Q for low-range and high-range σ and variations of f_{res} for mid-range σ. As will be shown in the next section, the conductivity boundaries for each type of extraction depend on the free-space operating frequency, f_0, the geometric parameters of the system, and the acceptable error in f_{res} and Q.

2.3.4 Influence of system parameters on f_{res} and Q

As previously suggested, the various system parameters will significantly impact the extraction technique and its results. This section will analyse how f_{res} and Q vary with three most relevant parameters: the thickness of the sample, t, the free-space resonant frequency of the coil, f_0, and the relative distance between the coil and the sample, normalised to the coil radius, h/r_0.

All results presented are obtained using Eqs. (2.32), (2.35), and (2.36) from the analytical model presented in Section 2.2.

2.3.4.1 Thickness influence on f_{res} and Q

Figure 2.6 shows f_{res} (a) and Q (b) as a function of σ, for four values of slab thickness: $t = 0.5$ mm (blue), 2 mm (orange), 10 mm (green), 100 mm (red). Except for t, all other system parameters remain the same as in Fig. 2.4. The dotted lines indicate the conductivity where the skin depth, δ, is equal to the thickness of the sample.

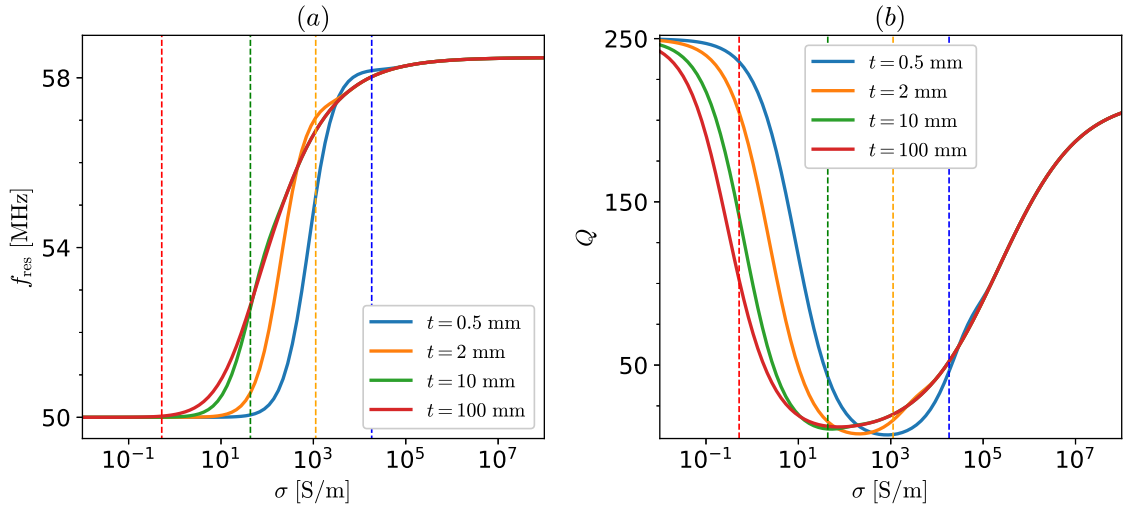

Figure 2.6: Variation of (a) f_{res} and (b) Q with σ, for slab thickness: 0.5 mm (blue), 2 mm (orange), 10 mm (green), and 100 mm (red). Other parameters are: $r_0 = 25$ mm, $w = 1$ mm, $f_0 = 50$ MHz, $h = 5$ mm, $Q_0 = 250$, and $\mu_r = \varepsilon_r = 1$. The dotted lines indicate when the skin depth equals the sample thickness. Reproduced from [26]. Ref. [26] is licensed under a Creative Commons Attribution 4.0 License. ©2023 MDPI by G. Dima, A. Radkovskaya, C. J. Stevens, L. Solymar and E. Shamonina.

When the thickness of the slab is infinite, the electromagnetic field penetrates down to

the skin depth, δ, inside the sample. For conductivities lower than 1 S/m, δ is larger than 100 mm, whilst, for high conductivities, δ drops down towards the µm range. When the sample is thinner than the skin depth, fields can only penetrate as deep as the sample allows. By comparison with an infinite slab, the energy dissipation in this case is lower, as eddy currents of the same magnitude are generated but are now confined to a narrower layer. This means smaller changes are noticed in f_{res} and Q. When the conductivity of a finite slab starts increasing from 0, much smaller changes in f_{res} and Q are noticed in comparison with the infinite slab scenario. In fact, the thinner the slab, the smaller the changes noticed. This trend continues until σ becomes large enough so that the skin depth, δ, matches the slab thickness. When this happens, the electromagnetic field can no longer penetrate further, regardless of increasing conductivity. Therefore, the changes in f_{res} and Q converge towards the values in the infinite slab scenario. This is illustrated in Fig. 2.6, where all the solid lines can be seen to converge towards the red solid line ($t = 100$ mm) with increasing σ once the corresponding dotted line is crossed. It is also noteworthy that as the slab thickness decreases, the minimum Q value occurs for higher σ. This happens because thinner slabs can build up higher current magnitudes before the decrease in skin depth becomes a relevant phenomenon. Overall, thinner slabs result in smaller changes in f_{res} and Q for low and mid-range σ.

2.3.4.2 Relative height influence on f_{res} and Q

The next parameter studied is the relative height of the coil, defined as the ratio between the height of the coil, h, and its radius, r_0. Figure 2.7 shows the variation of f_{res} (a) and Q (b) with σ for four values of the ratio h/r_0: 0.2 (blue), 0.5 (orange), 1 (green), and 2 (red). The remaining system parameters were maintained at the same values as in Fig. 2.4.

When the sample is closer to the coil, a larger amount of the electromagnetic field generated by the slab currents influences the coil directly, resulting in steeper f_{res} changes. Previously, it was established that, for $\sigma \to \infty$, a slab can be seen as an ideal shield, so that a coil placed at height h above the slab behaves like a system of two axially

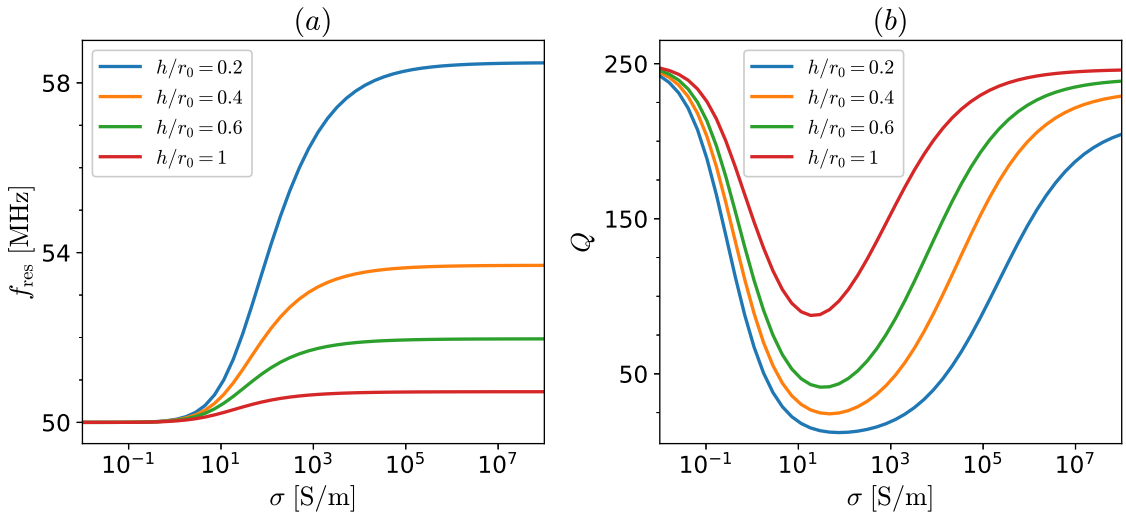

Figure 2.7: Variation of (**a**) f_{res} and (**b**) Q with σ for four values of h/r_0: 0.2 (blue), 0.4 (orange), 0.6 (green), and 1 (red). The other system parameters are $w = 1\,\text{mm}$, $f_0 = 50\,\text{MHz}$, $Q_0 = 250$, $t = 10\,\text{cm}$, and $\mu_r = \varepsilon_r = 1$. Reproduced from [26]. Ref. [26] is licensed under a Creative Commons Attribution 4.0 License. ©2023 MDPI by G. Dima, A. Radkovskaya, C. J. Stevens, L. Solymar and E. Shamonina.

arranged coils separated by a distance $2h$, where only the asymmetric resonance mode is supported. Relying on this analogy again, if the coil is closer to the slab, this is analogous to the equivalent system of two coils being closer together. This results in an increase in mutual coupling, which generates a stronger split between the two resonances. In other words, the asymmetric resonance shifts further up, and so does the system's resonant frequency for an ideal slab.

When the coil and the sample are closer, the magnitudes of the eddy and displacement currents are larger, resulting in more pronounced changes in Q. Since the penetration depth does not change with the proximity of the coil and sample, the larger current magnitudes can counterbalance the reduction in skin depth for larger σ. This shifts the minimum location of Q towards higher values of conductivity.

Figure 2.7 indicates that minimising the distance between the sample and the coil results in larger f_{res} and Q changes, which is beneficial for extracting conductivity. Experimentally, reducing h/r_0 poses significant challenges. Firstly, stray capacitances, which are difficult to estimate analytically, are generated when the sample and the coil are placed in close proximity. Moreover, the required placement accuracy increases significantly with proximity. When h/r_0 is low, even small changes in h can greatly influence f_{res} and

Q and lead to erroneous conductivity extractions. The same pattern applies to manufacturing errors (such as uneven or imperfectly shaped coils) whose impact is magnified by proximity. It is, therefore, necessary to operate at a h/r_0 high enough for experimental errors to be manageable and low enough for f_{res} and Q to still change significantly. We shall return to examining these predictions in Chapter 3 when discussing experimental results for the conductivity sensor.

2.3.4.3 Free-space resonant frequency impact on f_{res} and Q

The final parameter influencing f_{res} and Q significantly is the free-space resonant frequency of the coil. Figure 2.8 shows the variation of the normalised resonant frequency (a), f_{res}/f_0, and Q (b) with σ for $f_0 = 10$, 20, 50, and 100 MHz. The other parameters are the same as in Fig. 2.4.

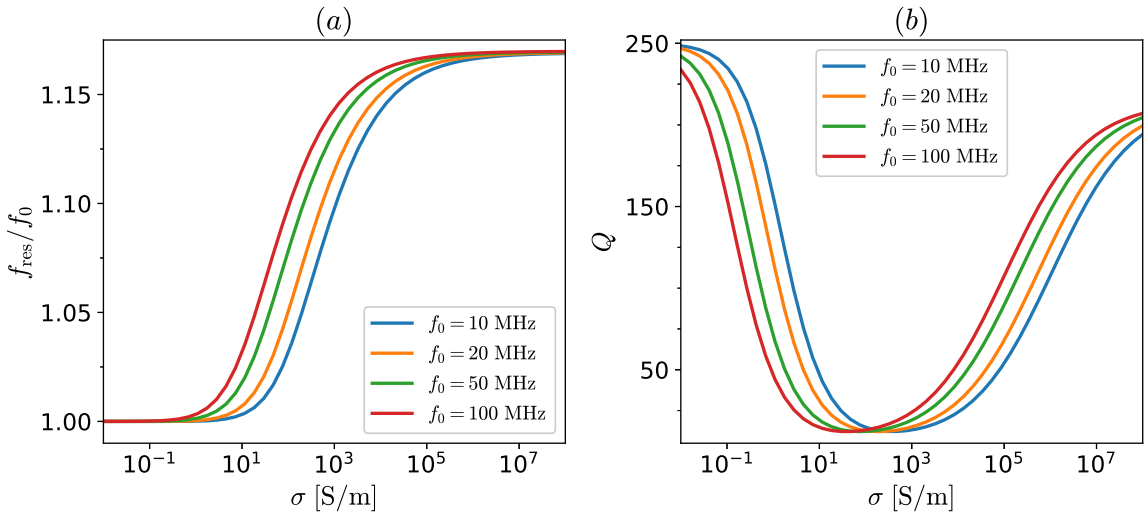

Figure 2.8: Variation of (a) normalized resonant frequency, f_{res}/f_0, and (b) Q with σ for four values of free-space resonant frequency, f_0 : 10 MHz (blue), 20 MHz (orange), 50 MHz (green), and 100 MHz (red). The other system parameters are $r_0 = 25$ mm, $w = 1$ mm, $h = 5$ mm, $Q_0 = 250$, $t = 10$ mm, and $\mu_r = \varepsilon_r = 1$. Reproduced from [26]. Ref. [26] is licensed under a Creative Commons Attribution 4.0 License. ©2023 MDPI by G. Dima, A. Radkovskaya, C. J. Stevens, L. Solymar and E. Shamonina.

As seen in Fig. 2.8(a), increasing f_0 shifts the $f_{\text{res}}(\sigma)$ curves to the left, equivalent to the same changes occurring for lower σ. This happens because the skin depth, δ, decreases faster for higher frequencies, making it possible to approximate the slab as an ideal shield at lower values of conductivity. The same reasoning can be applied for $Q(\sigma)$, which, as

can be seen in Fig. 2.8(b), also shifts to the left for higher values of f_0. Since the skin depth decreases faster for higher f_0, the narrowing of the skin depth becomes the driving mechanism for Q at lower values of σ.

We conclude that a suitable choice of the values of the free-space resonant frequency, f_0, is a way of focusing extraction on different conductivity ranges. Higher f_0 results in steeper changes in f_{res} and Q for low conductivities, whilst lower f_0 are suitable for distinguishing between high conductivities.

2.3.5 Conductivity detection using f_{res} and Q

In this section, the two parameters discussed extensively so far, f_{res} and Q, are used to simulate conductivity extraction in different ranges. As mentioned, Q is best suited for low and high conductivity detection, whilst f_{res}, for mid-range conductivity regions. To simulate conductivity extraction, the values of $f_{\text{res}}(\sigma_{\text{test}})$ and $Q(\sigma_{\text{test}})$ corresponding to σ_{test} are computed using the analytical model descried in Section 2.2. Artificial errors of $\epsilon_f = 0.01\%$ in f_{res} and $\epsilon_Q = 0.5\%$ in Q are added to the values computed analytically, to mimic the presence of noise in experimental data. These values are in line with the expected experimental errors. The newly obtained parameters, $f_{\text{res}}(\sigma_{\text{test}}) \pm \epsilon_f$ and $Q(\sigma_{\text{test}}) \pm \epsilon_Q$, are treated as inputs for a bisection algorithm which tries to find the analytical conductivity which would result in the best match between the inputs and the analytical model:

$$\sigma_{\text{extracted, f}} = \arg\min_{\sigma}\{|f_{\text{res}}(\sigma) - [f_{\text{res}}(\sigma_{\text{test}}) \pm \epsilon_f]|\} \tag{2.42}$$

$$\sigma_{\text{extracted, Q}} = \arg\min_{\sigma}\{|Q(\sigma) - [Q(\sigma_{\text{test}}) \pm \epsilon_Q]|\} \tag{2.43}$$

The percentage error in extraction is calculated as:

$$\text{extraction error} = \frac{|\sigma_{\text{test}} - \sigma_{\text{extracted}}|}{\sigma_{\text{test}}} \times 100 \tag{2.44}$$

When using the bisection method for Q on the entire range, the resonant frequency

associated with the minimum of Q, f_{min}, is pre-stored and used to identify the transition point between decreasing and increasing Q, enabling correct application of the bisection method in both low and high σ regimes. If the target f_{res} is larger than f_{min}, Q is considered to be increasing, and if it is smaller, Q is considered to be decreasing.

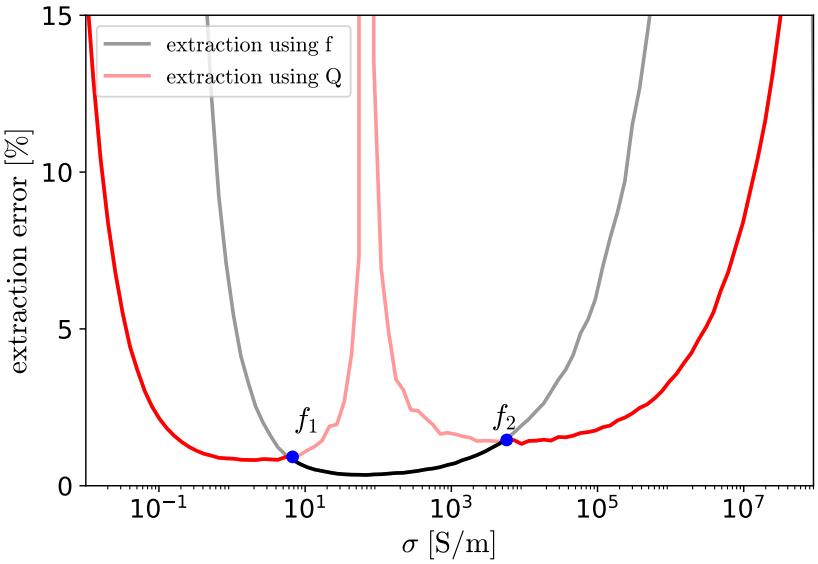

Figure 2.9: Extraction in the two presented regimes: f_{res} (black line) and Q (red line). The opaque lines represent areas where each method was selected. f_1 and f_2 are cut-off frequencies for changing the selection criteria. The system parameters are $r_0 = 25\,\text{mm}$, $w = 1\,\text{mm}$, $f_0 = 50\,\text{MHz}$, $h = 5\,\text{mm}$, $Q_0 = 250$, $t = 10\,\text{cm}$, and $\mu_r = \varepsilon_r = 1$. The artificial errors are 0.01% in f_{res} and 0.5% in Q. Reproduced from [26]. Ref. [26] is licensed under a Creative Commons Attribution 4.0 License. ©2023 MDPI by G. Dima, A. Radkovskaya, C. J. Stevens, L. Solymar and E. Shamonina.

Figure 2.9 shows the percentage difference between the extracted and actual conductivity for the entire σ range. The red line indicates extraction using Q whilst the black one shows extraction using f_{res}. The parameters of the system are as follows: $r_0 = 25\,\text{mm}$, $w = 1\,\text{mm}$, $h = 5\,\text{mm}$, $t = 10\,\text{cm}$, $f_0 = 50\,\text{MHz}$, $Q_0 = 250$. The results in Fig. 2.9 fall in line with the expected behaviour of our system. Q factor extraction is appropriate for $\sigma < 10\,\text{S/m}$ and $\sigma > 10^4\,\text{S/m}$ whilst f_{res} extraction is appropriate for the values in between. Figure 2.9 also aids in developing the extraction method for experimental samples. The transition between the two methods (Q extraction and f_{res} extraction) is marked by the blue breakpoints, for which the resonant frequencies, f_1 and f_2, are stored and used in further extractions. If the experimental resonant frequency, $f_{\text{res,exp}}$ is smaller than f_1, extraction is performed using decreasing Q. If $f_1 < f_{\text{res,exp}} < f_2$, the

resonant frequency is used for extraction, whilst if $f_{\text{res,exp}} > f_2$, increasing Q is used for extraction. This way, the most efficient method for each scenario will be used to extract conductivity experimentally.

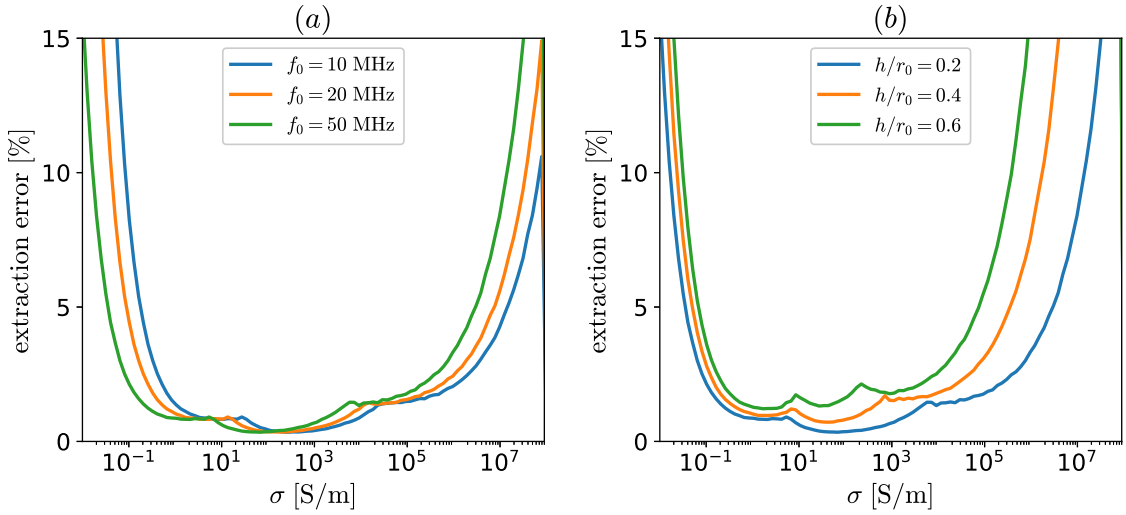

Figure 2.10: Errors in extraction for different (a) free-space frequencies, f_0, (b) height and coil radius ratios h/r_0. The artificial errors are 0.01% in f_{res} and 0.5% in Q. Unless otherwise specified in the legend, the system parameters are $r_0 = 25\,\text{mm}$, $w = 1\,\text{mm}$, $f_0 = 50\,\text{MHz}$, $h = 5\,\text{mm}$, $Q_0 = 250$, $t = 10\,\text{cm}$, and $\mu_r = \varepsilon_r = 1$. Reproduced from [26]. Ref. [26] is licensed under a Creative Commons Attribution 4.0 License. ©2023 MDPI by G. Dima, A. Radkovskaya, C. J. Stevens, L. Solymar and E. Shamonina.

Following the same steps, the analytical extraction error for different free space resonant frequency values, f_0, is shown in Fig. 2.10(a). It can be seen that decreasing f_0 results in a shift of the lines towards higher conductivities. Notably, this shift does not change any other salient features of the lines. This supports the earlier observation that increasing f_0 enhances detection of low conductivities, while lower f_0 improves performance for high-σ. The green line ($f_0 = 50\,\text{MHz}$) achieves the best low-σ detection with an extraction error lower than 3% for $\sigma = 0.1\,\text{S/m}$, but the poorest high-σ detection. In contrast, the blue line ($f_0 = 10\,\text{MHz}$) results in the most accurate high σ detection with an error lower than 10% for $\sigma \approx 10^8\,\text{S/m}$, but in the poorest low-σ detection, with an error higher than 15% for $\sigma = 0.1\,\text{S/m}$.

Figure 2.10(b) shows the analytical extraction error for different relative height values. As expected from the proximity analysis, reducing the coil-to-sample distance improves accuracy, especially in the high-conductivity regime. Figure 2.10(b) indicates that the high-σ range is more sensitive to changes in the relative distance. This suggests a different

approach towards relative distance choice for different σ. As previously mentioned, placing the coil very close to the probe is not always experimentally feasible because of stray capacitances or inaccuracies in positioning and manufacturing, which are amplified by increased proximity and lead to significant errors. These problems can be bypassed by investing in sophisticated distance measurement techniques, improving fabrication processes and creating complicated analytical models for stray capacitances. From Fig. 2.10(b), it is clear that this is unnecessary for low σ since simply operating at a higher relative distance leads to similar results. This is not the case for high σ, where a small distance is required for accurate results, and this kind of investment is justified.

These results will be experimentally validated in Chapter 3 for low-σ saline solutions. The remainder of this chapter is dedicated to exploring the feasibility of the developed method for extracting permeability, μ, and permittivity, ε.

2.4 Permeability detection

Electromagnetic permeability, μ, quantifies a material's ability to support magnetic fields. Formally, it is defined as the ratio between the B, the magnetic flux density, and H, the magnetic field strength. The ratio between the permeability of a material, μ, and the permeability of free space, μ_0, is the relative permeability of the material μ_r: $\mu = \mu_r\mu_0$. The relative permeability of materials varies widely from $\mu_r = 1$ in vacuum to $\mu_r = 10^2 - 2\times10^5$ for iron, depending on its purity, and to values as high as $\mu_r = 10^6$ for certain alloys such as supermalloy [140]. However, the strength of the applied magnetic fields and the operating frequency heavily impact these values.

Magnetic materials play a significant role in our society [141–143]. They are used as cores for rotors and stators in electrical motors and generators, aiding in developing more efficient electrical motors [141] and as laminated cores for transformers, increasing the coupling between the primary and the secondary. Magnetic materials are also used to shield highly sensitive components from external electromagnetic fields or to store data in hard drive memory in response to external fields. Because of the wide range of applications, research into magnetic materials is extensive, and permeability sensing

techniques play an important role in quality control and widespread usage. Eddy current techniques are extensively researched and used for permeability detection [84, 144–146]. This section examines the impact of permeability on f_{res} and Q, contributing to the existing literature by analysing how different system parameters affect detection.

2.4.1 Permeability impact on f_{res} and Q

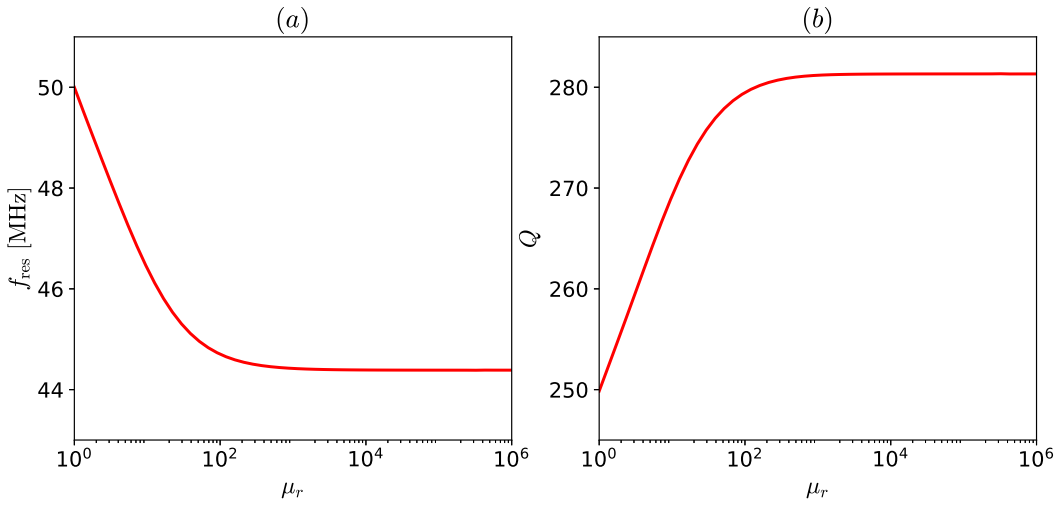

Figure 2.11: Variation of (a) f_{res} and (b) Q with sample's relative permeability, μ_r. The system parameters are $r_0 = 25\,\text{mm}$, $w = 1\,\text{mm}$, $f_0 = 50$ MHz, $h = 5\,\text{mm}$, $Q_0 = 250$, $t = 5\,\text{mm}$, $\sigma = 0\,\text{S/m}$, and $\varepsilon_r = 1$.

Figure 2.11 shows the variation of f_{res} and Q with μ_r, calculated using Eqs. (2.32), (2.35), and (2.36) from Section 2.2. The system uses a resonant element of radius $r_0 = 25\,\text{mm}$, wire thickness $w = 1\,\text{mm}$, free-space resonant frequency $f_0 = 50$ MHz and $Q_0 = 250$, placed above a slab of thickness $t = 5\,\text{mm}$, conductivity $\sigma = 0\,\text{S/m}$ and relative permittivity $\varepsilon_r = 1$. It can be noticed that f_{res} decreases until $\mu_r \approx 100$. After this point, f_{res} settles to a constant saturation value. Similarly, Q increases to $\mu_r = 100$ and settles to its own value. From a physical perspective, the magnetic sample concentrates the magnetic flux. Since the self-inductance of a coil is defined as the ratio between the magnetic flux within it and its current, the presence of the magnetic material increases the magnetic flux, resulting in a larger self-inductance. If the coil's self-inductance increases, the element's resonant frequency decreases, and its quality factor increases. The amount of flux the sample can concentrate depends on its permeability, resulting in an approximately linear behaviour of f_{res} and Q up to $\mu_r = 100$. When saturation is achieved,

the magnetic flux is almost entirely concentrated within the sample and increasing μ_r further cannot attract additional flux. It is important to note that the term saturation refers here to the flux being fully captured by the magnetic sample and should not be confused with the magnetic saturation of ferromagnetic materials.

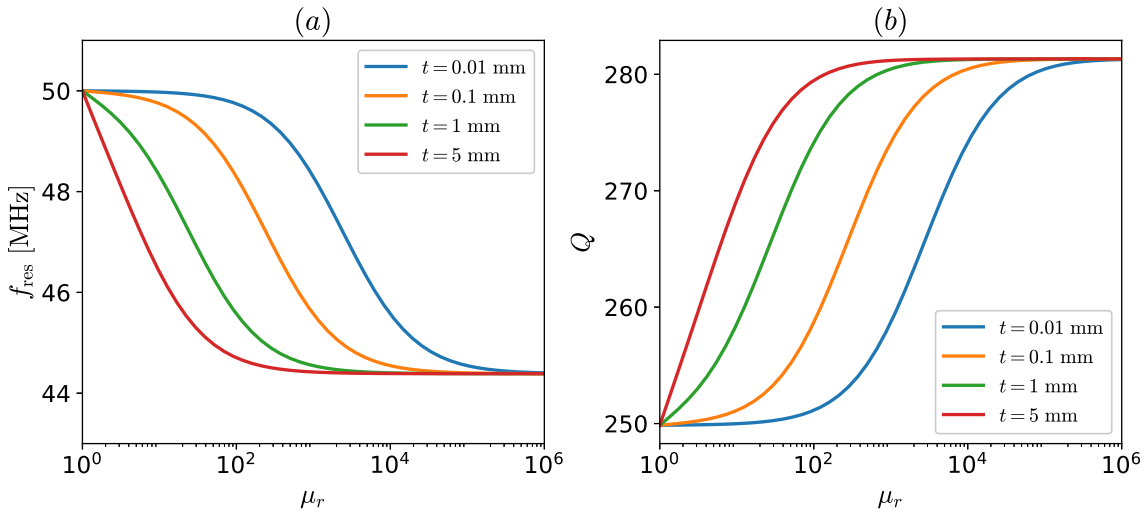

Figure 2.12: Variation of (a) f_{res} and (b) Q with μ_r for four values of sample thickness: $t = 0.01\,\text{mm}$ (blue), $t = 0.1\,\text{mm}$ (orange), $t = 1\,\text{mm}$ (green), and $t = 5\,\text{mm}$ (red). The other system parameters are $r_0 = 25\,\text{mm}$, $w = 1\,\text{mm}$, $f_0 = 50\,\text{MHz}$, $h = 5\,\text{mm}$, $Q_0 = 250$, $\sigma = 0\,\text{S/m}$, and $\varepsilon_r = 1$.

Figure 2.12 shows the evolution of $_{\text{res}}$ and Q with μ_r for different values of slab thickness: $t = 0.01\,\text{mm}$ (blue), $t = 0.1\,\text{mm}$ (orange), $t = 1\,\text{mm}$ (green), and $t = 5\,\text{mm}$ (red). The remainder parameters are maintained as in Fig. 2.11. When the thickness of the slab reduces, larger permeabilities are required to concentrate the entire field due to the limited amount of material. This results in a shift towards higher μ_r for thinner samples. For very small thickness, for example, for $t = 0.01\,\text{mm}$ (blue curve), low μ_r values (up to ≈ 100)result in no significant changes in f_{res} and Q as the sample is too thin to affect the magnetic flux in any relevant way. The sample thickness is, therefore, a mechanism for tuning permeability detection. Samples with $\mu_r < 100$ can be characterised using slabs of thickness in the mm range, whilst very thin slabs (in the μm range) can be used to detect μ_r>100.

The variation of f_{res} and Q with μ_r for four different values of relative height ($h/r_0 = 0.2$ (blue), $h/r_0 = 0.4$ (orange), $h/r_0 = 0.6$ (green), $h/r_0 = 1$ (red)) is shown in Fig. 2.13. The other parameters are the same as in Fig. 2.11. When the coil is closer to the

magnetic slab, more of the magnetic flux can be captured by it, and therefore, larger f_{res} and Q changes occur (i.e. L increases). Regardless of the relative distance of the coil from the test material, the saturation point remains the same. Relative distance influences the strength of interaction but does not change the physical phenomena inside the sample. As in the case of conductivity, stronger interactions occur when the coil is closer to the sample.

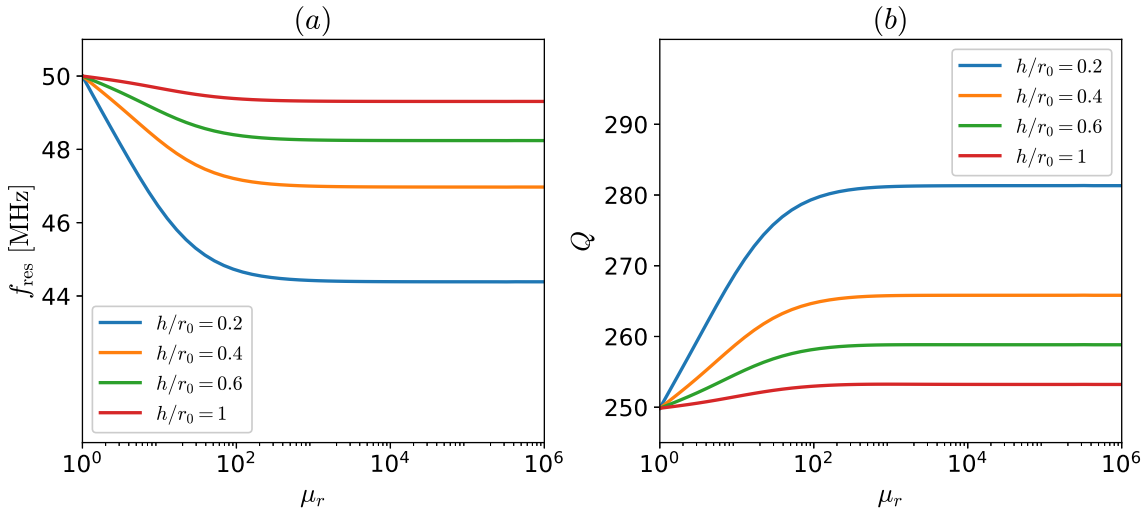

Figure 2.13: Variation of (a) f_{res} and (b) Q with μ_r for four values of relative height: $h/r_0 = 0.2$ (blue), $h/r_0 = 0.4$ (orange), $h/r_0 = 0.6$ (green), $h/r_0 = 1$ (red). The other system parameters are: $w = 1\,\text{mm}$, $f_0 = 50\,\text{MHz}$, $Q_0 = 250$, $t = 5\,\text{mm}$, $\sigma = 0\,\text{S/m}$, and $\varepsilon_r = 1$.

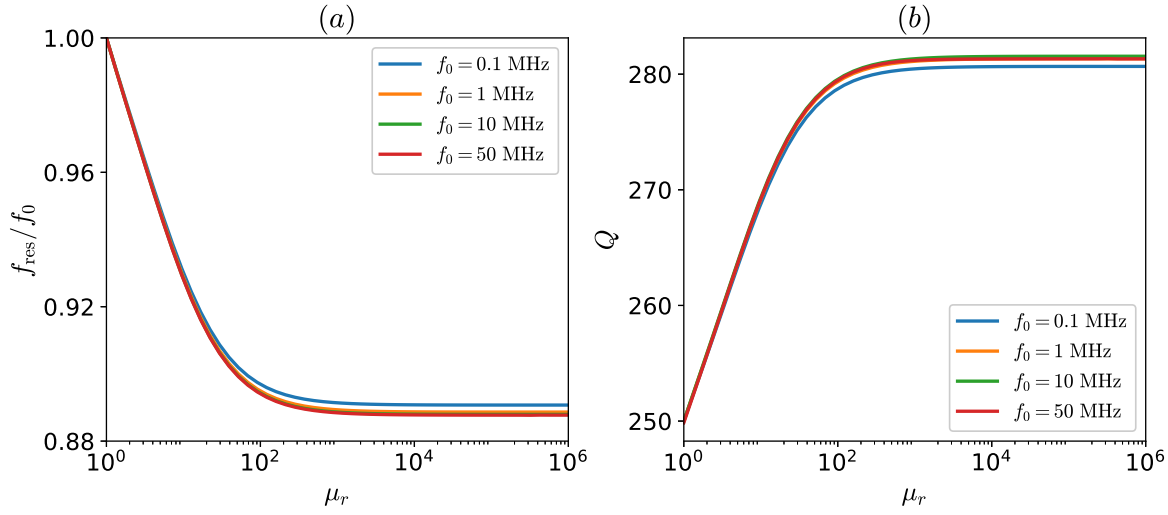

Figure 2.14: Variation of (a) f_{res} and (b) Q with μ_r for four values of free-space resonant frequency: $f_0 = 0.1\,\text{MHz}$ (blue), $f_0 = 1\,\text{MHz}$ (orange), $f_0 = 10$ MHz (green), and $f_0 = 50$ MHz (red). The other system parameters are $r_0 = 25\,\text{mm}$, $w = 1\,\text{mm}$, $h = 5\,\text{mm}$, $Q_0 = 250$, $t = 5\,\text{mm}$, $\sigma = 0\,\text{S/m}$, and $\varepsilon_r = 1$.

The next parameter studied is the free-space resonant frequency of the coil, f_0. Figure

2.14 shows the evolution of the same two parameter with μ_r for different values of f_0: $f_0 = 0.1\,\text{MHz}$ (blue), $f_0 = 1\,\text{MHz}$ (orange), $f_0 = 10\,\text{MHz}$ (green), and $f_0 = 50\,\text{MHz}$ (red). The remainder parameters are maintained as in Fig. 2.11. The differences between different curves are small, indicating that f_0 does not greatly impact the system's behaviour. It is expected that f_0 will, therefore, have a negligible effect on detection. In reality, a material's permeability μ_r can vary significantly with f_0 due to dispersion effects. In many applications, the operating frequency is constrained by the system design, making a frequency-independent detection method particularly advantageous.

So far, this study has assumed that the conductivity of the slab is $\sigma = 0\,\text{S/m}$. In practice, this is not a feasible assumption, as magnetic materials are often lossy. Figure 2.15 shows the variation in f_{res} and Q with μ_r for four different conductivity values: $\sigma = 0\,\text{S/m}$ (blue), $\sigma = 100\,\text{S/m}$ (orange), $\sigma = 10^4\,\text{S/m}$ (green), and $\sigma = 10^6\,\text{S/m}$ (red).

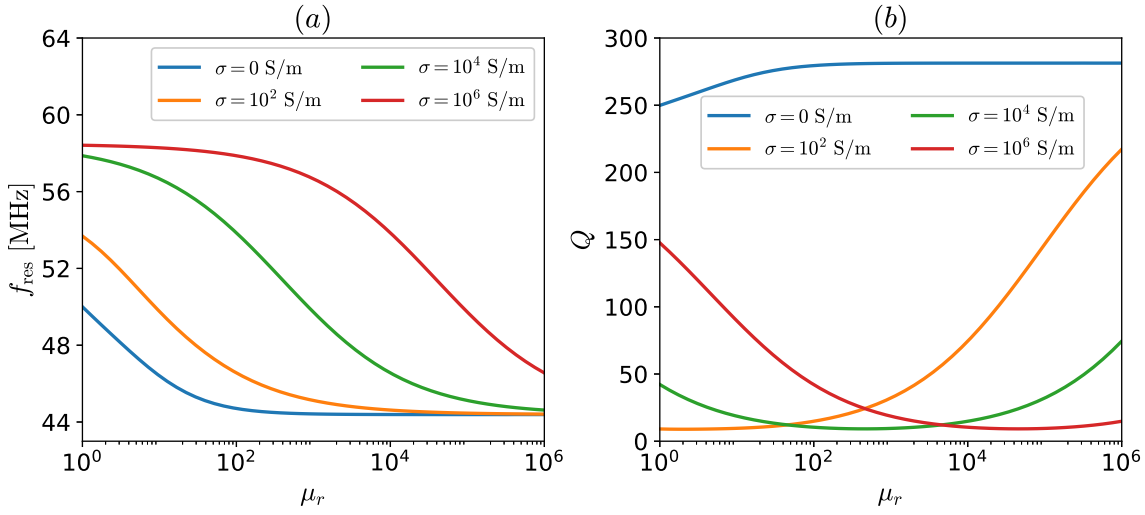

Figure 2.15: Variation of (a) f_{res} and (b) Q with μ_r for four values of sample conductivity σ: $\sigma = 0\,\text{S/m}$ (blue), $\sigma = 10^2\,\text{S/m}$ (orange), $\sigma = 10^4\,\text{S/m}$ (green), and $\sigma = 10^6\,\text{S/m}$ (red). The other system parameters are $r_0 = 25\,\text{mm}$, f_0, $w = 1\,\text{mm}$, $h = 5\,\text{mm}$, $Q_0 = 250$, $t = 5\,\text{mm}$, $\sigma = 0\,\text{S/m}$, and $\varepsilon_r = 1$.

It can be seen that conductivity influences heavily the evolution of the two parameters of interest. At $\mu_r = 1$, the resonant frequency f_{res} starts higher for larger values of σ. This is in agreement with the analysis in the previous section. As μ_r increases, the conductivity effects are counterbalanced, and the resonant frequency starts decreasing. For small σ (e.g. $\sigma = 10^2\,\text{S/m}$), the permeability quickly counteracts the conductivity effect and leads to a rapid drop in the resonant frequency as μ_r increases further. For

large conductivities (e.g. $\sigma = 10^6\,\mathrm{S/m}$), the shielding effect at the sample's surface is strong, and larger permeabilities are required to overcome it. The value of Q at $\mu_r = 1$ also depends on σ. When losses are low (e.g. $\sigma = 10^2\,\mathrm{S/m}$), the self-inductance of the coil increases strongly enough with permeability for Q to rise back quickly. As conductivity increases, the flux concentrated by the magnetic material results in larger eddy currents, which, in turn, result in larger dissipation losses within the sample. This is noticeable for $\sigma = 10^4\,\mathrm{S/m}$ and $\sigma = 10^6\,\mathrm{S/m}$, where Q initially starts decreasing as μ_r increases. At some point, the losses due to eddy currents are neutralised by the increase in the coil's self-inductance, resulting in an increasing Q. The lower the material conductivity, the sooner this transition occurs.

2.4.2 Permeability detection using f_{res} and Q

Whilst in the conductivity case, f_{res} and Q provided different, complementary trends which aided in detection, in the case of permeability when $\sigma = 0\,\mathrm{S/m}$, these two parameters can be used interchangeably since both their variation stems from the coil's self-inductance variation.

From an optimisation point of view, varying the slab's thickness, t, and the relative distance between the slab and the coil, h/r_0, are the two mechanisms that can affect detection. Different thicknesses can be used to target different ranges of μ_r, whilst proximity between the slab and the coil can result in larger, easier-to-detect changes. As in the case of conductivity, when the coil is too close to the slab, errors in correctly assessing the distance between them result in very large detection errors. It is important to operate as close as our distance measurement technique allows. This can be analytically studied by imposing artificial height differences and deciding when the detection error is unacceptable.

Analytical extraction of μ_r was performed using the same method outlined in 2.3.5. Artificial input data was computed by adding noise to the data obtained from the analytical model described in Section 2.2. A bisection algorithm was used to determine μ_r, which minimises the difference between the analytical data and the artificial input data. The

percentage difference between the actual value of μ_r and the extracted value is referred to as the analytical error in extraction.

Figure 2.16 shows the error between the extracted relative permeability and the actual relative permeability value when an artificial error of 0.1% in f_{res} is imposed and different systems parameters are varied: (a) thickness t, (b) relative height h/r_0 and (c) conductivity of the sample σ. Unless otherwise stated in the figure legend, the system's parameters are the same as in Fig. 2.11.

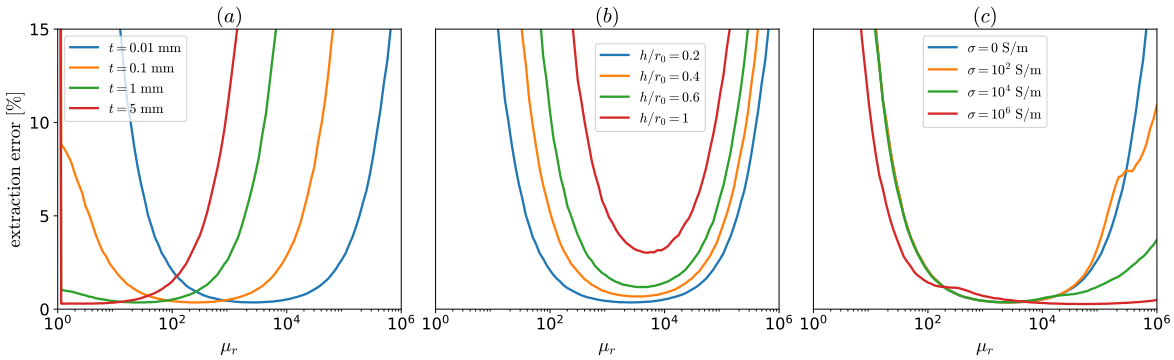

Figure 2.16: Permeability extraction results for (a) different sample thicknesses, (b) different relative distances between the slab and the sample, and (c) different conductivities. Unless otherwise stated in the legend, the parameters of the system are: $r_0 = 25\,\text{mm}$, $w = 1\,\text{mm}$, $f_0 = 50\,\text{MHz}$, $h = 5\,\text{mm}$, $Q_0 = 250$, $t = 5\,\text{mm}$, $\sigma = 0\,\text{S/m}$, and $\varepsilon_r = 1$.

Figure 2.16(a) shows the error in extraction as a function of relative permeability, μ_r, for different thicknesses: $t = 0.01\,\text{mm}$ (blue), $t = 0.1\,\text{mm}$ (orange), $t = 1\,\text{mm}$ (green), and $t = 5\,\text{mm}$ (red). As from the previous section, decreasing the thickness of the slab shifts the accurate detection range towards higher permeabilities, making it possible to tune the measurement device to a specific range. Whilst $t = 5\,\text{mm}$ is suitable for relative permeabilities lower than 100, decreasing the thickness to $t = 1\,\text{mm}$ leads to the possible detection of relative permeabilities up to $\mu_r = 1000$. The thinnest considered slab ($t = 0.01\,\text{mm}$) is no longer suitable for $\mu_r < 100$ but is capable of detecting permeabilities as high as $\mu_r = 10^5$ with an extraction error lower than 5%.

Figure 2.16(b) shows the error in extraction as a function of relative permeability, μ_r, for different relative distances between the coil and the sample: $h/r_0 = 0.2$ (blue), $h/r_0 = 0.4$ (orange), $h/r_0 = 0.6$ (green), and $h/r_0 = 1$ (red). The detection error reduces as the relative distance decreases. This allows for a wider range of relative

permeabilities to be detected when the sample is closer to the coil. When the relative distance between the coil and the sample is $h/r_0 = 1$, the relative permeabilities that can be detected are in the range $\mu_r \in (10^4, 3 \times 10^4)$. However, if the distance is reduced to $h/r_0 = 0.2$, the range changes to $\mu_r \in (10^2, 10^5)$.

Figure 2.16(c) shows the error in extraction as a function of relative permeability, μ_r, for different sample conductivities: $\sigma = 0\,\mathrm{S/m}$ (blue), $\sigma = 10^2\,\mathrm{S/m}$ (orange), $\sigma = 10^4\,\mathrm{S/m}$ (green), and $\sigma = 10^6\,\mathrm{S/m}$ (red). The low relative permeability range is not significantly affected by the increase in conductivity. However, in the higher permeability range, increasing σ reduces the error in permeability detection. This is because additional changes are present for large μ_r when conductivity is larger.

2.5 Permittivity detection

Permittivity, ε, quantifies the ability of a material to store and transmit electric energy in the presence of electric fields. Formally, it is the ratio between the total electric flux density, $\mathbf{D}$, and the electric field, $\mathbf{E}$, which causes polarisation within the sample. The permittivity of materials, ε, is often related to the permittivity of free space, ε_0, through the relative permittivity, ε_r: $\varepsilon = \varepsilon_r \varepsilon_0$.

Permittivity has a wide range of standard applications. In capacitor design, higher permittivities allow more charge to be stored within the same physical capacitor size. In microwave and RF design, permittivity can be tailored to optimise device performance by determining wave propagation speed. In optics, permittivity determines the refractive index of a material, which is the key to designing lenses, fibre optics, or photonic crystals. Negative permittivity, achieved through rods by [34] and [35], contributed to the birth of the field of metamaterials, which have exciting applications in areas such as optics and waveguiding.

As with conductivity and permeability, permittivity can vary significantly for different materials. Air and vacuum have a relative permittivity of $\varepsilon_r = 1$; water has a relative permittivity of $\varepsilon_r \approx 80$ whilst ceramics can reach values around $\varepsilon_r = 100$. Body tissues also have varying permittivities, as illustrated in Fig. 2.3. This property is used in various

body imaging techniques. Some materials, known as colossal permittivity materials [147], can have permittivity above $\varepsilon_r = 10^4$. As in the case of permeability, these values can vary significantly with operating frequency.

Because permittivity quantifies the electrical energy stored, it is expected that it will not significantly impact our system, which relies on the magnetic fields generated by the excited coil. The variation of f_{res} and Q with relative permittivity, ε_r is shown in Fig. 2.17. The change in f_{res} up to $\varepsilon_r = 1000$ is lower than 0.1%, and the change in Q is lower than 0.6%. These kinds of changes are comparable to the level of experimental error, and hence, they would be challenging to detect. When σ starts increasing, the impact of permittivity is even less remarkable, with multiple publications omitting this term in their analysis.

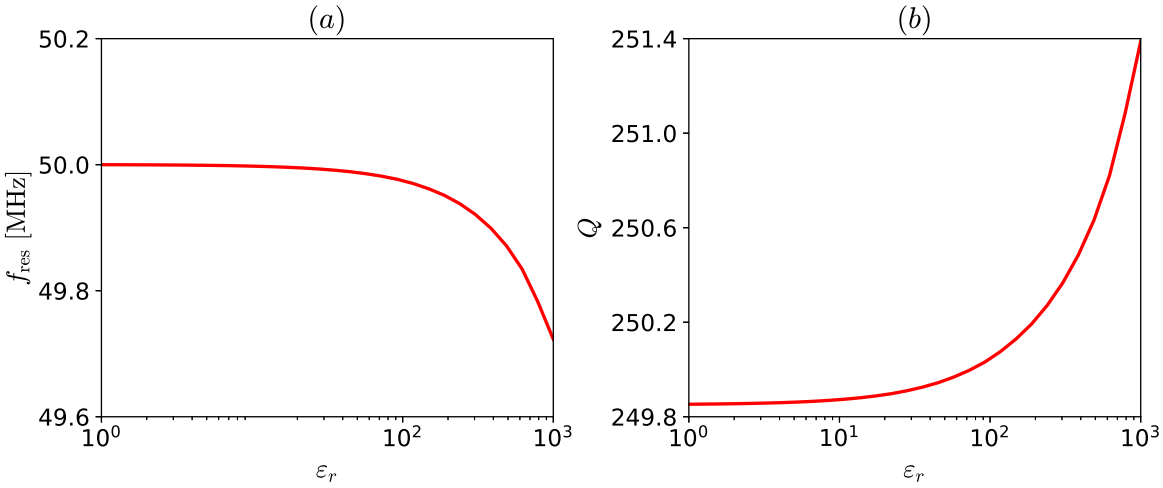

Figure 2.17: Variation of (a) f_{res} and (b) Q with relative permittivity, ε_r. The parameters of the system are: $r_0 = 25\,\text{mm}$, $w = 1\,\text{mm}$, $f_0 = 50\,\text{MHz}$, $h = 5\,\text{mm}$, $Q_0 = 250$, $t = 5\,\text{mm}$, $\sigma = 0\,\text{S/m}$, and $\mu_r = 1$.

More accurate permittivity detection can be achieved by leveraging electric fields. One effective approach is using an open split-ring resonator, where the resonator's gap is placed directly above the sample – as demonstrated in [148].

2.6 Discussion and conclusions

This chapter analytically explored the usage of a split-ring resonator for the electromagnetic characterisation of materials.

An analytical model was built, starting from and improving upon the method presented by Dodd and Deeds. Relative permittivity is included in the model to improve accuracy when operating at high frequencies, and the computation speed was significantly improved by computing the self-inductance using the geometric mean distance (GMD) approach. An additional element of novelty introduced in this thesis is the focus on the resonant frequency, f_{res}, and quality factor, Q, of the probe. These parameters more comprehensively capture the probe's electromagnetic response and can be measured with greater accuracy and robustness than the subtle changes in self-inductance alone.

After successfully implementing the analytical model, the focus of the chapter shifted towards conductivity detection. A thorough parametric study was carried out, in which various system parameters (probe radius, probe resonant frequency and sample thickness) were varied, and the resonant frequency and quality factor changes were carefully analysed. Based on these changes, it was found that the quality factor changes are suitable for low (usually $<10\,\text{S/m}$) and high-conductivity detection (usually $>10^5\,\text{S/m}$), whilst the resonant frequency changes can be best applied to mid-range conductivities. It was found that frequencies around 50 MHz enhance the probe's sensitivity for low conductivities, enabling the detection of conductivities as low as $0.05\,\text{S/m}$ with an accuracy of 95%. It was also demonstrated that lower frequencies, such as 10 MHZ, improve detection in the high conductivity range. The ratio between the probe radius and the distance between the probe and the sample was also an important point of discussion. It was concluded that, whilst a relatively closer probe aids in analytical detection, the uncertainties in height measurements represent a potential risk. The system parameters change significantly when the probe is closer to the sample, meaning that even minor deviations in the position can cause significant errors. An accurate position mechanism is strongly suggested when implementing this method in practice.

Permeability detection was investigated in a similar manner. The resonant frequency and the quality factor were found to vary in a similar manner; hence, both parameters are suitable for detection in the same regions. It was found that the frequency of the probe does not significantly impact detection. Since material permeability varies widely

with frequency, this finding was positive. Even if the frequency cannot be used to aid detection, as in the case of conductivity, the robustness of the probe to frequency variations implies that the probe can be used to characterise the material in a wide frequency range. It was found that modifying the thickness of the sample is the most successful way of targeting different permeability regions, with larger sample thicknesses being optimal for high permeability detection and smaller ones for low permeability detection.

It is noteworthy that simultaneous permeability and conductivity detection is also possible, as in [149, 150]. This is possible since combining the two electromagnetic properties results in partially independent resonant frequency and quality factor variations.

Finally, the changes in permittivity were analysed. It was shown that these changes are too small to support any accurate detection using magnetic fields. An alternative, superior method, which exploits the electric properties of materials, was discussed. This method can be implemented by using an open split-ring resonator whose gap is placed immediately above the sample, as in [148].

Overall, this chapter proved that monitoring the resonant frequency and quality factor changes of a split-ring resonator can lead to successful localisation. More importantly, the system, its advantages, and its limitations were better understood, which provides a strong foundation for the following chapters. Chapter 3 will translate these analytical insights into numerical and experimental validation, further assessing the practicality of this approach for sensitive and accurate remote sensing of material parameters using a single resonant element.

The single SRR sensor is also the foundation for the distributed sensors of coupled resonators discussed in Chapters 4 and 5. In an array of resonators, when an object is placed on the array, the changes in the behaviour of an individual resonator (discussed in this chapter) result in additional reflections of the propagating magnetoinductive (MI) waves. These reflections allow for localisation and characterisation of the objects placed on the distributed sensors, which will be the focus of Chapters 4 and 5.

CHAPTER 3

Low-conductivity detection

3.1 Introduction

Over the last three decades, high-conductivity materials have been extensively researched, with eddy-current testing techniques capable of measuring high conductivities [72–76, 80, 81, 83], permeabilities [84, 144–146], sample thicknesses [70–79, 114] and defect locations [87–97]. The low-conductivity spectrum has only recently started to gain popularity for applications related to human-body imaging. Yin et al. [82] investigated the conductivity and the thickness of saline samples and detected these properties with an error of 3%. However, samples with only four conductivities (3.7, 6.4, 8.3, and 10.2 S/m) were studied in these experiments. Magnetic induction tomography (MIT) and electric impedance tomography (EIT) are also becoming popular areas of research [14, 102, 103, 151], with work being carried out in areas such as breathing monitoring [100, 101].

This chapter focuses on the low-conductivity range by first detecting the conductivity of saline solutions in the range of $(0 - 20)$ S/m. Experimentally obtained resonant frequencies and quality factors are compared both with the predictions from our analytical

model and with numerical results obtained using CST Studio Suite [17]. The conductivity of each sample is extracted using analytical and numerical data. The analytical model performs conductivity detection with an error of only 5.5% over the entire range of conductivities considered. This outperforms the extraction performed using the numerical model, whose error is 9.7%. Having validated our new sensing approach for low-σ, the second part of this chapter moves on to perform a feasibility study on detecting the presence of water in human lungs by numerical simulation. For these simulations, a 3D body model will be used in CST Studio Suite to determine if the changes occurring in f_{res} and Q for a probe placed on the back of the human phantom justify using this method to detect the presence of water in lungs. The electromagnetic properties of all human body tissues are determined using the Cole-Cole model, previously introduced in Section 2.3.2. Four probe radii are trialled to determine the optimum geometry for detecting fluid accumulation in the lungs. The standard VNA errors are analysed against the changes in f_{res} and Q associated with different lung states. The chapter proves that a simple split-ring resonator is not only capable of measuring conductivities in the range (0.04-20) S/m, but also shows great potential for applications related to human body monitoring.

The body model used is the VHP Female CAD v2.2 (Nelly) [152, 153] provided free of charge by Neva Electromagnetics. Their contribution is gratefully acknowledged.

The work in this chapter is linked to the following publication, and some of the figures in the chapter (for which permission to reproduce was received) are adapted from it:

- G. Dima, A. Radkovskaya, L. Solymar, *et al.*, "Inductive sensing of lung conductivity for fluid accumulation detection," in *Proc. 19th Int. Congr. Artif. Mater. Novel Wave Phenom. (Metamaterials 2025)*, 2025. under review
- G. Dima, A. Radkovskaya, C. J. Stevens, *et al.*, "Design of a remote, multi-range conductivity sensor," *Sensors*, vol. 23, 9711, 2023

3.2 Conductivity detection for saline solutions

3.2.1 Experimental arrangement

The experimental arrangement in Fig. 3.1(a) was used for low-σ detection. The probe, placed underneath a low-σ sample of thickness $t = 10$ cm, is connected via a 50 Ω cable and an SMA connection to an 8753ES Hewlett Packard Vector Network Analyzer (VNA). The detection probe was created by fixing a wire of thickness $w = 1.04$ mm in a circular support of radius $r_0 = 25$ mm. The support was 3D-printed using high-impact polystyrene (HIPS), chosen because of its low dielectric constant and dissipation factor. Figure 3.1(b) shows a photograph of the coil embedded in the 3D-printed support, whilst Fig. 3.1(c) shows a picture of the bottom of the coil with the SMA support. The coil was covered with a Rohacell foam sheet to ensure its secure placement. This foam's electromagnetic properties are similar to air, ensuring that the presence of the support will not affect the final results. The coil was placed at a distance $h = (5.32 \pm 0.11)$ mm from the sample, shown in Fig. 3.1(d). The sample is a tank of dimensions 300 mm $\times$ 300 mm, filled with a water layer of thickness $t = 10$ cm. The conductivity of the water was measured using a Hanna HII-8633 multi-range conductivity meter. Salt was added gradually to the water to vary its conductivity from 0.04 S/m to 20 S/m. The lowest conductivity ($\sigma = 0.04$ S/m) corresponds to tap water with no additional salt.

When collecting the data, the impact of the wire and SMA connection is removed through a one-port calibration procedure. The reflection scattering parameter, S_{11}, is collected for a power of 0 dBm. Each spectrum collected had 1601 frequency points and was averaged twice to reduce the system noise. The measurement for each value of conductivity was repeated 20 times to obtain a confidence interval for the measured data. The impedance spectrum, which is the same as the coil impedance, $Z_{11} \equiv Z_0$, was extracted from the S_{11} parameter using the following formula, where $Z_L = 50$ Ω is the known VNA load:

$$Z_{11} = Z_L \frac{S_{11} + 1}{S_{11} - 1}. \tag{3.1}$$

The resonant frequency, f_{res}, and quality factor, Q, are extracted using the 3dB method

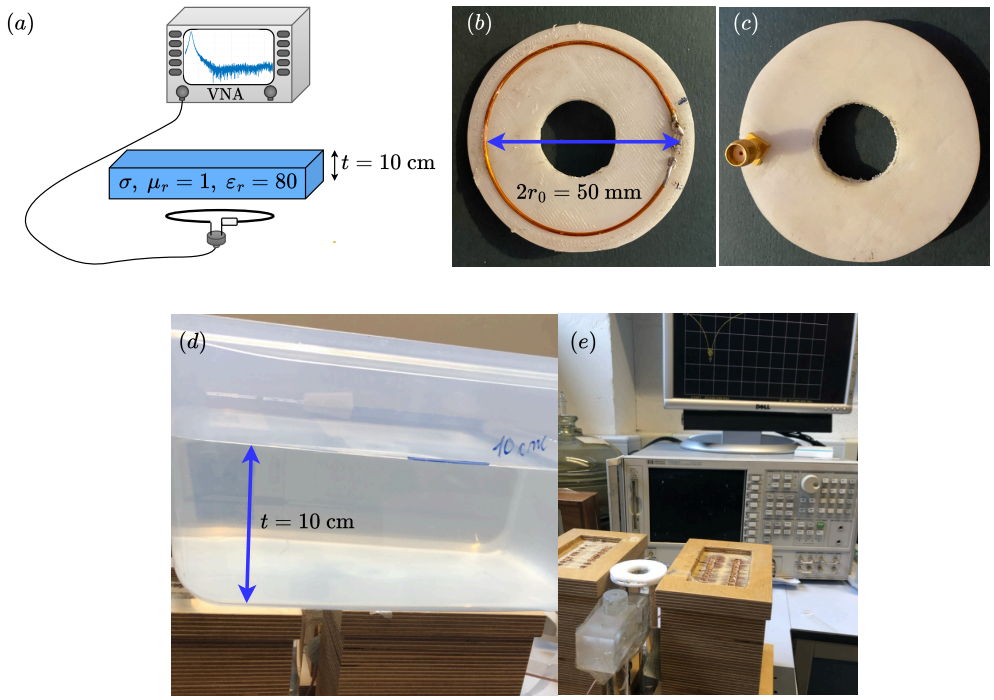

Figure 3.1: (a) Schematic representation of experiment, (b) photograph of top of and (c) bottom of detection coil, (d) sample, and (e) coil connected to VNA without sample (d).

outlined in Section 1.2.2. The extracted data is filtered using a Savitzky–Golay filter of window length 32 and order 2. A Savitzky–Golay filter is able to reduce noise in the data while minimising distortion of the underlying signal shape. To achieve optimal filtering, the window length and order of the filter were gradually varied. After filtering, 10^4 values were interpolated to avoid errors in Q estimation, which could arise from the limited number of frequency points. f_{res} is the frequency where the impedance parameter reaches the minimum, whilst Q is the ratio between f_{res} and the 3dB bandwidth, BW. The properties of the coil in the absence of any sample were found to be: $f_0 = 49.78\,\text{MHz}$ and $Q_0 = 256$. Having extracted f_{res} and Q, it is possible to estimate σ for each data point using the method developed in Chapter 2.

3.2.2 Numerical model

The performance of the analytical model was validated by comparing its predictions with numerically simulated data in CST Studio Suite [17]. CST Studio Suite is a commercial electromagnetic simulation tool based on the Finite Integration Technique. It numerically solves Maxwell's equations over a meshed geometry, with accuracy depend-

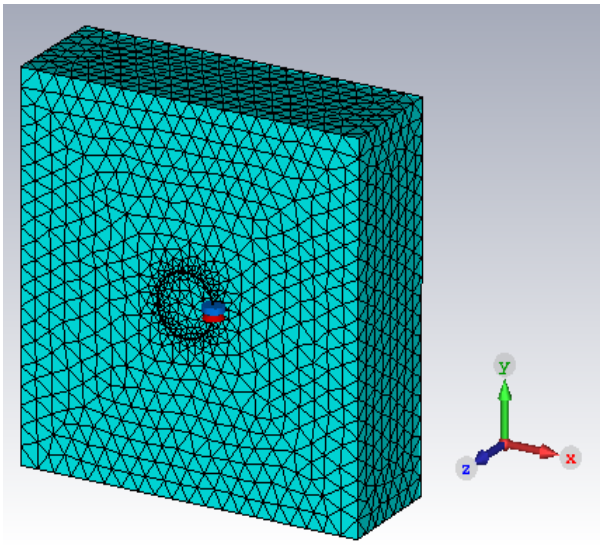

Figure 3.2: Screenshot of CST model showing the conductive sample under test (blue rectangle) and the testing probe (circular black ring). The figure also presents an example of a mesh for the structure. Reproduced from [26]. Ref. [26] is licensed under a Creative Commons Attribution 4.0 License. ©2023 MDPI by G. Dima, A. Radkovskaya, C. J. Stevens, L. Solymar and E. Shamonina.

ing on mesh resolution (number of unit elements, i.e. tetrahedrons), solver settings, and material definitions. While finer meshes improve accuracy, they significantly increase computation time, which can range from minutes to several hours, or even days, depending on the model complexity. Since the analytical model developed in Section 2.2 assumes an infinitely wide sample, CST Studio Suite can be used to test this assumption and establish the applicability range of the analytical model.

The CST model used in this section and an example of a generated mesh are illustrated in Fig. 3.2. The blue rectangle shown in Fig. 3.2 is the tested sample, which has a thickness of $t = 10\,\text{cm}$ and a width six times wider than the coil diameter. This was found to be the width after which increasing the size further does not result in any significant variations of f_{res} and Q for a resonator placed in the vicinity of the sample, i.e. the size where the infinitely wide slab assumption is adequate. The circular ring in Fig. 3.2 is the measurement probe of radius $r_0 = 25\,\text{mm}$ and wire width $w = 1.04\,\text{mm}$. The distance between the probe and the material was set to $h = 5.32$ mm, and the coil was excited by a $50\,\Omega$ S-parameter excitation source (red marker). The element was tuned to $f_0 = 49.78\,\text{MHz}$ using a lumped capacitor (blue marker) placed in series with the excitation source. The resistance of the lumped capacitor was varied until the

free-space quality factor was $Q_0 = 256$.

The distance between the air-filled bounding box and the sample was set to 500 mm in all directions. The simulation boundary condition was defined as `open (add space)`, which approximates a free-space experimental environment. The background mesh used five cells per wavelength, while the local mesh was refined to a maximum of 0.5 mm for the coil and 15 mm for the sample. These values were selected to balance accuracy with computation time. The sample meshing presents the most significant trade-off: a finer mesh is necessary to ensure multiple tetrahedral layers within the sample and to capture the field variation accurately. However, increasing the number of layers raises the computational cost dramatically due to the sample's large volume.

The simulations were performed using the `Frequency Solver`, and the Z_{11} parameter was computed from the resulting S_{11} parameter. The resonant frequency, f_{res}, and the quality factor, Q, are then extracted using the 3dB method.

3.2.3 Experimental results

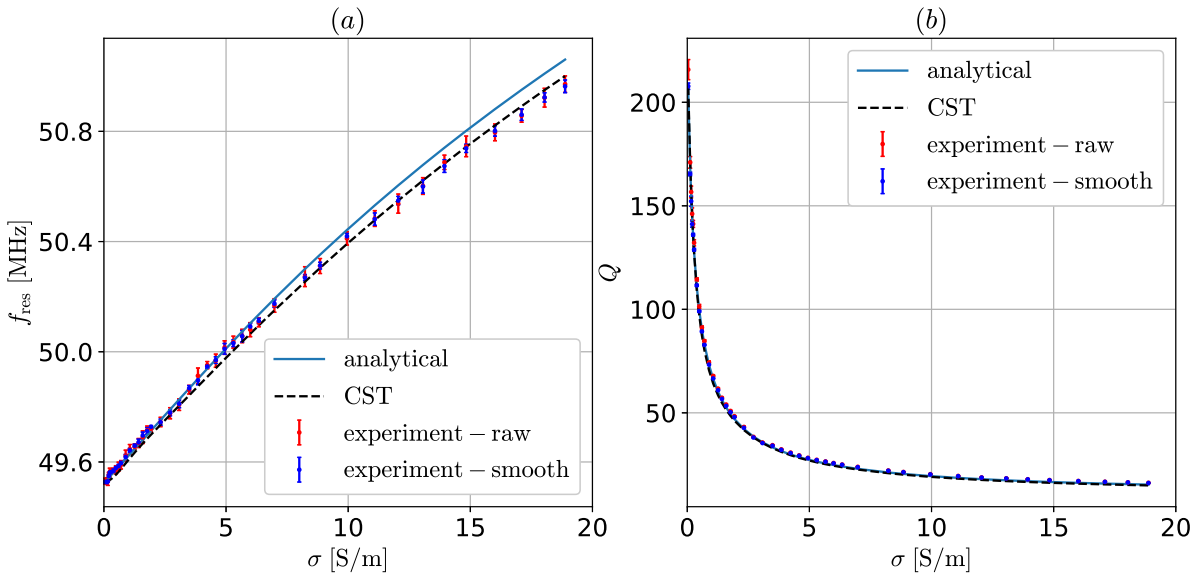

Figure 3.3: Variation of (a) f_{res}, and (b) Q with σ in the analytical model (blue solid line), the raw experimental data (red data points), the smoothed experimental data (blue data points), CST data (black dashed line). The system parameters are $r_0 = 25$ mm, $w = 1.04$ mm, $h = 5.32 \pm 0.11$ mm, $f_0 = 49.78$ MHz, $Q_0 = 256$, $t = 10$ cm, $\mu_r = 1$, and $\varepsilon_r = 80$. The experimental data errors are shown through the error bars in the corresponding data points. Reproduced from [26]. Ref. [26] is licensed under a Creative Commons Attribution 4.0 License. ©2023 MDPI by G. Dima, A. Radkovskaya, C. J. Stevens, L. Solymar and E. Shamonina.

Figure 3.3 shows the variation of f_{res} and Q as σ increases from 0.04 S/m to 20 S/m: the analytical model (blue solid line), the raw experimental data (red data points), the smoothed experimental data (blue data points), and the CST data (black dashed line). The error bars indicate the mean errors in the experimental data. The mean and the variance are calculated based on the 20 experimental points obtained for each σ. The variance in the experimental data decreases significantly once the data is smoothed.

The results in Fig. 3.3 are normalised to the first point corresponding to water without salt ($\sigma = 0.04$ S/m). This is necessary because the close proximity between the resonator and the water layer results in errors associated with stray capacitances and geometrical imperfections of the system. The normalisation was also performed for the CST data.

It can be seen from Fig. 3.3 that the analytical and numerical data match the experimental data very well. The experimental resonant frequency can be seen to deviate from the analytical curve once σ is increased due to stray capacitance effects. However, the match between the analytical, the experimental and the numerical quality factor, Q, is strong enough to support the assumption that σ extraction is possible.

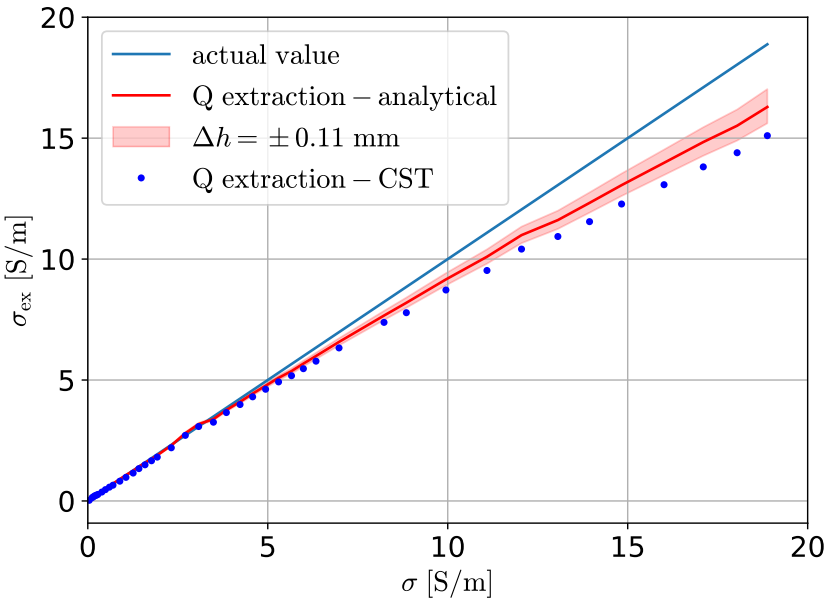

Figure 3.4: Extracted conductivity from the analytical model (red line) with the error bar for height uncertainty (red shaded area) and from CST data (blue dots). The parameters of the system are $r_0 = 25$ mm, $w = 1.04$ mm, $h = 5.32 \pm 0.11$ mm, $f_0 = 49.78$ MHz, $Q_0 = 256$, $t = 10$ cm, $\mu_r = 1$, and $\varepsilon_r = 80$. Reproduced from [26]. Ref. [26] is licensed under a Creative Commons Attribution 4.0 License. ©2023 MDPI by G. Dima, A. Radkovskaya, C. J. Stevens, L. Solymar and E. Shamonina.

Figure 3.4 shows the extracted conductivity, σ_{ex}, against the actual conductivity, σ. The blue solid straight line is the actual conductivity, σ, included to aid interpretation. The extraction result using the analytical model is shown using the red solid line, with the red shaded area representing the full range of extracted values of σ when the height uncertainty is accounted for. The blue dots show the extracted values of σ using the CST data, which was performed by interpolating between the pre-stored CST values, shown in Fig. 3.3. In both cases, the quality factor, Q, was used as the extraction parameter.

Using the analytical model, $\sigma < 20$ S/m detection is performed with an error lower than 6% while conductivities of up to 5 S/m are detected with a mean error of 3%. Table 3.1 shows the mean extraction error in different σ ranges for the analytical and CST extraction. We can conclude that using Q as a separation criterion is indeed an effective technique for characterising very low-σ samples, as the mean error in detection for $\sigma < 1$ S/m is 4.5%, when using the analytical model.

Table 3.1: Comparison between the mean error in conductivity extraction using the analytical model and the CST numerical results for different conductivity ranges.

Range	Nb. of Samples	Analytical Extraction	CST Extraction
$\sigma < 1$ S/m	11	4.5%	9.2%
$\sigma < 5$ S/m	25	3.0%	7.1%
$\sigma < 12.5$ S/m	35	3.9%	7.9%
$\sigma < 20$ S/m	42	5.5%	9.7%

Table 3.1 supports using the analytical model for extraction as all the errors are lower than the ones from the interpolation extraction using CST. The analytical model extraction has an error of 5.5% for the entire range, whilst using the CST extraction leads to a 9.7% extraction error. The comparison is valid for all σ ranges, where the error in CST extraction is almost double the analytical extraction. The main reason why the analytical model outperforms CST is the intrinsic errors associated with the numerical meshing. While finite element analysis is a powerful technique, obtaining quantitatively reliable results is challenging. Accurately representing a continuous system with a discrete mesh requires a very large number of tetrahedrons - often to the point where the computational time becomes impractical. In this case, the limited mesh density and

discrete sampling points contributed to higher errors. Although the data points used for extraction matched the experimental positions, this had little impact due to the system's nonlinearity. When interpolating on a non-linear curve, even small deviations can produce large errors. By contrast, the analytical model offers consistent results and computes f_{res} and Q for a full-range of conductivities within seconds, compared to over 30 minutes required by CST for a single conductivity value.

An important consideration in extraction is the accuracy of determining the distance between the sample and the coil. When the distance h varies by 0.11 mm, the mean extraction error for the analytical model goes from 5.5% to 6.6%. This implies that accurate height measurements should be a priority when implementing this method.

The results presented in this thesis are comparable in accuracy to those reported by Yin et al. [70], who achieved a 3% error, versus 5.5% in this work. The two methods, however, rely on different principles: Yin et al. use a dual-coil inductive system, while the approach developed here uses a single coil and extracts conductivity from shifts in resonant frequency and quality factor. Although both methods apply a form of normalisation—introduced as a scaling factor in their work and through direct normalisation here—the experimental setup in this thesis is considerably simpler. Another important distinction lies in the number and range of tested samples. While Yin et al. report results for four samples, this work demonstrates accurate conductivity detection across 42 samples, including 11 with conductivities below 1 S/m, achieving an average error of 4.5%. Their lowest reported conductivity was 3.7 S/m, whereas this method proves effective well into the sub-1 S/m range.

This work contributes to the literature by extending the measurable conductivity range to lower values, demonstrating the viability of a single-coil approach, and enabling faster, simpler characterisation across a larger sample set.

3.3 Numerical analysis for water detection in lungs

This section builds upon the principles outlined in Chapter 2 and the experimental validation presented previously, aiming to assess whether a resonant probe can detect

abnormalities in the human body. Specifically, it explores whether changes in lung conductivity – such as those caused by the presence of water – can be detected using the designed probe. With the emergence of COVID-19, there is a growing need for affordable, non-invasive tools for continuous respiratory monitoring. A simple resonant probe could offer a low-complexity solution for long-term observation, flagging abnormal increases in lung conductivity associated with fluid accumulation.

Two relevant techniques for conductivity-based imaging are Electric Impedance Tomography (EIT) and Magnetic Induction Tomography (MIT). EIT uses surface electrodes to inject currents and measure voltage responses, reconstructing conductivity distributions from these data [104, 105, 154, 155]. Although EIT is clinically used, for example, in lung monitoring [104–106], it suffers from poor spatial resolution, sensitivity to electrode placement, and the need for direct contact. MIT, by contrast, is a contactless alternative that induces eddy currents using magnetic fields and detects the resulting secondary fields with receiver coils [103, 156, 157]. The measured secondary field depends on the local conductivity, magnetic permeability, and geometry of the object, allowing the problem to be formulated as an inverse reconstruction of conductivity from field measurements. MIT can map the conductivity distribution of tissues and detect strokes or monitor lung ventilation without direct patient contact [156]. Recent developments in MIT instrumentation have focused on increasing sensitivity and resolution. High-sensitivity magnetic field sensors such as optically pumped magnetometers (OPMs) and superconducting quantum interference devices (SQUIDs) have been integrated into MIT systems to detect secondary fields from very low conductivity targets [158]. MIT avoids many of EIT's limitations and has shown promise in stroke detection [159], lung ventilation monitoring [160], and tissue characterisation [103]. However, MIT is still researched, since it is not yet a widespread industrial or medical standard.

The method developed in this work shares similarities with MIT but uses a single resonant coil rather than a full tomographic setup. While it does not offer spatial imaging, it is significantly simpler and faster to implement. The results in this chapter serve as a proof-of-concept, demonstrating the feasibility of detecting conductivity changes due to

water in the lungs. This approach could be extended to include multiple coils in future work, aligning more closely with full MIT systems.

In this section, the resonant frequency and the quality factor of a probe placed on the back of a human phantom will be monitored whilst the conductivity of the lung is varied. The properties of all used human tissues are computed using the Cole-Cole model presented in Section 2.3.2.

3.3.1 CST body model and system description

A body model with a body mass index (BMI) of 36 [152, 153], shown in Fig. 3.5(a), was imported into CST to determine the impact of lung conductivity variation. Figure 3.5(b) shows a clearer picture of the inside of the body model without the external layers of skin, muscle and fat. Since this work focused on the lung area, the model was simplified by cutting around the lung region, as shown in Fig. 3.5(c). In other words, instead of modelling the entire body [Fig. 3.5(a)] only a rectangular area in the xy direction was kept, with the rest of the body removed. The size of the rectangle was chosen to be 28 cm $\times$ 25 cm. This simplification was justified as the removed body parts would have a negligible effect on the sensor coil [back circle in 3.5(c)] placed on the back of the human subject. This simplification was necessary as the complexity of the entire model was too large for the computational capacities of the computer used. Simplifications were also made when assigning tissues to each body element. The heart was modelled in its diastolic phase—the relaxed portion of the cardiac cycle during which it is filled with blood. This represents a worst-case scenario for the detection probe, as cardiac conductivity is at its highest ($\sigma_{\text{heart,50MHz}} = 1.19\,\text{S/m}$) during this phase. The presence of such a highly conductive tissue increases the likelihood of masking smaller variations in lung conductivity, making detection more challenging. All bones were considered cortical bones, which is also the most conductive kind of bone tissue. The final model used nine tissues: cartilage, cortical bone, blood, lung, grey matter, white matter, muscle, fat, and skin.

A loop of mean radius r_0 and wire width $w = 1$ mm was placed on the back of the

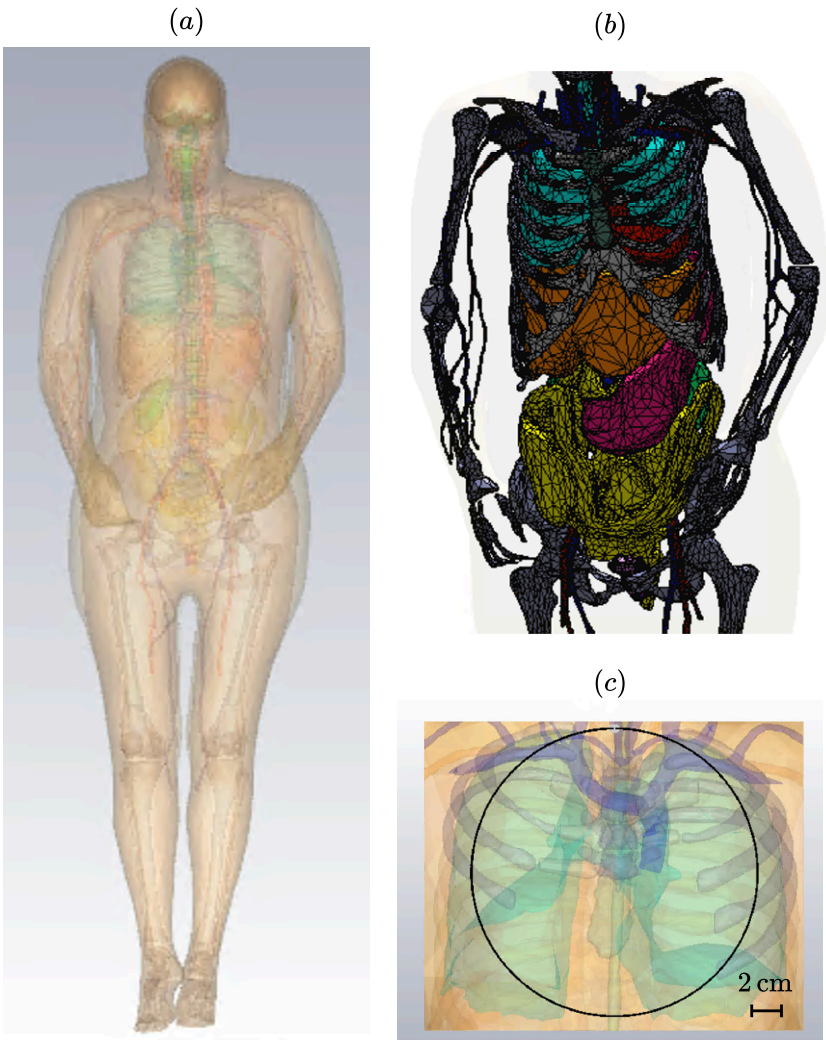

Figure 3.5: Body model [152, 153] used for CST simulations (VHP-Female Computer-Aided Design (CAD) v2.2 Nelly): (a) entire Computer-Aided Design (CAD) model, (b) inner components of the model with meshing, and (c) truncated model section with resonant probe above it (black circle).

body phantom. Its position was varied until the probe was as close as possible to the human body without touching it. The probe was excited by a 50 Ω lumped S-parameter excitation source. A tuning lumped capacitor was added in series with the S-parameter excitation and used to set the probe's free-space resonant frequency to $f_0 = 50\,\text{MHz}$. The distance between the air-filled box and the structure is 500 mm in all directions, and the simulation boundary condition is `open (add space)`. Considering the complex nature of the model, the meshing was coarser compared to the numerical simulations performed for the saline solution and coil in the previous section. The maximum number of cells per model box edge was one per wavelength for the air-filled background and six per

wavelength for the model. The number of tetrahedrons in each of the 20 simulations performed was over 260,000, compared to $\approx 60,000$ for the saline solution and coil simulations performed in the previous section.

Similar to the previous section, the S_{11} parameter was used to compute the Z_{11} parameter. The 3dB method outlined in Section 1.2.2 was used to extract f_{res} and Q of the resonator from Z_{11}.

Figure 3.6 presents a schematic of the body-coil system, where the heart is shown in red, the lungs in blue, and the yellow background contains fat, muscle and skin. The phantom is positioned on its back and the coil is placed underneath it, so that $z = 0$ mm (top of Fig. 3.6) is actually on the back of the body.

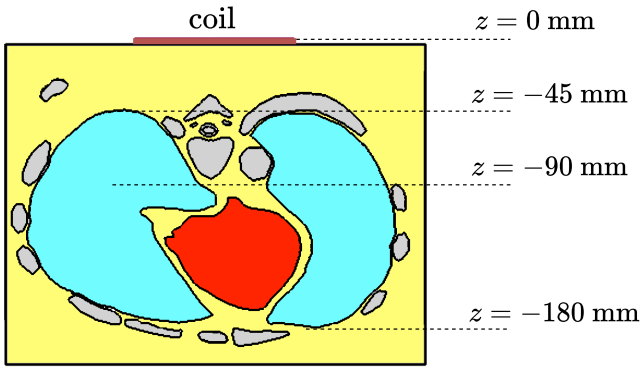

Figure 3.6: Simplified model geometry cross-section of the body placed on its back.

The simulations were performed at $f_0 = 50\,\text{MHz}$, as this was proven in Section 2.3.3 to be an adequate frequency for detecting low conductivities experimentally. The average penetration depth at $f_0 = 50$ MHz for the considered tissues is 90 mm, which ensures that the coil interacts primarily with the closest lung region. When a patient lies on their back, gravity shifts fluid towards this region, enhancing the coil's sensitivity to pathological changes. This shallow penetration depth reduces interaction with the heart (the most conductive tissue in the model), which increases the likelihood that observed changes originate from the lungs rather than from highly conductive surrounding tissues.

In Chapter 2, it was found that for infinitely wide samples, increasing the radius of the coil enhances detection. Here, the lung size is a limiting factor to how much the radius of the

coil can be increased. If the coil is much bigger than the lung, the fields generated around the coil track will circulate in the air instead of penetrating the model. It is, therefore, safe to assume that the findings of Chapter 2 apply when selecting the minimum allowable size of the probe, but the lung size determines the extent to which increasing r_0 aids in detection. Four values of r_0 were used in testing: $r_0 = 50,\ 100,\ 150,$ and $200\,\text{mm}$. The lower limit is close to the distance between the probe and the closest lung cell, whilst the upper limit is set close to the lung's vertical dimension.

For each radius, the tuning capacitance was computed using the analytical model from Chapter 2. The capacitances used for each case and the actual achieved free-space frequency are outlined in Table 3.2, alongside the resulting free-space quality factor of the coil, Q_0. In practical implementation, the quality factor values will be smaller due to additional resistances caused by capacitors and soldering. However, since the focus of this chapter is to distinguish between different lung states, the free-space quality factor is less significant for this analysis.

Table 3.2: Capacitances used for tuning CST probe depending on radius, r_0 and actual resulting free-space resonant frequencies, f_0.

$\mathbf{r_0}$ [mm]	C [pF]	$\mathbf{f_0}$ [MHz]	$\mathbf{Q_0}$
50	40.00	46.06	479.8
100	17.00	46.04	523.1
150	10.50	45.14	512.9
200	7.45	43.86	430

The conductivity and permittivity were modified for each frequency used according to the Cole-Cole model [129] introduced in Section 2.3.2. These values are summarised in Table 3.3. The conductivity of the lung infiltrated with water was assumed to be $0.7\,\text{S/m}$ (inflated) and $0.9\,\text{S/m}$ (deflated) at $50\,\text{MHZ}$. It is important to note that the conductivities of infiltrated lungs are estimated based on the available literature [107, 132–139]. While several studies have investigated the impact of water accumulation on lung conductivity in both animal models [131, 136–139] and humans [130, 133, 134] and strongly support the increase in conductivity, a comprehensive model describing how lung conductivity varies with both frequency and water content does not exist. Moreover, even if such a model were available, the conductivity values would likely vary significantly

between individuals due to physiological differences. The values used approximate to a 50% infiltration with fluid of conductivity similar to that of blood.

Table 3.3: Conductivity, σ, and relative permittivity, ε_r, of tissues used in the CST model at 50 MHz. Values were computed according to [126–128].

Tissue	σ **[S/m]**	ε_r
cartilage	0.44	68.5
cortical bone	0.06	17.7
blood	1.19	94.2
inflated lung	0.28	41.3
deflated lung	0.52	81.3
grey matter	0.41	92.2
white matter	0.27	111.1
muscle	0.68	76.3
fat	0.03	77.1
skin	0.41	6.9

3.3.2 Results

Figure 3.7(a) shows the ratio of the probe's resonant frequency, f_{res}, to its free-space resonant frequency, f_0, as a function of lung conductivity. Figure 3.7(b) presents the same ratio for the quality factor(Q/Q_0). All the ratios are presented as percentages. The numerical values of f_{res} and Q are provided in Table 3.4, with differences between lung states indicated in parentheses. The conductivities considered represent four states of interest: (A) healthy inflated lung ($\sigma = 0.28\,\text{S/m}$), (B) healthy deflated lung ($\sigma = 0.52\,\text{S/m}$), (C) infiltrated inflated lung ($\sigma = 0.7\,\text{S/m}$), and (D) infiltrated deflated lung ($\sigma = 0.9\,\text{S/m}$). It is important to note again that the infiltrated lung conductivities are approximations based on literature, where water presence in the lungs can result in conductivity doubling [130, 131, 138, 139]. The values used in this thesis are at the upper boundary of the reported values, and further work is needed to explore the impact of partial lung infiltration.

The most significant deviations from the free-space state occur for $r_0 = 100\,\text{mm}$, as the coil tracks, where the magnetic field is strongest, are positioned immediately below the lungs. For larger coils, although stronger fields are generated, they are displaced and interact less with the lungs. This is illustrated in Fig. 3.8, which presents the power loss density inside the body for different coil radii: (a) $r_0 = 50\,\text{mm}$, (b) $r_0 = 100\,\text{mm}$,

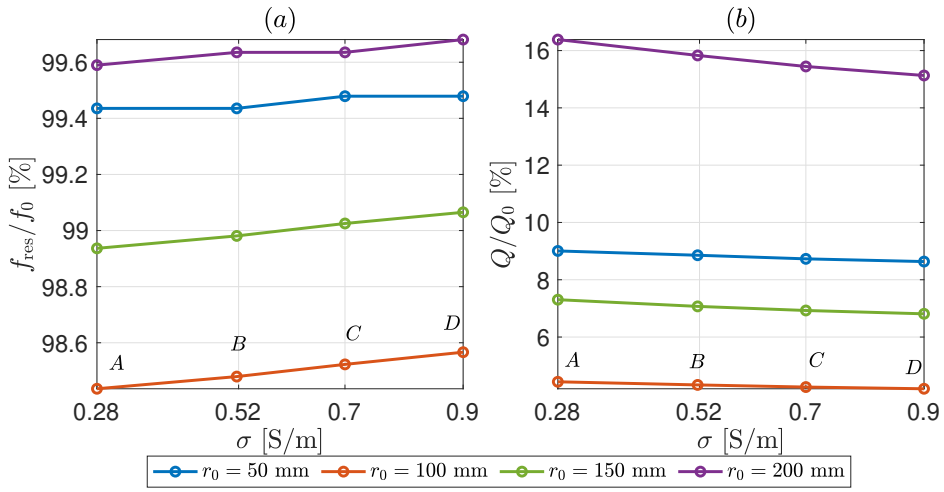

Figure 3.7: Ratio of the: (a) resonant frequency, f_{res} and (b) quality factor, Q, to their respective free-space values as a function of lung conductivity, σ, for 5 different radii ($r_0 = 50,\ 100,\ 150,\ 200\,\text{mm}$). The four relevant lung states: (A) healthy inflated lung ($\sigma = 0.28\,\text{S/m}$), (B) healthy deflated lung ($\sigma = 0.52\,\text{S/m}$), (C) infiltrated inflated lung ($\sigma = 0.7\,\text{S/m}$), and (D) infiltrated deflated lung ($\sigma = 0.9\,\text{S/m}$) are marked on the figure.

Table 3.4: Resonant frequency, f_{res}, and quality factor, Q, changes for different coil radii, r_0, and different lung conductivities, σ, at $f_0 \approx 50\,\text{MHz}$.

$\mathbf{r_0}$ [mm]	σ [S/m]	$\mathbf{f_{res}}$ [MHz]	Q
50	0	46.06	479.8 (Q_0)
	0.28	45.80	43.2
	0.52	45.80 (+0)	42.5 (-0.7)
	0.7	45.82 (+0.02)	41.9 (-0.6)
	0.9	45.82 (+0)	41.4 (-0.5)
100	0	46.04	523.1 (Q_0)
	0.28	45.32	23.2
	0.52	45.34 (+0.02)	22.6 (-0.6)
	0.68	45.36 (+0.02)	22.3 (-0.3)
	0.9	45.38 (+0.02)	21.9 (-0.4)
150	0	45.14	512.9 (Q_0)
	0.28	44.66	37.5
	0.52	44.68 (+0.02)	36.3 (-1.2)
	0.7	44.70 (+0.02)	35.5 (-0.8)
	0.9	44.72 (+0.02)	34.9 (-0.6)
200	0	43.86	430.0 (Q_0)
	0.28	43.68	70.4
	0.52	43.70 (+0.02)	68.1 (-2.3)
	0.7	43.70 (+0)	66.4 (-1.7)
	0.9	43.72 (+0.02)	65.1 (-1.3)

(c) $r_0 = 150\,\text{mm}$, and (d) $r_0 = 200\,\text{mm}$. When $r_0 = 100\,\text{mm}$, the highest power loss regions are concentrated above the lungs, maximising interaction. Increasing r_0 further shifts these regions away, reducing the overall changes in system response. Consequently, for f_{res}, a consistent increase of 20 kHz between conductivity states is observed when

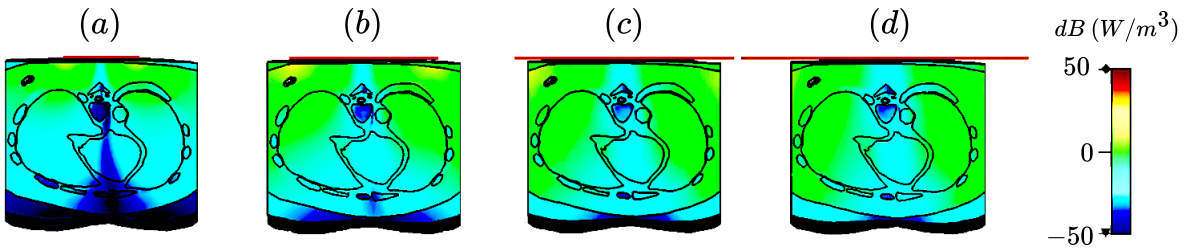

Figure 3.8: Power loss density inside the human body model for different radii: (a) $r_0 = 50\,\text{mm}$, (b) $r_0 = 100\,\text{mm}$, (c) $r_0 = 150\,\text{mm}$, and (d) $r_0 = 200\,\text{mm}$. The power loss is calculated at the actual resonant frequency in each case.

$r_0 = 100\,\text{mm}$ and $r_0 = 150\,\text{mm}$. However, for $r_0 = 100\,\text{mm}$, the strong interaction results in a saturation effect on Q. The average change in Q across the four states is -0.4 for $r_0 = 100\,\text{mm}$, whereas weaker interactions for other radii allow for greater variations: -0.6 for $r_0 = 50\,\text{mm}$, -0.9 for $r_0 = 150\,\text{mm}$, and -1.8 for $r_0 = 200\,\text{mm}$.

These variations must be compared against the resolution of a standard Vector Network Analyser (VNA) used to measure f_{res} and Q experimentally. Operating at $f_0 \approx 50\,\text{MHz}$ ensures a good signal-to-noise ratio, allowing for comparison with instrumental error. A VNA with 1601 frequency points and a frequency range of $f_{\text{range}} = 4.2\,\text{MHz}$ covers the entire range of Q and f_{res} measured. The frequency resolution is $\Delta f = 3\,\text{kHz}$, resulting in an instrumental frequency error of only 1.5 kHz – well below the observed frequency shifts of $\approx 20\,\text{kHz}$ for $r_0 = 100\,\text{mm}$ and $r_0 = 150\,\text{mm}$. Similarly, the instrumental error in Q is below 0.13, confirming that the numerically observed quality factor changes can be experimentally tracked.

We conclude that the most effective radii are $r_0 = 150\,\text{mm}$ and $r_0 = 200\,\text{mm}$. The latter provides the largest variation in Q, making it the most sensitive for detection when monitoring Q. However, $r_0 = 150\,\text{mm}$ allows for both f_{res} and Q monitoring, offering a combined approach for detecting anomalies. Practical constraints on coil size should also be considered when implementing this method. The significant changes in f_{res} occurring when $r_0 = 100\,\text{mm}$ can be employed in separating different lung states, with the additional benefit of a more compact system.

3.4 Discussion and conclusions

This chapter focused on detecting low conductivities similar to those of human tissue. The first section of this chapter presented the experimental implementation of a low-conductivity detection probe with a 25 mm radius and resonant around 50 MHz. The sample used to simulate the electromagnetic properties of human body tissue was a saline solution, whose conductivity was changed gradually by adding more salt to the mixture. Comparing the analytical model with the experimental data enabled detection up to 20 S/m with an accuracy above 94%. For conductivities closer to human body ones (<5 S/m), the mean error in detection was only 3%. The analytical extraction was compared with an extraction made using interpolation between CST Studio Suite numerical data points. The analytical model outperformed the numerical one, which only managed to detect conductivities up to 20 S/m with an accuracy of 90%.

After successfully extracting experimental results, a more realistic system was simulated in CST Studio Suite, using a CAD model of a human body. The electromagnetic properties of each tissue were calculated using a literature-based model and included in the simulation. The specific aim of this section was to evaluate whether the changes in resonant frequency and quality factor caused by variations in tissue conductivity are significant enough to detect the presence of water in the lungs. The simulations were performed at a frequency of 50 MHz, which, as shown earlier in this chapter, enables accurate detection of low conductivities. This frequency offers two further advantages. First, it enables strong interaction with only half of the lung closest to the coil. Since the coil is placed on the patient's back, gravity naturally causes fluid to accumulate in this region during real-life scenarios, making it the most relevant for testing. The second advantage is that the limited penetration depth reduces interaction with the heart, the organ with the highest conductivity. The feasibility study in this thesis shows that even in the worst-case scenario of a diastolic heart (filled with blood), separation between different lung states is possible. Future work should explore the possibility of a more realistic time-varying heart conductivity, which would improve the sensitivity of the probe, as it would allow for reduced interaction when the heart conductivity is at its minimum.

Based on the operating frequency, the instrumental error of a standard VNA was estimated as 3 kHz for the resonant frequency and 0.13 for the quality factor. All tested coil radii met the quality factor requirement, but only the 100 mm and 150 mm coils showed measurable changes in resonant frequency. Unlike in Chapter 2, where increasing the probe radius consistently improved sensitivity, it was found that for the finite sample studied here, a radius of 100 mm maximised interaction between the coil and the body. This is because the coil tracks sit directly underneath the lungs, allowing the strongest magnetic fields to penetrate the tissue. In larger coils, the strongest fields are located further from the sample, and some of the field propagates through air, reducing the effect on the probe's properties.

Although the 100 mm coil maximises the interaction, a larger radius may be more effective for distinguishing between different lung states: A — healthy, inflated; B — healthy, deflated; C — infiltrated, inflated; and D — infiltrated, deflated. A 200 mm coil generates the largest average change in quality factor between these states, but does not show trackable changes in resonant frequency. For the 100 mm and 150 mm coils, the quality factor changes are smaller, but the resonant frequency shifts are consistent and can be used for differentiation. While the 150 mm coil appears to be the most effective overall, several practical constraints must be considered. First, physical limitations may require smaller coils. This study has shown that even the smallest tested coil, with a radius of 50 mm, produced a measurable difference in Q. Second, patient size matters. The CST model used in the simulation corresponds to a female with obesity. For patients with a lower body mass index (BMI), smaller coils might perform better. In the current case, the body phantom represents a patient with BMI = 36, which is well within the obesity range. Patients with normal BMI ($18.5 < \text{BMI} < 24.9$) would have thinner fat layers and experience stronger interactions between the lungs and smaller coils.

This work proposes and numerically tests an eddy-current-based lung monitoring technique. Further research is needed to experimentally validate the results and to optimise the sensor design. First of all, more simulations are required to validate the frequency choice and verify that such a method could work on subjects of different sizes. More-

over, it is important to simulate more conductivities and permittivities for the affected tissues in order to assess the sensitivity range of the probe. Further research into the conductivity of infiltrated lungs is necessary to understand how much infiltration could be problematic for real patients and what sensitivity the probe must provide. Before moving on to testing the method on human subjects, the specific absorption rate of the probe under test must be calculated such that the device does not threaten patients. Experimental tests can first be performed on saline solutions mimicking the human body. This would provide a proof-of-concept without endangering possible patients.

With respect to probe design, one possible direction for further research is testing different coil geometries. For example, the so-called pancake coils [161] (flat, spiral-shaped coils with multiple turns) might offer stronger coupling with lung tissue, leading to improved sensitivity. Another possibility is to design a rectangular coil, rather than a circular one, to maximise the coverage of the lungs. Rectangular pancake coils might prove to be an even better alternative.

A further improvement involves replacing the single coil with a system of distributed resonators, i.e. a magnetoinductive array. The next two chapters will focus on localising objects in 1D and 2D arrays based on changes in the response of individual resonant cells. Applying such an array to body imaging could improve spatial resolution and help pinpoint abnormalities more accurately. This concept may extend beyond lung monitoring. For instance, malignant tissue often has higher conductivity, suggesting that this approach might also be suitable for tumour detection. More research is needed to evaluate the feasibility of this method in human subjects and to understand the influence of individual variability.

CHAPTER 4

Frequency-domain reflectometry

4.1 Introduction

Localising objects non-invasively without direct human interaction and monitoring is an important technology with applications in asset tracking, medical diagnosis, security and human-computer interaction. Localisation platforms based on electromagnetic fields can offer multiple advantages, including interaction with various types of materials and the ability to be integrated into various devices in a compact manner. As established in previous chapters, when a conductive object is placed on a magnetoinductive array, the properties of the coil directly beneath it change, thus creating a partial 'defect' in the array. This modifies the propagation of MI waves, causing additional reflections from the affected tile. For a monochromatic excitation at frequency ω, these reflections will result in a standing wave pattern within the structure. The actual form of the standing wave pattern will be frequency-dependent due to the dispersive nature of MI waves. These changes can be mapped to object location and provide the basis of a localisation platform. Previously, Yan et al. [18] proposed an algorithm for localising an M6 metallic bolt on a

1D array comprising 17 single-turn, square resonant elements, tuned at 13.56 MHz. The algorithm uses the changes in the relative position and magnitude of peaks in the input impedance spectra to infer the position of the bolt analytically.

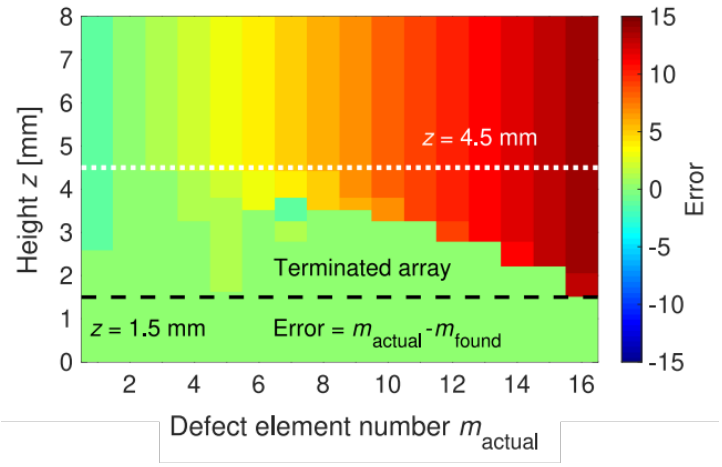

Figure 4.1: Figure from [18] showing localisation error in a terminated 1D array for an M6 metallic bolt height up to 8 mm. Reproduced from [18]. Ref. [18] is licensed under a Creative Commons Attribution 4.0 License. ©2021 by J. Yan, C. J. Stevens, and E. Shamonina.

The difference between the real bolt location (m_{actual}) and the inferred location (m_{found}) was presented in [18] as a function of object location (m_{actual}) and object's vertical position (height, z), and is reproduced under CC BY 4.0 in Fig. 4.1 for a terminated array (i.e. an array whose last element is loaded with the same impedance as the array input impedance). In Fig. 4.1, the error is shown as a contour map, where green indicates error-free localisation. It is important to note that the results presented in Fig. 4.1 are obtained from analytical simulations. Perfect localisation can be seen to be achieved for heights up to 1.5 mm whilst an object located further than the 10^{th} element cannot be found accurately past 4 mm in height. This limitation is inherently linked to the algorithm, which is designed for strong de-tuning objects. When objects which interact weakly with the array are present, the changes in the spectra are not large enough to change the number or order of the peaks as required in [18]. To address this limitation, a more sensitive method that can detect weak interactions is required. In this chapter, the input admittance spectra are mapped to object positions using a machine learning–based approach, enabling localisation even for weakly interacting objects and offering a substantial improvement over the method in [18]. Beyond improving accuracy,

this work extends frequency-domain reflectometry–based localisation to two-dimensional arrays while using only a single measurement point. This approach opens up new opportunities for sensitive and efficient sensing platforms, including advanced touchscreen arrays [162]. Touchscreen technology is ubiquitous in modern electronics (smartphones, laptops, tablets, vending machines, and smartwatches) and encompasses a range of sensing principles optimised for specific requirements. The most widely adopted commercial approach is projected capacitive sensing, which measures mutual capacitance between intersecting transmitter and receiver electrodes [163, 164]. It offers high spatial resolution, excellent optical clarity, and robust multi-touch capability, making it the standard in consumer devices. A closely related method, self-capacitive sensing, measures the capacitance between individual electrodes and ground. It provides higher sensitivity and the ability to detect "hover" gestures several centimetres above the surface, but is more prone to ghost touches in multi-touch operation [165]. Other established methods include resistive touchscreens, which are low-cost and operable with a variety of input tools but limited in multi-touch capability and optical clarity [163], and surface acoustic wave (SAW) touchscreens, which detect touch via attenuation of ultrasonic waves and offer excellent clarity but reduced robustness to surface contamination [163]. Optical approaches, such as infrared (IR) grid frames and frustrated total internal reflection (FTIR), allow for large-scale, multi-touch operation and can detect objects several centimetres above the surface [163].

Recent advances have pushed sensing into the volume above the surface. Pre-touch self-capacitive systems and IR proximity sensors can track inputs at 10–12 cm [165], while millimetre-wave radar systems (e.g., Google's Soli) detect mid-air gestures at tens of centimetres using frequency-modulated continuous wave (FMCW) or impulse radar techniques [166]. These volumetric methods have coarser resolution than capacitive touch but enable 3D interactions and maintain performance under surface contamination. Industrial efforts, led by companies such as Synaptics, Goodix, Novatek, Infineon/Cypress, and Microchip, focus on enhancing projected capacitive performance under varying overlays [167, 168], while suppliers like Elo and Neonode specialise in SAW and optical IR solutions for large-scale or industrial human–machine interfaces [169, 170]. Academic

work explores multi-frequency excitation, hybrid self/mutual-capacitive approaches, and machine learning–based signal processing for noise rejection, user identification, and spatial super-resolution [163].

The machine learning localisation method proposed in this chapter could significantly reduce touchscreen system complexity by requiring only a single measurement point to identify an object's position. This advantage also extends to other sensing scenarios. For example, the approach could be adapted for detecting and localising defects on the outer surfaces of stealth aircraft or spacecraft, where structural integrity is critical, or for identifying foreign objects on wireless charging platforms to prevent interference and damage. By combining high sensitivity, weak-interaction detection, and minimal hardware requirements, the technique offers a flexible sensing framework with broad practical applications.

This chapter aims to localise high- and low-conductivity objects on both 1D and 2D arrays of coupled resonators. To match each sample's individual properties, different platforms are designed for each sample type. Beyond localisation, this approach is extended to classification in Section 4.5.4, where different high-conductivity objects are distinguished.

The work in this chapter resulted in three publications, and most figures in this chapter are adapted from them:

- G. Dima, C. Stevens, H. Dai, "Neural network based remote localiser for two objects," in *Proc. 19th Int. Congr. Artif. Mater. Novel Wave Phenom. (Metamaterials 2025)*, 2025. under review
- G. Dima, C. J. Stevens, "Spatial localisation and sensing in two dimensions via metasurfaces," *Sci. Rep.*, vol. 14, 24156, 2024
- G. Dima, I. Spanos, C. J. Stevens, "2D localisation using magneto-inductive waveguides," in *Proc. 18th Int. Congr. Artif. Mater. Novel Wave Phenom. (Metamaterials 2024)*, 2024

Writing this chapter would not have been possible without the contributions of Huirui Dai, who programmed the robotic arm in Section 4.6, and Ioannis Spanos, who created the surface used in Section 4.7.

4.2 Theoretical foundations

4.2.1 1D array

The 1D localisation is performed using a magnetoinductive waveguide of 17 resonators, identical in design to that used by Yan et al. [18].

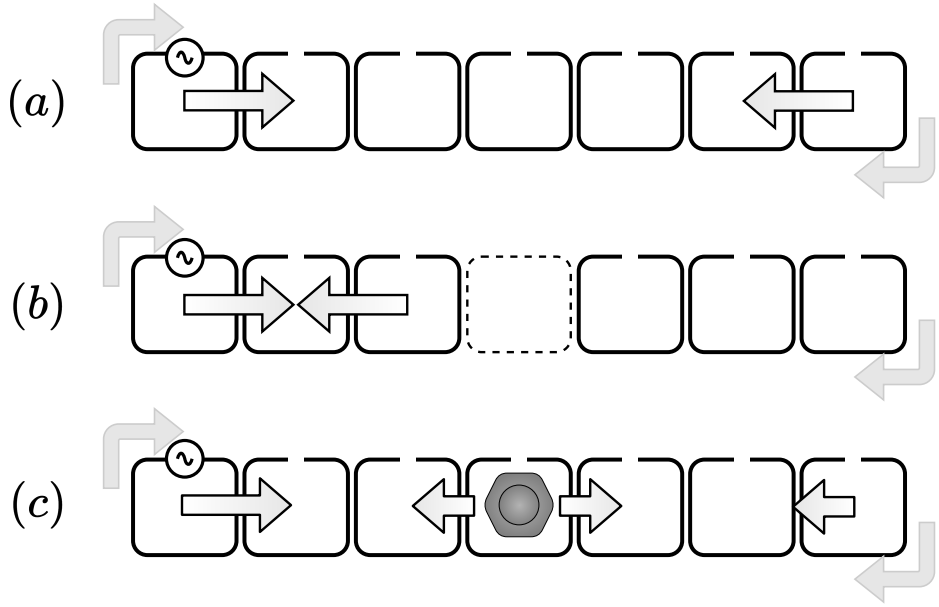

Figure 4.2: Wave propagation in (a) an unloaded array, (b) an array loaded with an ideal defect, and (c) an array loaded with a real-life object. The straight arrows inside the arrays indicate MI waves' travelling directions inside the array. The curved arrows outside the arrays are added for completeness and indicate the continuous movement of MI waves and the creation of standing waves.

When the first element of a 1D array of resonators is excited by a time-varying signal, MI waves propagate and are reflected at the end of the array, as shown schematically in Fig. 4.2(a). All the arrays used in this thesis are considered to be unterminated (or open-ended), which means that the reflections occurring at the array boundaries are perfect reflections. The injected wave and the reflected one interfere, resulting in a standing wave pattern which, in the frequency domain, is characterised by a series of minima and maxima. The propagation of 1D MI waves is described in detail in Section 1.2.4.

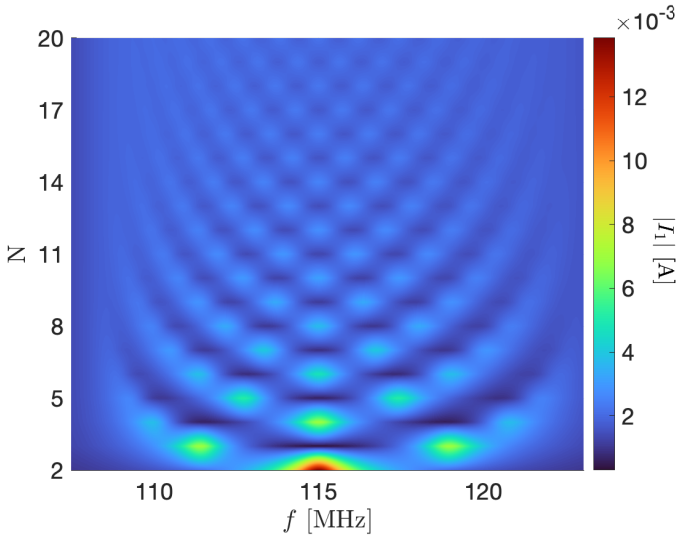

Figure 4.3: Current spectrum for a 1D array with $\kappa = -0.13$, $f_{\text{res}} = 115\,\text{MHz}$, and $Q = 100$ when an ideal defect is successively placed on different elements, N.

An ideal defect (i.e. $Z_0 \to \infty$) placed on the array results in a complete cancellation of the resonating cell immediately below it. Assuming that the second-order coupling is much smaller in comparison with the nearest-neighbour coupling (usually by a factor of 10, for the planar configuration), adding an ideal defect results in the array behaving very closely to an array that terminates at the ideal defect. In other words, when an ideal defect is placed on element $N + 1$, the magnetoinductive waveguide behaves as if it had N resonators, as the signal injected is fully reflected when it encounters the ideal defect. This is illustrated schematically in Fig. 4.2(b).

Figure 4.3 shows the amplitude of the current in the first element, which is excited, for a 1D array with $\kappa = -0.13$, $f_{\text{res}} = 115\,\text{MHz}$, and $Q = 100$ when an ideal defect is successively placed on different elements, N. As the defect moves along the line, the number of peaks, their position and their separation are modified. The algorithm presented by Yan et al. in [18] maps these changes onto defect locations.

Generally, an object placed on the array acts as a partial defect (i.e. with $Z_0 \neq \infty$). In such cases, when the travelling wave encounters such a partial defect, the wave is partially transmitted and partially reflected, as shown schematically in Fig. 4.2(c). The proportion of the signal being reflected depends on the strength of interaction between the object and the cell immediately below it. The change in the standing wave pattern is, therefore, less significant, but its magnitude can be used to infer characteristics of the

object, such as conductivity or height above the array.

4.2.2 2D array

The sensing platform used for the 2D frequency-domain localisation is a metasurface array created by arranging meta-atoms in a rectangular 7×5 grid. When selecting the array dimensions, asymmetry was a key consideration. For every position on the array to be uniquely identifiable, each element must have a distinct response relative to the probing point. A 7×5 asymmetrical surface satisfies this requirement more naturally than alternatives such as introducing randomness by slightly detuning individual elements. The rationale for this choice, along with a detailed justification of the role of asymmetry, will be presented later in this section. The maximum practical array size is limited by the quality factor of the individual elements, as well as by the noise level and measurement accuracy. Standing waves propagate further and experience greater attenuation when interacting with defects located farther from the excitation point, meaning that the influence of an object on the array diminishes with increasing distance from the feeding location. When an array becomes too large, the changes caused by some of the defects will be comparable to the noise, leading to impossible localisation.

The meta-atoms in the array are resonant elements coupled together through their mutual inductance, M, which allows 2D MI waves to propagate when one of the surface's resonators is excited. Similar to the 1D case, the waves interfere with one another and suffer perfect edge reflections, leading to a standing wave pattern. In the frequency domain, the standing wave pattern is a series of peaks and valleys in the spectra of the input impedance, Z_{in}, defined as the ratio between the injected voltage and the current in the excited cell:

$$Z_{\text{in}} = \frac{V_{\text{in}}}{I_{\text{in}}}. \tag{4.1}$$

Monitoring the input impedance at the excitation location allows for the reflection spectrum of the entire surface to be measured at once. Placing an object above one of the lattice elements changes the element's resonant frequency, f_{res}, and quality factor, Q, creating, as explained earlier, a partial defect in an otherwise uniform array. This

element becomes a reflector which scatters incoming waves, resulting in changes in the standing wave pattern and in the input impedance of the array. Quantifying the strength of all possible interference modes is a complex problem. Hence, instead of calculating the scattering properties of a point defect, the focus of this work is on the impact on an individual resonator.

The most extreme case is when the object modifies the meta-atom underneath so much that it no longer interacts with the array, i.e. it is an ideal defect with $Z_0 \to \infty$. This tile acts now like a 'vacancy' where no current is present: $I_i = 0$. Here, i is the index of the 'vacancy'. A way of modelling this is to assume that the 'vacancy' is a virtual source placed in the otherwise unperturbed cell with the extra current generated in the meta-atom set as the exact anti-phase to that arriving from the original feed, F, at that point in the unperturbed lattice so as to result in a net zero current.

The current circulating in the feed meta-atom at location F when a defect is present at location i can be expressed as:

$$I_F = \frac{V_{\text{source}}}{Z_{\text{in}}(F)} + I'_F(i) = \frac{V_{\text{source}}}{Z'_{\text{in}}(F)}, \tag{4.2}$$

where $Z_{\text{in}}(F)$ is the unperturbed metasurface's input impedance as measured at the feed location, and V_{source} is the source amplitude applied at the feed point. $I'_F(i)$ is the additional current arriving at the feed point from the virtual source at the defect location i. $Z'_{\text{in}}(F)$ is the new input impedance of the perturbed metasurface.

Equation (4.2) indicates that the presence of a 'vacancy' can be modelled at the feeding location by leveraging the superposition principle and adding the additional current that would arrive at the feed from a virtual source placed at the 'vacancy' location. An easier way to visualise this is by looking at the input admittance, $Y_{\text{in}} = \frac{1}{Z_{\text{in}}}$, instead of the input impedance of the surface. This can be done by dividing both sides of Eq. 4.2 through the source amplitude V_{source}:

$$Y_{in}(F) = Y_0 + Y'_F(i), \tag{4.3}$$

where Y_0 is the unperturbed input admittance and $Y'_F(i) = I'_F(i)/V_{\text{source}}$ is the *referred admittance*, the additional admittance measured at the feed meta-atom F when a defect is formed at meta-atom i.

This reasoning stands when the object does not completely cancel a meta-atom's current, but the magnitude of the referred admittance differs. Equation (4.3) can, therefore, be generalised for more than one object placed on the array:

$$Y'(F) = a_1\ Y'_F(i_1) + a_2\ Y'_F(i_2) + \cdots = \sum_p a_p Y'_F(i_p), \tag{4.4}$$

in which the admittances $Y'_F(i_p)$ are those generated by virtual sources placed at the locations i_p and the complex coefficients a_p are their relative amplitudes.

Partially disrupting defects result in smaller values of the coefficients. Even if there are two or more ideal defects, the coefficients might still be less than one because the currents from the defects can combine to either strengthen or weaken each other. These coefficients can also be complex numbers, meaning they account for differences in phase or how the objects affect the system's electrical properties.

Whilst determining these coefficients analytically is a complex problem, Eq. 4.4 indicates that the net input admittance for multiple defects is, in fact, the sum of a series of admittance terms. By subtracting the unperturbed input admittance, the remainder is the sum of scaled referred admittances. The presence of any object will be indicated by this sum being different from zero.

The ability to uniquely determine the position of a perturbation is closely linked to the symmetry of the metasurface, as shown in Fig. 4.4 where the configurations and input admittance of a metasurface formed from resonators with a $Q = 1000$ interacting through a nearest-neighbour coupling of $\kappa = -0.16$. Figure 4.4(a) shows a structure excited centrally, which exhibits a large degree of symmetry. In this case, there are multiple identical meta-atoms from the perspective of the feeding point. Manhattan distances (or m-distances) [171] are a useful way of quantifying the position of meta-atom with respect to the exited tile. They measure the distance travelled along axes

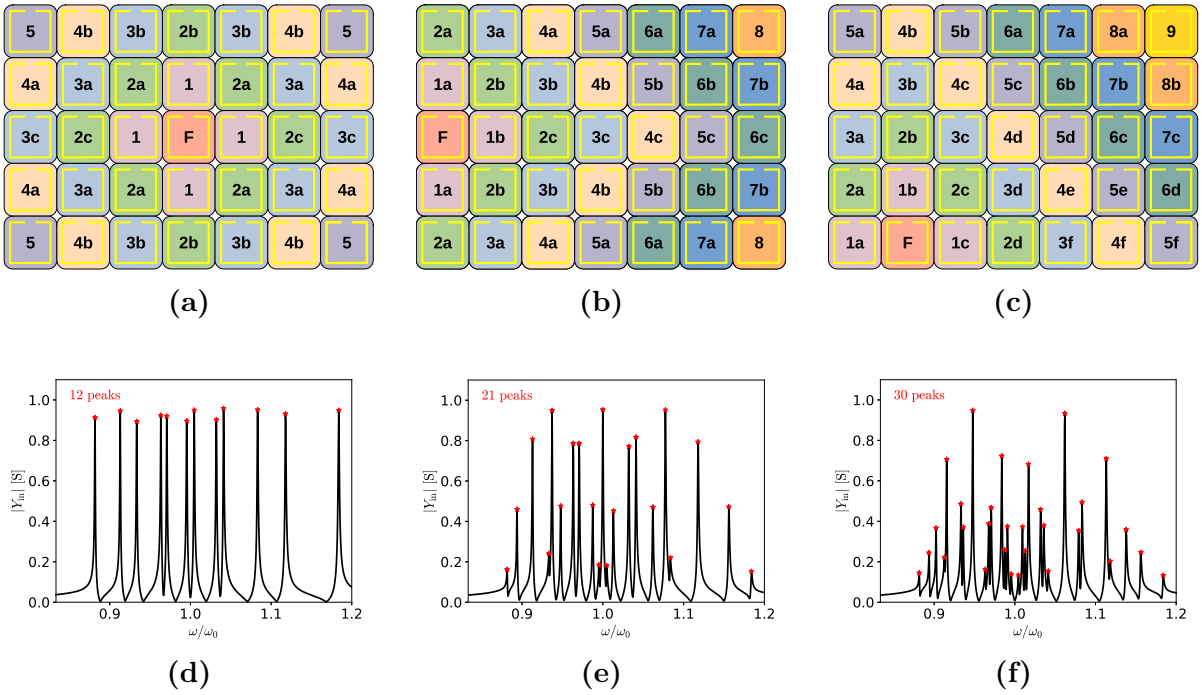

Figure 4.4: Three identical metasurfaces driven from different feed locations, F: (a) central, (b) edge, and (c) asymmetric. Their corresponding input admittance spectra are shown in (d), (e), and (f). Meta-atoms are labelled according to their Manhattan distance from the feed and their uniqueness in terms of symmetry. Reproduced from [22]. Ref. [22] is licensed under a Creative Commons Attribution 4.0 License. ©2024 Springer Nature by G. Dima, and C. J. Stevens.

at right angles, like navigating a grid of city blocks. Meta-atoms can have the same Manhattan distance but still be unique, depending on their secondary interaction with other elements. For example, using an m-distance of two leads to four identical elements on the immediate diagonal from the feed (indicated by 2a in the figure), two on the edge of the metasurface (2b) and two inside the surface (2c). Tiles identified as 2a, 2b and 2c would generate different changes in the standing wave pattern. However, all tiles identified by the same label would generate identical changes in the standing wave pattern and input admittance spectrum. Therefore, an object placed at any 2a location cannot be identified uniquely. Degeneracy between equivalent locations is why a high-symmetry surface cannot be used for localisation. In the centrally fed structure of Fig. 4.4(a), the 12 unique locations correspond to the 12 peaks in the input admittance spectra of the surface, shown in Fig. 4.4(d). The same issues arise for the side feed, shown in Fig. 4.4(b), where only 21 unique locations exist. However, in the asymmetrical feed shown in Fig. 4.4(c), all the locations are unique, leading to an expectation that all positions can be localised using the input admittance spectra. Figure 4.4(f) shows the

input admittance spectra for the asymmetrical feed, where 30 peaks are present. In this case, the number of non-degenerate unique locations in the standing wave pattern differs from the number of peaks detected in the input admittance spectrum. Lower symmetry results in more peaks appearing; even if we expect 35 peaks, only 30 can be seen. This happens due to the first neighbour coupling assumptions and because the proximity of some peaks makes them difficult to resolve.

Using an asymmetrical feed location results in a non-degenerate standing wave pattern structure that can uniquely identify each location based on the changes in the referred admittance spectrum at the feed location. Recording the admittance for all possible defect locations allows a machine learning algorithm to map the changes onto positions.

Having understood the principle of operation of the localisation sensor, the next sections will discuss the choice of localisation algorithm. This will be followed by experimental results for high- and low-conductivity objects.

4.3 Machine learning algorithm

In the work of Yan et al. [18], analytical localisation of all possible locations on a one-dimensional array was possible only up to a height of 1.5 mm, as seen in Fig. 4.1. This limitation arises because defects placed further away no longer resemble the ideal defect scenario. The changes in the standing wave pattern are much smaller and are now harder to predict analytically. In this chapter, the work of Yan et al. is extended past this limitation through the use of a machine learning algorithm.

A simple neural network with a single hidden layer is used for localisation. Machine learning approaches gained popularity in recent years in healthcare [172, 173], business and economics [174, 175] and many other research fields, as well as in popular media with platforms such as ChatGPT [176], which are capable of interacting seamlessly with the user. More importantly, such approaches have been employed in the radio-frequency and metamaterials fields, where this tool was used to design new cells and antennas or to predict system behaviours [177–181]. This rising popularity supports the use of neural network techniques for systems that were previously too complex for full analytical

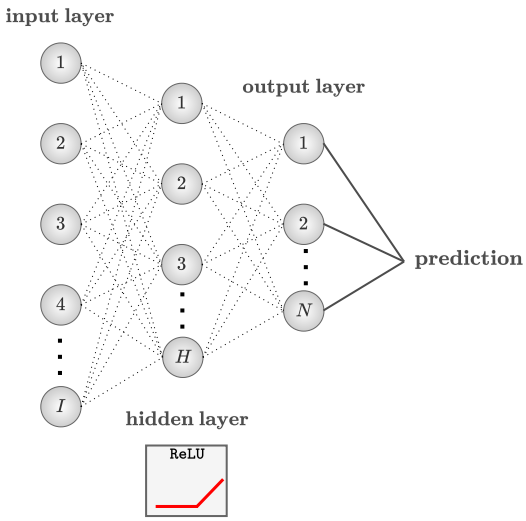

Figure 4.5: Neural network architecture.

characterisation, such as the localisation system implemented in this chapter.

The schematic architecture of the neural network used is shown in Fig. 4.5. The input features of the algorithm used are the 1601 frequency points in the normalised S_{11} dataset. A linear operation transforms the 1601 input nodes into H hidden layer nodes, with the number of hidden nodes optimised for the application. The hidden layer nodes undergo a Rectified Linear Unit (`ReLu`) activation operation, defined as $f(x) = max(0, x)$. The `ReLu` operation introduces non-linearity by setting all negative inputs to zero while leaving positive inputs unchanged. This helps the network learn complex patterns and speeds up training by mitigating the vanishing gradient problem. The resulting nodes are then linearly mapped into the output layer. Each location is represented in the output layer by a coefficient linked to its likelihood of being the correct location. The maximum value of the resulting nodes corresponds to the location of the object. This neural network was implemented using the open-source `PyTorch` package [182]. The optimiser used is the `Adam` optimiser, and the loss function is the `CrossEntropy` function. The learning rate and the number of iterations (also known as the number of 'epochs') are optimised for each application to correctly model the system characteristics. The number of iterations (epochs) is increased gradually to avoid overfitting.

This algorithm was chosen because it combines the effectiveness of machine learning

approaches with the ease of implementation provided by a simple architecture. The other methods considered were logistic regression and gradient-boosted trees. Whilst the complexity of the logistic regression is low, making it an attractive method from an ease of implementation standpoint, the linear decision boundary means that this method is unable to model the non-linear aspects of the system and is, therefore, expected to result in low accuracies. Gradient-boosted trees were a better option, capable of capturing non-linear effects. However, neural networks were found in the literature to perform inference at a faster speed when compared to similarly complex gradient boosting methods [183–185]. This is an important feature for our system as we aim to create a low-latency prediction model. A convolutional neural network (CNN) could also be used and would be appropriate given that this can also be seen as a two-dimensional prediction problem. Given the limited number of observations, this is an unnecessarily complicated approach.

4.4 Localisation of high-conductivity objects on 1D MI arrays

4.4.1 Experimental implementation

A schematic representation of the 1D localisation platform is shown in Fig. 4.6(a). Figure 4.6(b) shows a photograph of the array used experimentally. The array is the same as the one used in [18] and is used here for direct comparison with the results in [18]. Each array element is a printed-circuit board (PCB) square resonator with one-layer, outer diameter of 10 mm and conductor width of 1 mm. The elements were tuned to a frequency of 114 MHz through a lumped, surface-mount capacitor. The first element of the array is connected through an SMA port and a cable to a VNA, which measures the S_{11} parameter. The object, which is the bolt seen in Figure 4.6(b), is placed on the centres of all elements from 2 to 17 whilst its height is modified from $h = 0$ mm to $h = 15$ mm in steps of 0.25 mm. A background measurement (S_{11}^0) without the presence of the object is collected and subtracted from the loaded-array data (S_{11}). The absolute value of this difference ($\Delta S_{11} = |S_{11} - S_{11}^0|$) is shown in Fig. 4.7 for three different heights ($h = 0, 5, 10$ mm). Whilst the position of the standing wave pattern peaks is maintained constant for all three presented heights, the overall intensity of the changes decreases as the bolt is moved further away from the array. This observation is in line

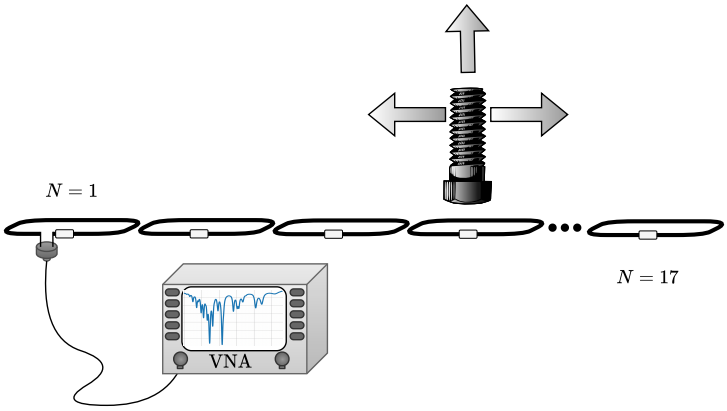

(a)

(b)

Figure 4.6: Experimental schematic of the 1D frequency-domain experiment (a) and photograph of the experiment showing the array, the object (bolt) and the SMA connector used (b).

with the reduced interaction between the array and the object. The similar pattern in these figures is essential when using the spectra as a way to localise the object position.

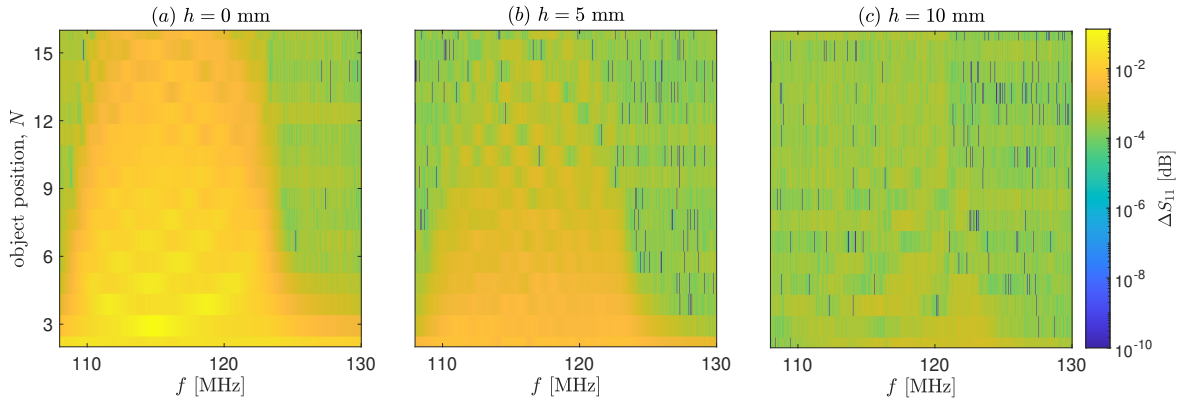

Figure 4.7: Difference between the reflection scattering parameter of a loaded and unloaded array, $\Delta S_{11} = |S_{11} - S_{11}^0|$as a function of object position, N, and frequency, f, for different object vertical position: (a) $h = 0\,\text{mm}$, (b) $h = 5\,\text{mm}$, and (c) $h = 10\,\text{mm}$.

4.4.2 Localisation results

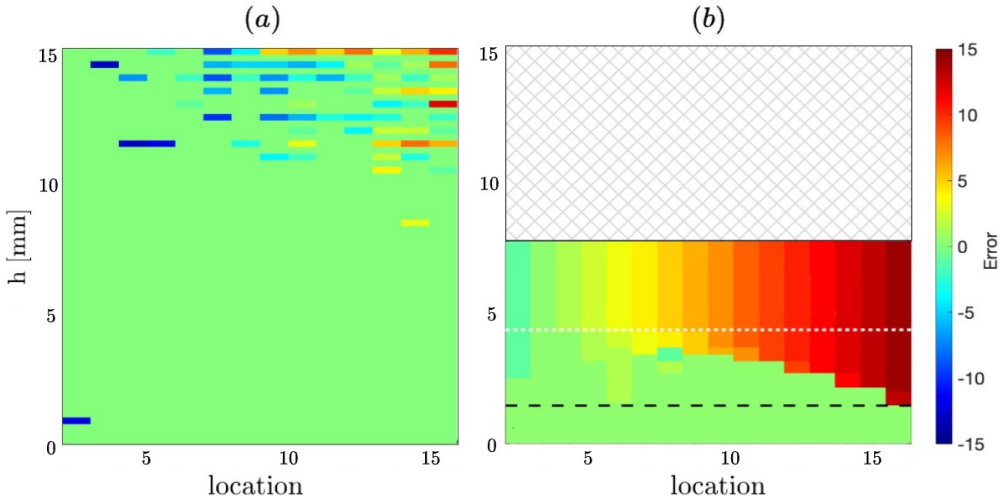

Figure 4.8: Error between actual and identified object positions as a function of height, h, and location, N, for frequency-domain localisation in a) this work, b) in [18], (figure reproduced from [18]. Ref. [18] is licensed under a Creative Commons Attribution 4.0 License. ©2021 by J. Yan, C. J. Stevens, and E. Shamonina.)

The neural network for the 1D frequency-domain localisation was trained using a hidden layer of size $H = 600$. A learning rate of 10^{-3} was used for 2000 epochs. In terms of training and testing, the full dataset was split in a 1:1 ratio, with all the data at heights which are integer multiples of 0.5 (i.e. $h = 0,\ 0.5,\ 1,\ 1.5, \cdots\ 15\,\text{mm}$) being used for training and all the other data being used for testing.

After training, the accuracy (calculated as the percentage of locations identified accurately) on the testing data set is 82% and on the full dataset is 91%. Figure 4.8(a) shows the error in localising the object as a function of height and position, alongside the error distribution previously reported in [18] in Fig. 4.8(b). As clearly seen from Fig. 4.8, using the novel ML-based frequency-domain localisation results in nearly perfect localisation up to 8 mm, which is a dramatic improvement over the results in [18]. Having validated the ML method on a 1D array, we can now extend it to a 2D array and to more testing samples.

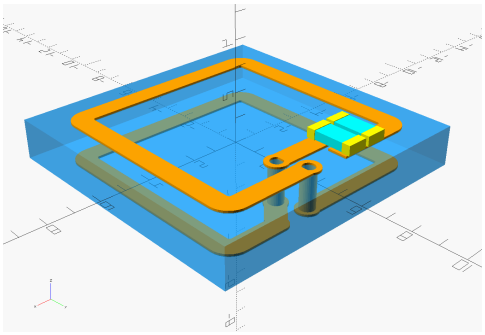

Figure 4.9: 3D model of the meta-atom used in the experimental implementation of the sensing platform. Reproduced from [22]. Ref. [22] is licensed under a Creative Commons Attribution 4.0 License. ©2024 Springer Nature by G. Dima, and C. J. Stevens.

4.5 Localisation of high-conductivity objects on 2D MI arrays

4.5.1 Experimental implementation

A surface with the symmetry of Fig. 4.4(c) was used to localise and distinguish between high-conductivity samples in two dimensions. Figure 4.9 shows a rendering of the resonator used in the surface. The meta-atoms are created using a two-layer printed circuit board with two vertical connections.

Geometrically, they are square, two-turn, helical resonators with outer square dimensions of 10 mm, track width of 0.6 mm and thickness of copper tracks of 35 μm. A 10 pF tuning capacitor changes the free-space resonant frequency, f_{res}, from 657 MHz to 183 MHz. The tuning also increased the quality factor, Q, from 44 to 132. There is an additional via in the centre of each resonator, which marks its centre for aligning purposes, but is not connected to the resonator tracks. The resonators are similar in shape and size to the ones used in [18], but the number of layers was doubled in order to increase the self-inductance of the elements and hence, obtain a higher quality factor. The distance between adjacent cells in the metasurface is 0.4 mm, resulting in a lattice period of 11 mm. The surface was originally a large array of meta-atoms, but to fit the desired symmetry constraints, only a 7×5 grid of resonators was populated with capacitors. This is shown in Fig. 4.10(a), where the red lines indicate the region with tuned capacitors. The resonators in the array interact through a nearest neighbour coupling coefficient of $\kappa = -0.16$ [186]. Each resonator was assigned a unique label, shown in Fig. 4.10(b). This unique identification

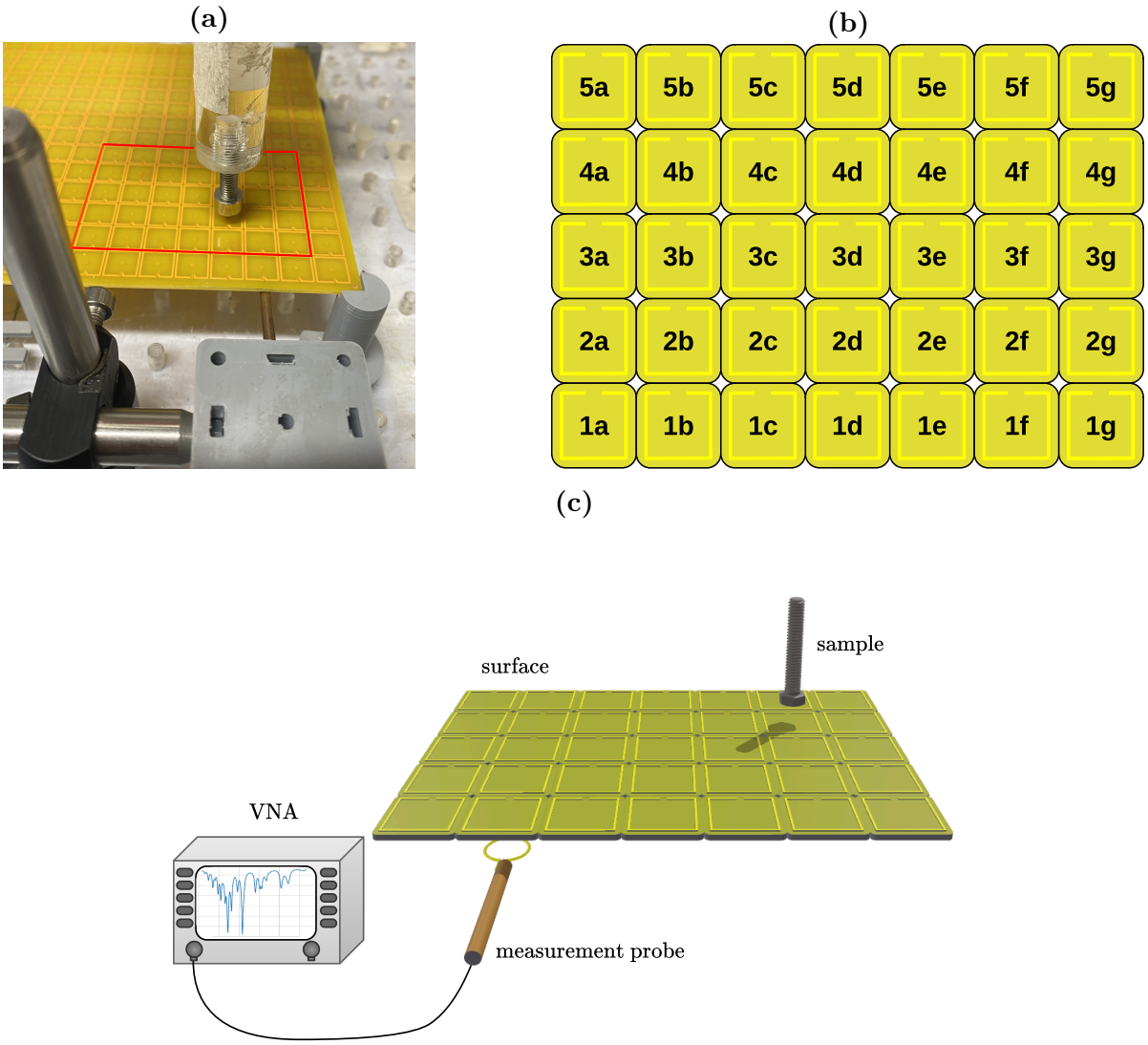

Figure 4.10: Experimental diagrams: (a) photograph of structure where red lines delimit the tuned meta-atoms, (b) surface diagram with labels for each meta-atom, and (c) experiment schematic. Reproduced from [22]. Ref. [22] is licensed under a Creative Commons Attribution 4.0 License. ©2024 Springer Nature by G. Dima, and C. J. Stevens.

simplifies the machine learning algorithm implementation when compared to an x-y coordinate representation of each resonator.

Figure 4.10(c) shows the experimental arrangement used for data collection. A non-resonant inductive loop, connected to one of the Vector Network Analyser's (VNA) ports through a coaxial cable, was placed underneath location 1b, which corresponds to the asymmetric feed placement of Fig. 4.4(c). The object was moved using an x-y-z gantry scanner across all 35 tiles' centres and in a $h = 0 - 10\,\text{mm}$ altitude range in steps of 0.25 mm. A single non-averaged scattering reflection measurement (S_{11}) was collected for each point in the scan.

The eight objects used in experiments are described in Table 4.1 and shown in Fig. 4.11. Using high-conductivity samples ensures a strong interaction with the magnetically coupled array of resonators. The objects are of different sizes and made of different materials, allowing for testing the proposed localisation method under various conditions. The large objects used were comparable in size to the array period, whilst the small ones had a diameter of roughly half a period. A square lossy ferrite plate with dimensions comparable to the period was also used.

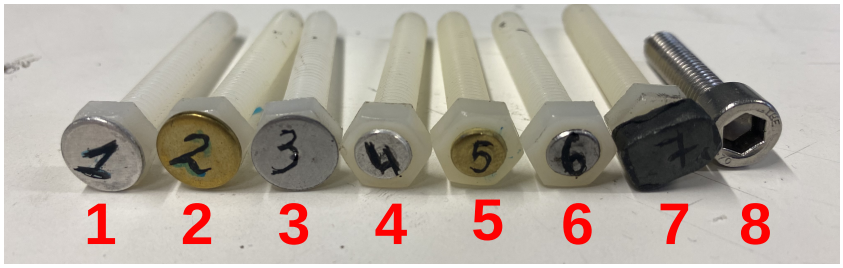

Figure 4.11: Photograph of the high-conductivity objects used experimentally. RReproduced from [22]. Ref. [22] is licensed under a Creative Commons Attribution 4.0 License. ©2024 Springer Nature by G. Dima, and C. J. Stevens.

Table 4.1: Description of high-conductivity objects used experimentally.

id	name	description
1	large aluminium	disc $\varnothing = 10.3\,\text{mm}$, thickness $= 1.0\,\text{mm}$
2	large brass	disc $\varnothing = 10.3\,\text{mm}$, thickness $= 1.2\,\text{mm}$
3	large steel	disc $\varnothing = 10.3\,\text{mm}$, thickness $= 0.8\,\text{mm}$
4	small aluminium	disc $\varnothing = 6.8\,\text{mm}$, thickness $= 1.0\,\text{mm}$
5	small brass	disc $\varnothing = 6.6\,\text{mm}$, thickness $= 1.2\,\text{mm}$
6	small steel	disc $\varnothing = 6.6\,\text{mm}$, thickness $= 0.8\,\text{mm}$
7	ferrite	plate $8.4 \times 11.5 \times 4.7\,\text{mm}$
8	bolt	M6 Hex head Stainless Steel Machine screw

When placing an object close to an individual resonator, the magnetic field generated by the currents circulating in the resonator is modified, resulting in a different, complex self-inductance, as discussed exhaustively in Chapter 2. As before, the change in self-inductance results in modifications in the resonant frequency, f_{res}, and quality factor, Q. Before performing the scans, the impact of each one of the objects on an isolated helical resonator was studied. Two non-resonant coupling loops of 5 mm diameter were placed near a single isolated meta-atom, and a transmission, S_{21}, measurement between them was performed as the object was moved further and further away from the meta-atom.

Each dataset was averaged eight times to minimise noise impact on f_{res} and Q extraction. Background transmission measurements were collected by removing the meta-atom but maintaining the moving object. The background measurements were subtracted from the averaged data to isolate the response of the helical resonator. The subtraction of the background removes the noise and interference caused by the cable and lab environment, as well as the direct interaction between the object and the measurement probes. The phase method introduced in Chapter 2 was used to extract f_{res} and Q from the collected data for each object and each (x, y, z) position. The S_{21} parameter was obtained by placing two non-resonant loops, connected to a VNA, close to the element and then used to extract f_{res} and Q. The experimental setup for the resonant frequency, f_{res}, and quality factor, Q, measurements is shown in Figure 4.12.

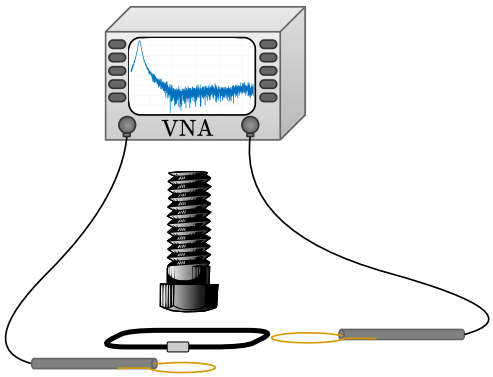

Figure 4.12: Experimental arrangement for single coil characterisation.

Figure 4.13 shows the variation of f_{res} and Q with object height, h. Larger samples (1, 2, 3, 7 and 8) display the most significant changes in f_{res} and Q, whilst smaller metallic objects cause comparatively smaller changes. As expected from the analysis in Chapter 2, metallic samples cause an increase in f_{res} whilst the ferrite sample causes a significant drop in f_{res}. Conductivity and size determine the magnitude of changes in f_{res}: larger samples cause the biggest changes, and, when comparing samples of the same size, the magnitude of the change is arranged based on the object's conductivity. The amount of loss in the system determines the changes in the quality factor, Q. Whilst conductive samples influence Q, magnetic samples (the ferrite and the steel samples) have a more dramatic effect because the field concentration enables larger currents to be induced and,

hence, larger losses to occur.

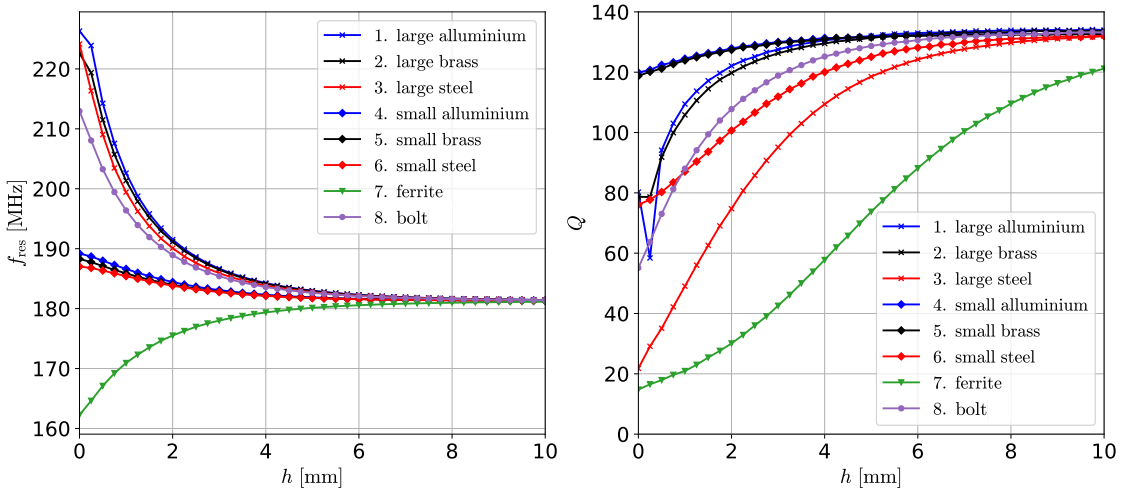

Figure 4.13: Variation of resonant frequency, f_{res}, (left) and quality factor, Q, (right) of a single meta-atom with object altitude for all used high-conductivity objects. Reproduced from [22]. Ref. [22] is licensed under a Creative Commons Attribution 4.0 License. ©2024 Springer Nature by G. Dima, and C. J. Stevens.

The results in Fig. 4.13 show substantial changes in f_{res} and Q for all presented samples, leading to the expectation that localisation based on the overall surface changes is possible. Additionally, the differences between samples are significant enough to justify the implementation of an algorithm that separates different samples.

4.5.2 Analytical results

Before performing the experiments, analytical simulations were used to confirm the choice of asymmetrical feed position and assess the impact of noise on the system.

The analytical model was created using circuit theory. The resonators were assumed to be RLC circuits coupled to their nearest neighbours through the coupling coefficient $\kappa = -0.16$. The surface was excited by a frequency-invariant voltage of amplitude $V = 1$ V, and the impedance matrix was computed using the properties of the helical resonators described in Section 4.5.1. The current in the feeding element was found by inverting the generalised Kirchhoff's law $\mathbf{V} = Z\mathbf{I}$. This method was outlined in Chapter 2 and described in detail in [58]. The analytical simulations used the stainless steel bolt (sample 8 in Fig. 4.11) data. The object's presence was simulated by changing f_{res} and Q of the helical resonator where the object was to be placed. The values of f_{res} and Q used were

the ones obtained experimentally when the bolt was swept vertically above the helical resonator, shown in Fig. 4.13 (i.e. the light purple curves).

The machine learning algorithm was trained using the difference between the input admittance of the loaded array, Y_{11}, and the unloaded one, Y_{11}^0, $|\Delta Y_{11}| = |Y_{11} - Y_{11}^0|$. For the 2D array, the size of the hidden layer was set to $H = 100$, and the learning rate was initially set to 2×10^{-5} and then modified depending on the surface and object interaction. The full dataset was split in a ratio of 3:1 between testing and training data. The data at integer heights (i.e. $h = 0,\ 1,\ 2 \cdots$ mm) were used for training, whilst all other data points (i.e. $h = 0.25,\ 0.5,\ 0.75 \cdots$ mm) were used for testing. During training, the dataset was split into batches of 25 spectra, each containing 1601 features.

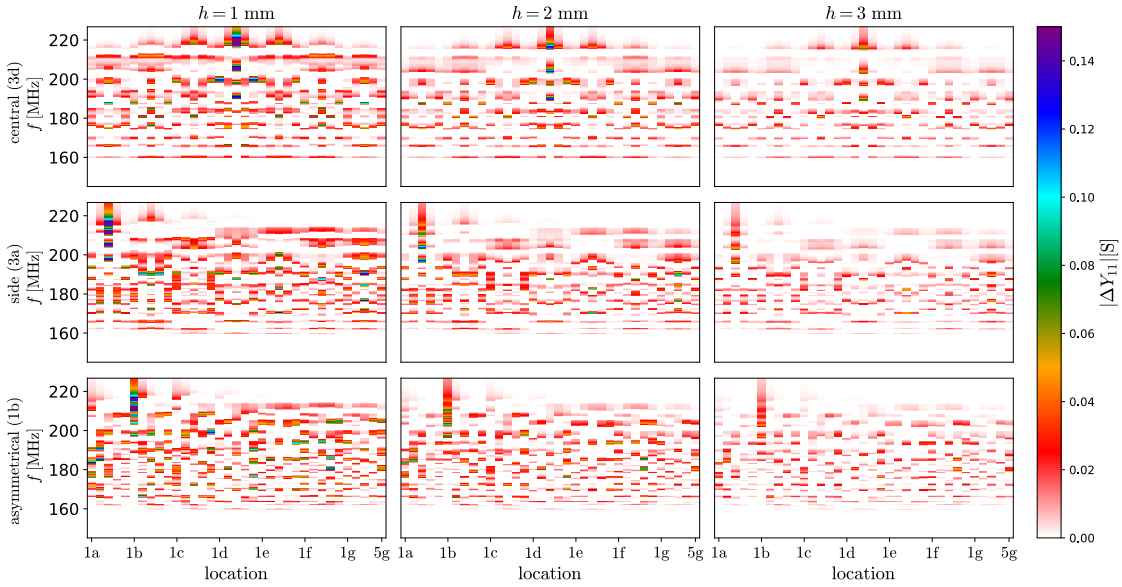

Figure 4.14: Variation of absolute value of analytical input admittance, $|\Delta Y_{11}|$ with frequency, f, and location for different vertical locations ($h = 1,\ 2,\ 3$ mm) and different feed points (central - 3d, side - 3a and asymmetrical - 1b). RReproduced from [22]. Ref. [22] is licensed under a Creative Commons Attribution 4.0 License. ©2024 Springer Nature by G. Dima, and C. J. Stevens.

Figure 4.14 shows the $|\Delta Y_{11}|$ spectrum for different locations, labelled according to 4.10(b), three different vertical positions of the object ($h = 1,\ 2,\ 3$ mm) and three different feed locations which were introduced earlier in Fig. 4.4(a), 4.4(b), and 4.4(c). The white areas indicate that the loaded and unloaded spectra are identical, whilst all other colours highlight differences between the two cases. For the central (F =3d) and

edge (F =3a) feeds, the spectra are not unique, i.e. there are locations for which the spectra are identical. In fact, the map has a central axis of symmetry for the central feed (i.e. half of the locations are not unique), whilst, for the edge feed, each column (identified from a-g in Fig. 4.14) has two pairs of identical spectra. For asymmetrical excitation, F =1b, each vertical slice representing the $|\Delta Y_{11}|$ spectrum is unique for all object locations.

Moving on to the impact of the object's vertical placement, Fig. 4.14 shows that whilst placing the object further away results in less intense changes in the input impedance spectra, the symmetry of the maps and the position of the peaks remain unchanged. This implies that the $|\Delta Y_{11}|$ spectrum for all locations is independent of the strength of interaction between the object and the surface. Moving the object closer to the surface only amplifies the change in input admittance and increases the contrast between its peaks and troughs. As a result, the pattern described by the position of peaks and the relative magnitude between them can be used to localise the object.

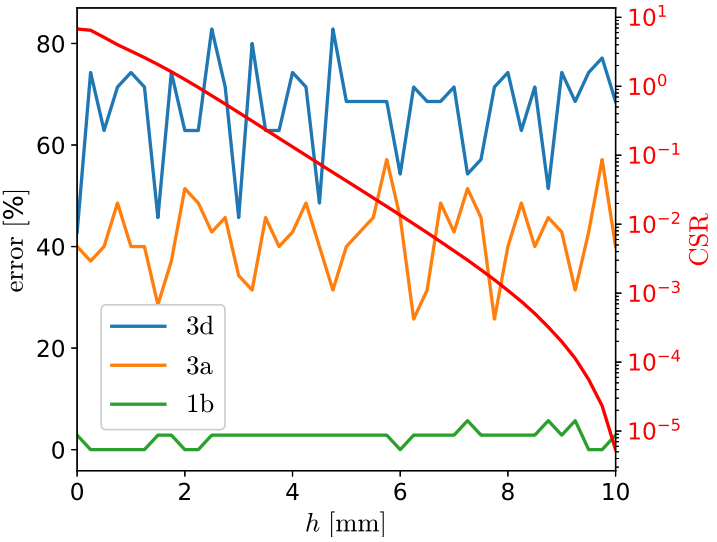

Figure 4.15: Mean error in bolt localisation for each object vertical position, h. The three lines indicate the location of the feed: blue (central feed - 3d), orange (side - 3a), and green (asymmetrical - 1b). The red curve corresponds to the secondary y-axis and represents the mean ratio between the change's PSD and the unperturbed signal's PSD. RReproduced from [22]. Ref. [22] is licensed under a Creative Commons Attribution 4.0 License. ©2024 Springer Nature by G. Dima, and C. J. Stevens.

Figure 4.15 shows the percentage of misidentified object locations as a function of vertical position, h, for three feed locations discussed previously: central feed 3d (blue line), side feed 3a (orange line), and asymmetric feed 1b (green line). The neural network was

trained for 10^4 iterations (epochs). The additional red curve, plotted using the right-side vertical axis, shows the mean change to signal ratio, CSR, as a function of the object's vertical position, h. Here, CSR is used as a measure for the strength of interaction between the object and the metasurface. It is defined as the ratio between the power spectral density (PSD) of the change and the PSD of the signal:

$$\mathrm{CSR} = \frac{\sum_i \sum_j |\Delta Y_{11,i,j}|^2}{\sum_i \sum_j |Y_{11,i,j}|^2}. \tag{4.5}$$

In Eq. 4.5, i and j are the coefficients for the frequency points and location points, respectively.

With the bolt as the sample, the strength decreases exponentially until $\approx 9\,\mathrm{mm}$. Above this point, the changes are so small that they can be considered almost negligible. It is, therefore, reasonable to use the measurement recorded for $h = 10\,\mathrm{mm}$ as a baseline for the unperturbed structure.

When the surface is excited centrally, the extraction accuracy is 33.2%. This system has only 12 unique locations, leading to an expected accuracy of $12/35 = 34.3\%$. The accuracy obtained in training is, therefore, in line with the expected system behaviour. In the case of side excitation, where there are 21 unique locations, the expected accuracy is $21/35 = 60\%$, and the accuracy after training is 58.4%. In the asymmetric case, where all locations are unique, the accuracy is 97.6%, supporting the need for asymmetric feed location and proving that the method can accurately identify all locations. Regarding CSR, since the height, h, does not cause a significant deterioration in localisation accuracy, it can be implied that detection is possible down to a ratio of 10^{-5}.

The analytical model was also used to study the impact of noise on localisation quality. White Gaussian noise was added to the analytically simulated data. The noise has a mean of 0 and a standard deviation σ_{noise}. Figure 4.16 shows the overall localisation accuracy variation with the percentage ratio between σ_{noise} and the maximum amplitude of $|\Delta Y_{11}|$. The resulting admittance spectra are shown using black, purple and blue solid lines for three selected points. When the ratio of noise to signal is 0.1%, which is equivalent

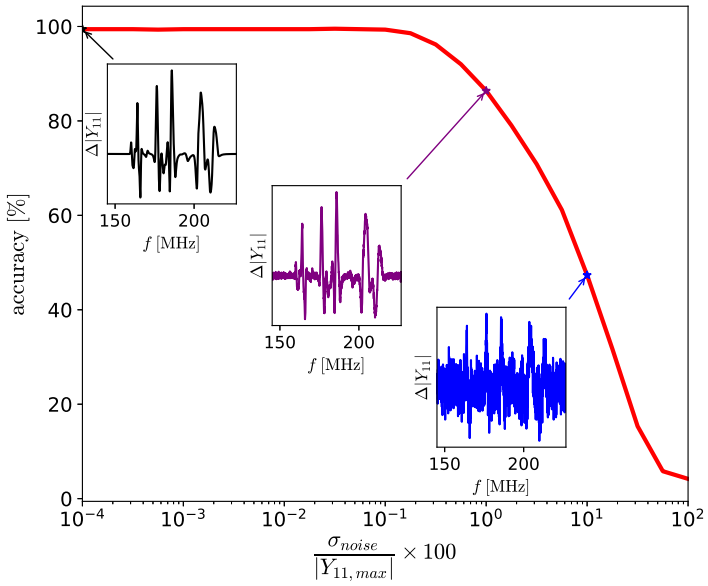

Figure 4.16: Variation of overall localisation accuracy with the ratio between noise variance and maximum signal amplitude. Insets of $\Delta|Y_{11}|$ are provided for different noise-to-signal ratios. Reproduced from [22]. Ref. [22] is licensed under a Creative Commons Attribution 4.0 License. ©2024 Springer Nature by G. Dima, and C. J. Stevens.

to SNR = 60 dB, the localisation starts to degrade. Usually, VNA collected data has an SNR higher than 40 dB, equivalent to an accuracy in localisation of 86%. For the specific system and the frequency range used in this chapter (100-600 MHz), SNR≈ 80 dB, which suggests that noise should not affect the localisation accuracy.

4.5.3 Experimental localisation results

With confirmation that the asymmetrical feed position is suitable for localisation and that noise is negligible, it is now possible to present and analyse the experimental results for localisation.

First, the number of spectral points N (the same as the number of features of the neural network) was varied between 100 and 1601 by uniformly sampling the experimental data. This study aims to cater to situations where dense admittance spectra cannot be collected and identify the minimum number of features required for accurate localisation. The neural network was retrained with the experimental data for 10^4 iterations. Different neural network models were created for different objects and different numbers of features. Figure 4.17 presents the localisation accuracy for different objects as a function of the number of features. As can be seen, the accuracy drops significantly when fewer

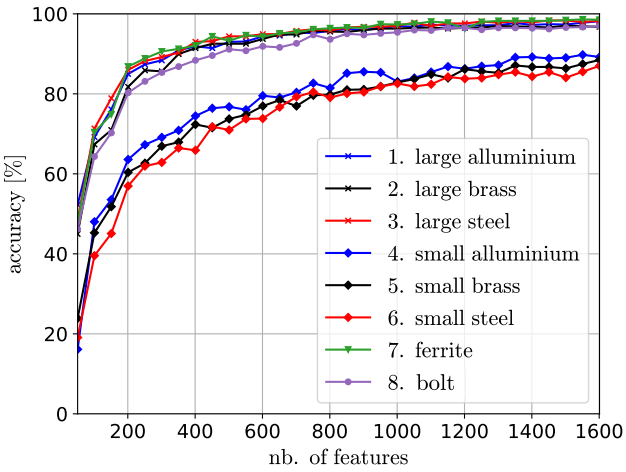

Figure 4.17: Variation of overall localisation accuracy with the number of features used in the neural network for all objects used experimentally. Reproduced from [22]. Ref. [22] is licensed under a Creative Commons Attribution 4.0 License. ©2024 Springer Nature by G. Dima, and C. J. Stevens.

than 201 features are used for training. When the number of features grows above 201, the accuracy increases gradually until it reaches a steady region at roughly 800 features. An accuracy of over 98% is achieved for samples comparable in size with the resonator's period (11 mm), i.e. samples 1, 2, 3, 7, and 8 in Fig. 4.11.

The number of features in the neural network is directly linked to the size of the neural network. Reducing the number of features leads to smaller memory requirements and faster localisation. This is particularly useful if the neural network must be integrated into low-memory, off-the-shelf chips. Whilst the architecture with 1601 features results in a model of size 657 kB, the memory requirement goes down to 337 kB for 801 features and drops further to 177 kB for 401 features and 97 kB for 201 features. One can sacrifice some accuracy for a faster, less computationally expensive system, depending on the system requirements. The loss in accuracy can be mitigated through further retraining or by selecting training features that better represent the system.

Smaller samples (i.e. samples 4, 5 and 6 in Fig. 4.11) are localised with lower accuracies because they generate more minor changes in the standing wave pattern of the surface. Figure 4.18(a) shows the change to signal ratio [CSR - defined in Eq. (4.5)] for every object as a function of its vertical position, h. For every object, the data collected at

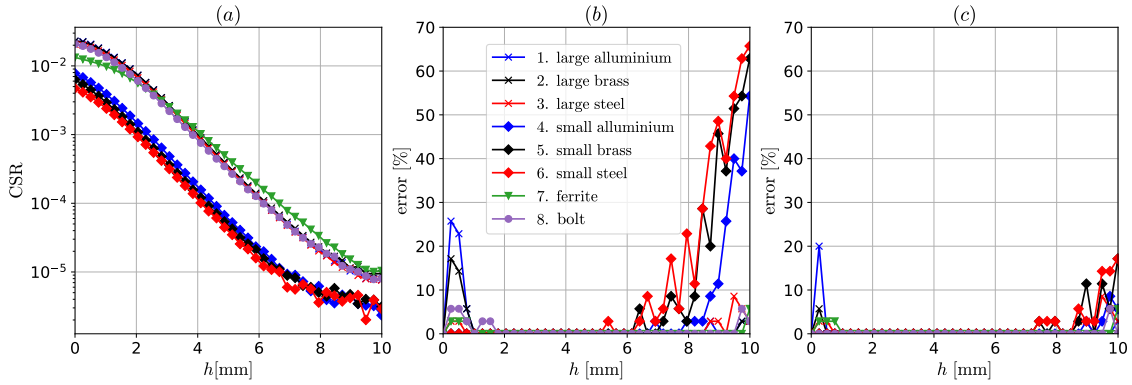

Figure 4.18: Experimental localisation results for a neural network trained with 1601 features: (a) mean change to signal ratio as a function of altitude, h, (b) average accuracy for all objects as a function of altitude, h, before retraining, and (c) after retraining. Reproduced from [22]. Ref. [22] is licensed under a Creative Commons Attribution 4.0 License. ©2024 Springer Nature by G. Dima, and C. J. Stevens.

location 1a and $h = 10\,\text{mm}$ is used as the unloaded spectra in computing CSR. This avoids modelling random variations in the background and cable positioning, instead of meaningful changes associated with the object location. CSR for small objects (4, 5, and 6) is lower than 10^{-5}, which explains why the model could not fully capture the variations associated with the small objects after 10^4 iterations (or epochs). This becomes clearer when looking at Fig. 4.18(b), which shows the localisation mean errors for all vertical positions of the object. Here, the localisation mean error for each height was calculated as the percentage of correctly identified locations at that particular height. The training was performed using all 1601 features available. The accuracy in localising small objects degrades significantly after $h = 6\,\text{mm}$, which is the height where CSR drops below the level of 10^{-5}. To mediate this issue, the neural networks for small objects (4, 5, and 6) were retrained for 5×10^4 iterations, and the learning rate was reduced by 10% every 10^4 iterations. During the retraining, a new model was generated for each of the small samples (4,5, and 6). Changing the learning rate allows for finer adjustments, necessary when modelling the small changes associated with smaller objects. Figure 4.18(c) shows the results after retraining. Here, the mean errors for small objects when $h > 6\,\text{mm}$ have decreased significantly, from a maximum of 65% to one of only 20%.

A second feature of interest in Fig. 4.18(b) is the low accuracy of the large aluminium (1), large brass (2) and bolt (8) samples when $h < 1\,\text{mm}$. This error arises from the

discontinuity occurring in Fig. 4.13 for the quality factor, Q, at $h = 0.5\,\text{mm}$. One possible explanation for the discontinuity is a short-range electrostatic interaction between the sample and the resonator. Retraining these samples with a training dataset which includes the $h = 0.5\,\text{mm}$ data addressed this issue. After retraining, the errors reduced significantly, as evidenced in Fig. 4.18(c).

Table 4.2: Accuracies for all objects on the full data set before and after retraining.

id	object	before retraining	after retraining
1	large aluminium	98.5 %	99.4 %
2	large brass	98.7 %	99.7 %
3	large steel	99.2 %	99.2 %
4	small aluminium	94.5 %	99.5 %
5	small brass	90.0 %	98.7 %
6	small steel	88.0 %	98.2 %
7	ferrite	99.5 %	99.5 %
8	bolt	98.9 %	99.7 %

Figure 4.18(c) shows that after taking into account the particularities of each sample and retraining accordingly, nearly error-free (<2%) localisation in the range $1 - 8\,\text{mm}$ is possible for all objects. The overall accuracy for the full dataset before and after retraining is summarised in Table 4.2. After retraining, the localisation accuracy for all objects exceeds 98%.

4.5.4 Experimental characterisation results

Having successfully achieved localisation, in this section, we shall focus on whether we can distinguish between different samples. Distinguishing between different objects is done through the same neural network architecture, this time with an output layer of size 8 instead of 35. The number of iterations used during training is 10^5, and all 1601 collected features were used. An $h = 10\,\text{mm}$ data point was used for normalisation to avoid training on differences accumulated between different scans instead of system characteristics.

The quality of separation between different samples is shown using the 'Confusion Matrix' in Fig. 4.19. The map shows how many times an object (labelled as *actual object* on the y axis) was identified as any other object (labelled as *identified object* on the x axis). The

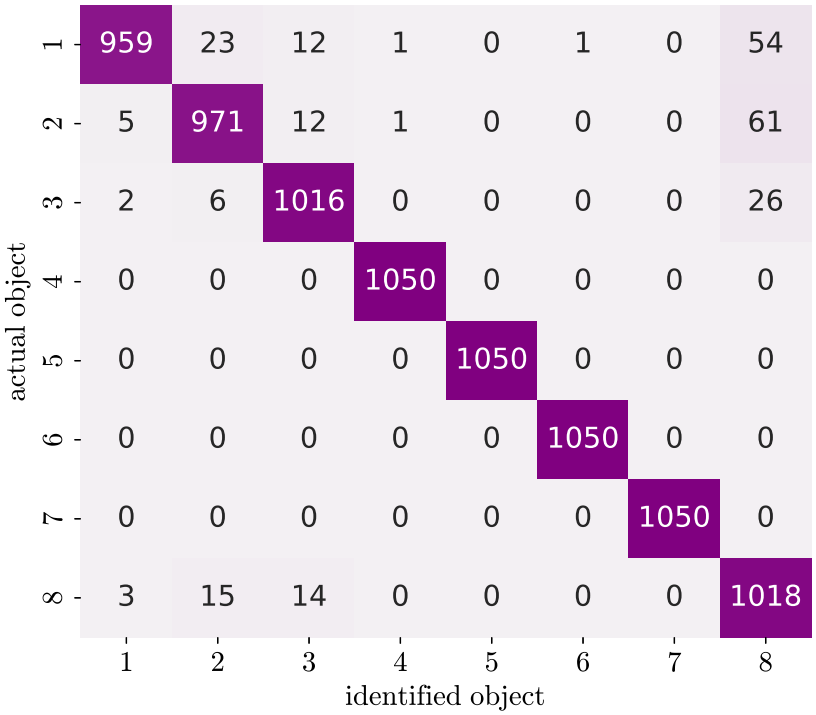

Figure 4.19: Confusion matrix for the test data set showing the number of times each object was identified correctly (diagonal cells) and misidentified as a different object (off-diagonal cells). Reproduced from [22]. Ref. [22] is licensed under a Creative Commons Attribution 4.0 License. ©2024 Springer Nature by G. Dima, and C. J. Stevens.

final separation accuracy is 97.2% on the testing data set, and 97.9% on the full data set. The most significant errors occur when separating samples 1, 2, 3, and 8, i.e. large aluminium, large brass, large steel and bolt. This behaviour aligns with expectations because these objects are similar in size and impact on the material.

4.5.5 Experimental cross-training results

When implementing a localisation system, collecting data and storing models for all possible objects is usually impossible. Instead, the more efficient solution is to create classes of objects. In this work, objects can be separated based on material and size to simulate a real-system implementation. We will refer to cross-training as the process of localising samples through the ML model created by training on a different sample's dataset. In other words, cross-training involves training the model on a fictitious sample X and then testing it on a different sample Y. Analysing the cross-training between different samples can offer insight into the regions where the impacts of the samples overlap and the regions where they diverge. In this way, the specific similarities and differences

between samples can be studied. This allows for the creation of groups of samples for which individual neural-network models can be generated, such that broader categories are stored and recognised by the model. In this section, two main classifications will be considered: material and size.

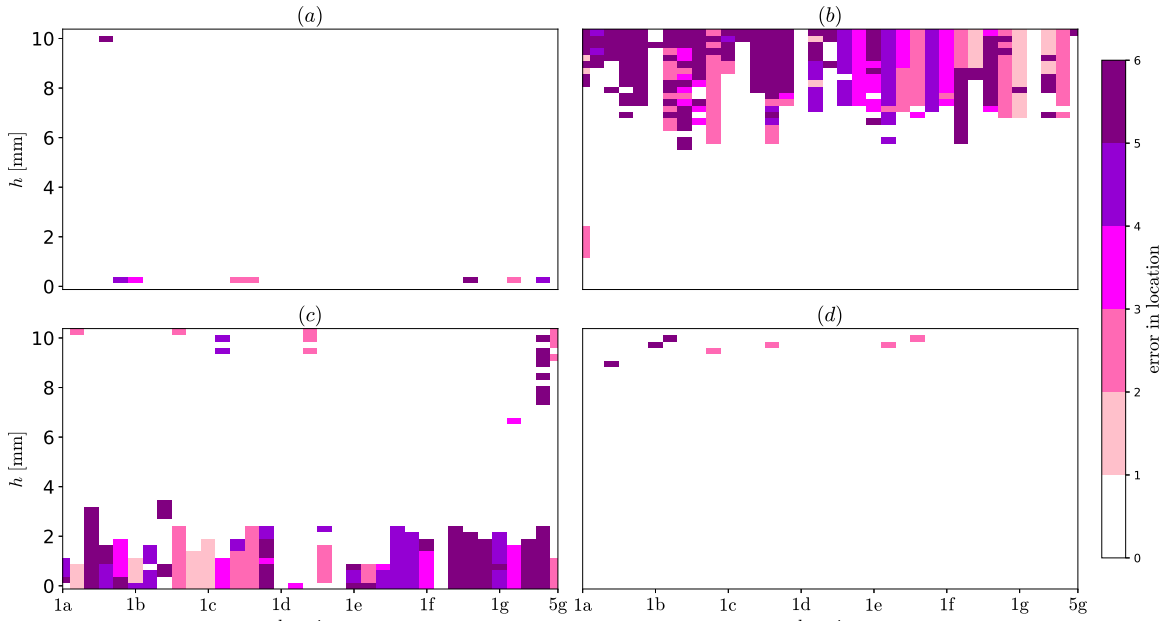

Figure 4.20: Cross-training error in localisation between large and small aluminium discs: (a) training with the large object and testing with the large one, (b) training with the large object and testing with the small one, (c) training with the small object and testing with the large one and (d) training with the small object and testing with the small one. The localisation error is computed as the Manhattan distance (defined in Section 4.2.2) between the correct location and the estimated one. Reproduced from [22]. Ref. [22] is licensed under a Creative Commons Attribution 4.0 License. ©2024 Springer Nature by G. Dima, and C. J. Stevens.

The first considered classification is based on material. Figure 4.20 shows the error in estimating location as a function of the object's vertical position, h, when the large aluminium and small objects are used in all possible combinations of training and testing. The first column of maps in Fig. 4.20 uses large aluminium for training, and the second column uses small aluminium. Similarly, the first row of maps corresponds to testing using large aluminium and the second to using small aluminium. When training and testing with the same object (Fig. 4.20(a) and (d)), the results are nearly error-free, as previously presented. Using the small sample for training and testing with the large one leads to poor localisation up to $h = 2.5\,\text{mm}$, whilst using the large disc for training and testing with the small one leads to large errors above $h = 6\,\text{mm}$. These results can be better understood by looking at the objects' interaction with the resonator from Fig.

4.13. The small object causes much smaller changes in f_{res} and Q when compared to the large one. For instance, the large aluminium disc changes f_{res} from 183 MHz to 226 MHz, and Q from 130 to 80. The changes caused by the small disc are only a fraction of those caused by the large disc, with f_{res} going up to only 190 MHz and Q dropping down to only 118. This shows that some $|\Delta S_{11}|$ values for small objects are included within the range of the large objects. Essentially, large objects placed further away from the metasurface can look similar to small but more proximate ones. This is demonstrated in Fig. 4.20(b), where small objects placed close to the surface are correctly identified even if the training was performed using the large object data. When the small object is far from the surface, the changes in $|S_{11}|$ are much smaller than any of the changes for the large objects and cannot be correctly mapped. This leads to significant errors at high altitudes when training with a large object and testing with a small one. Detection deteriorates at $h \approx 6$ mm where CSR drops below 10^{-5}. From Fig. 4.18, it is clear that such low values of CSR only occur for small objects and cannot be identified by the networks trained with large ones. Similarly, when a large object is placed close to the surface, the changes are much larger than those for small objects. This means that the network trained only on small objects would not identify the location of large objects placed close to the surface, as similar changes were not encountered in the training process. In Fig. 4.20(c), where training is done with the small object and testing is done with the large one, detection is poor when $h < 2.5$ mm. This height roughly corresponds to the point where the change in f_{res} caused by the large aluminium corresponds to the maximum change in f_{res} caused by the small aluminium sample.

For completeness, the cross-training maps for the brass and steel objects are provided in Fig. 4.21 and 4.22, respectively. The same characteristics mentioned previously hold for the other two metals.

New training data sets were created by combining the training data sets in each of the following categories: 1) aluminium objects, 2) brass objects, 3) steel objects, 4) ferrite and 5) bolt. Applying the same procedures as before and using 5×10^4 iterations for training, the full data set accuracies for the new categories are: 1) 98.0%, 2) 98.3%

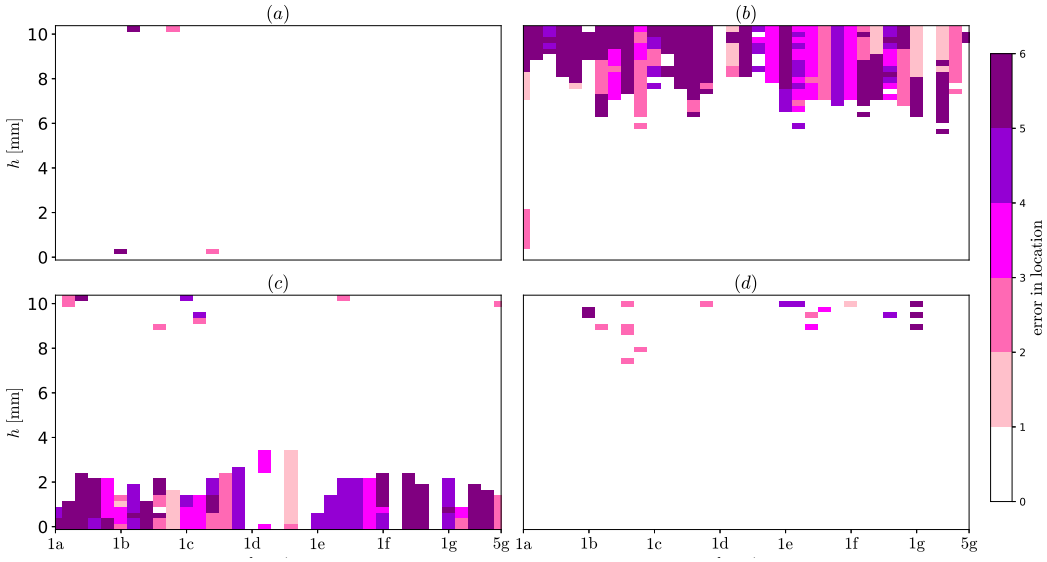

Figure 4.21: Cross-training error in localisation between large and small brass discs: (a) training with the large object and testing with the large one, (b) training with the large object and testing with the small one, (c) training with the small object and testing with the large one and (d) training with the small object and testing with the small one. Reproduced from [22]. Ref. [22] is licensed under a Creative Commons Attribution 4.0 License. ©2024 Springer Nature by G. Dima, and C. J. Stevens.

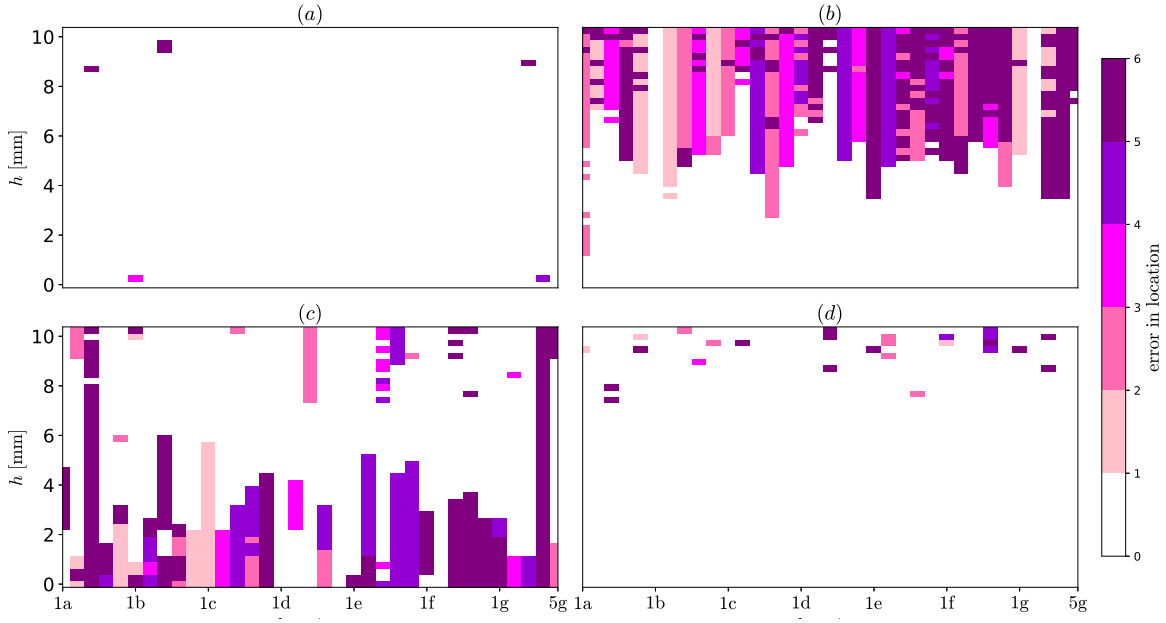

Figure 4.22: Cross-training error in localisation between large and small steel discs: (a) training with the large object and testing with the large one, (b) training with the large object and testing with the small one, (c) training with the small object and testing with the large one and (d) training with the small object and testing with the small one. Reproduced from [22]. Ref. [22] is licensed under a Creative Commons Attribution 4.0 License. ©2024 Springer Nature by G. Dima, and C. J. Stevens.

and 3) 98.6%, with the accuracy for the bolt and ferrite remaining the same as before. Additionally, the five categories are separated with 96.7% accuracy for the test dataset and 97.5% for the full dataset after 5×10^4 iterations.

The same principle can be applied to separate objects by size. The cross-training maps for small objects and large objects are shown in Fig. 4.24 and 4.23, respectively.

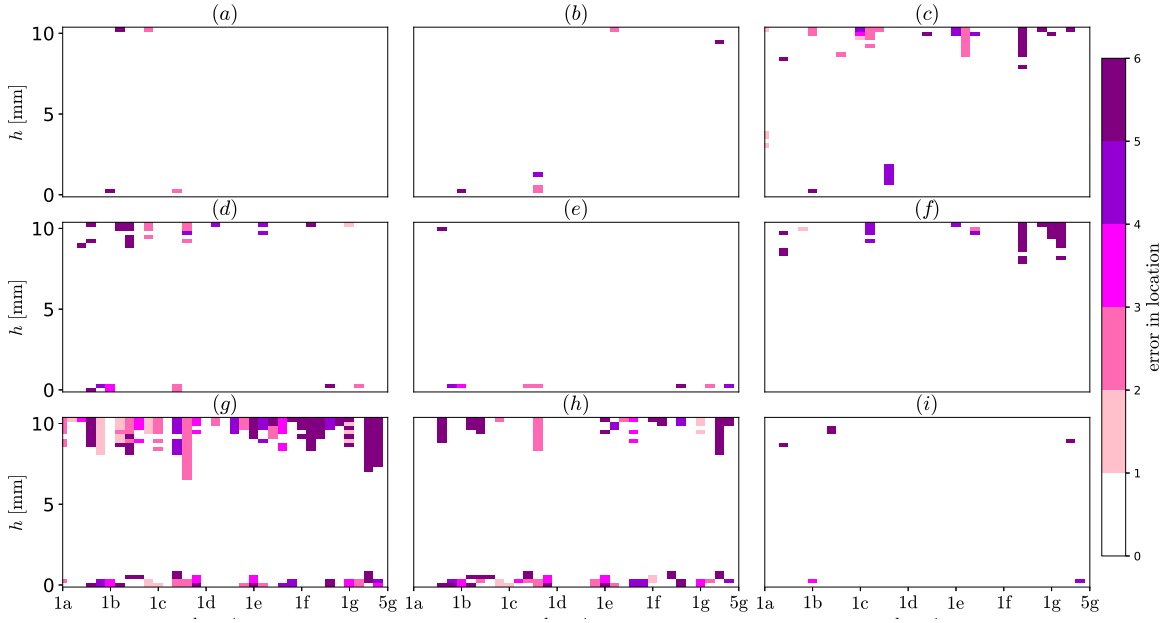

Figure 4.23: Cross-training error in localisation between large discs. The first row of maps uses aluminium for training, the second uses brass, and the third uses steel. The first column uses aluminium for testing, the second uses brass, and the third uses steel. The localisation error is computed as the Manhattan distance (defined in Section 4.2.2) between the correct location and the estimated one. Reproduced from [22]. Ref. [22] is licensed under a Creative Commons Attribution 4.0 License. ©2024 Springer Nature by G. Dima, and C. J. Stevens.

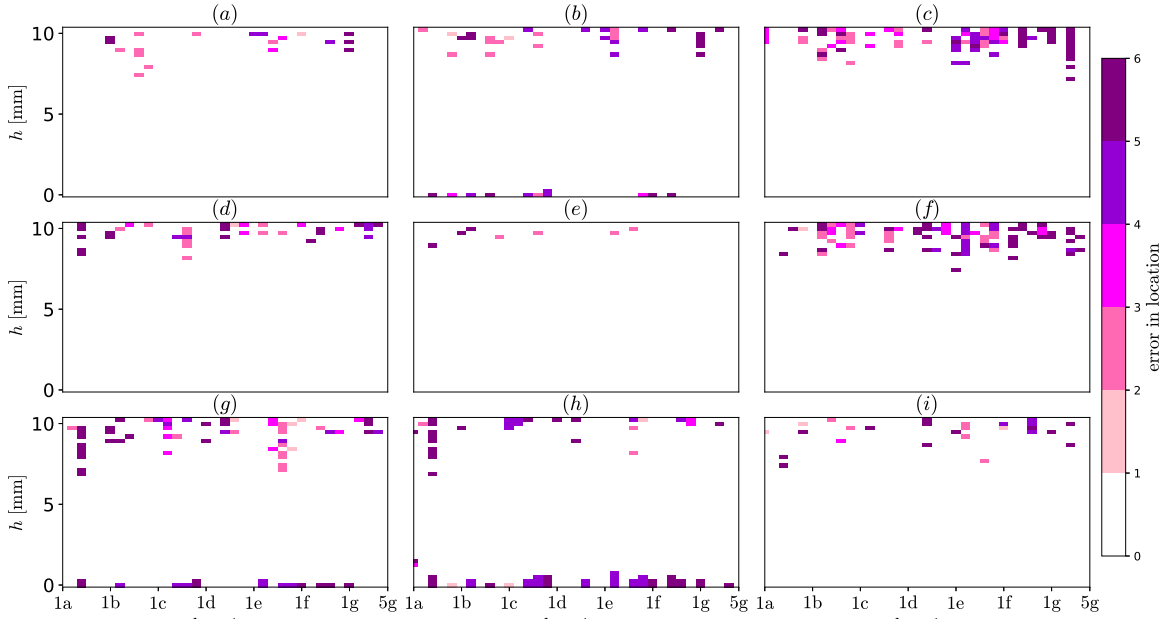

Figure 4.24: Cross-training error in localisation between small discs. The first row of maps uses aluminium for training, the second uses brass, and the third uses steel. The first column uses aluminium for testing, the second uses brass, and the third uses steel. Reproduced from [22]. Ref. [22] is licensed under a Creative Commons Attribution 4.0 License. ©2024 Springer Nature by G. Dima, and C. J. Stevens.

One can create three new categories: 1) large objects (containing bolt, large aluminium, large brass and large steel), 2) small objects (containing small aluminium, small brass and small steel) and 3) ferrite. The localisation accuracies on the full data set for the new categories are 1) 98.9% and 2) 99.5%. The large objects category was trained for 10^4 iterations and the small objects one for 5×10^4. Separating between these three categories was done with 99.5% accuracy for the testing dataset and 99.6% for the full dataset.

The cross-training study allows for grouping different samples into categories. All the objects in a certain category can then be localised using a single neural network model. In practical applications, this is an important feature as the real number of possible samples is impossible to predict, and models cannot be generated and stored for all samples. Grouping samples into categories is more efficient and allows for improved performance. If a device such as a metamaterial wireless power transfer platform [187, 188] uses a neural network to localise receivers, one can group the allowed receivers into a category and the most common foreign objects (such as keys, human hand, RFID tags, etc.) into a different one. If the algorithm identifies a receiver, it can localise it, and if it identifies a foreign object, it can stop powering the surface in order to avoid damage.

4.5.6 Real-time implementation

Following the analytical and experimental results, the method was further tested through a real-time implementation. The bolt was the object used during these tests. The VNA was connected to the laboratory computer, which stored the pre-trained bolt localisation neural network. The computer read the S_{11} parameter from the VNA in a loop. The pre-stored background S_{11} was removed every time, and localisation was performed using the stored neural network. For every S_{11} reading, the computer plotted two relevant maps: the surface map with the guessed location highlighted in red and the map with the output for each possible location. The bolt was placed in multiple positions, while a video recording of the screen and the bolt location was made. When placed in central positions, the bolt was successfully identified within 2 seconds. This is expected since the neural network has already seen the data. The localisation delays are mostly associated

with the continuous plot updating. In reality, the neural network postprocessing time is lower than 1 ms. Additionally, the system uses a single probing location, which means that the testing time could be lower than other methods, such as capacitive arrays. Whilst speed optimisation was not tackled, it is an area where further research could significantly improve the approach.

The practical implementation was able to answer a more complex question: what happens when the bolt is slightly misplaced, i.e. placed slightly off-centre.

Figure 4.25 shows the 14 random locations trialled. Each figure shows a photograph of the surface and the bolt location (left), the identified location highlighted in red (centre), and the neural network outputs for all locations (right). No colorbar is provided for the neural network outputs, as their values change dramatically during real-time testing. Instead, the numerical values for the outputs are provided in each case. The pictures were extracted from the video, and the time taken to localise is displayed for each location. Out of 14 trialled locations, 13 were successfully localised within 2 seconds, while one was not. The failed location (location 12) was the corner between four tiles. Since this is an entirely new location, with no reference point for the neural network, it is understandable why localisation failed. It is, however, noteworthy that slight misalignments did not affect the accuracy of localisation. In this regard, the machine learning algorithm has managed to localise never-before-seen positions based on nearby previously provided ones.

1) localisation time = 0.2 s

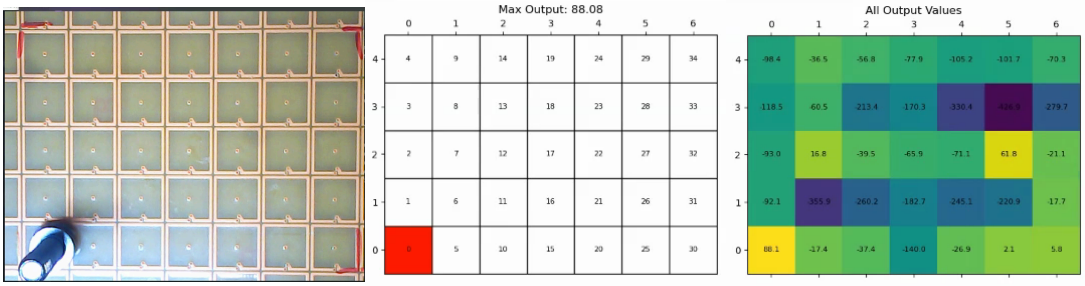

(a)

2) localisation time = 1.6 s

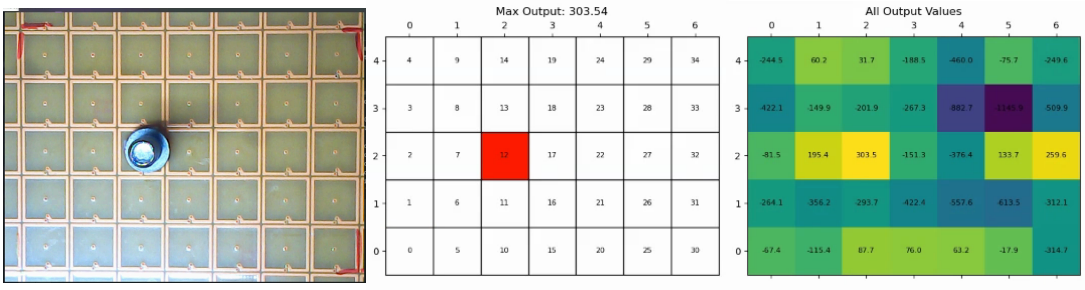

(b)

3) localisation time = 1.8 s

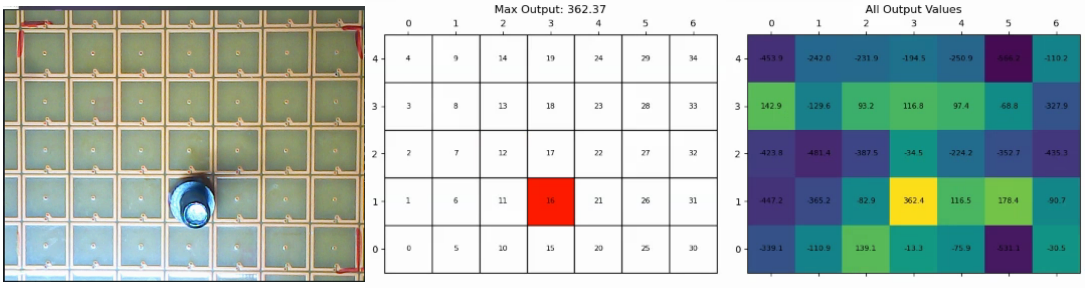

(c)

4) localisation time = 0.4 s

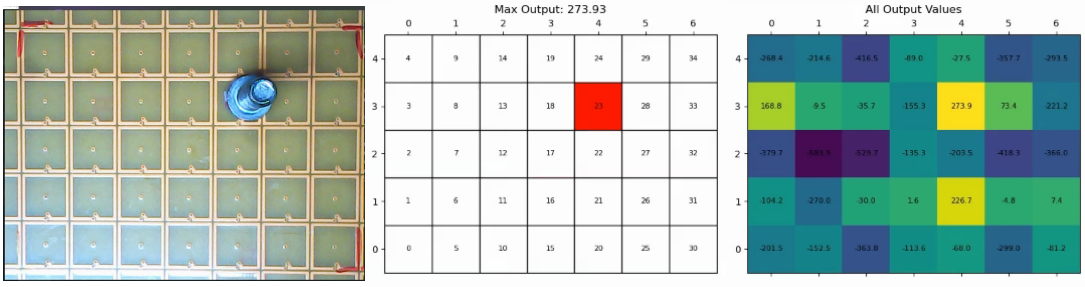

(d)

Figure 4.25: Localisation demo showing a photograph of the surface and the bolt location (left), the identified location highlighted in red (centre), and the neural network outputs for all locations (right). Part 1/4 showing locations 1 to 4.

5) localisation time = 0.9 s

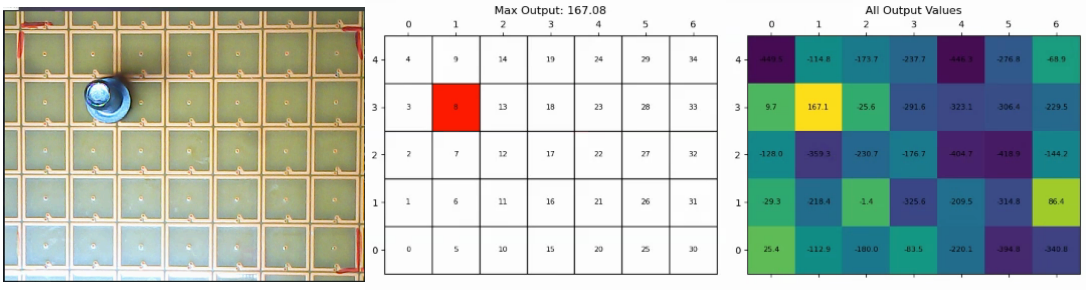

(e)

6) localisation time = 0.1 s

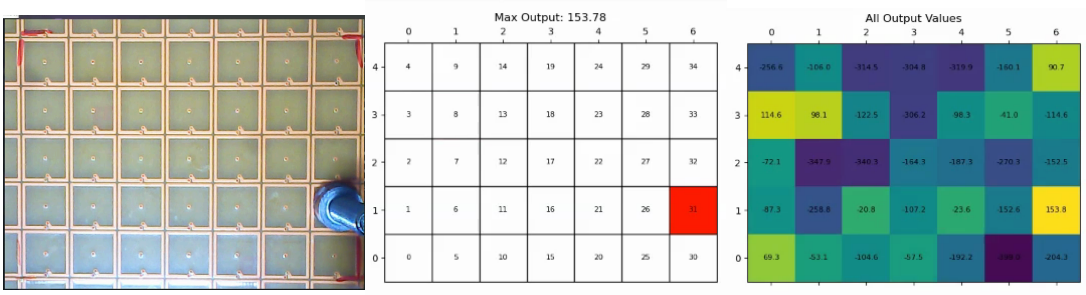

(f)

7) localisation time = 0.9 s

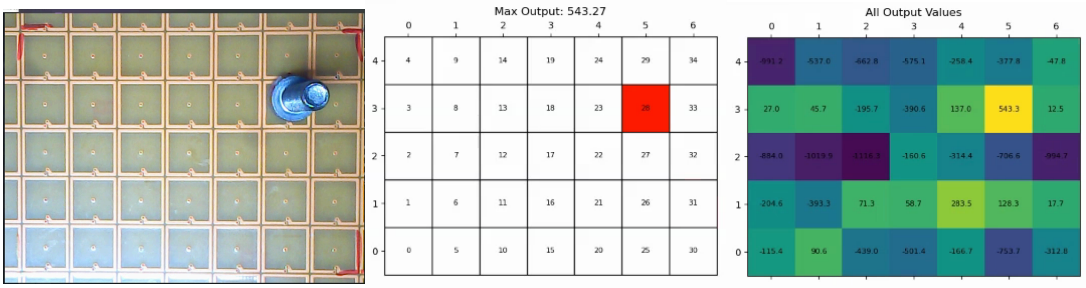

(g)

8) localisation time = 1.6 s

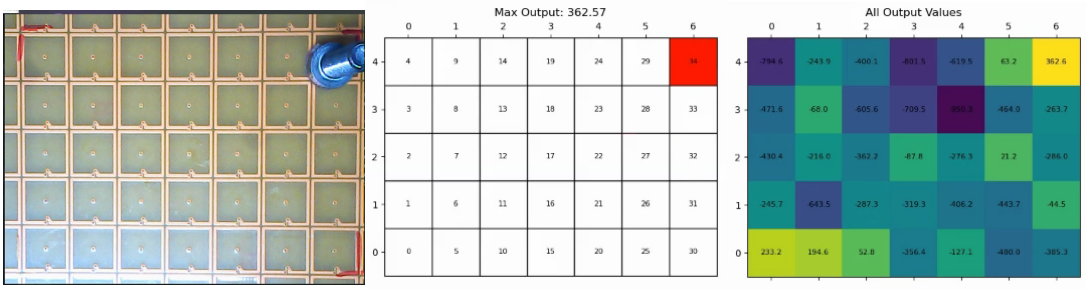

(h)

Figure 4.25: Localisation demo (continued) - part 2/4 showing locations 5 to 8.

9) localisation time = 0.4 s

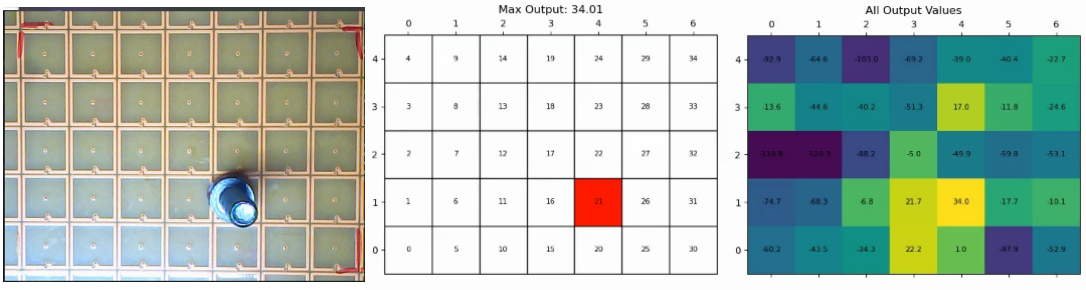

(i)

10) localisation time = 1.5 s

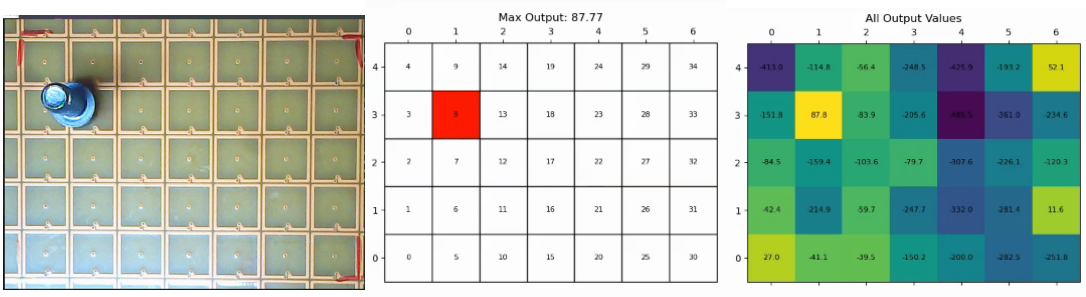

(j)

11) localisation time = 1.9 s

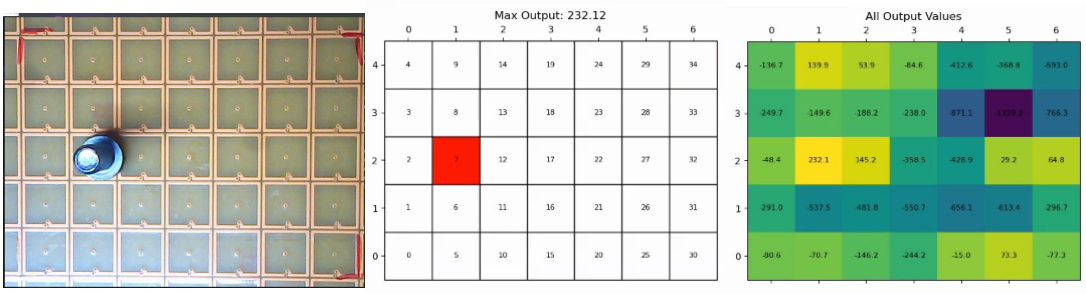

(k)

12) failed localisation

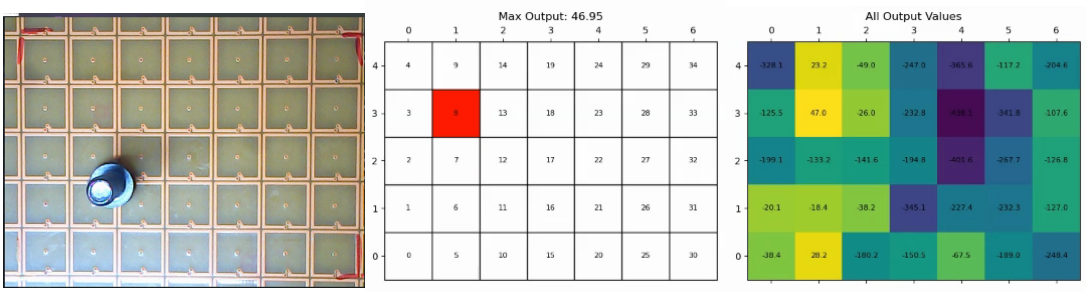

(l)

Figure 4.25: Localisation demo (continued) - part 3/4 showing locations 9 to 12.

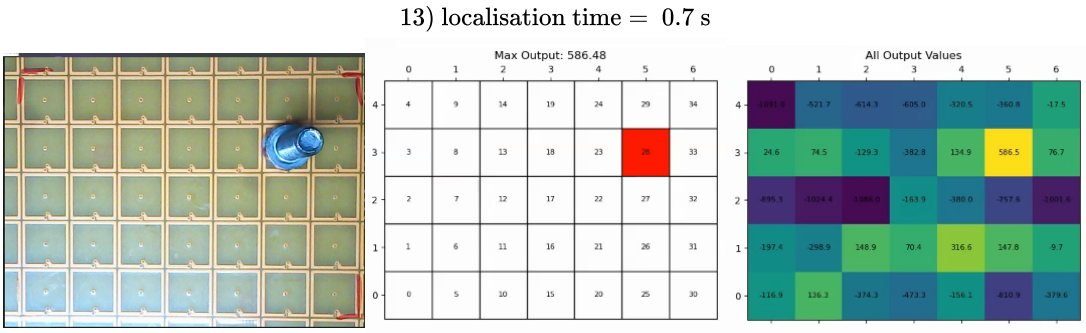

(m)

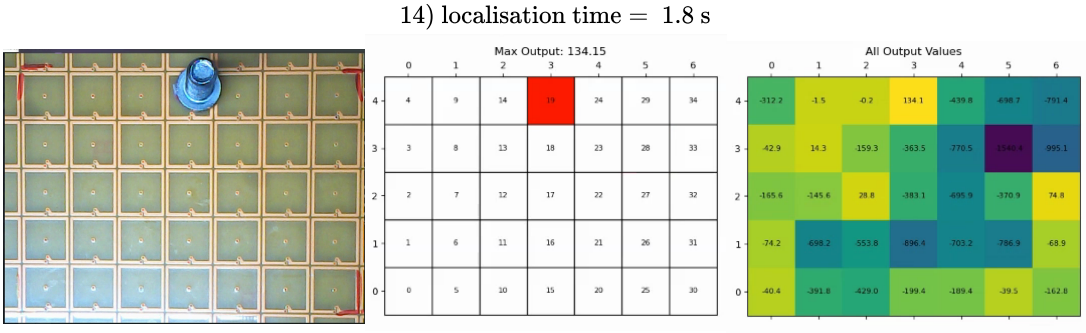

(n)

Figure 4.25: Localisation demo (continued) - part 4/4 showing locations 13 to 14.

4.6 Localisation of two high-conductivity objects

Localisation of multiple objects is a natural next step after successfully achieving single-object localisation and characterisation. Based on the virtual source model presented in Section 4.2.2 it is reasonable to expect that it is possible to localise multiple vacancy locations from the admittance spectrum as the overall change in input admittance, ΔY_{11}, is the sum of individual changes occurring from each affected location. However, adding more defects significantly increases the complexity of the problem. Firstly, from an algorithmic perspective, a larger number of categories has to be used as the neural network output to accommodate all the possible combinations of objects' locations. Alternatively, one can employ a multi-output neural network, adding more complexity to the problem. Moreover, using multiple defects dramatically increases the number of combinations of different objects that can be considered. Adding the different vertical positions of each object adds further complexity to the problem. From an experimental perspective, obtaining all the necessary data for training is a challenge. A simple x-y-z gantry scanner

can no longer ensure that both objects are placed in all desired positions. The number of combinations makes it impossible to gather the data manually.

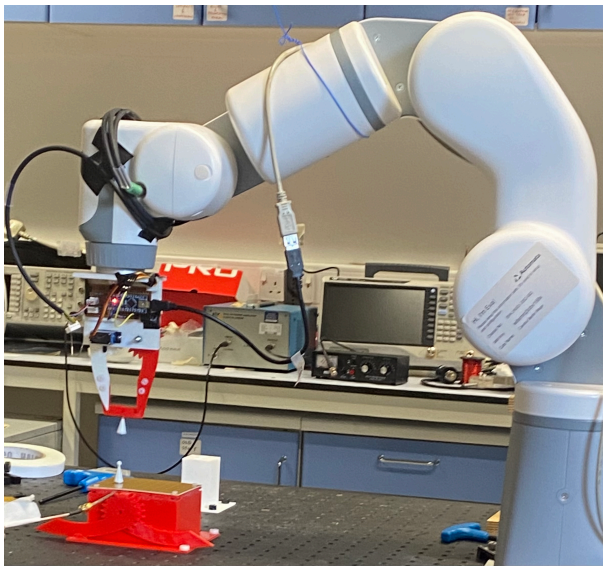

Figure 4.26: Experimental diagram showing the surface used for localisation and the robotic arm used for placing the objects.

To simplify some of these complexity layers, this section's scope will be narrowed to two identical large aluminium discs. The vertical position of both objects will be maintained at $h = 0\,\text{mm}$. The neural network algorithm will be adapted to account for all 595 unique combinations of positions. The surface previously described in Section 4.5.1 was cut and placed on a 3D-printed PCB support. The support fixed the probe's location and surface in place during experiments, thereby reducing variations caused by probe and cable movements. The resulting surface is shown in Fig. 4.26.

The objects were glued onto 3D-printed supports that an Eva Automata robotic arm could grab and move. The robotic arm can also be seen in Fig. 4.26. The robotic arm was programmed to move the objects in all possible combinations of locations. After placing the objects, the S_{11} parameter was collected from the VNA. A background measurement was collected and removed from the S_{11} parameter during the post-processing step. Whilst the x-y-z gantry scanner ensured precise location down to 0.025 mm, the robotic arm placement was less accurate, with errors of $\approx 1-2\,\text{mm}$. These inherent errors of the systems were used as an advantage for the localisation procedure, as each scan is slightly different and can offer helpful information for training. Six scans were performed for a single aluminium disc placed in all 35 locations, and six scans were performed for two

aluminium discs placed in all 595 possible combinations of locations. Single object scans were performed to test whether a neural network can distinguish between a single object placed on the surface and two objects placed on the surface. Three types of simulations were performed using the obtained data: (1) single object localisation, (2) two objects localisation, and (3) separation between a single object and two objects.

Starting with the single object localisation, which was already achieved successfully. Three scans were used as training data, and three were used as testing data. As before, the hidden layer's size was 100, and the learning rate was 2×10^{-5}. However, considering the limited training data, only 5000 iterations were performed. The object was localised with an accuracy of 100% on the testing data set. Whilst the testing dataset covers all the positions of the object, the error in positioning makes every position seen by the neural network in the testing dataset unique.

For the two objects localisation, the full data set was split in a ratio of 1:1 between training and testing, as in the case of a single object. Since the number of outputs increased significantly (from 35 to 595), the hidden layer size was increased to 1000, whilst the learning rate and the number of iterations were maintained the same as in the single object case. The positions of both objects in the test dataset were identified with an accuracy of 99.9%, which is equivalent to a single misslabelled location.

In practical applications, such a system must determine the number of objects before localisation. Hence, a neural network with three outputs was trained: 1) empty surface, 2) single object, and 3) two objects. Half of the collected data was used for training and half for testing for both the single and two-object cases. The empty array was simply simulated as an array of zeros since the changes caused by the background are expected to be minor. The overall separation accuracy between the three categories is 99.6%.

Whilst this study is limited in scope, the results presented here show that multiple object localisation is possible using the platform developed in this chapter.

4.7 Localisation of low-conductivity objects on 2D MIW

Having successfully localised highly conductive objects, the next step was to localise a low-conductivity object. The aim here was to successfully identify the position of an object similar in geometrical and electromagnetic properties to a finger. Such an object can never create a complete vacancy in the structure, meaning that the change in the input admittance is much smaller due to the incomplete cancellation of the current in the affected cell. Nonetheless, the virtual source analogy described in 4.2.2 is still valid, but the amplitude of the virtual source is significantly lower. This section aims to prove that this approach can be adapted to become a faster, easier-to-implement touchscreen methodology.

4.7.1 Experimental arrangement

A different surface, shown in Fig. 4.27(a), is used to localise a low-conductivity object. The surface was created by filling a 3D-printed high-impact polystyrene (HIPS) mould with Field's metal. Each element is a square helical coil with two turns and a wire diameter of 0.8 mm. The outer dimension of the elements is 12.8 mm. The track arrangement is identical with that presented in Figure 4.9. This new surface was chosen due to its high operation frequency, $f_{\text{res}} = 666.6$ MHz, which aids in low conductivity detection and its high quality factor at this frequency, $Q = 119.5$. The fabrication of the individual elements was studied and optimised in our group and is presented in detail in [189]. The coil is unloaded (i.e. its terminations are open), so its resonant frequency is determined by the inductance of the winding and the distributed capacitance across its structure. This distributed capacitance gives rise to electric fields above and below the coil, which allows for stronger interaction with dielectric objects. In the case of water or human tissue, permittivity is relatively high (≈ 80), which means that in addition to the electromagnetic changes caused by conductivity, the object's presence will also induce a higher capacitance when interacting with the open terminations. Figure 4.27(b) shows a photograph of a single element. The surface characteristics and manufacturing steps are presented in [189].

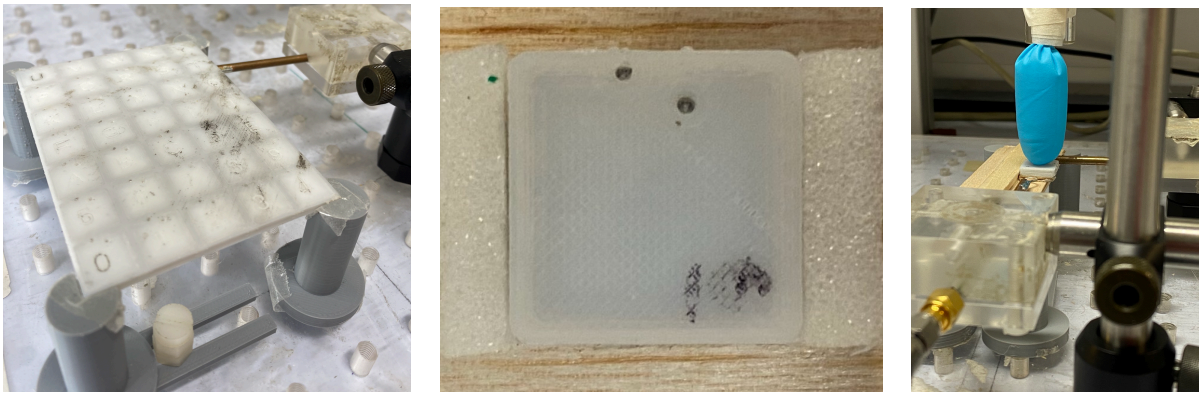

(a) **(b)** **(c)**

Figure 4.27: Experimental arrangement for low-conductivity detection: (a) photograph of the used surface with measurement probe placed underneath element 1f, (b) individual meta-atom photograph where the open terminations are clearly shown, and (c) photograph of finger phantom above the single meta-atom during the characterisation process. Reproduced with permission from [23].

The object used is a finger phantom, obtained by filling the finger of a glove with a saline solution of conductivity 0.64 S/m. This conductivity is in the range of human body conductivities and was measured using a Hanna HI-8633 multi-range conductivity meter. The saline solution also has the benefit of a large permittivity, $\varepsilon_r = 80$, similar to human tissue. Figure 4.27(c) shows the finger phantom during the tile characterisation process, which assessed the strength of interaction between the finger and a single cell. The resonant frequency, f_{res}, and the quality factor, Q, were measured by placing two non-resonant loops in the proximity of the cell. The loops were connected to the VNA, and the transmission scattering parameter (S_{21}) was measured. S_{21} was then post-processed and used to extract f_{res} and Q through the 3dB method outlined in Section 1.2.2. During the characterisation process, the finger phantom was moved in the range 0 - 12 mm above the cell in steps of 0.25 mm. The resulting variation of f_{res} and Q with vertical position, h, is shown in Fig. 4.28.

Both f_{res} and Q are impacted significantly by the presence of the finger. The resonant frequency changes, $f_{\text{res}} = 666.6$ MHz to $f_{\text{res}} = 645.3$ MHz, whilst the quality factor, Q, goes from $Q = 119.5$ to $Q = 68.2$. These changes are large enough to enable localisation, and the surface characteristics can explain them. The open terminations allow for larger f_{res} changes due to their interaction with the dielectric object, and the higher frequency results in larger overall changes, as presented in Section 2.3.3.

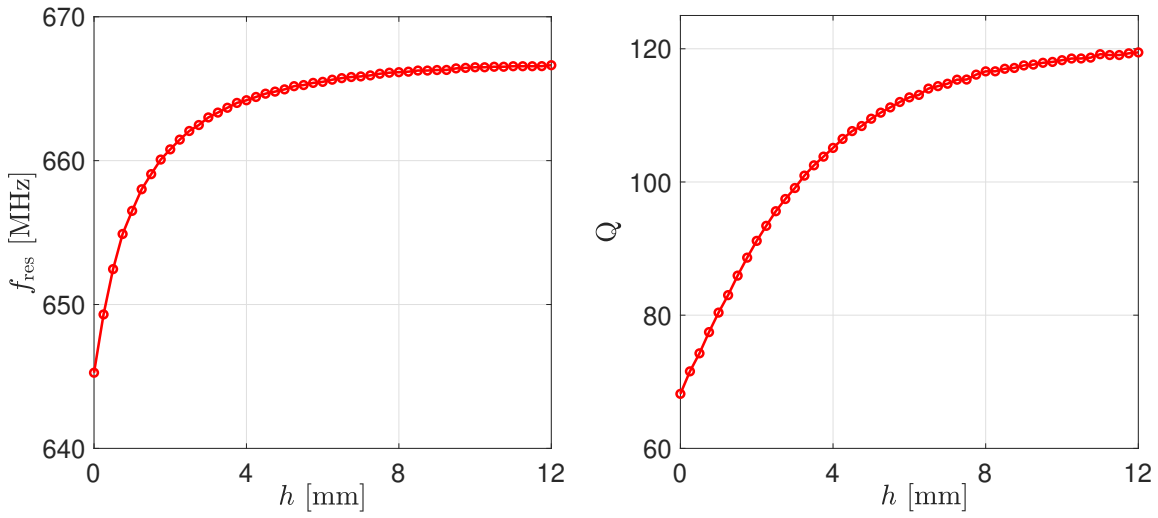

Figure 4.28: Variation of resonant frequency, f_{res}, (left) and quality factor, Q, (right) with vertical position, h, of finger phantom. Reproduced from [23]. Ref. [23] is licensed under a Creative Commons Attribution 4.0 License. ©2024 Springer Nature by G. Dima, I. Spanos, and C. J. Stevens.

4.7.2 Experimental results

The neural network presented in Section 4.3 was adapted for the localisation of a low-conductivity object. The data set was split into training and testing in a ratio of 1:3, with integer vertical position data used as the training points. The learning rate was set to 2×10^{-5} for the first 10^4 iterations and then reduced by 0.9 for every 10^4 iterations. The total number of iterations used in training was 10^5. All 1601 points in the S_{21} spectrum were used as features for the neural network, whose hidden size was maintained at 100.

The overall accuracy of finger localisation is 99.3% for the test data set and 99.2% for the full dataset. The error for each location and each vertical position of the object is shown in Fig. 4.29. Nearly error-free localisation is possible up to 10 mm of finger vertical position. The localisation method used can therefore be further developed to become a fast, easy-to-implement touchscreen technology.

4.8 Discussion and conclusions

This chapter investigated the extent to which a metamaterial array can be used for object localisation. The method used for localisation maps the changes in the standing wave pattern when an object is placed on a metamaterial array to the position of the

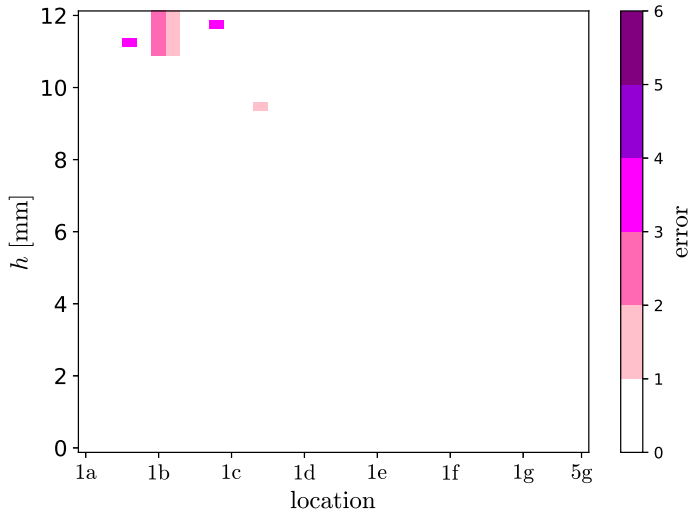

Figure 4.29: Manhattan distance between the correct location of the finger phantom and the identified location for all locations and all vertical positions, h. Reproduced from [23]. Ref. [23] is licensed under a Creative Commons Attribution 4.0 License. ©2024 Springer Nature by G. Dima, I. Spanos, and C. J. Stevens.

object. The entire surface is monitored through a single feeding point, which allows for the input admittance spectrum extraction. The single measurement point simplifies the localisation algorithm's computation and circuitry requirements. It represents an element of novelty of the method compared to other localisation techniques, such as touchscreen array technologies.

A neural network algorithm with a single hidden layer maps the changes in the standing wave pattern to an object's location. This algorithm was chosen because it can model complex, non-linear systems, is easy to implement, and has a low detection time.

The first part of this chapter focused on localising a single high-conductivity object on a one-dimensional array. The experimental localisation performed using the machine learning algorithm was directly compared to the analytical results presented by Yan et al. in [18]. Whilst Yan et al. obtained error-free localisation only up to 1.5 mm, using the neural network approach resulted in nearly error-free localisation up to 10 mm. This significant improvement in sensitivity, alongside the ability to use experimental data for training and testing, leads to the conclusion that localisation using a neural network algorithm is a stronger alternative which can be employed for more complex tasks, such as localisation on two-dimensional surfaces.

The next step in this chapter was localising a single high-conductivity object on a two-dimensional array. Before proceeding with the experiments, analytical simulations were used to assess the impact of the feed position and noise on the system. The feeding point location was a key point of discussion, closely tied to the structure's symmetry. For successful localisation, all the locations in the array must be unique, which can only be achieved by choosing an asymmetrical feeding position. Analytical results show that a centrally fed surface with only 12 unique locations had an accuracy just under $12/35 = 34.3\%$, whilst a side feed with 21 unique locations had an accuracy slightly below $21/35 = 60\%$. Most notably, the asymmetric feed led to an accuracy close to 100%, supporting the need for an asymmetrical feeding location during localisation. However, it is important to note that changing the feed position is one way to ensure array asymmetry. Slight variations in each tile's tuning frequency or quality factor would also introduce disorder, which can aid in uniquely identifying each tile.

The impact of noise was also studied analytically. It was found that systems with a signal-to-noise ratio, SNR, higher than 40 dB can localise objects with an accuracy better than 86%. For the systems used in this Chapter, the SNR did not fall below 80 dB, which ensured that white random noise is not a significant system concern.

Experimentally, eight high-conductivity objects of different sizes and materials, placed at a vertical distance above the surface of at most 10 mm, were localised with an accuracy exceeding 98%. Smaller objects generated more minor changes in the input admittance spectrum and required finer tuning of the neural network for accurate localisation. After increasing the number of iterations by five and reducing the learning rate by 10% every 10000 iterations, the localisation of small objects was nearly error-free up to 8 mm. Detection above this point is significantly improved by the neural network changes. However, the inherent system limitations still induce an approximate error of 10%. This suggests that half of the array period is a safe lower bound for the object size if successful localisation is desired up to 10 mm. The upper limit on the object size appears when the object placed on the array is so large that one or more resonators are impacted similarly by the object's presence. In Chapter 3 and in [25], an object six times larger than the

array period was indistinguishable from larger objects. It is, therefore, safe to assume that objects larger than six times the array period will impact multiple cells in the same manner and result in localisation failure.

Practical system implementations were also considered by varying the number of features in the admittance spectra used for training. Whilst the VNA used in the experiments has 1601 spectral features available, smaller and easier-to-integrate VNAs usually can collect fewer data points. The number of features also affects the model size, with more inputs creating models that occupy more memory space. Reducing the number of features could help integrate the model into cheap, commercially available microcontroller chips and reduce the cost associated with the measurement of VNA. During the study, reducing the number of features to 201 spectral points led to an accuracy of up to 85%, which increased to more than 90% for 401 features. Using 801 features was found to have only a minor impact on the overall accuracy. It is, therefore, possible to reduce the system's complexity with only a minor reduction in accuracy. One area of further research not explored in this chapter was carefully selecting relevant peaks for training. This has the potential to significantly reduce the system complexity in practical system applications.

Classifying the high-conductivity objects was also possible with an accuracy of 97%, since samples of different sizes and materials impact the metamaterial array differently. Additionally, the cross-training capabilities of the structure were assessed. In essence, this determined if using the model trained for a specific sample could localise other samples. This was possible within a limited altitude range, particularly when considering training and testing with samples of varying conductivities or sizes. The limitations come from the specific behaviour of each sample, which affects the quality factor and the resonant frequency in a unique way. It was found that grouping objects by size or shape is a more successful way of reducing the number of models required. In both cases, localisation of the classes was achieved with accuracy above 98%, and separation between the newly created samples was possible roughly 97% of the time. These findings offer a way of simplifying the system in practice. Taking a metamaterial array used for wireless power transfer [187, 188, 190, 191] as an example. Before any power delivery can happen,

an object placed on the surface must be localised and ensured that it is an acceptable receiver. In such a case, having two classes of objects (i.e. allowed receivers and foreign objects) would avoid transmitting power to foreign objects, which could badly damage the charging surface. The classification would simplify the procedure, as a class of foreign objects can contain all objects that should not be charged without storing an exhaustive number of models for every possible type of foreign object.

To fully address the practical considerations, a lab-based demo which uses a pre-trained model was implemented and used to localise objects in real-time. The localisation was successful for all 35 central positions, and out of 14 off-centre locations, 13 were identified accurately. Each time, the localisation process lasted less than two seconds, which supports the system's ability to operate in real-time. Additionally, the most time-consuming part of the demo was plotting the visualisation maps using `matplotlib`. Since this is not required in a real system, it can be expected that the localisation can happen in less than one second.

This Chapter also provided a proof of concept for the two-object localisation, which was done with an accuracy above 99%. A single object type was used during these tests, and both objects were always in contact with the surface. A robotic arm collected multiple scans, split into testing and training sets. The inherent errors in positioning caused by the robotic arm made each data set unique and allowed for a simplified two-object localisation system. Whilst limited in scope, this demonstrates that two-object localisation is possible. Further avenues yet to be explored in this area include modifying the localisation algorithm, changing the vertical position of each object and using different objects for localisation.

Finally, this chapter's last section concerned localising a low-conductivity object that mimics a human finger. Localisation was possible with accuracy above 99% up to 12 mm. This accuracy was made possible by the surface characteristics. First, the operating frequency was approximately 666 MHz, which allowed the low-conductivity finger phantom to impact the surface more, as seen in Chapter 2. The open terminations of each meta-atom also contributed to changes in the resonant frequency since they could interact with

the permittivity of the finger phantom (≈ 80). The results for low-conductivity detection prove that this surface can be successfully used as a touchscreen array. The single excitation/measurement point could reduce the hardware and computation requirements of the usual touchscreen array.

This work presents a proof-of-concept localisation method whose defining advantage is the use of a single probing point, in contrast to most state-of-the-art techniques that require extensive electrode networks or multiple measurement locations. By reducing the sensing interface to a single point, the system greatly simplifies hardware design, lowers wiring complexity, and opens the door to lighter, more compact, and more robust sensing platforms. Unlike conventional approaches optimised for fixed laboratory conditions, this method can be adapted to a variety of environments and geometries, including both 2D and 3D surfaces, by constraining the machine learning model to operate within the relevant conditions. This adaptability is particularly valuable in harsh or unconventional settings, such as underwater environments, where the system could be trained to enable submerged touchscreens, or aerospace applications where structural health monitoring must be performed without intrusive hardware.

The method demonstrates the ability to detect objects of varying sizes positioned up to 10 mm above the array. Although the current implementation operates more slowly than state-of-the-art systems, this is a direct consequence of the lack of computational optimisation in this proof-of-concept stage. Intrinsically, probing a single point offers a benefit that could potentially speed up the response time.

In the present study, localisation was demonstrated for up to 35 discrete positions, with the maximum limit set by the quality factor of the array. Importantly, this limit is not fundamental: by including intermediate, or "interstitial," positions during training, the method can achieve substantially higher spatial resolution than the physical sampling grid suggests. This capability not only extends the applicability of the method to fine-resolution tasks but also positions it as a scalable approach that could be deployed in large-area sensing systems without the prohibitive complexity typically associated with dense measurement networks.

CHAPTER 5

Time-domain reflectometry

5.1 Introduction

The previous chapter focused on extending the frequency-domain localisation method developed by Yan et al. [18]. Using a machine learning algorithm enabled the localisation of objects with various conductivities using magnetoinductive arrays, in one and two dimensions. The frequency-domain changes are caused by the reflections that occur from a resonator whose individual characteristics are modified by the presence of an object. In the frequency domain, accurately predicting the location and magnitude of these changes analytically for different objects is challenging, as shown by [18]. However, in the time domain, when a pulse is injected in a 1D metamaterial array, the reflections are localised in time, allowing for localisation based on the time of arrival. This principle was theoretically presented by Trivedi et al. [19] for ideal defects (i.e. objects with infinite self-impedance, $Z_0 \to \infty$).

This chapter studies a one-dimensional metamaterial array from a time-domain perspective. It begins by analysing the wave propagation in unloaded arrays, arrays with ideal

defects, and arrays with partial defects. The time of flight of an injected pulse is then used to localise an object, and the magnitude of the reflection is leveraged to obtain information about the object. The results for the 1D array are dramatically improved in comparison with the frequency-domain results, achieving perfect localisation of a bolt placed up to a height of 12 mm. The accuracy for objects placed up to 15 mm in height increases dramatically from 91% in the frequency-domain to 98% in the time-domain. This is caused by the time-localised nature of the reflection in the time domain, which is a more robust and trackable change.

This chapter is connected to the following publications [24, 27–30]:

- G. Dima, C. McMahon, A. Radkovskaya, *et al.*, "Time-domain reflectometry for imaging conductive environment," in *Proc. 18th Int. Congr. Artif. Mater. Novel Wave Phenom. (Metamaterials 2024)*, 2024
- X. Li, G. Dima, A. Radkovskaya, *et al.*, "Neural network-based conductivity imaging using time-domain reflectometry," in *Proc. 19th Int. Congr. Artif. Mater. Novel Wave Phenom. (Metamaterials 2025)*, 2025. under review
- D. Dhayaa, C. Long, A. Radkovskaya, *et al.*, "Sensing using magnetoinductive waves," in *Coupled Structures for Microwave Sensing*, 427, Springer, Cham, 2024
- C. Long, A. Radkovskaya, G. Dima, *et al.*, "Metamaterials for characterisation of conductive objects using time-domain reflectometry of magnetoinductive waves," in *Proc. 17th Int. Congr. Artif. Mater. Novel Wave Phenom. (Metamaterials 2023)*, 205, 2023
- D. Dhayaa, A. Radkovskaya, J. Yan, *et al.*, "Metamaterials for sensing conductive objects using time-domain reflectometry of magnetoinductive waves," in *Proc. 16th Int. Congr. Artif. Mater. Novel Wave Phenom. (Metamaterials 2022)*, 125, 2022

5.1.1 Signal propagation in unloaded array

Figure 5.1 shows the propagation of a pulsed signal for a magnetoinductive line of split ring resonators with no perturbations. When the array is unperturbed, the signal trav-

els to the end of the line and is then fully reflected, before travelling back. All the reflections from the surface edges in this thesis can be considered ideal since the array is unterminated (or open-terminated).

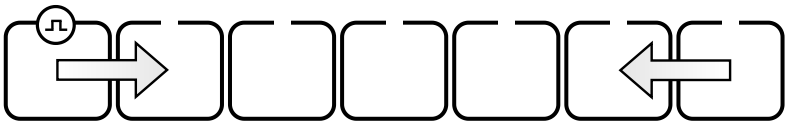

Figure 5.1: Wave propagation in a one-dimensional array without a defect.

The behaviour of a one-dimensional line is described in detail in Chapter 1.2.4. The signal travels through the array with the group velocity, which can be derived from the dispersion equation presented in Chapter 1.2.4:

$$v_g = \Re\left(\frac{\omega^3}{\omega_{\text{res}}^2} a\kappa \sin ka\right), \tag{5.1}$$

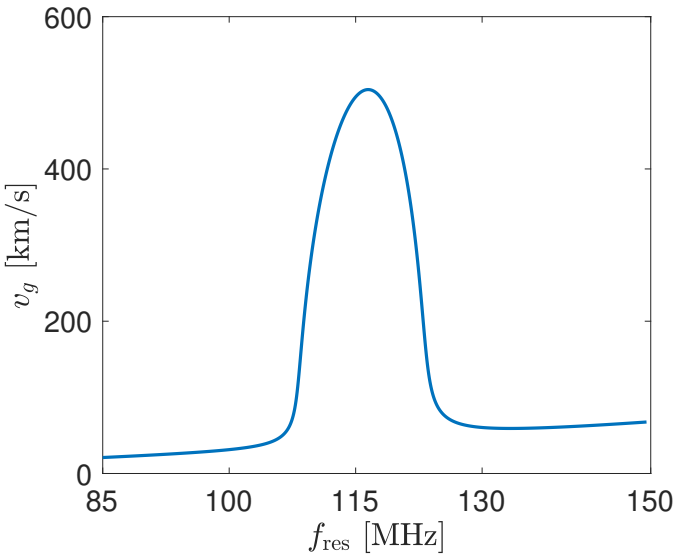

Figure 5.2: Group velocity in an array with $a = 10.5\,\text{mm}$, $\kappa = -0.13$, $f_{\text{res}} = 115\,\text{MHz}$, and $Q = 100$.

where a is the distance between elements, κ is the nearest-neighbour coupling, and k is the wave number, which can be extracted from the dispersion equation. The group velocity as a function of frequency, f_{res} for an array with $a = 10.5\,\text{mm}$, $\kappa = -0.13$, $\omega_{\text{res}} = 2\pi f_{\text{res}} = 2\pi \times 115\,\text{MHz}$, and $Q = 100$ is shown in Fig. 5.2. It can be seen that components in the passband travel much faster than all the other components, which can be expected to be mostly attenuated by the array.

When the array is excited by applying a voltage pulse to the element, different frequency components will travel at different velocities, causing the pulse to spread due to the dispersive nature of the MI wave. Two types of excitation pulses will be considered: a square pulse and a modulated Gaussian pulse. Figure 5.3(a) shows a square pulse (red) of period $T = 10\,\mu$s, amplitude $A = 1\,$V and duty cycle 50% alongside a modulated Gaussian pulse (blue) with the same period and amplitude, pulse width, τ, of 100 ns and modulation frequency, f_{m}, of 115 MHz. Figure 5.3(b) shows the Fast Fourier Transform (FFT) of these pulses. The Gaussian pulse is defined as follows:

$$V_{\mathrm{Gaussian}} = A\cos\left(2\pi f_m t\right)\mathrm{e}^{-\left(\frac{\pi t}{\tau}\right)^2}. \tag{5.2}$$

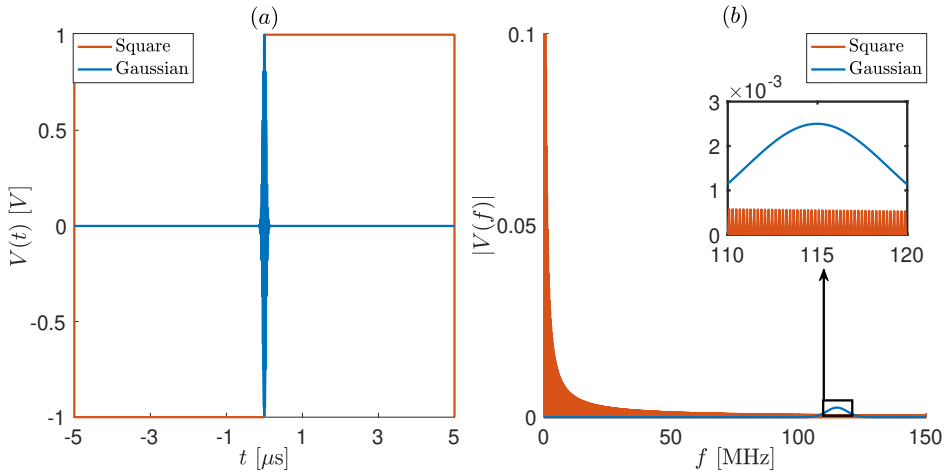

Figure 5.3: (a) Square pulse of period $T = 10\,\mu$s, amplitude $A = 1\,$V, and duty cycle 50% (red) and modulated Gaussian pulse with the same period and amplitude, pulse width $\tau = 100\,$ns and modulation frequency $f_m = 115\,$MHz (blue); (b) Fast Fourier Transform of the pulses.

The $\mathbf{V} = Z\mathbf{I}$ method presented in Section 1.2.4 can be adapted such that the magnitude of the excitation voltage at each frequency corresponds to the magnitude of the FFT spectrum of the pulse used.

$$\begin{bmatrix} V(\omega) \\ 0 \\ \dots \\ 0 \end{bmatrix} = \begin{bmatrix} Z_0 & j\omega M & \dots & 0 \\ j\omega M & Z_0 & \dots & 0 \\ \vdots & \vdots & \vdots & \vdots \\ 0 & 0 & \dots & Z_0 \end{bmatrix} \begin{bmatrix} I_1(\omega) \\ I_2(\omega) \\ \dots \\ I_N(\omega) \end{bmatrix} \tag{5.3}$$

The time-domain current variations in each element are obtained by taking the inverse FFT of each current spectrum. Figure 5.4 shows the time variation of the current in

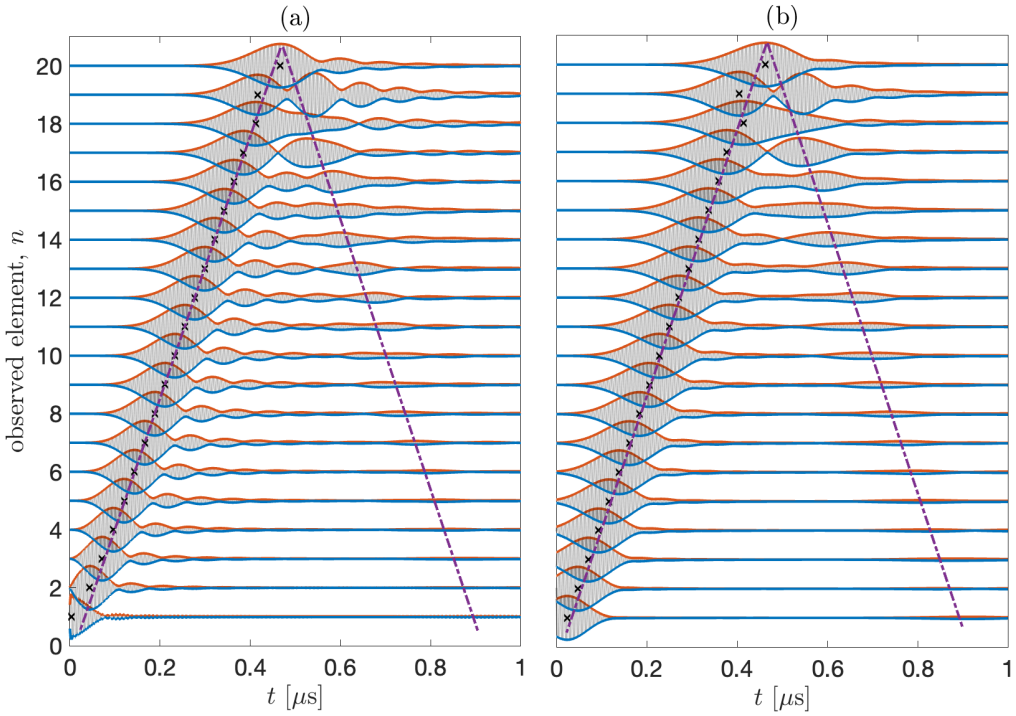

Figure 5.4: Time variation of current for all the elements in an array with $a = 10.5$ mm, $\kappa = -0.13$, $\omega_{\text{res}} = 2\pi f_{\text{res}} = 2\pi \times 115\,\text{MHz}$, and $Q = 100$ for a square pulse (a) and a Gaussian pulse (b). For better visualisation, each current, I_n, is normalised and shifted vertically by the element number, n. Currents (grey) are shown together with the upper (red) and lower (blue) envelopes. Black crosses mark the time when currents reach their maxima. The purple lines are plotted to aid in the visualisation of the pulse travelling path.

each element of an array with $a = 10.5$ mm, $\kappa = -0.13$, $\omega_{\text{res}} = 2\pi f_{\text{res}} = 2\pi \times 115\,\text{MHz}$, and $Q = 100$ for both a square (a) and a Gaussian modulated pulse (b). The signal travels from one coil to the next, which can be seen from the time delay between the peaks of each current. The speed of the signal can be estimated by dividing the distance between two neighbouring unit cells, a, by the time delay between the peaks in the current of the two elements. The velocity of the signal propagation is $\approx 467\,\text{km/s}$ for the square wave and 476 km/s for the Gaussian wave. These numbers are in line with the values expected from the group velocity plot (Fig. 5.2). The Gaussian pulse travels slightly faster than the square pulse because its voltage spectrum peaks at the resonant frequency, where the group velocity is larger. In the case of the square pulse, the voltage spectrum decreases slightly over the passband, which leads to slightly higher amplitudes for the lower frequencies.

Once the signal reaches the end of the unterminated array, it is fully reflected and begins travelling back, as indicated by the purple dashed lines in Fig. 5.4. Due to the attenuation in the magnetoinductive array, the magnitude of this reflection decreases in comparison with the primary peak.

5.1.2 Signal propagation in an array with ideal defects

Having understood the signal propagation in an ideal line, it is now possible to present the effects of an ideal defect on the line. An ideal defect is modelled as a missing cell in the line, i.e. as an element with infinite self-impedance, $Z_0 \to \infty$. Trivedi et al. [19] studied the impact of an ideal defect on the signal's propagation in the time domain. Considering that the second-order coupling is much smaller in comparison with the nearest-neighbour coupling (typically by a factor of 10 in a planar array), an ideal defect results in the array behaving very closely to an array that terminates right where the ideal defect is placed. In other words, when an ideal defect is placed on element $N + 1$, the magnetoinductive waveguide behaves as if it had N resonators, as an injected pulse is fully reflected when it encounters the ideal defect. This is shown schematically in Fig. 5.5.

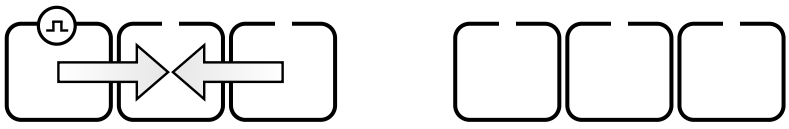

Figure 5.5: Wave propagation in a one-dimensional array with an ideal defect.

Figure 5.6 shows in blue the time-domain current in the second element, $I_2(t)$, when the defect is placed on element 10 for a square and a Gaussian modulated pulse injected in the first element of the array previously described. The second element is monitored because, in practice, it is not easily possible to monitor the current in the first element, which is also affected by the presence of physical connectors. The first peak corresponds to the injected signal, whilst the second peak is the reflection of the signal from the ideal defect. The reflection can be isolated by subtracting the unperturbed-array current from the current of the array with the ideal defect present. This is shown in Fig. 5.6 in red.

The isolated reflections for different defect locations are shown in Fig. 5.7. By identifying

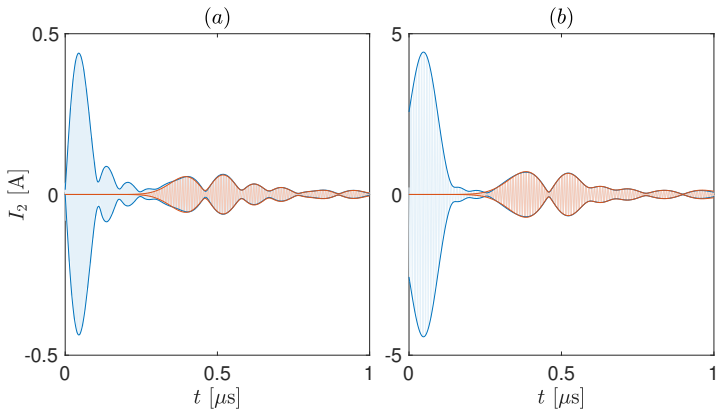

Figure 5.6: Current (blue) and isolated reflection (red) in the second element of an array excited by a square pulse (a) and a modulated Gaussian pulse (b) when an ideal defect is placed on element 10. Currents (grey) are shown together with the upper (red) and lower (blue) envelopes. Black crosses mark the time when currents reach their maxima.

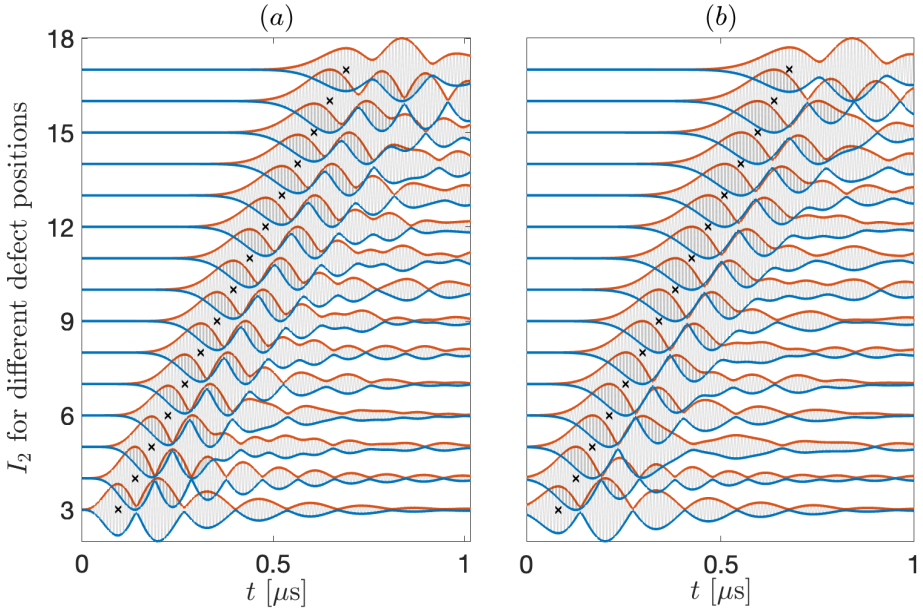

Figure 5.7: Normalised isolated reflection observed on element 2 for different defect locations for a square excitation pulse (a) and a modulated Gaussian pulse (b).

the peak position of each reflection, one can calculate the time spent by the signal travelling, Δt. Using the known mean speed of each pulse, v_g, the distance travelled by the signal can be approximated. The following formula can then be used to approximate the position of the defect from the arrival time, Δt, speed of travel, v_g, and unit cell size, a:

$$N = \frac{v_g \Delta t}{2a} + 2. \tag{5.4}$$

5.1.3 Wave propagation in an array with a real object

Whilst understanding the impact of ideal defects on the propagation of magnetoinductive waves provides a strong foundation, in practice, most applications focus on localising objects whose effect on the array is weaker. In such cases, when the travelling wave encounters the object, the wave is partially transmitted and partially reflected, as shown in Fig. 5.8. The proportion of the signal being reflected depends on the strength of interaction between the object and the cell immediately below it. The reflection strength can, therefore, be used to infer properties of the defect placed on the array, such as conductivity or height above the array.

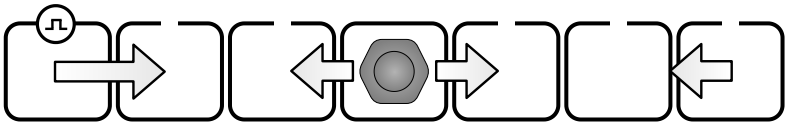

Figure 5.8: Wave propagation in a one-dimensional array with a real object.

The strength of the interaction can be formally quantified through the ratio between the peak magnitude of the reflected signal at element N and the peak magnitude of the incident signal. Figure 5.9 shows the isolated reflection in an array excited by a square pulse (a) and a modulated Gaussian pulse (b) when an object placed on element 10 causes the quality factor of the tile immediately below it to drop from 100 to $Q_{\text{def}} = 70$ (red), $Q_{\text{def}} = 40$ (blue) and $Q_{\text{def}} = 10$ (green). Whilst the arrival time of the reflection is unaltered by the different defect strengths, the magnitude of the reflection decreases as the quality factor of the defective cell rises, as more of the incident energy is absorbed instead of reflected.

We provide an analytical derivation for the reflection coefficient at element N [28], arriving at the following equation:

$$R_N = -\frac{\Delta}{\Delta - 2jZ_M \sin(kd)} \mathrm{e}^{-2jkdN}, \tag{5.5}$$

where $\Delta = Z_{\text{def}} - Z_0$ and Z_{def} is the impedance of the element immediately below the object.

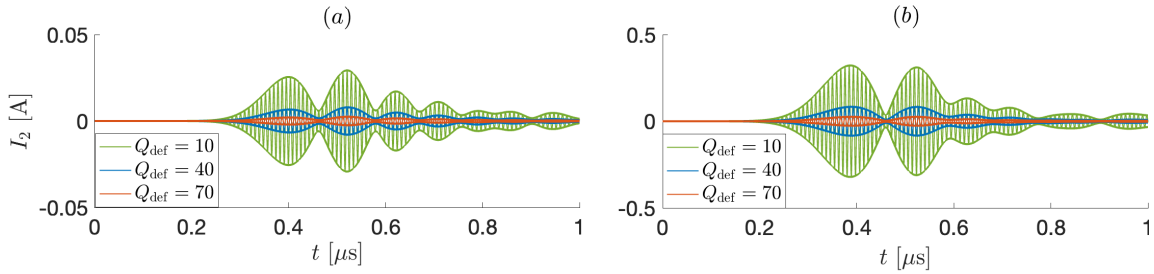

Figure 5.9: Isolated reflection in the second element from an object placed on tile 10 which changes the quality factor of the tile to $Q_{\text{def}} = 70$ (red), $Q_{\text{def}} = 40$ (blue) and $Q_{\text{def}} = 1$ (green).

Localisation and characterisation in the time-domain were achieved by our group [28–30] for a square pulse input signal and preliminary results for a modulated Gaussian pulse were presented in [24].

The remainder of this chapter will focus on localising and characterising objects experimentally using time-domain reflectometry.

5.2 Tile characterisation

The first step in the experimental localisation is quantifying the strength of interaction between the object and the array. The resonant frequency, f_{res} and the quality factor, Q, of a single element were measured whilst a bolt was placed at different heights above it. The same elements used in the work of Yan et al. [18] and in Section 4.4.1 of this thesis are used throughout this chapter. This allows for direct comparison between the different localisation methods. Each element is a single-layer square PCB coil of outer size $D = 10\,\text{mm}$, track width $w = 1$ mm, free-space resonant frequency $f_0 = 114.3\,\text{MHz}$ and free-space quality factor $Q_0 = 84$. The coil is excited by a non-resonant loop, and the altered field is measured by a second non-resonant loop. Figure 5.10(a) shows the experimental diagram, whilst Fig. 5.10(b) shows a photograph of the experiment. Both measurement probes are connected to a Hewlett-Packard 8753ES Vector Network Analyser (VNA), which measures the S_{21} parameter (i.e. the power drop due to the presence of the resonator). The background signal, without the presence of the coil, was collected for all bolt vertical positions and extracted from each measurement. This ensures that changes in the background, as the bolt is moved vertically, are accounted

for.

The position of the measurement probes plays an important role when characterising a tile. When the two probes are placed in close proximity to the tile, the properties of the measured element are affected by the conductive loops of the probes, but the measured S_{21} signal has a high signal-to-noise ratio. As the probes move further and further away, the measured parameters of the coil are closer to the real ones since the influence of the metallic loops decreases. However, the SNR deteriorates, leading to larger errors when extracting the parameters. This can represent a significant problem when relatively small changes in the resonant frequency and quality factor are monitored, as the error can become comparable to the change. The chosen configuration ensures maximum SNR whilst not affecting the free space quality factor significantly. The excitation probe was placed roughly 7 mm below the centre of the coil, whilst the measurement probe was placed in-plane with the coil, ≈ 5 mm away from it.

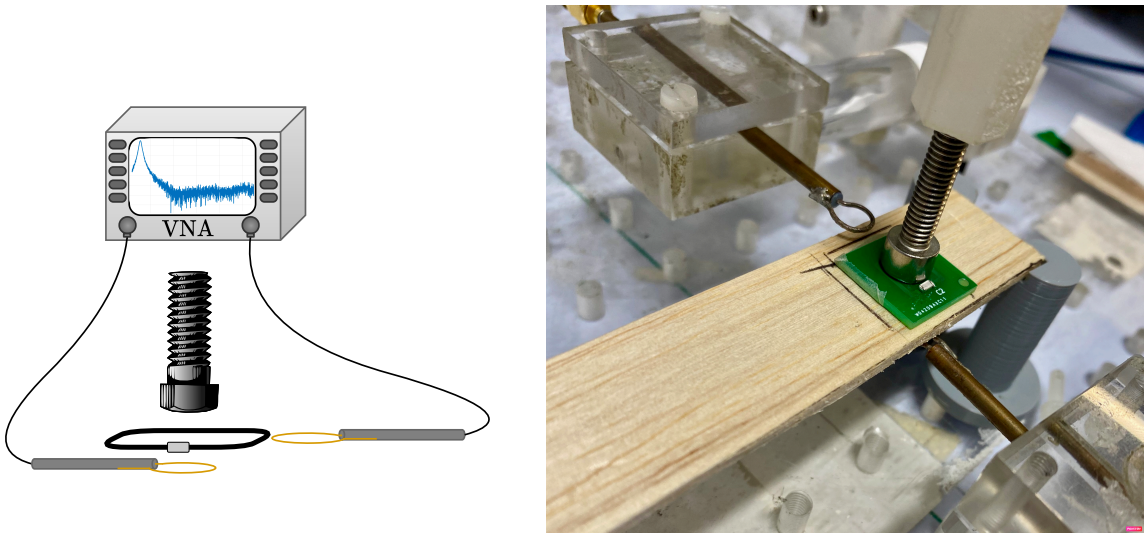

(a) **(b)**

Figure 5.10: Experimental diagrams for single coil characterisation: (a) schematic diagram, (b) photograph of the experiment.

The properties of the coils were determined using the 3dB method and the Lorentzian fit method, both of which were described in Section 1.2.2. Before using the 3 dB method, the data was filtered using a Savitzky–Golay filter of order 2 and window size 21 and 10^4 points were interpolated in the resulting data. The fit for the extreme vertical positions of the bolt, $h = 0\,\text{mm}$ and $h = 15\,\text{mm}$ are shown in Fig. 5.11.

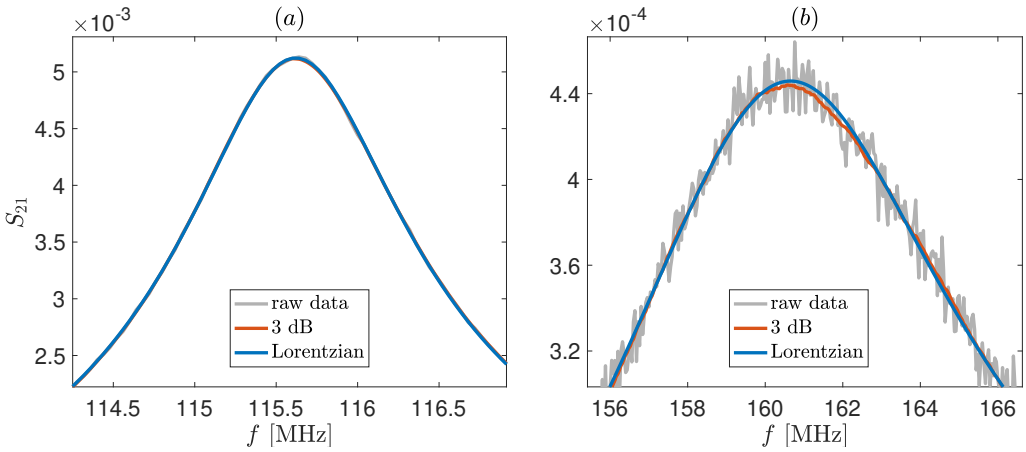

Figure 5.11: 3dB (red) and Lorentzian fit (blue) for the measured S_{21} (black) when the bolt is placed at height $h = 0\,\text{mm}$ (a) and $h = 15\,\text{mm}$ (b).

The resulting resonant frequency, f_{res} and quality factor, Q, are shown in Fig. 5.12. The two methods perform similarly and exhibit a reasonably smooth profile, which is important when trying to quantify the height of an object. The Lorentzian fit results were chosen based on the fit in Fig. 5.11(b), which is more accurate. The 3dB method is less desirable when characterising coils under the influence of objects which generate strong changes in Q. This is because the optimal parameters of the smoothing filter change slightly depending on the noise in the data. A consistent extraction protocol is, therefore, difficult to achieve, and a method such as the Lorentzian fit is more desirable as it fine-tunes the results obtained from the 3dB method.

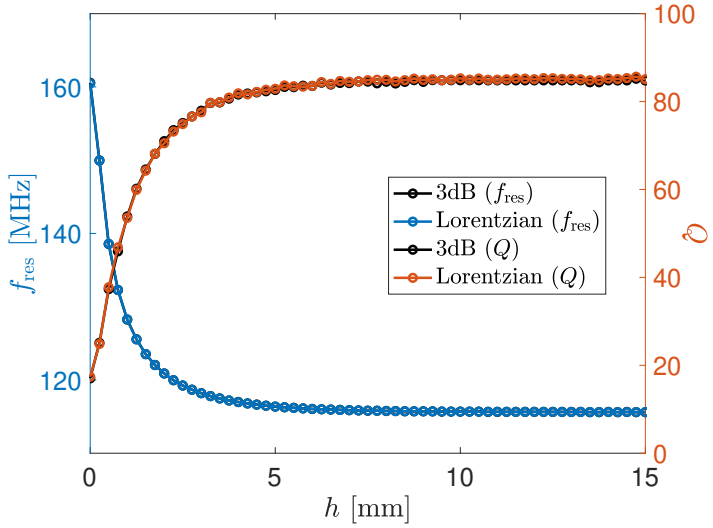

Figure 5.12: Extracted resonant frequency f_{res} (a), and quality factor Q (b) for a square single layer square PCB resonator of size $D = 10\,\text{mm}$ and track width $w = 1\,\text{mm}$ as an M6 bolt is moved vertically from $h = 0\,\text{mm}$ to $h = 15\,\text{mm}$ in steps of $0.25\,\text{mm}$.

5.3 Results

5.3.1 Localisation based on time-of-flight

The one-dimensional array used for localisation contains 20 elements with the distance between the centres of two adjacent elements of $a = 10.5$ mm. The same array was also used for localisation in [18, 24, 28–30]. The coupling coefficients used in these publications are $\kappa_1 = -0.13$, $\kappa_2 = -0.0062$ and $\kappa = -0.0005$. The same values will be adopted here when performing analytical simulations alongside the values of resonant frequency, f_{res}, and quality factor, Q, presented in the previous section.

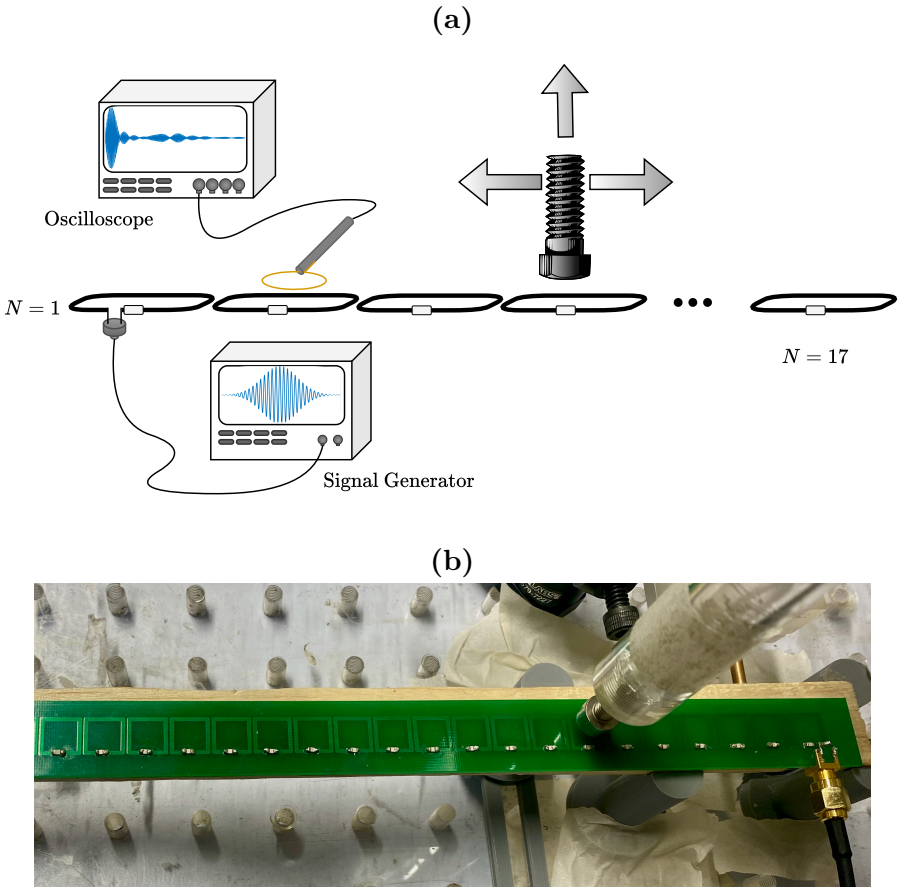

Figure 5.13: Schematic of the experiment used for time-domain localisation (a) and photograph of the array and connections (b).

Figure 5.13 presents a diagram of the experiment (a) and a photograph of the array and connections (b). The first coil of the array is connected to a signal generator via a cable and an SMA connection. A non-resonant loop connected to a KeySight MSOX3034G oscilloscope is used to monitor the current variation in the second element. The probe location underneath the element was modified, and the envelope of the signal was moni-

tored on the oscilloscope in order to obtain a smooth envelope, indicative of a signal not distorted by fields from the neighbouring elements.

The SMA connection changes the characteristics of the first element, which needs to be accounted for in the analytical model. Its quality factor, Q_{01}, and resonant frequency, $f_{\mathrm{res},01}$, can be approximated from the current spectrum in the second element when the array is unloaded. The Fourier transform of the current spectrum is divided by the spectrum of the excitation pulse to remove its impact on the spectrum. Figure 5.14 shows the normalised spectrum in dB extracted from the data with the square pulse (blue) and the modulated Gaussian pulse (red). The resonant peak of the first element stands out after the bandpass. The characteristics of this peak lead to the following approximations: $Q_{01} \approx 22$ and $f_{\mathrm{res},01} \approx 132.3\,\mathrm{MHz}$.

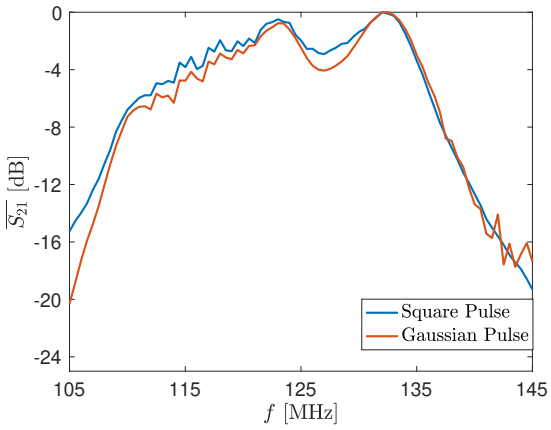

Figure 5.14: Normalised S_{21} spectrum as obtained from the square pulse data (blue) and the Gaussian pulse data (red).

The collected signal undergoes a series of postprocessing steps, which aim to enhance the identification of the reflection peak. These postprocessing steps are shown schematically in Fig. 5.15.

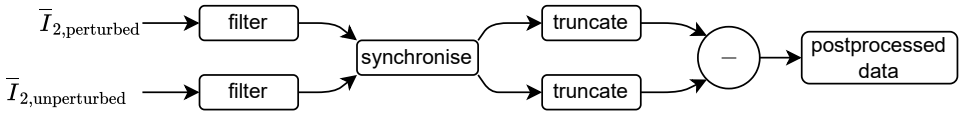

Figure 5.15: Postprocessing steps performed on the current collected at element 2.

The postprocessing aims to address two major sources of errors. The first source of error is noise, which is addressed by using a bandpass filter between 108.5 and 136.5

MHz, similar to [28]. The second source of error is the small time mismatch between the unperturbed array signal and the signal in the loaded array. In both cases, the first peak occurs at the first arrival of the pulse in the monitored element. When the signals are not synchronised over this time range, subtracting them leads to an artefact peak close to $t = 0$ s, which is described in detail in [28]. The magnitude of the isolated reflection decreases as the defect is placed further on the line or is moved vertically further away from the array, which results in the artefact becoming larger than the reflection. Synchronising the signals over the range where the pulse first reaches the monitored element is, therefore, necessary. This can be done by using the time-shifting property of the Fourier transform:

$$x(t - t_0) = \mathrm{e}^{-j\omega t_0} X(\omega). \tag{5.6}$$

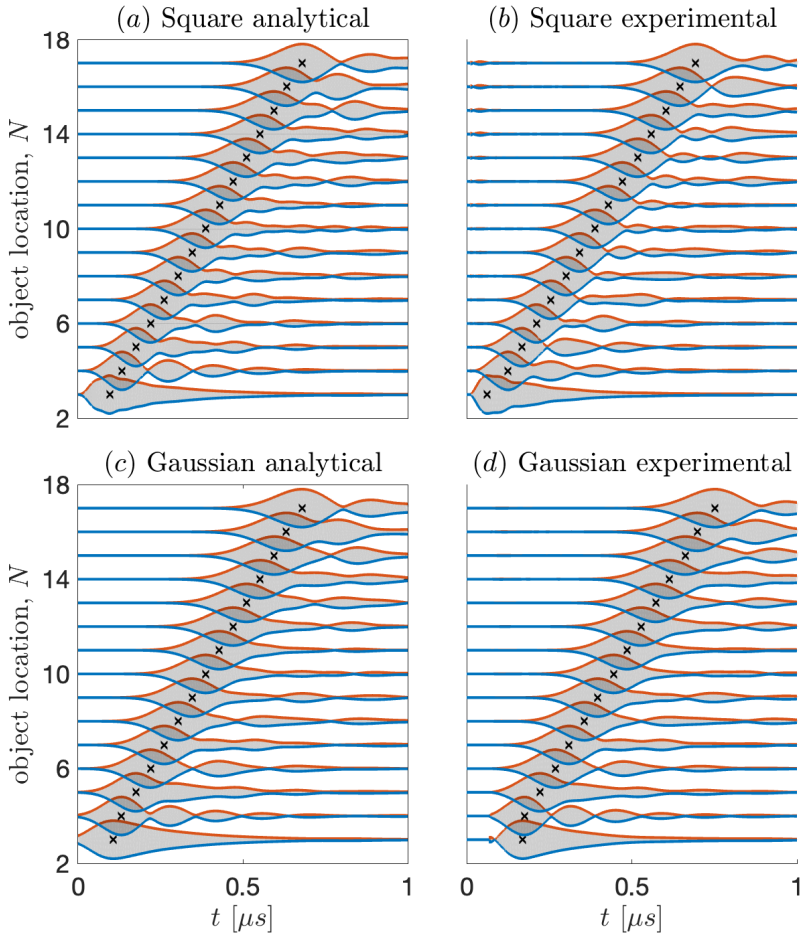

Figure 5.16: Comparison between experimental and analytical isolated reflections for multiple object locations at $h = 0$ mm. For each object location, identified on the y-axis, the normalised isolated reflection current is plotted.

The time delay is varied until the difference between the two signals over the range of interest is minimised. Truncating the signal over the range where reflection is expected is an additional method of addressing the presence of the artefact.

Figure 5.16 shows the isolated reflection when the object is placed on elements 3 to 17 at a vertical position of $h = 0$ mm for a square and a modulated Gaussian pulse. It can be seen that, after postprocessing, the resulting experimental reflections have a similar behaviour to those obtained analytically.

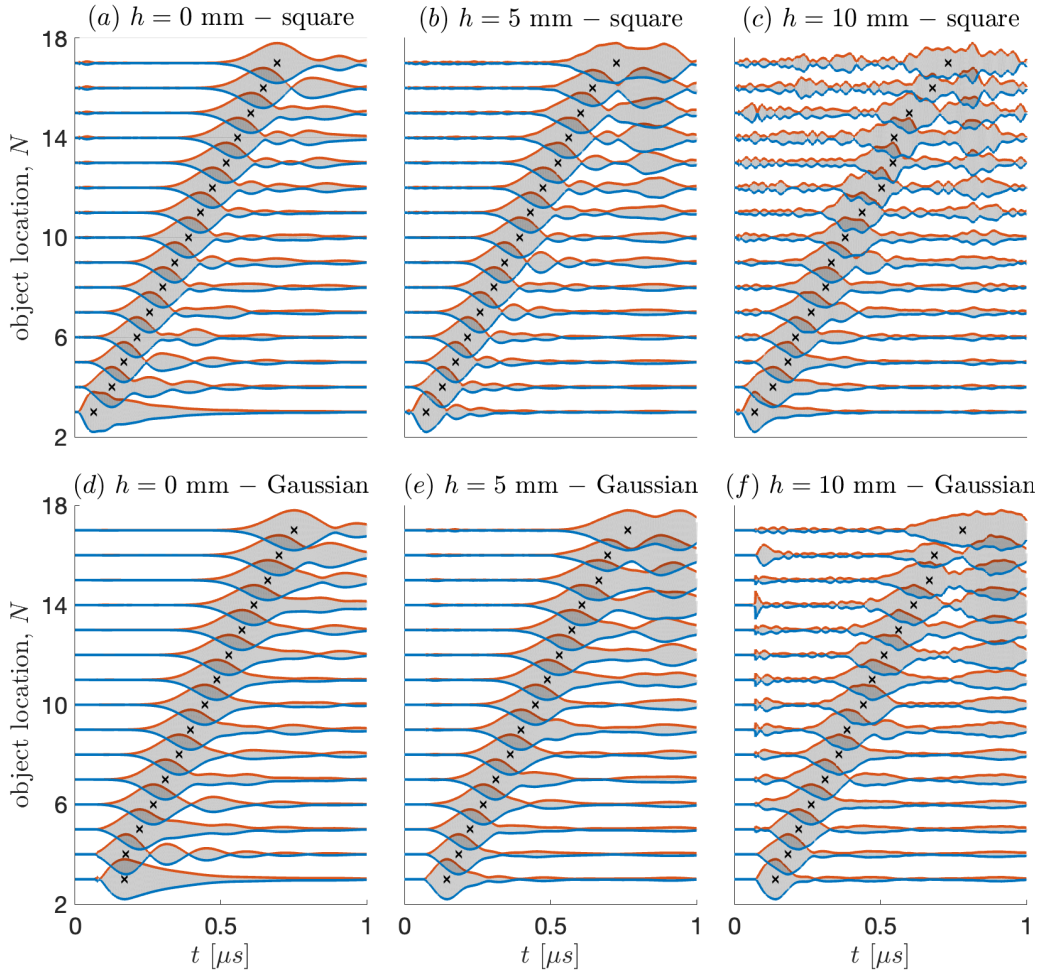

Figure 5.17: Isolated reflections for a square input signal (a) - (c) and for a modulated Gaussian signal (d) - (f) for multiple defect positions with heights $h = 0\,\text{mm}$, $h = 5\,\text{mm}$ and $h = 10\,\text{mm}$. For each object location, identified on the y axis, the normalised isolated reflection current is plotted.

The experimental isolated reflections are shown for both types of input signals in Fig. 5.17 for three different vertical positions: $h = 0\,\text{mm}$, $h = 5\,\text{mm}$ and $h = 10\,\text{mm}$. The signal is significantly less noisy for the modulated Gaussian input, which is expected as the excitation spectrum is stronger within the passband of the MI waves for this type of

input.

The data for $h = 0\,\text{mm}$ was used to evaluate the speed of signal propagation in the array. For the square pulse, the speed was found to be $v_S = 477\,\text{km/s}$, whilst for the modulated Gaussian pulse it was found to be $v_G = 485\,\text{km/s}$. These numbers are in line with the ones obtained experimentally and with the analytical group velocity values computed in Section 5.1.1. The error in localising the object's position on the array for different heights, computed as the Manhattan distance between the actual bolt position and the identified bolt position, is shown in Fig. 5.18 for a square pulse (a) and for a modulated Gaussian pulse (b). Almost perfect localisation is achieved up to $h = 10\,\text{mm}$. For the particular object used (i.e. the bolt), once the object height is larger than the size of an element in the 1D line, the interaction between the object and the cell is significantly weaker, and localisation is poorer. This height would become lower for objects with lower conductivity (such as a finger), which would interact in a much weaker manner with the array. In the modulated-Gaussian case, the situations where the method fails are linked to the inability of the postprocessing techniques to fully eliminate the artefact. It is, however, noteworthy that a measuring device with higher sampling rates could moderate this issue and improve localisation significantly. This is not the case for the square-wave input, whose failures can mostly be associated with the fact that the magnitude of the response is comparable to the noise within the pass band.

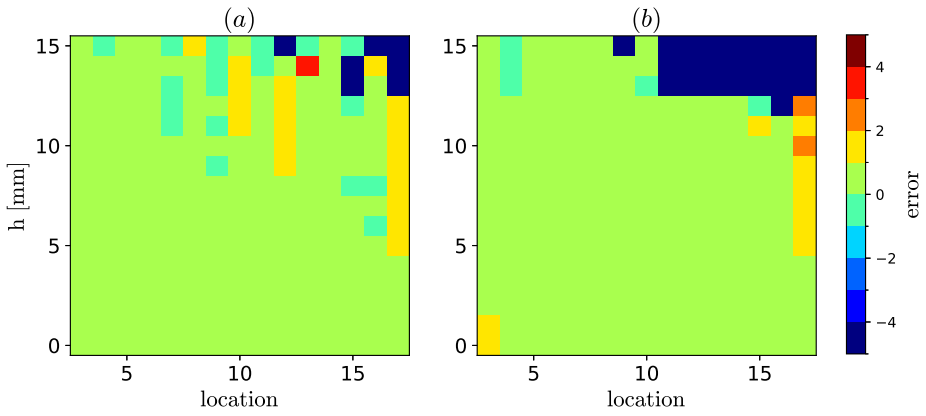

Figure 5.18: Distance between the actual position and the identified position of an object for a square input (a) and a modulated Gaussian input (b) as a function of object location, N, and height, h. Localisation was performed using the time-of-flight approach.

5.3.2 Machine learning localisation results

While the improvement demonstrated in Fig. 5.18 is significant, similarly to Chapter 5, these results can further be improved through the use of machine learning modelling. Monitoring the reflection peak is a robust localisation approach when the impact of noise and time delays is small. When the vertical distance between the object and the array is small (i.e. $h < 10$ mm), the reflection peak is larger than the experimental error, allowing for accurate localisation of the object. However, as the object is moved further away, these inaccuracies become comparable to the signal and significantly affect the performance of the algorithm. The limitation of the analytical time-of-flight approach appears because only the arrival time of the reflection peak (i.e. a single data point) is used for localisation. Correctly identifying this point is crucial for correct localisation. The neural network approach presented in Section 4.3 can bypass this issue by creating a model which allows for all data points in the vicinity of the arrival time of the maxima to be considered when deciding on a correct defect location. The width of the peak (which is small for false maxima caused by noise or time delays) can be accounted for, and results can be improved further.

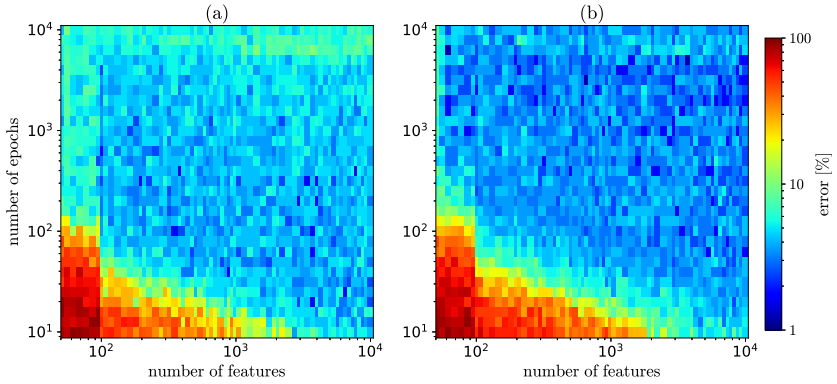

Figure 5.19: Error in localisation on the testing dataset as a function of the number of features and the number of iterations (epochs) for both a square input signal (a) and for a modulated Gaussian input (b).

The same neural network architecture presented in Section 4.3 is employed for localising an object based on the isolated time-domain reflection signal. The envelope of the isolated reflection was used as the input of the neural network. The number of points in this signal (10001) is significantly larger than the one in the frequency-domain signal

(1601) used in Chapter 4. Using all the points in the isolated reflection envelope would, therefore, lead to a much larger neural network, which would take a long time to train and would require more storage space. This problem can be addressed by sampling the time-domain data. Figure 5.19 shows the percentage of correctly labelled locations in the testing dataset as a function of the number of features and the number of iterations (epochs) for both a square input signal (a) and for a modulated Gaussian input (b). The dataset was split into a 1:3 training-to-testing ratio. The data for $h = 15$ mm was then included in the training dataset. This was done to ensure the training is performed on the entire range of interest [$h = (0 - 15)$ mm]. The training dataset contained the data for $h = 0,\ 4,\ 8,\ 12,\ 15$ mm, whilst the testing dataset contained all the other data points. The size of the hidden layer was set to $H = 100$ for all cases with more than 100 points, and to $H = 30$ otherwise. The optimal learning rate was found to be 5×10^{-4}. Figure 5.19 suggests that accurate localisation can be achieved when the number of points in the isolated reflection pulse exceeds 100 for the square pulse and exceeds 50 for the Gaussian pulse. There exists a trade-off between the number of input features of the neural network and the number of iterations performed during the training process. More features result in faster convergence, whilst fewer features converge more slowly, but allow for a more compact network, easier to store in off-the-shelf memory chips. Here, for optimal performance, 400 features were used for 200 iterations, which yielded a testing accuracy of 96.7% for the square pulse, and 97.6% for the Gaussian pulse.

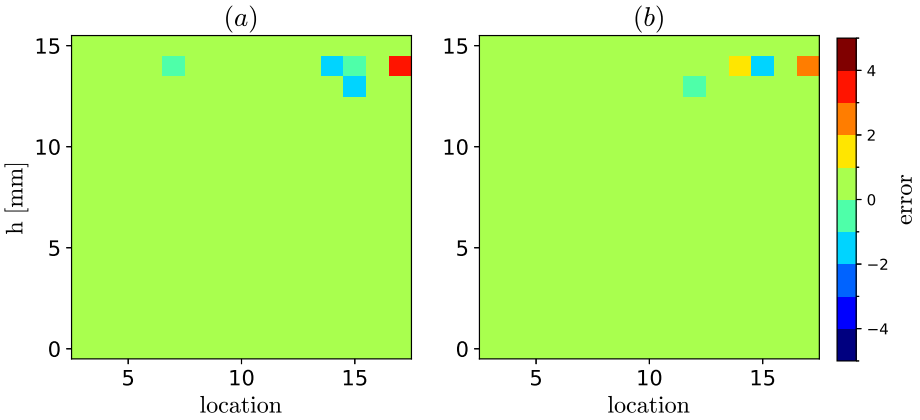

Figure 5.20: Distance between the actual position and the identified position of an object for a square input (a) and a modulated Gaussian input (b) as a function of object location, N, and height, h. Localisation was performed using a neural network.

Figure 5.20 shows the error distribution when using the square pulse (a) and the modu-

lated Gaussian pulse (b) as a function of object location and distance above the array. For both pulses, error-free localisation is achieved up to $h = 12\,\text{mm}$, significantly improving on the performance achieved using the time-of-flight localisation approach, presented in Fig. 5.18. Most importantly, the localisation achieved in Fig. 5.20 significantly improves upon the work of Yan et al. [18] and on the 1D array results presented in Chapter 4. In Chapter 4, the percentage of correctly identified locations on a 1D line was 91%, which increased to 98% for the time-domain reflectometry implementation. This confirms that time-domain reflectometry offers a stronger localisation approach, as its inherently localised changes make the method more robust and physically grounded.

5.3.3 Object characterisation results

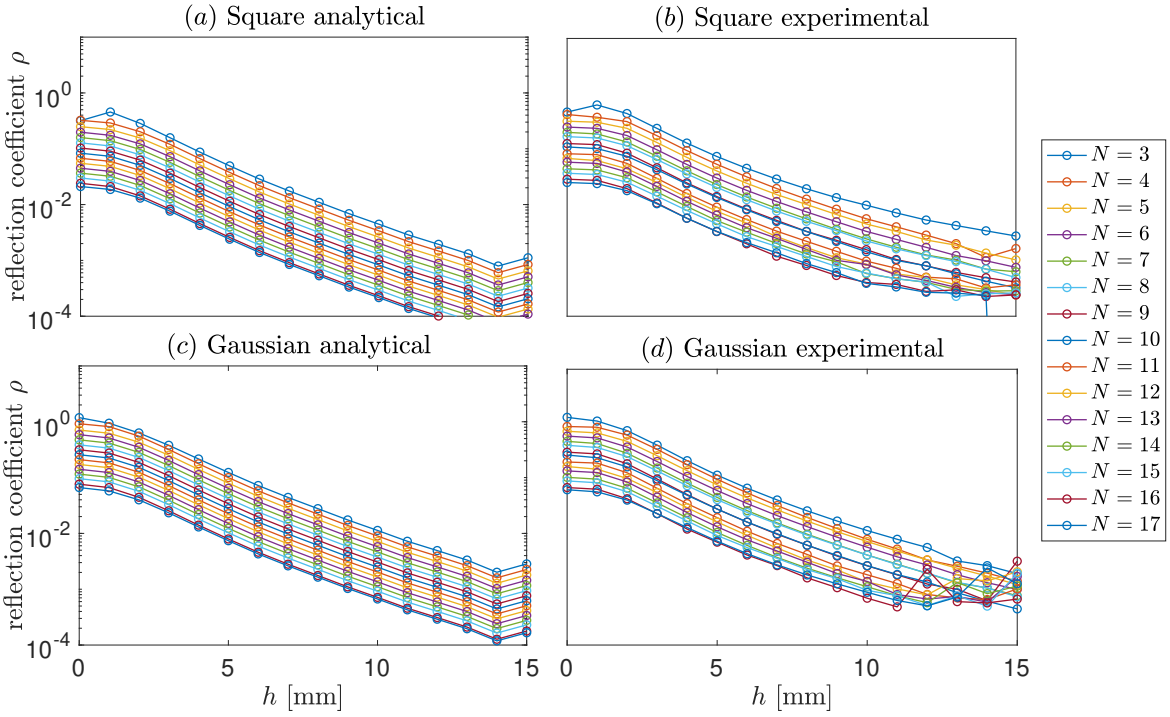

Figure 5.21: Analytical (a, c) and experimental (b, d) reflection coefficient as a function of vertical position for all object locations. Results are shown for an input square pulse (a, b) and for a Gaussian pulse (c, d).

As mentioned previously, from a time-domain perspective, the strength of the reflection can be used to determine the height of the object above the array. We refer to this step as characterisation, as in [28, 29]. Whilst the characterisation in this section focuses on object height estimation, the same principle can be applied to determine the conductivity of objects placed on arrays, provided a constant object height, h. Figure 5.21 shows the

variation of these reflection coefficients with height for different defect locations, N, both for a square and a modulated-Gaussian input wave.

Having found the position of the defect, one can compute the object's height by finding the closest analytical reflection coefficient for each experimental reflection coefficient. To ensure accuracy, prior knowledge of $h = 0\,\text{mm}$ data is assumed, and the reflection coefficients are normalised through it. The results obtained are shown in Fig. 5.22(a) for the square input and in Fig. 5.22(b) for the modulated Gaussian input. Accurate characterisation in terms of height is obtained up to 10 mm, which is the point where the localisation also deteriorates.

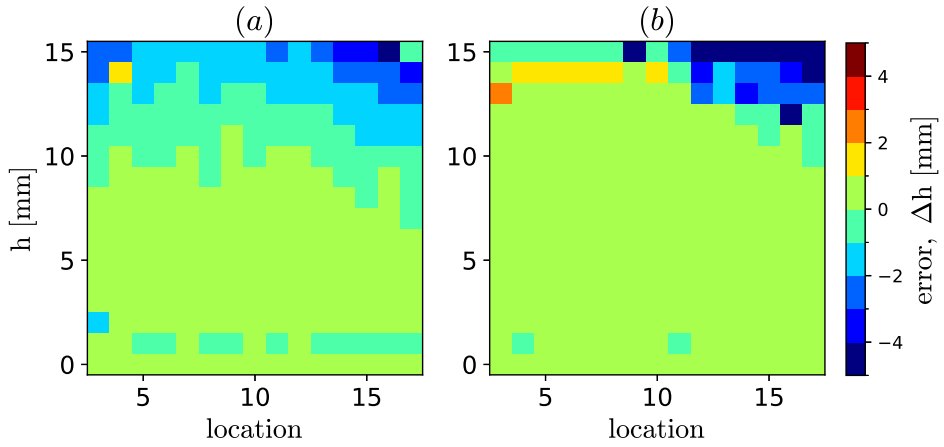

Figure 5.22: Distance between the actual vertical position of the object, h, and the identified one as a function of vertical object position, h, and object location, N. Results are shown for: (a) a square pulse and (b) a modulated Gaussian pulse. The results are computed using the reflection coefficient magnitude.

These characterisation results can further be improved through the use of a neural network, similar to the localisation presented in the previous section. In the characterisation case, a secondary hidden layer was added to the neural network described in 4.3. The full dataset was split in a 1:1 training-to-testing ratio, where the even object locations were used for training and the odd ones for testing. The location of the object was used as an additional feature. The optimal parameters of the neural network were computed by trial and error. The two hidden layer sizes were set to 500 and 100, respectively, the number of features in the input was 1001, and the learning rate was set to 4×10^{-4}. The number of iterations used in the training process was 5000. The testing accuracy for the square pulse was 80.4%, and for the modulated Gaussian pulse was 92%.

Figure 5.23 shows the error in identifying the height of the object as a function of object location and height, for the full dataset. The characterisation is significantly improved for both pulses, the modulated Gaussian one achieving error-free localisation for $h = 2 - 11$ mm. The machine learning method was trained directly on the isolated reflection, removing the need to normalise through the $h = 0$ mm point. This is an added benefit as less data must be stored for accurate localisation and characterisation.

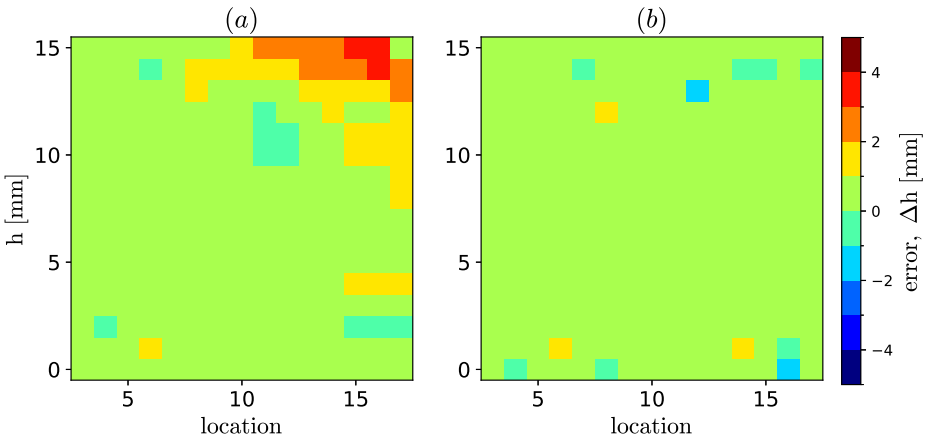

Figure 5.23: Distance between the actual vertical position of the object, h, and the identified one as a function of vertical object position, h, and object location, N. Results are shown for: (a) a square pulse and (b) a modulated Gaussian pulse. The results are computed using a neural network.

5.4 Discussion and conclusions

This chapter introduced and evaluated a technique for localising and characterising objects placed above a one-dimensional magnetoinductive array using time-domain reflectometry. The method is based on exciting the array with a short pulse and analysing the reflected signal to infer the presence and properties of an object. Two excitation types were compared – a square pulse and a modulated Gaussian. The modulated Gaussian was found to produce a clearer and more consistent response, particularly because its spectrum is centred around the resonant frequency of the array, resulting in stronger excitation of the system and cleaner reflections.

The experiments showed that the time-of-flight approach is effective when the object is up to 10 mm above the array, but its accuracy degrades for targets placed further away due to weaker reflections and increased overlap with background noise. To address

this, a neural network model was trained to perform localisation and regression on the time-domain response. The model achieved perfect localisation when the object was placed lower than 13 mm above the array, significantly extending the usable range. This is because the machine learning algorithm can extract more subtle patterns across the full time series that are otherwise hard to capture with peak-detection methods.

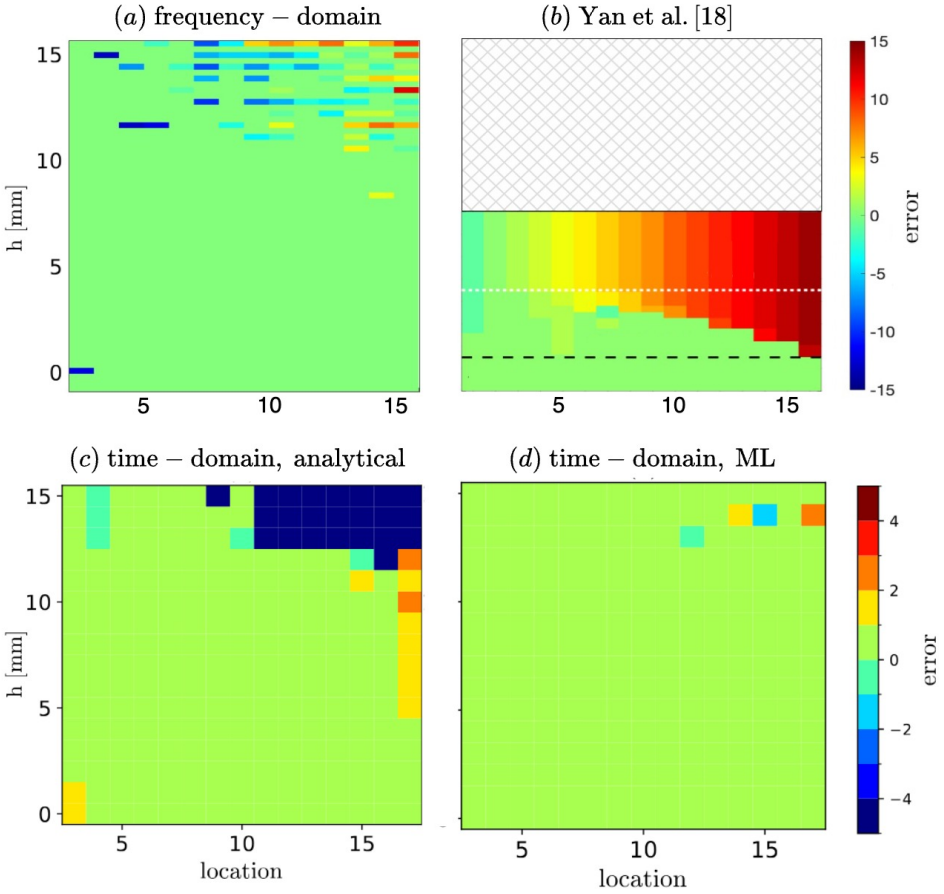

Figure 5.24: Comparison between four different localisation techniques using 1D MI arrays: (a) frequency-domain reflectometry used in Chapter 4, (b) work of Yan et al. (figure reproduced from [18]. Ref. [18] is licensed under a Creative Commons Attribution 4.0 License. ©2021 by J. Yan, C. J. Stevens, and E. Shamonina), (c) time-domain reflectometry based on the time-of-flight estimation, and (d) time-domain reflectometry combined with machine learning (ML).

These results represent a dramatic improvement over the Yan et al. [18] work and the 1D localisation performed in Chapter 4. Whilst 91% of locations were accurately identified on the 1D line in Chapter 4 using frequency-domain reflectometry, the localisation accuracy increased to 98% for the time-domain reflectometry case. The four methods used for localising objects on 1D arrays are summarised in Fig. 5.24. It is visually clear that the combination of machine learning and time-domain reflectometry outperforms all other

methods, as it combines the robust and localised physical changes of the time-domain approach with the powerful computational ability of the machine learning algorithm. In fact, the scales for the frequency-domain reflectometry and the method presented in Yan et al. [18] are different as the range of errors was wider.

The height of an object above the array was also determined using the time-domain reflectometry approach. Monitoring the magnitude of the reflections allowed for error-free height characterisation in the range $(0-8)$ mm. This range was further improved to $(3-11)$ mm through the use of a neural network. This finding means that a 1D MI array can not only localise an object, but it can also quantify the strength of interaction and infer one characteristic of the object (such as height, conductivity or permeability), provided that all other parameters are known or maintained as constant. Whilst in this chapter, characterisation was focused on height, the same principle can easily be translated to characterise conductivity or object geometry if the height is maintained constant or accurately known at all times.

These findings are especially promising for biomedical imaging. In Chapter 3, it was shown that a single coil could detect the presence of water in the lungs, with sensitivity to conductivity changes on the order of 0.3–0.9 S/m. Extending this to an array opens up the possibility of spatial localisation of anomalies such as tumours, which often produce localised changes in tissue conductivity or permittivity. A one-dimensional array may already offer some spatial resolution along a single axis, while extending the concept to two-dimensional arrays would enable full surface scanning, making real-time, non-invasive mapping of internal structures a potential long-term application.

Several areas for further research emerge. The array design itself can be tailored to increase sensitivity to specific electromagnetic properties, such as permittivity, which remains more difficult to detect with magnetically coupled systems. Operating at higher frequencies could also help, especially for detecting smaller features, although this would reduce penetration depth. Finally, moving from one- to two-dimensional arrays is a natural progression and would allow more complex imaging tasks, including real-time mapping of organs or identification of localised conductivity anomalies in soft tissues.

Overall, this chapter shows that magnetoinductive arrays have potential for non-invasive sensing and imaging, and that combining them with modern signal processing and machine learning tools can significantly expand their capabilities.

CHAPTER 6

Conclusions and outlook

This thesis develops novel inductive sensing techniques for remote localisation and characterisation of objects with unknown electromagnetic properties, specifically conductivity, permittivity, and permeability.

The sensors developed in this thesis are based on metamaterials – man-made structures which can exhibit unusual electromagnetic properties due to their subwavelength structuring. The basic building block of a metamaterial is the meta-atom, a resonant element smaller than the wavelength of the electromagnetic radiation, which can respond strongly to surrounding electric and magnetic fields. In this thesis, the focus is placed on magnetic metamaterials comprising circular resonators that can be modelled as LCR circuits. Two types of sensors are presented: a localised, single-resonator-based sensor and a distributed sensor implemented through a metamaterial array. Both 1D and 2D arrays are studied. Through a combination of analytical modelling, numerical simulations, and experimental validation, this work demonstrates the capabilities and limitations of these sensing strategies.

The core principle underpinning the sensing techniques is the interaction between an excited magnetic resonator and a material with different electromagnetic properties. When a resonator (referred to as split-ring resonators or SRRs throughout this thesis) is placed near a conductive, dielectric, or magnetic material, the electromagnetic fields generated by the resonator interact with the sample, causing changes in its resonant behaviour. The changes induced in the resonant characteristics can be used to draw conclusions about the electromagnetic properties of an object and its relative location with respect to the resonator. The interaction between the sample and the resonator occurs without direct contact, which is a key characteristic and benefit of electromagnetic techniques with practical applications in non-invasive medical diagnosis, quality control, or concealed object detection.

Chapter 1 provides an introduction to the field of metamaterial research, providing the theoretical foundation used in subsequent chapters. Starting from the description of SRRs and their interaction, Chapter 1 then introduces the concept of magnetoinductive (MI) waves (slow waves of inter-element coupling) propagating along magnetic metamaterials via magnetic induction between resonators, and derives dispersion characteristics for MI waves in 1D and 2D arrays.

Chapter 2 develops an analytical model, describing the response of a single circular resonator to nearby conductive, magnetic and dielectric materials. The developed framework is based on the Dodd and Deeds model [16]. It involves the analytical calculation of the vector potential in a stratified medium, which includes a layer with the test sample and a circular probe whose resonant response is affected by the sample. The analytical solution is formulated by solving a partial differential equation (PDE), derived from Maxwell's equations [60], for the vector potential of the system. Solving the PDE requires employing boundary conditions for the electric and magnetic fields at each of the interfaces of the stratified model. After computing the vector potential, the new self-inductance of the resonator is calculated by approximating it as a system of two coupled resonators placed a geometric mean distance (GMD) apart [61].

The model developed in Chapter 2 expands significantly upon the original model by

Dodd and Deeds in a number of ways. Firstly, the model can be used to translate the changes in self-inductance of a resonator placed near a sample to changes in its resonant characteristics: f_{res} and Q. This extends the method developed by Dodd and Deeds to metamaterial-based sensors, which, due to their resonant properties, exhibit a heightened sensitivity. Secondly, the model developed avoids simplifying assumptions in the original formulation by Dodd and Deeds [16], which limited its validity to low frequencies where the impact of permittivity is negligible, and, originally, to studies of conductivity only. In our model, retaining all the terms allows for accurate low-conductivity detection, as it was found that the permittivity term, often omitted in prior literature, becomes more relevant in this conductivity range.

Our analytical model enables analysis of the proposed sensor's ability to determine conductivity, permeability and conductivity. The changes in the resonant frequency f_{res} and quality factor Q are analysed for different system parameters: electromagnetic properties and thickness of the sample, free-space resonant frequency, radius of the resonator, and the distance between the resonator and the testing material. It was found that for low (< 10 S/m) and high conductivities ($> 10^6$ S/m), Q changes more abruptly with σ and is therefore a more significant parameter to monitor when attempting to measure conductivity. For mid-range conductivities (≥ 10 S/m, $\leq 10^6$ S/m), f_{res} changes more abruptly with σ, meaning that f_{res} is better suited for conductivity detection in this case. Conductivity and permeability extraction is then successfully simulated by adding artificial noise to the analytical data, which analytically validates the proposed detection method. Chapter 2 also offers design guidance for conductivity and permeability detection. Permittivity is discussed briefly in this chapter, however, given its interaction is mainly with electric fields, the magnetic fields from the coil do not generate a strong enough response to justify permittivity detection.

In **Chapter 3**, the single-resonator probe analytically designed in Chapter 2 is used experimentally to determine the conductivity of saline solutions and to perform a numerical feasibility study on the probe's ability to detect the presence of fluid in lungs. Firstly, the probe designed using the principles developed in Chapter 2 was built and

tested using a saline solution. Conductivity was gradually increased in the range 0–20 S/m. The conductivity of the solution was estimated using the analytical model with a mean error of 5.5%. These results were compared with CST Studio Suite numerical simulation results. Using linear interpolation within the CST data resulted in extraction with a 9.7% mean error. The analytical model outperformed the numerical simulations and detected eleven very low conductivities, similar to those of the human body.

Considering the proposed sensor's non-invasiveness and its ability to sense low conductivities, a natural application of the proposed sensor is biomedical monitoring. In Chapter 2, this application is assessed by analysing whether the sensor can identify the presence of fluid in lungs in simulation. The analysis is performed numerically using CST Studio Suite and a phantom body model described in [152, 153]. The electromagnetic parameters of the body model tissues are calculated using the Cole-Cole model [129], and the parameters provided by Gabriel et al. [126–128]. Four different lung states were considered: inflated healthy lung, deflated healthy lung, inflated infiltrated lung, and deflated infiltrated lung. The probe's changes in f_{res} and Q are compared with the instrumental error of a standard VNA, and it is concluded that a 50 MHz single split-ring resonator has the potential to detect the presence of fluid in lungs. Contrary to the belief that penetration depth should be maximised for increased interaction with the human body, a 50 MHz resonator, which only partially penetrates the lungs, can avoid interaction with the heart, the most conductive human organ, and enhance sensitivity to changes in the lung. Four coil radii were tested: 50 mm, 100 mm, 150 mm and 200 mm. It was found that, when the diameter of the probe is the width of one lung ($\approx$ 100 mm), the changes in f_{res} and Q are the most dramatic because the tracks of the probe are closer to the sample. The probe of 100 mm radius exhibited the most consistent variation in f_{res} between the different lung states, but the smallest variations in Q, as it achieved saturation for lower conductivities due to its proximity to the lungs. It is concluded that the 150 mm coil (which exhibits relatively strong changes both in f_{res} and Q) and the 100 mm coil (which exhibits a strong, reliable response in f_{res}) are the best alternatives in the considered system. It is important to note that the body phantom used in this work was modelled on an individual with obesity, resulting in thicker layers of fat com-

pared to a person with a lower body mass index (BMI). This suggests that smaller coil radii could be used for individuals with lower body fat, which would be advantageous for sensor design. In particular, smaller resonators would facilitate the development of a distributed sensor array composed of multiple elements. Such an array could enable more precise localisation of defects, the detection of multiple abnormalities simultaneously, and, ultimately, contribute toward a low-cost, remote human-body imaging technique.

The changes in the conductivity of the lungs are calculated based on a 50% fluid infiltration, which would correspond to a serious medical emergency. However, this extreme scenario is counterbalanced by the assumption that the heart is in its diastolic phase (i.e. filled with blood, hence at its peak conductivity). In reality, the impact of the heart varies with time and is less significant than in this study.

The analysis of distributed sensors in 1D and 2D using frequency-domain reflectometry is explored in **Chapter 4**. MI arrays are used to localise and characterise objects in a remote fashion. The principle of operation is strongly linked to the findings in Chapter 2; when an object is placed in the proximity of the array, the resonant response of the tile immediately underneath is altered. This resonator becomes a partial defect in the array, which scatters an incoming monochromatic MI wave, resulting in a different standing wave pattern, depending on the properties of the defect. This interaction changes the input impedance of the array. The advantage of this method is the ability to monitor any changes in the array through a dual excitation-measurement port (an S_{11} port) connected to a VNA. We expand on the work of Yan et al. [18] who proposed a method for localising objects on a 1D MI array using the changes in the relative position of peaks in the input impedance spectrum of the array. A neural network with a single hidden layer is then developed to analyse the changes in the input impedance spectra caused by the presence of an object. This algorithm was chosen as it can model small, non-linear variations. Other algorithms considered were either unable to model non-linear changes (linear regression), had higher inference times after model training (gradient boosted trees) or were too complex for the limited amount of experimental data available (convolution neural network). A dramatic improvement in the operating range of the

sensor was achieved. Whilst Yan et al. [18] successfully localised objects placed up to 1.5 mm above the array only analytically, using our model extended this range to 10 mm for experimentally obtained data. After confirming the efficacy of the algorithm in the 1D case, Chapter 4 moves on to 2D arrays of resonators, successfully localising samples of different materials and sizes with an accuracy (calculated as the percentage of correctly identified locations) over 98% for objects placed up to 10 mm above the array. The algorithm was also adapted to accurately differentiate between different objects with an accuracy of over 97%. A real-time system which tests the real-life feasibility of the sensor is also implemented. The neural network model trained for the bolt is stored and used to localise the bolt in real-time for positions slightly misaligned from the original presented data. Out of 14 tested positions, 13 are localised successfully, which demonstrates the practical value of the method. Two-defect localisation is achieved successfully for identical defects, placed on top of the array at the same height, thus validating the potential of the method for more complex systems.

The last part of Chapter 4 focuses on localising a low-conductivity object, which mimics a human finger. The purpose of this section is to discuss the potential of this method for touchscreen array technologies. A different surface, more sensitive to dielectric materials due to its higher frequency and open-ended resonator terminations, is used to leverage the high permittivity of human tissue. The phantom finger, modelled as a glove filled with saline solution, was localised with a 99% accuracy for heights up to 15 mm above the array.

Chapter 5 extends the object localisation on MI waves by developing a time-domain approach. Whilst the frequency-domain method presented in Chapter 4 is robust and successful in localising and characterising objects, the behaviour of the neural network algorithm is difficult to interpret: we do not know exactly what features are modelled and whether they are related to the physical behaviour of the system or to environmental noise. Chapter 5 proposes an improved localisation method, which better leverages the system's physical characteristics. In the time domain, when a pulse is injected in the first element of a 1D array, the MI wave is reflected by the partial defect created by the

object, and travels back. This reflection can be isolated by monitoring the current in the second element. The travelling time of the pulse, linked to the travelled distance and, hence, the defect location, can be measured and used to localise the object. The strength of the reflection is also leveraged to infer the object's characteristics, such as its height. The main advantage of this method is that the change is localised in time, yielding a more robust, trackable change. Two pulse shapes were trialled, and two methods – an analytical one based on time-of-flight and a neural network – are used for localisation. The modulated Gaussian pulse yielded stronger reflections than the square pulse because of its larger spectral components within the MI passband. The analytical localisation method based on the time-of-flight of the pulse achieved accurate localisation for objects placed up to 12 mm above the array and up to 16 tiles away from the excitation. The errors associated with this approach are linked to the fact that a single point, subject to experimental noise and time delays, is used to localise an object. In this case, a machine learning algorithm can be used to bridge the gap and account for multiple points in the range of interest, where the reflection occurs. A neural network can accurately predict the localisation of objects placed up to 12 mm above any resonant element. This is a significant improvement over the results in Yan et al. [18] and also over the ones presented in Chapter 4 for the 1D line. The percentage of correctly labelled locations has increased from 91% to 98%, supporting the fact that the time-domain reflectometry is, at least in the 1D case, a more reliable way of localising objects than the frequency-domain reflectometry. We also performed object characterisation through two different methods: an analytical method based on the reflection strength generated by the object and a machine learning model. Using the analytical method resulted in an error-free object height characterisation in the range $3-8$ mm, whilst the machine learning model expanded this range to $3-11$ mm. While characterisation refers directly to determining the height of the object above the array in the chapter, the same principles can be employed to characterise other object properties, such as conductivity or size. To determine the conductivity of an object, the size of the object and its position above the array must be known and maintained constant for a single parameter, which determines the strength of interaction to be varied at a time.

In Chapters 4 and 5, it was found that both frequency-domain and time-domain reflectometry are possible ways of localising objects on metamaterial arrays. Time-domain reflectometry outperforms frequency-domain reflectometry for a one-dimensional array due to the time-localised nature of the reflection pulse. Since the position of the pulse in time only depends on the characteristics of the array, it is relatively easy to model the pulse behaviour analytically and predict the defect location. On the other hand, the changes in the frequency domain are subtler and more complicated to predict analytically. A machine learning algorithm can successfully track these changes and predict the location. The disadvantage of using the machine learning algorithm is the lack of transparency and the inability to predict when and why the algorithm has failed. In real-life applications, this translates to a need for more quality control before deploying the product, which can be expensive and time-consuming. However, for two-dimensional arrays, frequency-domain localisation is a more successful solution. The complexity of the algorithm does not increase significantly when moving into two dimensions due to the versatility of the machine learning approach. The same is not true for the time-domain reflectometry case. Adding a secondary dimension means that the pulse is no longer localised on a single travelling direction and that multiple reflections can occur from all the surface edges, as opposed to a single reflection from the defect and one from the array end. This makes the problem more complex and means that it is no longer possible to track the reflection from the object independently. Different techniques can be employed to enable localisation in two dimensions using time-domain reflectometry. The first approach utilises a machine learning algorithm to map changes onto object locations. However, due to the connection between the time domain and the frequency domain, this is identical to the frequency domain method presented in this thesis. Grading the resonant frequency of the tiles in the surface, such that the pulse spread is larger and the location of the defect is more easily identified, is another possible way to approach this. Yet another method is using two excitation sources in various configurations to maximise the impact of the object. All these methods are areas of further research which could improve upon the results obtained using the frequency domain reflectometry. A significant difference between the two methods is the required hardware equipment. The frequency

domain localisation requires a Vector Network Analyser (VNA), whilst the time domain localisation requires a signal generator and an accurate oscilloscope with time steps in the ns range. The hardware required for time domain reflectometry is more widely available and usually cheaper. However, the accuracy requirement restricts the implementation of the method using cheap oscilloscopes, as time delays affect the results significantly. On the other hand, whilst VNAs are usually more expensive, the frequency domain method is resilient to noise and can be implemented using fewer than 801 frequency points, as shown in Chapter 4. This means that newly developed nanoVNAs [192] could be used to implement the solution compactly and inexpensively. However, further research must be conducted to assess the accuracy of the method when using a nanoVNA.

In summary, this thesis has demonstrated that inductive meta-atoms and arrays can be used effectively for both material characterisation and object localisation. Resonators enable remote, non-contact detection of electromagnetic properties such as conductivity and permeability, with potential applications in biomedical diagnostics, non-destructive testing, and structural health monitoring. Arrays of strongly coupled resonators, supporting MI waves, allow the precise localisation and identification of conductive or dielectric objects, opening pathways toward applications in security screening, defect detection in industrial components, and low-cost human-body imaging technologies. Furthermore, the integration of machine learning has emerged as a powerful tool for interpreting complex, non-linear interactions that are difficult to model analytically, enhancing both localisation accuracy and object characterisation capabilities. Together, these advances demonstrate that resonant inductive systems provide a sensitive, flexible platform for a wide range of sensing and monitoring applications.

Several directions for further research emerge from this thesis. First of all, in relation to the single resonator sensing probe, extending the analytical model developed in Chapter 2 to finite-sized samples would offer more insight into complex systems and allow for its usage as a detection tool for much smaller samples.

For the lung monitoring system proposed in Chapter 3, the next immediate steps in developing the probe involve varying the resonator's resonant frequency and performing

simulations for lungs with a lower percentage of fluid infiltration. Trialling other types of resonators might also prove to be fruitful. We propose rectangular coils and pancake coils as strong candidates, which can interact strongly with the human body. Experimental testing on body phantoms is essential for validating any analytically or numerically drawn conclusion. The tissue monitoring sensor can be further developed by using a distributed array of resonators, which might be able to localise body abnormalities, such as tumours, more accurately than a single resonant element.

For the frequency-domain, the localisation platform developed in Chapter 4, can be extended by increasing the size of the array. This would make the sensor more suitable for applications where more than 35 locations are present (such as a touchscreen array). Further work could identify the limit on the array size and focus on interstitial positions within the array which were not explored in this thesis.

For the time-domain reflectometry, developed in Chapter 5, the method could be extended to a 2D MI array to assess if the location of the reflected pulses is still trackable. A new 1D array, capable of stronger interactions with dielectric materials, could be used for biomedical imaging after performing feasibility tests on human body phantoms. As in the case of the frequency domain, determining the limitation on array size is also an important factor for practical deployment of the system.

Finally, real-world deployment of all the techniques and sensors proposed throughout this thesis would benefit from further miniaturisation, improved calibration techniques, and the development of lightweight, low-power electronics for signal processing.

While several challenges remain, this work provides a strong foundation for developing practical electromagnetic sensing systems for biomedical and industrial applications. The results reinforce the promise of combining physics-driven models with data-driven methods to achieve sensitive, versatile, and intelligent sensors.

Bibliography

[1] Y. Das, "Effects of soil electromagnetic properties on metal detectors," *IEEE Trans. Geosci. Remote Sens.*, vol. 44, 1444, 2006.

[2] C. V. Nelson, "Metal detection and classification technologies," *Johns Hopkins APL Tech. Dig.*, vol. 25, 62, 2004.

[3] R. H. Gilkeson, S. R. Gorin, D. E. Laymon, "Application of magnetic and electromagnetic methods to metal detection," in *Proc. Symp. Appl. Geophys. Eng. Environ. Probl. (SAGEEP 1992)*, 309, 1992.

[4] E. Ramsden, *Hall-Effect Sensors: Theory and Application*. Elsevier, Oxford, 2011.

[5] M.-A. Paun, J.-M. Sallese, M. Kayal, "Hall effect sensors design, integration and behavior analysis," *J. Sens. Actuator Netw.*, vol. 2, 85, 2013.

[6] R. Popović, "Hall-effect devices," *Sens. Actuators A Phys.*, vol. 17, 39, 1989.

[7] J. A. Zhang, F. Liu, C. Masouros, *et al.*, "An overview of signal processing techniques for joint communication and radar sensing," *IEEE J. Sel. Topics Signal Process.*, vol. 15, 1295, 2021.

[8] S. Ahmed, K. D. Kallu, S. Ahmed, *et al.*, "Hand gestures recognition using radar

sensors for human-computer-interaction: A review," *Remote Sens.*, vol. 13, 527, 2021.

[9] J. A. Richards, *Remote Sensing with Imaging Radar*. Springer, Berlin, 2009.

[10] B. J. Roth, "The magnetocardiogram," *Biophys. Rev.*, vol. 5, 021305, 2024.

[11] D. Brisinda, P. Fenici, R. Fenici, "Clinical magnetocardiography: The unshielded bet—past, present, and future," *Front. Cardiovasc. Med.*, vol. 10, 1232882, 2023.

[12] A. L. Fred, S. N. Kumar, A. Kumar Haridhas, *et al.*, "A brief introduction to magnetoencephalography (meg) and its clinical applications," *Brain Sci.*, vol. 12, 788, 2022.

[13] V. P. Grover, J. M. Tognarelli, M. M. Crossey, *et al.*, "Magnetic resonance imaging: principles and techniques: Lessons for clinicians," *J. Clin. Exp. Hepatol.*, vol. 5, 246, 2015.

[14] M. Cheney, D. Isaacson, J. C. Newell, "Electrical impedance tomography," *SIAM Rev.*, vol. 41, 85, 1999.

[15] C. V. Dodd, J. Luquire, W. Deeds, *et al.*, "Some eddy-current problems and their integral solutions," tech. rep., Oak Ridge National Lab., Tenn., 1969.

[16] C. Dodd, W. Deeds, "Analytical solutions to eddy-current probe-coil problems," *Int. J. Appl. Phys.*, vol. 39, 2829, 1968.

[17] Dassault Systèmes, Darmstadt, Germany, *CST Studio Suite*, 2020.

[18] J. Yan, C. J. Stevens, E. Shamonina, "A metamaterial position sensor based on magnetoinductive waves," *IEEE Open J. Antennas Propag.*, vol. 2, 259, 2021.

[19] T. Trivedi, Y. Chen, I. A. Williamson, *et al.*, "Group velocity estimation and defect localization in magneto-inductive waveguides," *IEEE Trans. Microw. Theory Techn.*, vol. 69, 2072, 2021.

[20] G. Dima, A. Radkovskaya, L. Solymar, *et al.*, "Inductive sensing of lung conductivity for fluid accumulation detection," in *Proc. 19th Int. Congr. Artif. Mater. Novel Wave Phenom. (Metamaterials 2025)*, 2025. under review.

[21] G. Dima, C. Stevens, H. Dai, "Neural network based remote localiser for two objects," in *Proc. 19th Int. Congr. Artif. Mater. Novel Wave Phenom. (Metamaterials 2025)*, 2025. under review.

[22] G. Dima, C. J. Stevens, "Spatial localisation and sensing in two dimensions via metasurfaces," *Sci. Rep.*, vol. 14, 24156, 2024.

[23] G. Dima, I. Spanos, C. J. Stevens, "2D localisation using magneto-inductive waveguides," in *Proc. 18th Int. Congr. Artif. Mater. Novel Wave Phenom. (Metamaterials 2024)*, 2024.

[24] G. Dima, C. McMahon, A. Radkovskaya, *et al.*, "Time-domain reflectometry for imaging conductive environment," in *Proc. 18th Int. Congr. Artif. Mater. Novel Wave Phenom. (Metamaterials 2024)*, 2024.

[25] G. Dima, A. Radkovskaya, C. J. Stevens, *et al.*, "Design of a remote, multi-range conductivity sensor," *Sensors*, vol. 23, 9711, 2023.

[26] G. Dima, A. Radkovskaya, C. Stevens, *et al.*, "Full-range contactless conductivity detection," in *Proc. 16th Int. Congr. Artif. Mater. Novel Wave Phenom. (Metamaterials 2022)*, 128, 2022.

[27] X. Li, G. Dima, A. Radkovskaya, *et al.*, "Neural network-based conductivity imaging using time-domain reflectometry," in *Proc. 19th Int. Congr. Artif. Mater. Novel Wave Phenom. (Metamaterials 2025)*, 2025. under review.

[28] D. Dhayaa, C. Long, A. Radkovskaya, *et al.*, "Sensing using magnetoinductive waves," in *Coupled Structures for Microwave Sensing*, 427, Springer, Cham, 2024.

[29] C. Long, A. Radkovskaya, G. Dima, *et al.*, "Metamaterials for characterisation of conductive objects using time-domain reflectometry of magnetoinductive waves," in *Proc. 17th Int. Congr. Artif. Mater. Novel Wave Phenom. (Metamaterials 2023)*, 205, 2023.

[30] D. Dhayaa, A. Radkovskaya, J. Yan, *et al.*, "Metamaterials for sensing conductive objects using time-domain reflectometry of magnetoinductive waves," in *Proc. 16th Int. Congr. Artif. Mater. Novel Wave Phenom. (Metamaterials 2022)*, 125, 2022.

[31] D. Smith, W. Padilla, D. Vier, *et al.*, "Composite medium with simultaneously negative permeability and permittivity," *Phys. Rev. Lett.*, vol. 84, 4184, 2000.

[32] A. Schuster, *An Introduction to the Theory of Optics.* Edward Arnold, London, 1904.

[33] V. Veselago, "The electrodynamics of substances with simultaneously negative values of ε and μ," *Usp. fiz. nauk.*, vol. 92, 517, 1967.

[34] W. Rotman, "Plasma simulation by artificial dielectrics and parallel-plate media," *IEEE Trans. Antennas Propag.*, vol. 10, 82, 1962.

[35] J. Pendry, A. Holden, W. Stewart, *et al.*, "Extremely low frequency plasmons in metallic mesostructures," *Phys. Rev. Lett.*, vol. 76, 4773, 1996.

[36] G. Thompson, "Unusual waveguide characteristics associated with the apparent negative permeability obtainable in ferrites," *Nature*, vol. 175, 1135, 1955.

[37] J. Pendry, A. Holden, D. Robbins, *et al.*, "Magnetism from conductors and enhanced nonlinear phenomena," *IEEE Trans. Microw. Theory. Tech.*, vol. 47, 2075, 1999.

[38] B. Wang, K. Teo, T. Nishino, *et al.*, "Experiments on wireless power transfer with metamaterials," *Appl. Phys. Lett.*, vol. 98, 254101, 2011.

[39] N. Landy, D. Smith, "A full-parameter unidirectional metamaterial cloak for microwave," *Nat. Mater.*, vol. 12, 25, 2012.

[40] Z. J. Wong, Y. Wang, K. O'Brien, *et al.*, "Optical and acoustic metamaterials: superlens, negative refractive index and invisibility cloak," *J. Opt.*, vol. 19, 84007, 2017.

[41] E. Shamonina, L. Solymar, "Superdirectivity by virtue of coupling between meta-atoms," in *Proc. 17th Int. Cong. Artif. Mater. Novel Wave Phenom. (Metamaterials 2023)*, 97, IEEE, 2013.

[42] T. Chen, S. Li, H. Sun, "Metamaterials application in sensing," *Sensors*, vol. 12, 2742, 2012.

[43] W. Xu, L. Xie, Y. Ying, "Mechanisms and applications of terahertz metamaterial sensing: a review," *Nanoscale*, vol. 9, 13864, 2017.

[44] D. Prakash, others, "Applications of metamaterial sensors: a review," *Int. J. Microw. Wirel. Technol.*, vol. 14, 19, 2022.

[45] N. S. Kumar, P. Banerjee, "A review on metamaterials for device applications," *Crystals*, vol. 11, 518, 2021.

[46] W. Zhang, others, "Terahertz metamaterials for biosensing applications," *Biosensors*, vol. 14, 3, 2023.

[47] M. R. Islam, M. T. Islam, others, "Metamaterial sensor based on rectangular enclosed adjacent triple circle split ring resonator with good quality factor for microwave sensing application," *Sci. Rep.*, vol. 12, 6792, 2022.

[48] M. H. Khalid, others, "A dual-band metamaterial sensor for nondestructive evaluation of dielectric materials," *IEEE Access*, vol. 10, 75416, 2022.

[49] H. Chen, others, "Dual-mode metamaterial biosensor based on split ring resonators for detecting glucose," *Opt. Express*, vol. 20, 7728, 2012.

[50] H.-H. Lee, others, "Non-invasive wearable metamaterial sensor for continuous monitoring of glucose concentration," *IEEE Trans. Microw. Theory Tech.*, vol. 65, 5304, 2017.

[51] D. M. Pozar, *Microwave Engineering: Theory and Techniques*. John Wiley & Sons, Singapore, 2021.

[52] Z. Ma, *RF Properties of High-Temperature Superconducting Materials*. Stanford University, Stanford, 1995.

[53] P. J. Petersan, S. M. Anlage, "Measurement of resonant frequency and quality factor of microwave resonators: Comparison of methods," *J. Appl. Phys.*, vol. 84, 3392, 1998.

[54] R. W. Schafer, "What is a Savitzky-Golay filter? [lecture notes]," *IEEE Signal Process. Mag.*, vol. 28, 111, 2011.

[55] M. U. Bromba, H. Ziegler, "Application hints for Savitzky-Golay digital smoothing filters," *Anal. Chem.*, vol. 53, 1583, 1981.

[56] S. R. Krishnan, C. S. Seelamantula, "On the selection of optimum Savitzky-Golay filters," *IEEE Trans. Signal Process.*, vol. 61, 380, 2012.

[57] E. Shamonina, V. Kalinin, K. Ringhofer, *et al.*, "Magnetoinductive waves in one, two, and three dimensions," *Int. J. Appl. Phys.*, vol. 92, 6252, 2002.

[58] L. Solymar, E. Shamonina, *Waves in Metamaterials*. Oxford University Press, Oxford, 2009.

[59] F. Hesmer, E. Tatartschuk, O. Zhuromskyy, *et al.*, "Coupling mechanisms for split ring resonators: Theory and experiment," *Phys. Status Solidi B.*, vol. 244, 1170, 2007.

[60] J. C. Maxwell, *Electricity and Magnetism*. Dover, New York, 1954.

[61] E. B. Rosa, F. W. Grover, *Formulas and Tables for the Calculation of Mutual and Self-Inductance*. US Government Printing Office, Washington, 1948.

[62] C. Akyel, S. Babic, M.-M. Mahmoudi, "Mutual inductance calculation for non-coaxial circular air coils with parallel axes," *Prog. Electromagn. Res.*, vol. 91, 287, 2009.

[63] K.-B. Kim, E. Levi, Z. Zabar, *et al.*, "Mutual inductance of noncoaxial circular coils with constant current density," *IEEE Trans. Magn.*, vol. 33, 4303, 1997.

[64] O. Sydoruk, A. Radkovskaya, O. Zhuromskyy, *et al.*, "Tailoring the near-field guiding properties of magnetic metamaterials with two resonant elements per unit cell," *Phys. Rev. B Condens. Matter*, vol. 73, 224406, 2006.

[65] P. Gay-Balmaz, O. J. Martin, "Electromagnetic resonances in individual and coupled split-ring resonators," *J. Appl. Phys.*, vol. 92, 2929, 2002.

[66] E. Shamonina, V. Kalinin, K. Ringhofer, *et al.*, "Magneto-inductive waveguide," *Electron. Lett.*, vol. 38, 371, 2002.

[67] A. Vallecchi, S. Chu, L. Solymar, *et al.*, "Coupling between coils in the presence of conducting medium," *IET Microw. Antennas Propag.*, vol. 13, 55, 2019.

[68] A. Vallecchi, E. Shamonina, C. J. Stevens, "Wireless power transfer in the presence of a conducting interface: Analytical solution," *IET Microw. Antennas Propag.*, vol. 13, 725, 2019.

[69] S. Chu, A. Vallecchi, C. Stevens, *et al.*, "Fields and coupling between coils embedded in conductive environments," *EPJ Appl. Metamaterials*, vol. 5, 2, 2018.

[70] W. Yin, A. Peyton, "Thickness measurement of non-magnetic plates using multi-frequency eddy current sensors," *NDT E. Int.*, vol. 40, 43, 2007.

[71] Y.-K. Shin, D.-M. Choi, Y.-J. Kim, *et al.*, "Signal characteristics of differential-pulsed eddy current sensors in the evaluation of plate thickness," *NDT E Int.*, vol. 42, 215, 2009.

[72] J. Moulder, E. Uzal, J. Rose, "Thickness and conductivity of metallic layers from eddy current measurements," *Rev. Sci. Instrum.*, vol. 63, 3455, 1992.

[73] Y. Pan, C. Tai, "Thickness and conductivity analysis of molybdenum thin film in CIGS solar cells using resonant electromagnetic testing method," *IEEE Trans. Magn.*, vol. 48, 347, 2012.

[74] C.-C. Tai, J. H. Rose, J. C. Moulder, "Thickness and conductivity of metallic layers from pulsed eddy-current measurements," *Rev. Sci. Instrum.*, vol. 67, 3965, 1996.

[75] J. Xu, J. Wu, W. Xin, *et al.*, "Fast measurement of the coating thickness and conductivity using eddy currents and plane wave approximation," *IEEE Sens. J.*, vol. 21, 306, 2020.

[76] J. Burkhardt, "Determination of the conductivity and thickness of conductive layers on conductive base materials," *Adv. Mech. Eng.*, vol. 11, 1687814019854234, 2019.

[77] N. Said, B. A. Abu-Nabah, M. Alkhader, "Triple-frequency eddy current estimation of nonmagnetic metal clad thicknesses over nonmagnetic metals," *Meas. Tech.*, vol. 178, 109668, 2021.

[78] Z. Xue, M. Fan, B. Cao, *et al.*, "Enhancement of thickness measurement in eddy current testing using a log–log method," *J. Nondestruct. Eval.*, vol. 40, 1, 2021.

[79] C. D. Le, "Eddy current measurements of thin-film metal coatings using a selectable calibration standard." US Patent 6,549,006.

[80] F. Loete, Y. Le Bihan, D. Mencaraglia, "Contactless device for the fast conductivity characterization of a large range semiconductors," in *Proc. ISSM 2016*, 1, 2016.

[81] N. Bowler, Y. Huang, "Electrical conductivity measurement of metal plates using broadband eddy-current and four-point methods," *Meas. Sci. Technol.*, vol. 16, 2193, 2005.

[82] W. Yin, A. J. Peyton, G. Zysko, *et al.*, "Simultaneous noncontact measurement of water level and conductivity," *IEEE Trans. Instrum. Meas.*, vol. 57, 2665, 2008.

[83] C. Wang, M. Fan, B. Cao, *et al.*, "Novel noncontact eddy current measurement of electrical conductivity," *IEEE Sens. J.*, vol. 18, 9352, 2018.

[84] M. Lu, X. Meng, R. Huang, *et al.*, "A high-frequency phase feature for the measurement of magnetic permeability using eddy current sensor," *NDT E. Int.*, vol. 123, 102519, 2021.

[85] M. Lu, X. Meng, L. Chen, *et al.*, "Measurement of ferromagnetic slabs permeability based on a novel planar triple-coil sensor," *IEEE Sens. J.*, vol. 19, 2904, 2019.

[86] D. Desjardins, T. Krause, L. Clapham, "Transient eddy current method for the characterization of magnetic permeability and conductivity," *NDT E Int.*, vol. 80, 65, 2016.

[87] K. B. Ali, A. N. Abdalla, D. Rifai, *et al.*, "Review on system development in eddy current testing and technique for defect classification and characterization," *IET Cir., Devices Syst.*, vol. 11, 338, 2017.

[88] L. Cheng, G. Y. Tian, "Surface crack detection for carbon fiber reinforced plastic (CFRP) materials using pulsed eddy current thermography," *IEEE Sens. J.*, vol. 11, 3261, 2011.

[89] G. Zenzinger, J. Bamberg, W. Satzger, *et al.*, "Thermographic crack detection by eddy current excitation," *J. Nondestruct. Eval.*, vol. 22, 101, 2007.

[90] T. Chady, M. Enokizono, R. Sikora, "Crack detection and recognition using an eddy current differential probe," *IEEE Trans. Magn.*, vol. 35, 1849, 1999.

[91] G. Y. Tian, A. Sophian, D. Taylor, *et al.*, "Multiple sensors on pulsed eddy-current detection for 3D subsurface crack assessment," *IEEE Sens. J.*, vol. 5, 90, 2005.

[92] N. Nakagawa, "A model of eddy current nondestructive evaluation for a current leaking crack," *NDT E. Int.*, vol. 123, 102517, 2021.

[93] H. Sun, J. Yi, T. Wang, *et al.*, "A new interleaving eddy current array-based sensing film for fatigue crack quantification of bolted joints," *J Intell. Mater. Syst. Struct.*, vol. 32, 1045389X21990891, 2021.

[94] Y. Yu, K. Gao, T. Theodoulidis, *et al.*, "Analytical solution for magnetic field of cylindrical defect in eddy current nondestructive testing," *Phys. Scr.*, vol. 95, 015501, 2019.

[95] L. T. Cung, T. D. Dao, P. C. Nguyen, *et al.*, "A model-based approach for estimation of the crack depth on a massive metal structure," *Meas. Control.*, vol. 51, 182, 2018.

[96] N. Kuyvenhoven, C. Dean, J. Melton, *et al.*, "Development of a foreign object detection and analysis method for wireless power systems," in *Proc. 2011 IEEE Symp. Product Compliance Eng.*, 1, 2011.

[97] K. Chana, D. Cardwell, "The use of eddy current sensor based blade tip timing for FOD detection," in *Turbo Expo: Power for Land, Sea, and Air*, 169, 2008.

[98] K. Hollaus, C. Magele, R. Merwa, *et al.*, "Numerical simulation of the eddy current problem in magnetic induction tomography for biomedical applications by edge elements," *IEEE Trans. Magn.*, vol. 48, 623, 2004.

[99] N. Blaunstein, V. Yakubov, *Electromagnetic and Acoustic Wave Tomography: Direct and Inverse Problems in Practical Applications.* CRC Press, Boca Raton, 2018.

[100] A. Richer, A. Adler, "Eddy current based flexible sensor for contactless measurement of breathing," in *Proc. IEEE Instr. and Meas. Tech. 2005*, 257–260, 2005.

[101] S. Shahrestani, T.-C. Chou, K.-M. Shang, *et al.*, "A wearable eddy current based pulmonary function sensor for continuous non-contact point-of-care monitoring during the covid-19 pandemic," *Sci. Rep.*, vol. 11, 20144, 2021.

[102] M. S. B. Mansor, Z. Zakaria, I. Balkhis, *et al.*, "Magnetic induction tomography: A brief review," *Jurnal Teknologi*, vol. 73, no. 3, 2015.

[103] H. Griffiths, "Magnetic induction tomography," *Meas. Sci. Technol.*, vol. 12, 1126, 2001.

[104] M. Balleza, J. Fornos, N. Calaf, *et al.*, "Monitoring of breathing pattern at rest by electrical impedance tomography," *Arch. Bronconeumol. (Engl. Ed.)*, vol. 43, 300, 2007.

[105] V. Tomicic, R. Cornejo, "Lung monitoring with electrical impedance tomography: technical considerations and clinical applications," *J. Thorac. Dis.*, vol. 11, 3122, 2019.

[106] C. Putensen, B. Hentze, S. Muenster, *et al.*, "Electrical impedance tomography for cardio-pulmonary monitoring," *J. Clin. Med.*, vol. 8, 1176, 2019.

[107] S. A. Rezaeieh, A. Abbosh, "Review of systems for the detection and monitoring of accumulated fluids in the human torso," in *Proc. 2015 Int. Symp. Antennas Propag. (ISAP 2015)*, 1, 2015.

[108] A. H. Sihvola, *Electromagnetic Mixing Formulas and Applications*. The Institution of Electrical Engineers, London, 1999.

[109] E. Tuncer, S. Gubański, B. Nettelblad, "Dielectric mixture formulae and their application to polymer composites," *IEEE Electr. Insul. Mag.*, vol. 9, 809, 2002.

[110] J. Krupka, "Frequency domain complex permittivity measurements at microwave frequencies," *Meas. Sci. Technol.*, vol. 17, 55, 2006.

[111] B. A. Abu-Nabah, "Reduction of lift-off effect in high-frequency apparent eddy current conductivity spectroscopy," *IET Microw. Antennas Propag.*, vol. 28, no. 5, 055107, 2017.

[112] L. Dziczkowski, "Elimination of coil liftoff from eddy current measurements of conductivity," *IEEE Trans. Instrum. Meas.*, vol. 62, 3301, 2013.

[113] A. Yariv, P. Yeh, *Optical waves in crystal propagation and control of laser radiation.* John Wiley and Sons, Inc., New York, NY, 1983.

[114] X. Meng, M. Lu, W. Yin, *et al.*, "Evaluation of coating thickness using lift-off insensitivity of eddy current sensor," *Sensors*, vol. 21, 419, 2021.

[115] N. Vaidya, O. Solgaard, "3D printed optics with nanometer scale surface roughness," *Microsyst. Nanoeng.*, vol. 4, 1, 2018.

[116] P. F. Flowers, C. Reyes, S. Ye, *et al.*, "3D printing electronic components and circuits with conductive thermoplastic filament," *Addit. Manuf.*, vol. 18, 156, 2017.

[117] A. Khan, K. Rahman, D. S. Kim, *et al.*, "Direct printing of copper conductive micro-tracks by multi-nozzle electrohydrodynamic inkjet printing process," *J. Mater. Process. Technol.*, vol. 212, 700, 2012.

[118] C. M. Hong, S. Wagner, "Inkjet printed copper source/drain metallization for amorphous silicon thin-film transistors," *IEEE Electron Device Lett.*, vol. 21, 384, 2000.

[119] J.-U. Park, S. Lee, S. Unarunotai, *et al.*, "Nanoscale, electrified liquid jets for high-resolution printing of charge," *Nano Lett.*, vol. 10, 584, 2010.

[120] J. R. Jian, T. Kim, J. S. Park, *et al.*, "High performance 3D printed electronics using electroless plated copper," *AIP Adv.*, vol. 7, 035314, 2017.

[121] M. J. Kim, M. A. Cruz, S. Ye, *et al.*, "One-step electrodeposition of copper on conductive 3D printed objects," *Addit. Manuf.*, vol. 27, 318, 2019.

[122] J. Tan, H. Low, "Embedded electrical tracks in 3D printed objects by fused filament fabrication of highly conductive composites," *Addit. Manuf.*, vol. 23, 294, 2018.

[123] S. W. Kwok, K. H. H. Goh, Z. D. Tan, *et al.*, "Electrically conductive filament for 3D-printed circuits and sensors," *Appl. Mater. Today*, vol. 9, 167, 2017.

[124] Y. Xie, S. Ye, C. Reyes, *et al.*, "Microwave metamaterials made by fused deposition 3D printing of a highly conductive copper-based filament," *Appl. Phys. Lett.*, vol. 110, 181903, 2017.

[125] D. Zhang, B. Chi, B. Li, *et al.*, "Fabrication of highly conductive graphene flexible circuits by 3D printing," *Synth. Met.*, vol. 219, 79, 2016.

[126] S. Gabriel, R. Lau, C. Gabriel, "The dielectric properties of biological tissues: III. Parametric models for the dielectric spectrum of tissues," *Phys. Med. Biol.*, vol. 41, 2271, 1996.

[127] S. Gabriel, R. Lau, C. Gabriel, "The dielectric properties of biological tissues: II. Measurements in the frequency range 10 Hz to 20 GHz," *Phys. Med. Biol.*, vol. 41, 2251, 1996.

[128] C. Gabriel, S. Gabriel, Y. E. Corthout, "The dielectric properties of biological tissues: I. Literature survey," *Phys. Med. Biol.*, vol. 41, 2231, 1996.

[129] K. S. Cole, R. H. Cole, "Dispersion and absorption in dielectrics I. Alternating current characteristics," *J. Chem. Phys.*, vol. 9, 341, 1941.

[130] P. Ganguly, S. Das, A. Chakrabarti, *et al.*, "Modeling and analysis of lung water content using rf sensor," *IEEE Open J. Instrum. Meas.*, vol. 1, 1, 2024.

[131] F. L. Glauser, A. F. Wilson, L. Carothers, *et al.*, "Pulmonary parenchymal tissue volume measurements in graded degrees of pulmonary edema in dogs," *Circ. Res.*, vol. 36, 229, 1975.

[132] W. T. Joines, Y. Zhang, C. Li, *et al.*, "The measured electrical properties of normal and malignant human tissues from 50 to 900 MHz," *Medical physics*, vol. 21, 547, 1994.

[133] N. R. Lange, D. P. Schuster, "The measurement of lung water," *Crit. Care*, vol. 3, 1, 1999.

[134] Y. Wang, S. Yue, J. Chen, *et al.*, "Conductivity characteristics of human lung tissues," *Int. J. Imaging Syst. Technol.*, vol. 32, 178, 2022.

[135] M. J. Peters, J. G. Stinstra, I. Leveles, "The electrical conductivity of living tissue: A parameter in the bioelectrical inverse problem," in *Modeling and Imaging of Bioelectrical Activity: Principles and Applications*, 281, Springer, New York, 2005.

[136] E. Etoz, C. L. Brace, "Development of water content dependent tissue dielectric property models using mixture theory and genetic algorithm optimization," *IEEE Trans. Biomed. Eng.*, vol. 66, 3431, 2019.

[137] Y. Qin, Y. Chen, T. Wang, *et al.*, "Dielectric properties of rabbit lung tissue under different tidal volumes in vivo," *Bioeng.*, vol. 12, 445, 2025.

[138] J. W. Severinghaus, "Electrical measurement of pulmonary oedema with a focusing conductivity bridge," *J. Physiol.*, vol. 215, 53, 1971.

[139] D. P. Schuster, "The measurement of lung water," *Curr. Opin. Pulm. Med.*, vol. 5, 93, 1999.

[140] O. Boothby, R. Bozorth, "A new magnetic material of high permeability," *J. Appl. Phys.*, vol. 18, 173, 1947.

[141] O. Gutfleisch, M. A. Willard, E. Brück, *et al.*, "Magnetic materials and devices for the 21st century: stronger, lighter, and more energy efficient," *Adv. Mater.*, vol. 23, 821, 2011.

[142] C. Heck, *Magnetic Materials and Their Applications*. The Butterworth Group, London, 2013.

[143] N. A. Spaldin, *Magnetic Materials: Fundamentals and Applications*. Cambridge University Press, Cambridge, 2010.

[144] X. Ma, A. Peyton, Y. Zhao, "Eddy current measurements of electrical conductivity and magnetic permeability of porous metals," *NDT E. Int.*, vol. 39, 562, 2006.

[145] Z. Deng, Z. Yu, Z. Yuan, *et al.*, "Mechanism of magnetic permeability perturbation in magnetizing-based eddy current nondestructive testing," *Sensors*, vol. 22, 2503, 2022.

[146] A. Sophian, G. Tian, D. Taylor, *et al.*, "Electromagnetic and eddy current NDT: a review," *Insight*, vol. 43, 302, 2001.

[147] D. Chung, X. Xi, "A review of the colossal permittivity of electronic conductors, specifically metals and carbons," *Mater. Res. Bull.*, vol. 148, 111654, 2022.

[148] D. Isakov, C. J. Stevens, F. Castles, *et al.*, "A split ring resonator dielectric probe for near-field dielectric imaging," *Sci. Rep.*, vol. 7, 2038, 2017.

[149] W. Zhang, Z. Zhu, Y. Geng, "Simultaneous conductivity and permeability reconstructions for electromagnetic tomography using deep learning," *IEEE T. Instrum. Meas.*, vol. 72, 1, 2023.

[150] I. D. Adewale, G. Y. Tian, "Decoupling the influence of permeability and conductivity in pulsed eddy-current measurements," *IEEE Trans. Magn.*, vol. 49, 1119, 2012.

[151] A. Adler, D. Holder, *Electrical Impedance Tomography: Methods, History and Applications*. IOP Publishing, Bristol, 2021.

[152] S. N. Makarov, G. M. Noetscher, J. Yanamadala, *et al.*, "Virtual human models for electromagnetic studies and their applications," *IEEE Rev. Biomed. Eng.*, vol. 10, 95, 2017.

[153] G. M. Noetscher, P. Serano, W. A. Wartman, *et al.*, "Visible human project® female surface based computational phantom (Nelly) for radio-frequency safety evaluation in MRI coils," *PLoS One*, vol. 16, e0260922, 2021.

[154] A. Adler, A. Boyle, "Electrical impedance tomography: clinical applications and challenges," *J. Electr. Bioimpedance*, vol. 1, 17, 2009.

[155] D. Holder, "Electrical impedance tomography of brain function: imaging during epileptic seizures," *Clin. Neurophysiol.*, vol. 115, 823, 2004.

[156] M. Klein, M. Wolf, O. Oppitz, *et al.*, "Three-dimensional magnetic induction tomography," *Sensors*, vol. 21, 7602, 2021.

[157] M. J. Finnerty, R. J. Halter, A. Hartov, *et al.*, "Magnetic induction tomography: A review," *Prog. Electromagn. Res.*, vol. 159, 47, 2017.

[158] K. Jensen, M. A. Skarsfeldt, H. Stærkind, *et al.*, "Detection of low-conductivity objects using eddy current imaging with an optically pumped magnetometer," *Phys. Rev. Res.*, vol. 1, 033087, 2019.

[159] P. Schneider, A. Scharfetter, H. Brunner, *et al.*, "A 16-channel magnetic induction tomography system for monitoring stroke," *Physiol. Meas.*, vol. 38, 259, 2017.

[160] R. Yerworth, A. Isaacson, H. Griffiths, "Imaging changes in lung air and liquid volumes with magnetic induction tomography," *Physiol. Meas.*, vol. 32, S111, 2011.

[161] S. Jiao, X. Liu, Z. Zeng, "Intensive study of skin effect in eddy current testing with pancake coil," *EEE Trans. Magn.*, vol. 53, 1, 2017.

[162] H. Nam, K.-H. Seol, J. Lee, *et al.*, "Review of capacitive touchscreen technologies: Overview, research trends, and machine learning approaches," *Sensors*, vol. 21, 4776, 2021.

[163] Y. Nam, Y. Park, J. Kim, "Review of capacitive touchscreen technologies: Overview, research trends, and machine learning approaches," *Sensors*, vol. 21, no. 7, 2411, 2021.

[164] Texas Instruments, "Sensitivity, snr, and design margin in capacitive touch applications." https://www.ti.com/lit/an/slaa843a/slaa843a.pdf, 2019. Application Report SLAA843A.

[165] K. Hinckley, C. Holz, M. Sinclair, *et al.*, "Pre-touch sensing for mobile interaction," in *Proceedings of the 2016 CHI Conference on Human Factors in Computing Systems*, 2869–2881, 2016.

[166] J. Lien, N. Gillian, M. E. Karagozler, *et al.*, "Soli: Ubiquitous gesture sensing with millimeter wave radar," in *Proceedings of the 2016 CHI Conference on Human Factors in Computing Systems*, 841–850, 2016.

[167] Synaptics Incorporated, "Touch controller ics." https://www.synaptics.com/products/touch-controllers, 2023.

[168] Goodix Technology, "Touch controller solutions." https://www.goodix.com/en/product/touch, 2023.

[169] Elo Touch Solutions, "Touchscreen technologies overview." https://www.elotouch.com/touchscreen-components/touch-technologies.html, 2023.

[170] Neonode Inc., "Optical touch and gesture sensing." https://neonode.com/solutions/touch-and-gesture, 2023.

[171] S. Fred E., *The Linear Algebra Survival Guide*. Elsevier, London, 2015 ed., 2015.

[172] K. Shailaja, B. Seetharamulu, M. Jabbar, "Machine learning in healthcare: A review," in *Proc. 2nd Int. Conf. Electron., Commun. Aerosp. Technol. (ICECA 2018)*, 910, 2018.

[173] H. Habehh, S. Gohel, "Machine learning in healthcare," *Curr. Genom.*, vol. 22, 291, 2021.

[174] S. Athey, "The impact of machine learning on economics," in *The Economics of Artificial Intelligence: An Agenda* (A. Agrawal, J. Gans, A. Goldfarb, eds.), 507, University of Chicago Press, Chicago, 2018.

[175] P. Gogas, T. Papadimitriou, "Machine learning in economics and finance," *Comput. Econ.*, vol. 57, 1, 2021.

[176] K. I. Roumeliotis, N. D. Tselikas, "ChatGPT and open-AI models: A preliminary review," *Future Internet*, vol. 15, 192, 2023.

[177] G. Giovannetti, N. Fontana, A. Flori, *et al.*, "Machine learning for the design and the simulation of radiofrequency magnetic resonance coils: Literature review, challenges, and perspectives," *Sensors*, vol. 24, 1954, 2024.

[178] K. Youssef, L. Bouchard, K. Haigh, *et al.*, "Machine learning approach to RF transmitter identification," *IEEE J. Radio Freq. ID*, vol. 2, 197, 2018.

[179] A. Al-Jumaily, A. Sali, M. Riyadh, *et al.*, "Machine learning modeling for radiofrequency electromagnetic fields (RF-EMF) signals from mm-wave 5G signals," *IEEE Access*, vol. 11, 79648, 2023.

[180] L. Wu, L. Liu, Y. Wang, *et al.*, "A machine learning-based method to design modular metamaterials," *Extreme Mech. Lett.*, vol. 36, 100657, 2020.

[181] G. Cerniauskas, H. Sadia, P. Alam, "Machine intelligence in metamaterials design: A review," *Oxf. Open Mater. Sci.*, vol. 4, itae001, 2024.

[182] A. Paszke, S. Gross, F. Massa, *et al.*, "Pytorch: An imperative style, high-performance deep learning library," in *Advances in Neural Information Processing Systems 32*, Neural Information Processing Systems Foundation Inc., Vancouver, 2019.

[183] J. H. Friedman, "Greedy function approximation: A gradient boosting machine," *Ann. Stat.*, vol. 29, 1189, 2001.

[184] I. Goodfellow, J. Bengio, A. Courville, *Deep Learning.* MIT Press, Cambridge Massachusetts, 2016.

[185] T. Chen, C. Guestrin, "XGBoost: A scalable tree boosting system," in *Proc. 22nd ACM SIGKDD Int. Conf. Knowl. Discov. Data Min.*, 785, 2016.

[186] O. Sydoruk, A. Radkovskaya, O. Zhuromskyy, *et al.*, "Tailoring the near-field guiding properties of magnetic metamaterials with two resonant elements per unit cell," *Phys. Rev. B*, vol. 73, 224406, 2006.

[187] C. Rong, L. Yan, L. Li, *et al.*, "A review of metamaterials in wireless power transfer," *Materials*, vol. 16, 6008, 2023.

[188] C. J. Stevens, "Magnetoinductive waves and wireless power transfer," *IEEE Trans. Power Electron.*, vol. 30, 6182, 2014.

[189] C. J. Stevens, I. Spanos, A. Vallechi, *et al.*, "3D printing of functional metal and dielectric composite meta-atoms," *Small*, vol. 18, 2105368, 2022.

[190] C. J. Stevens, "A magneto-inductive wave wireless power transfer device," *Wirel. Power Transf.*, vol. 2, 51, 2015.

[191] E. Shamonina, "Slow waves in magnetic metamaterials: History, fundamentals and applications," *Phys. Status Solidi B*, vol. 245, 1471, 2008.

[192] M. Rai, *The investigation of MINIVNAPRO Vector Network Analyzer.* Vaasan ammattikorkeakoulu, 2015.